Supercapacitor Modelling, Analysis and Design



Ross Drummond

St Cross College

University of Oxford

A thesis submitted for the degree of

Doctor of Philosophy

Hilary 2017

Abstract

This thesis develops tools for the analysis and design of electrochemical energy storage devices known as supercapacitors. Supercapacitors are characterised by low internal resistances, high capacitances as well as limited degradation and temperature influence. They are typically used for high power applications, and have been successfully implemented within hybrid power sources and for wind turbine fault ride through amongst other applications. Methods from systems and control theory are employed in this thesis to form a reliable supercapacitor design methodology, based upon high fidelity modelling, for the construction of cheaper supercapacitors with improved performance.

The first part of the thesis considers supercapacitor model development and analysis. A model is introduced that describes the electrochemistry of the supercapacitor energy storage mechanism. This model is called a physics based model and is described by a set of partial differential equations (PDEs). A computationally efficient implementation of this model, based upon spectral collocation spatial discretisation of the PDEs, is proposed. This allows the model to be effectively implemented and analysed as a nonlinear finite dimensional system. The extent to which model information can be extracted from current-voltage data is considered using an observability and parameter estimation analysis. A mathematical transformation from the electrochemical PDEs to an equivalent circuit representation is described, linking the two main supercapacitor modeling approaches in a quantitative manner. A framework for supercapacitor design is proposed that relates energy storage properties, including the resistance, capacitance, dissipated energies and maximum safe voltages, to the electrochemical parameters, such as the diffusion coefficient of the electrolyte and the electrode's conductivity. This relationship is obtained via the solution of a convex optimisation problem and so can be easily obtained. Using this design approach reduces the number of physical experiments needed to be carried out, making the

design process faster, cheaper and more detailed. The problem of configuring the layers of supercapacitors with structured electrodes is considered, and it is shown that destroying the single phase nature of the electrodes radically alters their frequency response. These results bring a fresh perspective to the supercapacitor design problem, by adding rigorous mathematical modelling and analysis.

The second part of the thesis develops tools for the local stability analysis of nonlinear systems. A Lyapunov function is proposed for nonlinear systems that can be represented as the feedback interconnection of a linear system with a nonlinearity which is decentralised, sector bounded and slope restricted. A main result is to relax strict positivity of many of the terms of this Lyapunov function by utislising information about the nonlinearity. These results are extended to systems that evolve along a vector field which is a rational function of the states and the nonlinearity, with positivity of many terms of a polynomial Lyapunov function again being relaxed. Relaxing the strict positivity conditions of the terms of these Lyapunov functions results in less conservative stability certificates for the systems. Verification of the stability conditions is expressed as the solution to a convex semi-definite program, and so can be efficiently computed. The supercapacitor model was a particular example of the class of nonlinear systems considered, with the inspiration behind this work being the desire to obtain less conservative bounds for the supercapacitor resistance.

Contents

1 Introduction **16**

1.1 Energy Storage Devices 16

1.2 Supercapacitors 20

1.3 Objectives 29

1.4 Structure of Thesis 29

1.5 Contribution 30

2 Electrochemical Supercapacitor Model Development **33**

2.1 Introduction 33

2.2 Mathematical Description of Supercapacitor Model 33

2.3 Model Assumptions and Relations 36

2.4 Spectral Methods 43

2.5 Differential Algebraic Equations 46

2.6 Results 49

2.7 Conclusion 59

3 Model Parameter Estimation and Observability **62**

3.1 Observability Analysis 63

3.1.1 Local Nonlinear Observability 64

3.1.2 Unobservable Concentration States 66

3.1.3 Integrator Dynamics 69

3.2 Parameter Estimation of Electrochemical Supercapacitor Model . . . 71

3.2.1 Experimental Setup 71

3.3 Parameter Estimation 72

3.4 Conclusions 78

4 Circuit Synthesis of Electrochemical Supercapacitor Models **80**

4.1 Equivalent Circuit Models 81

4.2 Circuit Synthesis 83
4.3 Conclusion 92

5 Design Tools for Electrochemical Supercapacitors Using Local Absolute Stability Theory 93
5.1 State Transformed Electrochemical Supercapacitor Model 95
5.2 System Properties 101
5.2.1 Case 1: Stability 105
5.2.2 Case 2: Maximum Reachable Set with Unit Energy Impulse . 105
5.2.3 Case 3: Bounds on Stored and Dissipated Energy 106
5.2.4 Case 4: Capacitance and Resistance 107
5.2.5 Maximum Voltage Limits 109
5.2.6 Absolute Stability Theory for Energy Storage Devices 112
5.3 Conclusion 112

6 Supercapacitors With Structured Electrodes 114
6.1 Design Metrics: Real and Imaginary Capacitance 115
6.2 Structured Electrode Supercapacitor Model 118
6.3 Model Experimental Verification and Capacitances 122
6.4 Circuit Representation of Structured Electrodes 130
6.4.1 Series Circuit 130
6.4.2 Parallel Circuit 130
6.4.3 Circuit Realisations 131
6.5 Conclusion 135

7 Regional Analysis of Slope Restricted Lur'e Systems 139
7.1 The Sector Bounded Approach to Absolute Stability 140
7.1.1 Contribution 141
7.2 Problem statement 142
7.3 Sector inequalities 144
7.4 Main results 146
7.4.1 Inclusion conditions 149
7.4.2 Discussion on the proposed LF 151
7.5 Numerical Formulation and Examples 153
7.6 Conclusions 157

8 Generalised Absolute Stability using Lyapunov Functions that are not Sum-of-Squares **159**
8.0.1 Introduction . . . 159
8.1 Problem Statement . . . 160
8.2 Main Results . . . 161
8.3 Numerical Formulation . . . 163
8.3.1 SOS Formulation . . . 163
8.4 Examples . . . 165
8.4.1 Nonlinearities . . . 165
8.4.2 Numerical Example 1: Switched Systems . . . 165
8.4.3 Numerical Example 2: Vehicle Stability . . . 165
8.5 Conclusion . . . 167

9 Summary of Thesis **170**
9.1 Review of Chapters . . . 170
9.2 Future Research . . . 174

Bibliography **177**

List of Figures

1.1 Predicted growth in the hybrid electric vehicle (HEV) market. Image obtained from [134] 21
1.2 A dielectric capacitor. 22
1.3 The standard construction of a supercapacitor. Two electrodes are separated by an electrical insulator called a separator with an electrolyte containing ions flooding both the electrodes and separator. Attached to either end are current collectors which transfer current to and from the device. 22
1.4 The double layer at the interface between the solid electrode and the liquid electrolyte. The ions pack themselves in the different layers. . . 24
1.5 A commercial supercapacitor from Maxwell Technology. 25
1.6 A Ragone plot showing energy and power densities of various energy storage systems. Image obtained form [173]. 26

2.1 The voltage/current responses of (2.33) and (2.34) for the standard charging profile discretised using the FDM and SEM with the experimental data of [163]. 51
2.2 The normalised errors of (2.33) and (2.34) discretised using the SEM and FDM, with the reference solution being obtained from COMSOL. 53
2.3 Simulation computing times for the standard charging profile of (2.33) and (2.34) discretised using the FDM and SEM. Computing times were recorded using the MATLAB 'tictoc' command. 54
2.4 The voltage/current response of the non-linear models and experimental data of [163] for the standard CC-CV charging profile. 55
2.5 The state distribution of the non-linear models after 23.2 s of the standard charging profile. 56

2.6 The state distribution of the non-linear models after 23.2 s of the standard charging profile with the electrolyte concentration reduced from 930 mol/m^3 to 250 mol/m^3. 57
2.7 The state distribution of the non-linear models after 130 s of the extended charging profile. 58
2.8 The variation of real and imaginary capacitance with input current frequency. Obtained using an electrochemical impedance spectroscopy simulation with an input current of 2 A overlaid with a small-amplitude 0.1 A sinusoidal signal. 60

3.1 Singular values of the observability matrix $\boldsymbol{O}$ for two different linearisation points and for when the transference numbers are chosen such that the model is linear. 68
3.2 Differences between the voltages from simulations of the linear and non-linear models starting from two different initial conditions, $\boldsymbol{c} = 200$ mol m^{-3} and $\boldsymbol{c} = 930$ mol m^{-3}. 69
3.3 Random walk dynamics of the model output v with a Kalman filter implementation of (3.19) and (3.20). 71
3.4 Identification in the time domain. 73
3.5 EIS data at a steady state voltage of 0.5 V. 76
3.6 EIS data at a steady state voltage of 1.5 V. 76
3.7 EIS data at a steady state voltage of 2.5 V. 76
3.8 The simulated diffusion of the ionic concentration during the square wave input charging profile. 77

4.1 Classical circuit. 82
4.2 Dynamic circuit. 82
4.3 Ladder circuit. 82
4.4 Bode plot of the three synthesized circuits and full order linearised physical model. 88
4.5 Singular values of the Hankel operator Γ_G. 89
4.6 Variation of the time constants of the dynamic circuit during a charge with sinusoidal current. 92

5.1 The supercapacitor model expressed in a feedback loop with the logarithmic nonlinearity being treated as an input. 98

5.2 The reformulated supercapacitor model loop structure with the separation of the integrator and dynamical subsystems. 100
5.3 The locally sector bounded nature of the shifted logarithm. 103
5.4 Simulation results and experimental data of the SAFT America supercapacitor. The data and the model parameters were obtained from [163]. The supercapacitor was rested for 5s before a 100A current was applied for 23s. After this charge, the current was removed and the voltage returned to an steady-state. 107
5.5 Simulation results and experimental data from [47] for the square wave charging of the Maxwell Technologies supercapacitor. 108
5.6 Variation in the $\mathcal{L}_2$ gain of the dynamical subsystem, describing resistance, and the capacitance as functions of the electrode lengths for the Maxwells Technologies supercapacitor. 108
5.7 The maximum voltage of the SAFT America supercapacitor such that potential across the double layer never exceeds the overpotential as a function of current I. 110

6.1 A supercapacitor with structured electrodes. The porous electrodes are formed of two layers with different material properties and thicknesses. 115
6.2 Schematic of the structured electrode spray forming process. Image obtained from [73]. 116
6.3 Evolution of the ionic concentration and potential difference across the double layer with a sinusoidal charging current $i = \sin(t)$ for the structured layer supercapacitor with two equal length layers in the electrode. 120
6.4 Impedance function plots for a supercapacitor with a structured electrode layer length ratio of $8L_1 = L_2$. Both Experimental and model simulation results are shown. 126
6.5 Impedance function plots for a supercapacitor with a structured electrode layer length ratio of $L_1 = L_2$. Both Experimental and model simulation results are shown. 127
6.6 Capacitances as a function of frequency. Model simulation results are shown for the structured electrodes with a layer length ratio of $L_1 = L_2$. Both spatial configurations of the electrode layers are plotted as well as single layer electrodes composed of each layer material. Experimental data is also shown for the first structured electrode configuration. . . 128

6.7 A sweep of real and imaginary capacitances over the ratio of the structured electrode layers. 129
6.8 The circuit realisation of the structured electrode supercapacitor. . . 132
6.9 The circuit realisation of the proposed structured electrode supercapacitor with the newly proposed layering. 133
6.10 Real and imaginary capacitances of single layer supercapacitors and their parallel and series interconnections. 134

7.1 History of the piecewise quadratic Lyapunov function for stability analysis of slope-restricted nonlinear systems. 152
7.2 Estimate of the region of attraction with the Lyapunov function (7.10) (dark blue). Trajectories asymptotically converging to the origin are shown in green, while diverging trajectories are depicted in red . . . 157
7.3 Induced $\mathcal{L}_2$ gain bounds for an idealised Stirling engine. 158

8.1 Feedback interconnection of sector bounded nonlinearity with a rational vector field. 160
8.2 Trajectories of (8.14) from different initial conditions are depicted in red solid lines. Level sets of the computed function $V(x, \phi(y(x)))$ are depicted in solid blue lines. The black dashed lines correspond to the set $\{x \in \mathbb{R}^2 || \tan^{-1}(y(x))| = 0.8\}$. 166
8.3 Estimate of the region of attraction (black solid) of the vehicle model of numerical example 4 obtained using the polynomial Lyapunov function of Proposition 8.3. Also shown are sublevel sets of the Lyapunov function (black dashed), stable trajectories of the system (blue) and unstable trajectories (red). 168

List of Tables

1 Parameters 10
2 Variables 11

1.1 Pros and cons of various energy storage mechanisms. Figures primarily obtained from [43]. 18

2.1 The supercapacitor model equations as described by [163]. The electrode length is denoted L_{elec} and the separator length by L_{sep}. 39
2.2 The supercapacitor model boundary conditions as described by [163]. 40
2.3 Supercapacitor model equations. 42
2.4 Parameters for the supercapacitor model [163]. 50
2.5 Separate parameters for both the separator and electrode regions [163]. 50

3.1 Identified parameters of the PB model for different steady state voltages V_{ss}. 72
3.2 Identified parameters of the EC for different steady state voltages V_{ss}. 72
3.3 Fixed parameters of the PB model. 74

4.1 Resistor and capacitor values for the synthesized classical, dynamic and ladder circuits. 88

6.1 Electrochemical model equations for a supercapacitor with two layer structured electrodes. 121
6.2 Boundary conditions for a supercapacitor with two layer structured electrodes. 121
6.3 Global parameters for the supercapacitor model with structured electrodes. 124
6.4 Local parameters for the different domains of the supercapacitor model with structured electrodes. 125

7.1 Local sector and slope bounds for the nonlinearities 151

7.2 Maximum bound on ϵ for global stability of system $G_1(s)$. The bounds were obtained using the bisection algorithm. 156

Notation

Symbol	Definition	Units
L_{elec}	Electrode length	m
L_{sep}	Separator length	m
N	Number of elements in the domain	
aC	Specific capacitance	F/m^3
U	Ionic flux	mol/m^2s
R	Universal gas constant	J/K mol
F	Faraday constant	C mol^{-1}
T	Temperature	K
ζ	Ionic charge	C
c_0	Initial Salt concentration	mol/m^3
κ	Electrolytic conductivity	S/m
κ_∞	Free solution electrolytic conductivity	S/m
σ	Electrode conductivity	S/m
D	Diffusion coefficient	m^2/s
Γ	Tortuosity	
t_j	Ion transference number	
$\frac{dq_j}{dq}$	Change in surface concentration of species j associated with a change on the surface charge of electrode	
ϵ	Porosity void fraction	
S	Electrode surface area	m^2
x	Spatial variable	m

Table 1: Parameters

Symbol	Definition	Units
c	Electrolyte concentration	$\mathrm{mol/m^3}$
ϕ_1	Electrode potential	V
ϕ_2	Electrolyte potential	V
v	Voltage	V
I	Current	A
i	Current density	$\mathrm{A/m^2}$
i_1	Current density in the solid phase	$\mathrm{A/m^2}$
i_2	Current density in the liquid phase	$\mathrm{A/m^2}$

Table 2: Variables

- Matrices and vectors are denoted in bold font.

Acknowlegements

The past three years of my DPhil would not have been the rewarding time that it was without the fantastic people that I had the pleasure to have around me. I would now like to take some time to express my gratitude towards these people, but, upon writing this section, I have found that I can not fully express my true feelings in the limited number of words here.

First and foremost, I would like to thank my supervisor Prof. Stephen Duncan. I could not have asked for a better supervisor, with your advice always seeming to be both smart, sensible and illuminating. You taught me to have an open mind, to not get carried away with oneself and to talk to those outside my field in a way such that a common language can exist between us, tools which I will carry with me for the rest of my life. The amount of "face time" that I experienced during my supervision was fantastic for a fresh faced DPhil student like myself, and it really pushed me forward during my research. In the same vein, I would to express my gratitude to Dr David Howey for our many chats, and I regret not going down to your office more. During my DPhil, I had the great pleasure of working with many brilliant people including Giorgio, Shi and Ann. Each of you were truly inspiring to work with and I hope to carry on our efforts in to the future!

To survive through a DPhil, one needs periodic burst of fun and joy to alleviate the long work hours. I was lucky enough to have such joyous moments thanks to my close band of wonderful friends, each of whom made the time pass too quickly in their own weird and uniquely fun way. Greg and Rachel, you guys are the best. I'm remembering all our meals, crafting and nature sessions with a smile on my face and am so grateful to have such a close band of friends in Oxford that I could always call on. It was always a good time with you. Then, I have to thank the London gang of Mickey, Kuba and Long. With you guys, the jokes came thick and fast and I've never laughed as much as when in your company. I would also like to thank the many diverse and intriguing characters that I shared the office with during these three

years. I will miss the late night chats, the heated debates and the diverse opinions which we shared and which made the office such a strangely special place at times. I will also say a special word to my family for their unwavering support during this time, thanks.

Finally, I have to thank Carolanne. Unfortunately due to the distance between us, we weren't able to spend as much time together during these 3 years as I would have liked, but it meant that I always looked forward to your weekend visits, where I would catch up on the many joys of life with you. To the times ahead and the many more adventures we will experience!

List of Publications

Journal Publications

- G. Valmorbida, R. Drummond and S. R. Duncan, "Regional Analysis of Slope Restricted Lur'e Systems," *Under Review at IEEE Transactions on Automatic Control.*
- R. Drummond, S. Zhao, D. A. Howey and S. R. Duncan, "Design Tools for Electrochemical Supercapacitors Using Local Absolute Stability Theory," *Under Review at IEEE Transactions on Control Systems Technology.*
- R. Drummond, S. Zhao, D. A. Howey and S. R. Duncan, "Circuit Synthesis of Electrochemical Supercapacitor Models," *Accepted for publication in the Journal of Energy Storage.*
- R. Drummond, D. A Howey and S. R. Duncan, "Low-order mathematical modelling of electric double layer supercapacitors using spectral methods," *Journal of Power Sources 277(2015):317-328.*

Conference Proceedings

- R. Drummond, G. Valmorbida and S. R. Duncan, "Equivalent Circuits for Electrochemical Supercapacitor Models," *Under review for the IFAC 2017 World Congress, Toulouse, France, 2017.*
- G. Valmorbida, R. Drummond and S. R. Duncan, "Positivity Conditions of Lyapunov Functions for Systems with Slope Restricted Nonlinearities," *2016 American Control Conference, Boston, MA, 2016.*

- R. Drummond, G. Valmorbida and S. R. Duncan, "Lyapunov Analysis of Nonlinear Systems With Rational Vector Field and Jacobian," *2016 UK Automatic Control Conference, Belfast, UK, 2016.*
- R. Drummond and S. R Duncan, "Parameter Estimation of an Electrochemical Supercapacitor Model," *2016 European Control Conference, Aarlberg, Denmark, 2016.*
- R. Drummond and S. R. Duncan, "On Observer Performance for an Electrochemical Supercapacitor Model," *2015 Multi-Conference on Systems and Control, Sydney, NSW, 2015.*
- R. Drummond and S. R. Duncan, "A Lyapunov Function for a PDE model of a Supercapacitor," *2015 Control and Decision Conference, Osaka, Japan, 2015.*

Chapter 1

Introduction

1.1 Energy Storage Devices

Energy storage is considered as a key technology for the coming century [50, 81, 129, 140]. The technology can be regarded as introducing a delay between the generation and consumption of energy to enable energy to be transferred between different mediums. In our solar system, all energy is ultimately derived from the sun and for millenia, different natural mechanisms have evolved to harvest this energy. The development of technology in the modern era has driven a need for energy that has been satisfied by the combustion of fossil fuels such as oil, natural gas and coal. Currently, these fuels have unmatched energy storage performance for the majority of applications, as they are reliable, simple to transport physically and provide large energy and power densities[1]. The utilisation of these fuel sources has enabled humanity to make rapid strides forward in our development, facilitating mass industrialisation and the widespread adoption of personal vehicles. Fossil fuels are at a stage of technological maturity, being well understood, relatively cheap and having large corporations, institutions and markets presiding over their usage. However, scientists are now in agreement that the combustion of these fuels is having a detrimental effect upon the world's climate, which will lead to unsustainable weather patterns in the future [112]. The combustion of fossil fuels also releases hazardous toxic fumes, making them unsuitable for personal applications. This implies that the future of energy storage does not lie with fossil fuels, with it being imperative that society is weaned off these resources.

[1]Density meaning per unit mass.

Energy storage is separate from power generation. Power generation supplies energy for the immediate consumption by a user. Recently there has been a sharp rise in the use of renewable energy generating systems, such as wind turbines and photoelectric cells, to replace coal burning plants. These "green" technologies are still developing, with cheaper generators capable of capturing energy more efficiently being needed to replace fossil fuels entirely. The impact on grid stability with the increased use of such green power generator systems also has to be better understood, as these generators take control away from the grid operator (who could previously burn coal in a plant when required) and hands it over to unpredictable natural forces, such as the wind strength. Nuclear energy has also been used in this context, but it suffers from many of the same problems as fossil fuels, with a dangerous waste that has to be managed for many years and issues with public confidence. Hydro electric generators store gravitational energy via damming water tributaries, which can lead to a fairly reliable source of cheap power at the expense of environmental disruption and population displacement.

The use of energy storage can benefit the performance and stability of a system. It can also allow energy to be arbitraged, by capturing energy in times of surplus and releasing it in times of scarcity. Several energy storage technologies are summarised in [77] with the advantages and disadvantages of some expressed in Table 1.1. Typical energy storage devices include flywheels where energy is stored via a rotating disk placed in a vacuum, compressed air where air is compressed and released during periods of low and high energy demand and thermal energy storage where energy is stored through the medium of heat. The most popular form of small scale energy storage uses electrochemical storage mechanisms, examples of such storage devices being fuel cells, batteries and supercapacitors.

Fuel cells convert the free energy associated with a chemical reaction into electrical energy, but differ from batteries as the fuel and oxidant are not contained within the storage device but are supplied externally [173]. A common fuel cell converts hydrogen and oxygen into water [145], with the only waste produced being usable water. This makes fuel cells theoretically very beneficial to the environment and they also have high energy densities as their fuel is supplied externally. However, fuel cells suffer from significant degradation when operating at high discharge rates and also suffer from the availability of their fuel, as hydrogen is expensive to extract and store.

Device	Advantage	Disadvantage
Supercapacitor	Very high power density ($\approx$ 2-10 kW kg^{-1}). Mildly temperature dependent. No significant degradation (cycle life $\approx 10^5 - 10^6$ cycles).	Low energy density ($\approx$ 0.5-15 Wh kg^{-1}).
Li-ion batteries	High energy density ($\approx$ 100-250 Wh kg^{-1}). High power density ($\approx$ 0.3 - 1.5 kW kg^{-1}).	Suffers from degradation (cycle life $\approx$ 50010^4 cycles). Temperature dependent. Expensive ($\approx$ 900-1300 \$ kW^{-1} h^{-1}).
Fuel cells	High energy density ($\approx$ 200-1000 Wh kg^{-1}). Clean waste.	Very low power densities. ($\approx$ 10-500W kg^{-1}) Suffers from degradation (cycle life $\approx 10^4$ cycles). Obtaining fuel can be costly.
Fly wheels	High energy density ($\approx$ 5-100 Wh kg^{-1}). No significant degradation (cycle life $\approx 10^5 - 10^7$ cycles). Not temperature dependent.	Space constrained. Expensive ($\approx$ 400-800 \$ kW^{-1} h^{-1})
Fossil fuels	Excellent power ($\approx$ 50 kW kg^{-1}) and energy density ($\approx$ 50-1000 Wh kg^{-1}). Cheap & easily transportable.	Damage the environment. Produce toxic fumes.
Hydroelectric	Energy can be release on demand. Appropriate for large scale storage.	For large scale applications. Environmental issues.

Table 1.1: Pros and cons of various energy storage mechanisms. Figures primarily obtained from [43].

Batteries are the most popular and mature form of electrochemical energy storage and are used for most small scale electrical energy storage applications including personal electronics and electric vehicles. They are constructed of two electrodes separated by an electrical insulator. One of the electrodes, called the anode, has a negative charge and is an electron donor while the other, called the cathode, has a positive charge and is an electron receiver. Each electrode is made from a different material, each with its own standard electrode potential. During charging, a reduction-oxidation (redox) reaction takes place within the battery cell with positive ions being attracted to the cathode and negative ions being attracted to the negative anode. Electrons flow through the wire connecting the two electrodes to complete the circuit.

The chemistry of the different components of the battery has a significant impact upon its performance. Traditional batteries are the so-called "lead-acid" batteries which power the electronics of the majority of cars with internal combustion engines [10]. Due to their age and popularity, these batteries are fairly well understood, but are being replaced by more modern devices. Since their commercial introduction in 1991 [111], the "lithium ion" battery (shortened to "Li-ion") has become the dominant player in this market. These batteries offer a combination of excellent energy and power densities together with relative reliability. The introduction of such batteries addressed the power and energy requirements for the growing portable personal electronics sector, which required high powers to increase computational capability and high energies that allow portability. The performance of the battery is often the limiting factor in these portable electronic technologies and the growth of this technology sector has stimulated the resulting growth in lithium ion battery technology. These batteries are now almost ubiquitous in modern society, since they are found in the majority of smart phones and laptops, and it is projected that they will become even cheaper with improved performance as manufacturing techniques improve and a better understand of their chemistry is acquired.

A step change in manufacturing capability of lithium ion batteries is being projected with the "Gigafatory" being developed by Tesla, which is bringing advanced automation techniques to lithium ion manufacturing. Economic factors will play a key role in enabling lithium ion batteries to satisfy the increased market demand, as expressed in Figure 1.1 which shows the predicted growth in hybrid electric vehicles (HEV) from [134]. However, Li-ion batteries still have many drawbacks. For example lithium is not an abundant material and will become even more expensive as deposits are exhausted [51]. The chemical reactions occurring within the battery are also highly

temperature dependent, which may result in the battery catching fire due to thermal runaway if charged too aggressively [168]. Recent examples of thermal runaway commercial products include the Samsung Note 7 and the Boeing Dreamliner 787 [172]. The battery also suffers from many mechanisms of degradation, reducing its energy and power capability, with lifespans limited to around 1000 charge-discharge cycles [164]. The dynamics of lithium ion batteries are also highly nonlinear and complex, making it difficult to predict the exact availability of power and energy remaining within the battery [108]. This uncertainty has hindered the mass adoption of lithium ion batteries in some sectors such as hybrid electric vehicles (HEVs), where "range anxiety", the driver's fear that they will run out of energy and not be able to rapidly recharge, is a key hurdle to the adoption of this technology. Other chemistries have been proposed to overcome these issues, including those with electrodes constructed from $LiMn_2O_4$ [152], magnesium [7, 109] and silicon [152], however, all of these new chemistries have not reached the level of maturity of Li-ion batteries and are a long time from being commercially viable.

1.2 Supercapacitors

Batteries and fuel cells are good at storing large amounts of energy, but are not suited to releasing energy at high rates, as this leads to degradation and unstable chemical reactions to occur [164]. Traditionally, the most common high power electrical energy storage element was the dielectric capacitor. This device has the structure of Figure 1.2 with two electrically conducting plates separated by an electrical insulator. When charged, one of the plates obtains a negative charge while the other obtains a positive charge. When the charging current is removed, the electromagnetic force between the two oppositely charged plates holds the charge of the plate, acting as the storage element. The energy stored in a capacitor satisfies

$$E = \frac{1}{2}CV^2 \tag{1.1}$$

where E is energy, C is capacitance and V is voltage. For the flat plate dielectric capacitor, capacitance is proportional to the surface area of the the plates A and is inversely proportion to the separating distance between the two plates d

$$C \propto \frac{A}{d}. \tag{1.2}$$

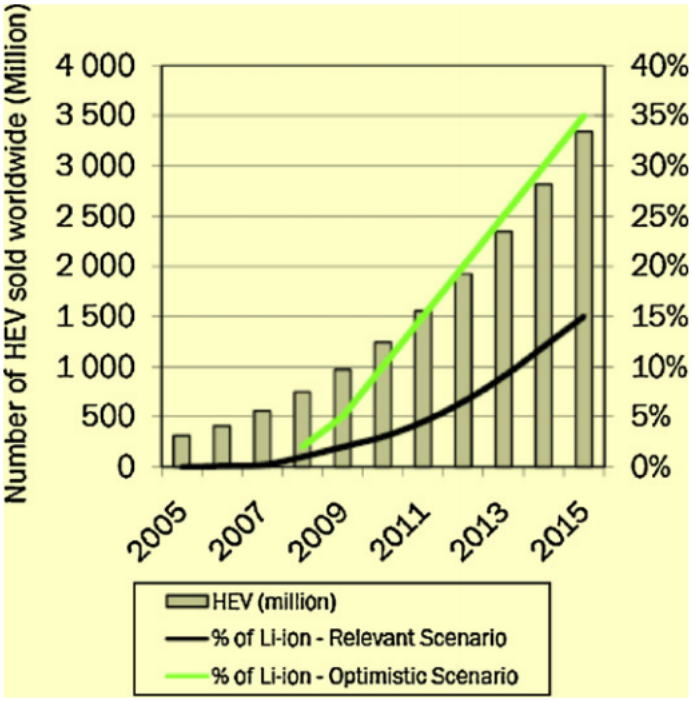


Figure 1.1: Predicted growth in the hybrid electric vehicle (HEV) market. Image obtained from [134]

The maximum voltage is determined from the breakdown voltage of the dielectric. The energy storage mechanism of a dielectric capacitor is electrostatic, which allows for rapid charging and discharging. However, as it is only possible to manufacture plates of finite size and spacing, the energy densities of such capacitors are low, which has limited their use in practice.

To overcome the issue of low energy density, devices known as supercapacitors, otherwise known as double layer capacitors, ultracapacitors and electrochemical supercapacitors, have been developed [95]. These are the electrical energy storage devices that are addressed in this thesis. A supercapacitor has a similar construction to a battery as shown in Figure 1.3 with a commercial supercapacitor from the company Maxwell Technology being shown in Figure 1.5. Two electrodes, typically made of porous carbon (often called activated carbon), are separated by an electrical insulator called the separator, which prevents the oppositely charged electrodes from short circuiting. In a supercapacitors, both the anode and the cathode can be identical since no chemical reactions are needed. An electrolyte containing ions floods both the electrodes and the separator. These ions carry charge through the supercapacitor, completing the circuit. Current collectors, typically made from a highly conductive metal such as copper, are attached at each electrode to transfer current to and from

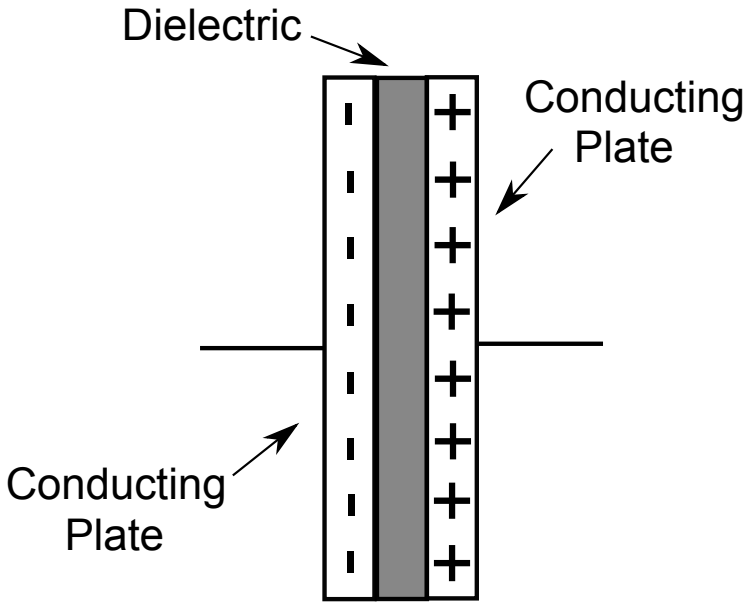


Figure 1.2: A dielectric capacitor.

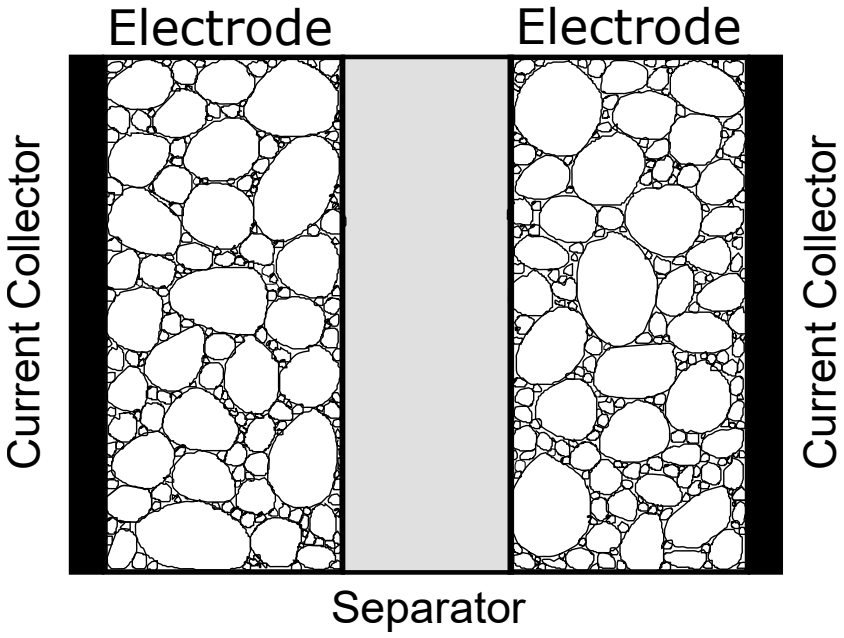


Figure 1.3: The standard construction of a supercapacitor. Two electrodes are separated by an electrical insulator called a separator with an electrolyte containing ions flooding both the electrodes and separator. Attached to either end are current collectors which transfer current to and from the device.

the supercapacitor. The main difference between a battery and a supercapacitor is that the dominant energy storage mechanism in supercapacitors is electrostatic, not chemical based. Even though supercapacitors use the same storage mechanism as standard dielectric capacitors, they have significantly greater energy densities. The two main reasons for the increased greater energy densities of supercapacitors are:

- The double layer.
- The porosity of the electrodes.

Each of these phenomena are now explained but are given a more detailed description in [95]. The double layer occurs at the boundary between the electrode and the electrolyte. Assume that the electrode is charged with a negative charge. This attracts positive electrolytic ions towards it which are adsorbed onto the surface. The separating distance between the positive charge of the adsorbed ion in the electrolyte and the negative charge in the solid electrode is at the molecular scale, which is the width of a solvated water molecule for the case of aqueous electrolytes. This region is known as the compact layer or the Stern layer [95]. Further away from this boundary, another layer forms, known as the diffuse layer, where a continuous distribution of electrolyte ions is driven by thermal motion [95]. This model of capacitance is often known as the Guoy-Chapman-Stern model [95]. It is noted that the term "double layer" does not refer to the combination of the Stern and Diffuse layers, but reflects the fact that a charge separating layers forms at each of the two electrodes [95]. A representation of the double layer is shown in Figure 1.4. The electrodes of a supercapacitor are typically made from porous carbon [120] with very high surface areas, as ions can "burrow" down inside the pores. From the definition of capacitance in (1.2), the double layer causes the supercapacitor to have a very small charge separation distance d (molecular due to the ionic adsorption) and a very large A due to the high surface area electrodes, which provides their large capacitance values and energy densities. In this context, a supercapacitor can be considered to almost be an ideal flat plate capacitor, which would have very large plates that are very close together.

The first description of what became known as double layer capacitance was described by Helmholtz in 1853 [137] and the first patent describing the concept of a supercapacitor was obtained by H.I. Becker of General Electric in 1957 [137]. The use of supercapacitors for an energy storage application was first patented by Robert Rightmire from Standard Oil of Ohio in 1966 [137]. The electrodes of these original supercapacitors were made from activated carbon (carbon with porosity) obtained from

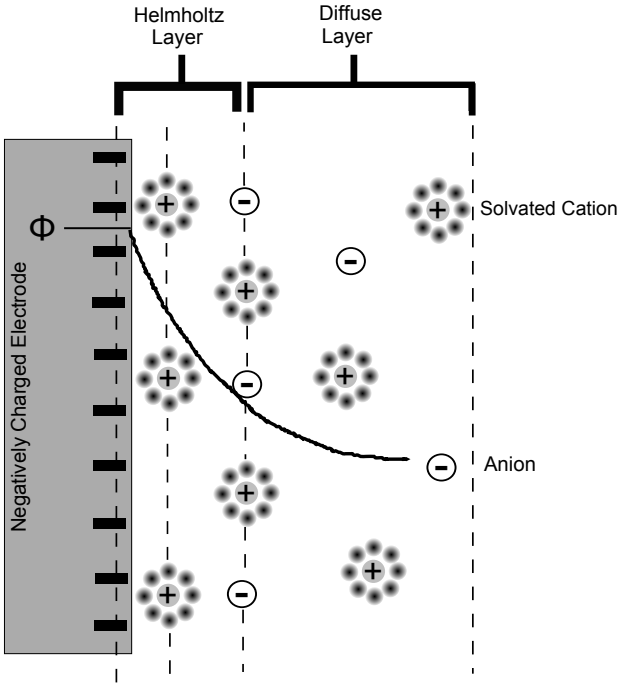


Figure 1.4: The double layer at the interface between the solid electrode and the liquid electrolyte. The ions pack themselves in the different layers.

coconuts. The use of coconuts as the electrode material meant that the electrodes were cheap but also had limited capacitance and high resistance. In recent years, material scientists have developed more advanced carbon based materials which have greatly improved electrode supercapacitor electrical energy storage performance, with electrode surfaces areas of the order of 1000 m^2 g^{-1} being recorded. These materials include carbon nanotubes, where the carbon atoms are connected in a cylindrical structure and graphene where the carbon atoms are in a honeycomb lattice structure [188, 189]. Researchers have also looked beyond carbon for electrodes, with materials such as metal oxide frames [138] being proposed as they have potentially much greater surface areas compared with carbon based electrodes.

There are three main types of supercapacitor electrolytes: organic, aqueous and solid state. Organic electrolytes have maximum voltages of 2-2.5V, giving large energy values [137]. Aqueous electrolyte have excellent conductivity but a limited a maximum voltage of around 1V [137]. Solid state electrolytes allow greater packing and safety, as they replace the flammable and air sensitive liquid electrolyte by an inert and flexible gel, but they have limited power rates [72]. To overcome the fundamental limitations connected with electrostatic energy storage, the use of pseudocapacitance has been



Figure 1.5: A commercial supercapacitor from Maxwell Technology.

proposed, where a capacitance mechanism is introduced through a highly reversible Faradaic reaction [31, 32]. This concept begins to blur the lines between a supercapacitor and a battery although it introduces many of the same problems associated with batteries, i.e. greater temperature dependence and increased degradation.

The performance of an energy storage device is normally evaluated using a Ragone plot [26]. An example of such a plot is shown in Figure 1.6 which shows the energy and power density of different devices for a given charging profile, with different publications using different charging profiles to construct the plot[27]. The Ragone plot highlights the spread of properties exhibited by each of the different energy storage devices, with the high power dielectric capacitors and the high energy batteries and fuel cells being linked via supercapacitors. This reinforces the notion that supercapacitors are "hybrid" devices that try and combine the benefits of both of these classes of storage systems. Ideally, an energy storage device should be at the top right hand corner of this plot, as is the case for the internal combustion engine. This shows that the performance of electrochemical energy storage devices currently cannot match the combustion of fossil fuels, but electrochemical energy storage technology is still far from mature with many significant performance gains being made each year.

Supercapacitor are generally used for applications with high power requirements. Such applications include shuttle buses where the supercapacitors recharge during each stop [65], UAVs [55] and many more as described in [30]. Perhaps their most exciting potential application is within a hybrid power source [28, 88, 153, 154]. As expressed by the Ragone pot, each electrochemical energy storage device is generally optimal for either high energy or high power applications and are not very robust to performance

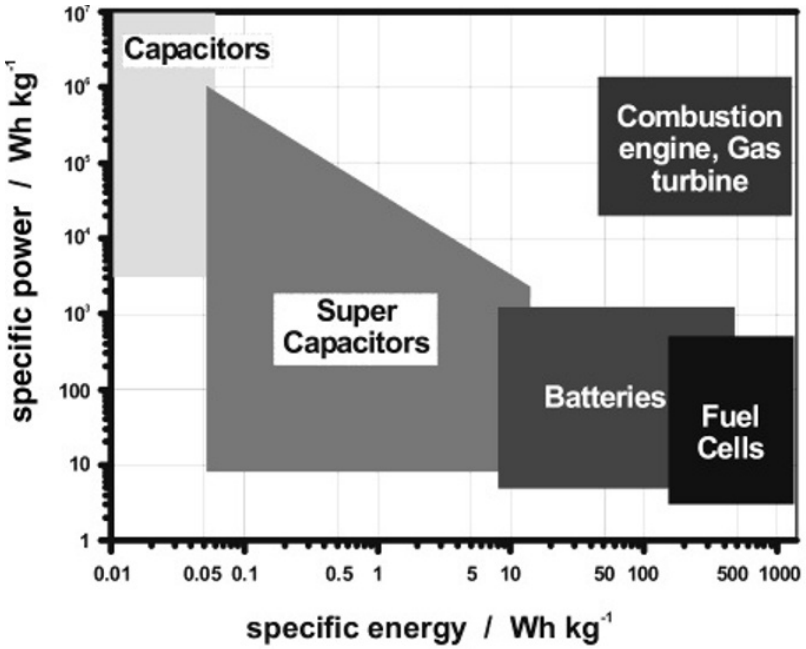


Figure 1.6: A Ragone plot showing energy and power densities of various energy storage systems. Image obtained form [173].

specifications. For example, lithium ion batteries can supply a large amount of energy but experience high degradation rates for fast charging and discharging. Degradation is not such an issue with supercapacitors, but they lack the energy required for most medium sized applications like electric vehicle driving. Combining these two devices together into a hybrid power source, alleviates each of the issues associated with the two devices, with their energy storage characteristics complimenting each other. In this context, the supercapacitor deals with the high power demands and acts as buffer to protect the more delicate batteries. This concept has been applied to electric vehicles, where the power demands have a steady-state behaviour when driving along a clear motorway but are highly transient when driving in the city. Another key supercapacitor application is wind turbines, where the incoming load is stochastic due to wind gusts. The supercapacitor can capture this load and also provide fault ride through, where a sudden loss in power is compensated for by a supercapacitor discharge [58].

This wealth of applications for supercapacitors has led to an increased demand on the performance. Improvements in performance have generally been achieved through advancements in electrochemistry, for example through the design of more advanced electrodes [178]. This approach requires exhaustive electrochemical testing to iterate towards a design with potentially long rest periods between tests to redesign the

device. Recently, systems theory based electrochemical models has been applied to energy storage devices to improve this design process by making predictions about the system properties so that an improved design can be achieved with fewer experiments [125]. Compared to the "experiment based" optimisation approach based upon experimental testing, this 'model based' approach is faster, cheaper and considers more potential designs.

Most existing studies on the design of electrochemical energy storage devices have focused on lithium ion batteries. For example, [91] considered the benefits in performance and lifespan of packs of lithium ion packs by charge balancing, [157] characterised the degradation of lithium ion batteries using impedance spectroscopy, [107] considered the optimal electrode length and porosity and [56] optimized the utilisation of the active material in a lithium ion electrode. Designing the microstructure of electrodes made from graphene was considered in [174]. The optimal grading of electrode porosity for lithium ion batteries was considered in [36, 59] but the designs were not validated by experimental results and manufacturing limitations were not considered, since electrodes with continuously spatially varying porosity gradients currently cannot be manufactured. Physical models of lithium ion batteries have also been used to develop optimal charging profiles both for reducing mechanical stress in the battery [148] and for reducing ageing effects [146]. In [147], the impact of the electrode design on capacity fade is investigated. Optimising physical model parameters for specific charging profiles to maximise the stored energy [37] and to minimise the Ohmic losses [124] have also been developed. By contrast, the design of supercapacitors has received less attention. In [128], an equivalent circuit model was used for the design of supercapacitors and the heat management of a supercapacitor for an electric vehicle application was outlined in [2]. These works show the growing importance that models, optimisation and systems analysis have in the field of energy storage.

One of the drawbacks of model based design is that the quality of the predictions depends upon the accuracy of the model. For this reason, a "good" model that effectively describes the device dynamics for a range of operating regimes is required. The literature on supercapacitor modelling is both large and growing, with the models being mainly differentiated by their accuracy, complexity and detail. The two main categories of supercapacitor models are equivalent circuits (EC) and physics based (PB) models which have completely different structures.

EC models are formed by the connection of passive circuit components such as resistors and capacitors [40, 139]. For supercapacitors, the resulting model equations are typically low-order linear ordinary differential equations (ODEs) which are relatively straight forward to solve. This makes EC models both simple to implement and to understand, resulting in them being the most popular form of model for application purposes. The various electrical components that form the circuit can be obtained using experimental data of electrical impedance spectroscopy, making circuit parameter identification fast and simple [18]. The main drawback of EC models is that the model states have little physical interpretation and the developed circuits are typically local approximations of the inherently nonlinear devices. This limits their use for design purposes and for gaining a detailed understanding about the physical state of the device during a charge. Numerous EC models have been presented in the literature [18, 123, 143], with three common circuits being compared in [185] for an electric vehicle application. One of the earliest supercapacitor equivalent circuit model was that developed by DeLevie in [38] that mimics the descent of an ion down a pore. Other circuits have been proposed to capture the charge redistribution [155] associated with the diffusion of the electrolyte ions and also capture electro-thermal effects [6]. Fractional order models have also been proposed to accommodate for the slow diffusion based dynamics [49, 121].

PB models are formed from a set of partial differential equations (PDEs) that describe the electrochemistry of the device. These PDEs typically describe diffusion equations coupled with algebraic constraints to enforce charge conservation [163]. Since the underlying equations are PDEs, PB models are generally more complex than EC models and are usually implemented with some form of spatial discretisation technique, such as the finite difference method [163]. In [163], the physical PDE equations were established and shown to match experimental data reasonably well. Several studies have extended this PB model, for example, by studying electrode 3D effects and parameter sensitivities [3], the computational implementation with an efficient spectral collocation discretisation [46], implementation with the multi-physics modelling programme COMSOL [97], a reduced order PDE system where concentration effects were ignored [130], the inclusion of temperature effects [39] and analytic solutions for constant current and electrical impedance spectroscopy charging profiles are given in [144]. Physics based models have also been developed for related electrical energy storage devices. For example, the Newman model [44] has been widely studied for lithium-ion batteries, both in terms of its implementation [8] and its incorporation within a control system [23].

Other, more complex, models for supercapacitors have also been proposed in the literature. These include neural networks [52] and those involving atomistic simulations [53, 92]. For this thesis, these models are deemed too complex for tractable analysis, so only PB and EC models are considered.

1.3 Objectives

The objectives of the first part of the thesis are to develop a set of tools for the analysis and design of supercapacitors. These tools are obtained using techniques from systems theory and are applied to many topics considered in the supercapacitor literature, including model discretisation, circuit realisations, parameter estimation, observers and design.

The objective of the second part of the thesis is to reduce the conservatism of local stability results for a class of nonlinear systems. The systems under consideration are those that can be expressed as the feedback interconnection of a linear system with a nonlinearity that is decentralised and locally sector bounded and slope restricted. The supercapacitor model considered in the first part of this thesis is shown to have this form. By reducing the conservatism of the stability results, a more accurate analysis for this class of system can be obtained which could lead to a more effective design process for these nonlinear systems.

1.4 Structure of Thesis

The thesis consists of two parts. The first part, consisting of chapters 2 to 6, develops and analyses a PB model of a supercapacitor. An efficient formulation of this model is proposed in chapter 2, with the impact of some of the electrochemical assumptions and properties also being studied. Chapter 3 analyses the applicability of this model, describing how much information about the model can be obtained from current-voltage responses. These results are expressed in terms of model observability and parameter estimation. Chapter 4 proposes a method to bridge the divide between circuit and PB supercapacitor models, with a set of circuits being synthesized from the PB supercapacitor model developed in chapter 2. Chapter 5 considers the problem of supercapacitor design and uses an absolute stability framework to bound properties such as the supercapacitor's resistance, capacitance and energy dissipation. These

energy storage properties are linked to the physical parameters of the supercapacitor. Chapter 6 extends both the modelling and design work to supercapacitors with structured electrodes. In this configuration, the electrodes are composed of layers of different materials with different electrochemical properties. Experimental data is used to verify a model for such electrodes and the effect of the introduction of the layers to the real and imaginary capacitances are studied.

The second part of the thesis considers the stability analysis using absolute stability theory of systems that evolve along a vector field incorporating a slope restricted nonlinearity. The class of systems considered in this part include the PB supercapacitor model, with the motivation behind this work being the desire to develop less conservative conditions for the resistance bounds of the supercapacitor. Chapter 7 develops less conservative conditions for the local stability analysis of systems that can be represented as the interconnection of a linear system with a slope restricted nonlinearity. Chapter 8 broadens these results to nonlinear systems whose vector field is a rational function of the states and the slope restricted nonlinearity. A main result of both of these chapters is to relax positivity conditions on the terms of the proposed Lyapunov functions by utilising the sector information.

1.5 Contribution

The main contributions of this these are:

1. The development of a computationally efficient model of a supercapacitor that describes the electrochemistry.
2. A control theoretical analysis of this model to quantify the extent to which information about the internal state of the model, including model parameters and state information, can be estimated from current-voltage data.
3. A general circuit synthesis procedure for the generation of equivalent circuits from the supercapacitor electrochemical equations.
4. Model formulation and analysis of supercapacitors with structured electrodes.
5. A methodical supercapacitor design procedure that relates the energy storage properties of the supercapacitor to its physical parameters and includes the model's nonlinearity within the analysis.

6. Less conservative conditions for absolute stability of slope restricted nonlinear systems in local domains using Lyapunov functions that may not be characterised by positive definite quadratic matrices.

7. Conditions for the construction of Lyapunov functions that may not be sum of squares for the generalised absolute stability problem.

These contributions extend existing results in both supercapacitor modelling and nonlinear systems analysis and links these two areas. The main theme of the thesis is to use control theoretical techniques to give a deeper understanding of electrochemical based supercapacitor models so as to enable supercapacitors to be designed in a more effective manner.

Part A

Chapter 2

Electrochemical Supercapacitor Model Development

2.1 Introduction

In this chapter, two non-linear models that simulate the partial differential algebraic equations that describe the electrochemistry of a supercapacitor are investigated. The first model includes the logarithmic non-linearity of the Nernst-Plank relation for the movement of charged ions in a fluid [163] while the second has a coupled quadratic (state) non-linearity, which accounts for the linear dependence between electrolyte conductivity and concentration, relaxing an assumption of dilute solution theory. The accuracy of the spectral element and finite difference numerical discretisation methods applied to these models is also investigated, with a finite element solution from COMSOL [105], which contains a large number of elements, being used as a reference solution. Using numerical discretisation schemes allows low order models to be obtained that retain the physical non-linearity as far as possible, so as to give an improved mathematical description of the supercapacitor. A low-order model has the advantage of being less computationally burdensome, making a real-time implementation possible, and also reduces the number of states needed to be estimated by an observer.

2.2 Mathematical Description of Supercapacitor Model

The supercapacitor models considered in this chapter are based on the four coupled partial differential algebraic equations given in [163]. The definition of the variables

and parameters used in the models are given in Tables 1 and 2. The model equations for each of the domains are expressed in Table 2.1. These equations are first introduced before the main model assumptions are discussed. The first of the model equations from [163] is the Nernst-Plank equation [90], describing the diffusion and migration of ions in the liquid electrolyte phase

$$U_j = -D_j \left(\frac{\partial c_j}{\partial x} - \zeta_j \frac{F}{RT} c_j \frac{\partial \phi_2}{\partial x} \right) \tag{2.1}$$

with ionic flux U, diffusion coefficient D, ionic concentration c, spatial variable x, ionic charge ζ, Faraday constant F, universal gas constant R, temperature T and potential in the electrolyte ϕ_2. The subscript $j = +, -$ refers to the positive and negative ions respectively. Under the assumption of electroneutrality, the concentrations of the positive and negative ions at a point in space are assumed to be equal, such that $c_+ = c_- = c$. From [163], this equation can be re-written in terms of the variables ionic concentration c, potential in the electrode ϕ_1 and potential in the electrolyte ϕ_2 as

$$i_2 = -\kappa \frac{\partial \phi_2}{\partial x} - \kappa \left(\frac{t_+ - t_-}{f} \right) \frac{\partial \ln c}{\partial x} \tag{2.2}$$

using the relations

$$U_j = \frac{i_2}{\zeta_j F} \tag{2.3a}$$

$$\kappa = \frac{F^2}{RT} \frac{1}{2} D \left(\frac{1}{t_-} + \frac{1}{t_+} \right) c \tag{2.3b}$$

$$D = \frac{2 D_- D_+}{D_+ + D_-} \tag{2.3c}$$

$$f = \frac{F}{RT} \tag{2.3d}$$

where i_2 is the current associated with ionic flux in the electrolyte, κ is the conductivity of the electrolyte and $t_{+/-}-$ are transference numbers associated with the relative charge of the positive and negative ions. The electrolyte conductivity κ is adapted to account for the effects of electrode porosity and tortuosity [163] via

$$\kappa = \kappa_\infty \frac{\epsilon}{\Gamma} \tag{2.4}$$

with κ_∞ the electrolyte conductivity in the free solution, electrode porosity coefficient ϵ and tortuosity coefficient Γ.

The second of the four supercapacitor equations is Ohm's Law, which applies in the electrode domains, but not in the separator,

$$i_1 = i - i_2 = -\sigma \frac{\partial \phi_1}{\partial x}. \tag{2.5}$$

with electrode conductivity σ and current in the electrode associated with the movement of electrons i_1. The total current i is the sum of the currents in the solid and liquid phases $i = i_1 + i_2$. The dynamics of the potential difference across the double layer is described by

$$aC \frac{\partial(\phi_1 - \phi_2)}{\partial t} = \frac{\partial i_2}{\partial x}, \tag{2.6}$$

with specific capacitance aC and the concentration of electrolyte ions evolve by the forced diffusion equation

$$\epsilon \frac{\partial c}{\partial t} = D \frac{\partial^2 c}{\partial x^2} - \frac{aC}{F} \left(t_- \frac{dq_+}{dq} + t_+ \frac{dq_-}{dq} \right) \frac{\partial(\phi_1 - \phi_2)}{\partial t}. \tag{2.7}$$

where the fractions $\frac{dq_j}{dq}$ are fixed parameters relating the change in surface concentration of species j associated with a change on the surface charge of the electrode. In the electrode, these four equations (2.2), (2.5), (2.6) and (2.7) can be written in the state-space form [5]

$$\begin{bmatrix} \epsilon & \frac{aC}{F}(t_- \frac{dq_+}{dq} + t_+ \frac{dq_-}{dq}) & -\frac{aC}{F}(t_- \frac{dq_+}{dq} + t_+ \frac{dq_-}{dq}) & 0 \\ 0 & aC & -aC & 0 \\ 0 & 0 & 0 & 0 \\ 0 & 0 & 0 & 0 \end{bmatrix} \begin{bmatrix} \dot{c} \\ \dot{\phi}_1 \\ \dot{\phi}_2 \\ \dot{i}_2 \end{bmatrix} = \begin{bmatrix} D\frac{\partial^2}{\partial x^2} & 0 & 0 & 0 \\ 0 & 0 & 0 & \frac{\partial}{\partial x} \\ 0 & \sigma \frac{\partial}{\partial x} & 0 & -1 \\ 0 & 0 & \kappa \frac{\partial}{\partial x} & 1 \end{bmatrix} \begin{bmatrix} c \\ \phi_1 \\ \phi_2 \\ i_2 \end{bmatrix} + \begin{bmatrix} 0 \\ 0 \\ 0 \\ \kappa\left(\frac{t_+ - t_-}{f}\right) \frac{\partial}{\partial x} \end{bmatrix} \ln c + \begin{bmatrix} 0 \\ 0 \\ 1 \\ 0 \end{bmatrix} i \tag{2.8}$$

and in the separator, the state-space form is

$$\begin{bmatrix} \epsilon & 0 \\ 0 & 0 \end{bmatrix} \begin{bmatrix} \dot{c} \\ \dot{\phi}_2 \end{bmatrix} = \begin{bmatrix} D\frac{\partial^2}{\partial x^2} & 0 \\ 0 & \kappa \frac{\partial}{\partial x} \end{bmatrix} \begin{bmatrix} c \\ \phi_2 \end{bmatrix} + \begin{bmatrix} 0 \\ \kappa\left(\frac{t_+ - t_-}{f}\right) \frac{\partial}{\partial x} \end{bmatrix} \ln c + \begin{bmatrix} 0 \\ 1 \end{bmatrix} i. \tag{2.9}$$

The different dynamics in the electrode and separator domains is due to the separator being an electrical insulator. As such, the electrode potential ϕ_1 and the double layer potential $\phi_1 - \phi_2$ do not exist in the separator, hence the lower order state-space system of (2.9) compared to (2.8). A non-dimensional version of this model is given in [163].

2.3 Model Assumptions and Relations

A good discussion of several of the assumptions of the model of [163] can be found in [80]. Dilute solution theory, in which the ions are assumed to have zero size, is used to describe the electrolytic solution within the pores, neglecting the concentration dependence of the governing model parameters. It is stated in [163] that a lack of knowledge regarding the variation of electrochemical parameters in complex porous mediums explains the use of this assumption. Several nonlinear models on the molecular scale have been proposed to describe this variation [78, 79, 95, 161], but in this work, it is deemed that, in general, the added complexity introduced by such models does not justify their inclusion, as their effects on the accuracy are limited [76, 102]. For this reason, the capacitance is treated as a lumped parameter, even though it has been shown to change with variables such as the voltage [176]. An investigation into the applicability of dilute solution theory was carried out in [90] where it was found that steric effects between ions due to excessive surface concentrations only occurs when the voltage exceeds a certain upper threshold. The model uses porous electrode theory, where the electrodes are modelled as a single continuum and is justified because the sizes of the electrode pores (of the order of nanometres) are much smaller than the electrode thickness (of the order of microns). As such, the electrodes are given volume averaged homogenised properties, for both the parameters and the states. The electrolyte is considered to be binary, dissociating into two separate ions. The electrolyte is also assumed to be inert, with the effect of pseudo-capacitance [19] and side reactions being disregarded. This means that the OCV curve of Li-ion batteries is not required in the model. The temperature of the supercapacitor is assumed to be fixed, which is reasonable as the supercapacitor does not generate much heat from chemical reactions. Self-discharge [127] is also neglected, but could be included by introducing a contracting term in the double layer potential dynamics equation (2.6), such as

$$aC\frac{\partial(\phi_1-\phi_2)}{\partial t}=\frac{\partial i_2}{\partial x}+\tilde{\epsilon}\frac{\partial^2(\phi_1-\phi_2)}{\partial x^2} \tag{2.10}$$

where $\tilde{\epsilon}$ is a small constant term. The model is assumed to be one dimensional in the spatial variable x, with the effect of 3D effects shown to be negligible in [3].

The total current density flowing through the supercapacitor i is the sum of the current density flowing in the solid phase i_1 and the liquid phase i_2

$$i_1+i_2=i. \tag{2.11}$$

In a similar manner, the transference number, a non-dimensional number relating the amount of charge carried by each ion, is defined to sum to 1

$$t_+ + t_- = 1. \tag{2.12}$$

The two relations (2.11) and (2.12) can be used to eliminate the variables i_1 and t_- from the model equations. The remaining unknown parameter, the ionic diffusion coefficient D, is then obtained from (2.3b), with the concentration c being set to the constant c_0 due to dilute solution theory.

The supercapacitor is a multi-domain system with different dynamics in the separator and the electrodes with the different domains connected via the boundary conditions given in Table 2.2. These boundary conditions are of the Neumann type, except for the Dirichlet condition $\phi_1 = 0$ at one of the current collectors that enforces a reference potential. The device is assumed to be self-contained with no leakage of the electrolyte through the current collector, giving the insulating condition

$$\frac{\partial c}{\partial x} = 0. \tag{2.13}$$

At the current collector, all of the current is assumed to be carried in the solid phase $i_1 = i$ with no current in the liquid phase $i_2 = 0$. Therefore, the flux conditions of (2.2) and (2.5) read

$$\frac{\partial \phi_1}{\partial x} = -\frac{i}{\sigma} \tag{2.14}$$

and

$$\frac{\partial \phi_2}{\partial x} = 0. \tag{2.15}$$

since

$$\frac{\partial \ln\, c}{\partial x} = \frac{1}{c}\frac{\partial c}{\partial x}. \tag{2.16}$$

Conversely, as the separator is an electrical insulator, all of the current is carried in the electrolyte $i_2 = i$ with no current in the electrode $i_1 = 0$, giving

$$\frac{\partial \phi_1}{\partial x} = 0. \tag{2.17}$$

The current is assumed to be continuous across the boundary so

$$i_2|_L = i_2|_R \tag{2.18}$$

$$\left[\kappa\frac{\partial \phi_2}{\partial x} + \kappa(\frac{t_+ - t_-}{f})\frac{\partial \ln\, \mathrm{c}}{\partial x}\right]_L = \left[\kappa\frac{\partial \phi_2}{\partial x} + \kappa(\frac{t_+ - t_-}{f})\frac{\partial \ln\, \mathrm{c}}{\partial x}\right]_R \tag{2.19}$$

with L and R denoting the left and right domains across the boundary. Furthermore, it is assumed that across the boundary there is no build up of concentration flux, implying that

$$\int_{dx} D\frac{\partial^2 c}{\partial x^2}\bigg|_L - D\frac{\partial^2 c}{\partial x^2}\bigg|_R dx = 0 \tag{2.20}$$

$$D\frac{\partial^2 c}{\partial x^2}\bigg|_L = D\frac{\partial^2 c}{\partial x^2}\bigg|_R. \tag{2.21}$$

Electrode	Separator	Electrode
$0 < x < L_{elec}$	$L_{elec} < x < L_{elec} + L_{sep}$	$L_{elec} + L_{sep} < x < 2L_{elec} + L_{sep}$
$aC\frac{\partial(\phi_1-\phi_2)}{\partial t} = \frac{\partial i_2}{\partial x}$	$i_2 = i$	$aC\frac{\partial(\phi_1-\phi_2)}{\partial t} = \frac{\partial i_2}{\partial x}$
$\frac{aC}{F}(t_-\frac{dq_+}{dq} + t_+\frac{dq_-}{dq})\frac{\partial(\phi_1-\phi_2)}{\partial t} + \epsilon\frac{\partial c}{\partial t} = D\frac{\partial^2 c}{\partial x^2}$	$\epsilon\frac{\partial c}{\partial t} = D\frac{\partial^2 c}{\partial x^2}$	$\frac{aC}{F}(t_-\frac{dq_+}{dq} + t_+\frac{dq_-}{dq})\frac{\partial(\phi_1-\phi_2)}{\partial t} + \epsilon\frac{\partial c}{\partial t} = D\frac{\partial^2 c}{\partial x^2}$
$0 = \frac{\partial\phi_2}{\partial x} + (\frac{t_+-t_-}{f})\frac{\partial \ln c}{\partial x} + \frac{i_2}{\kappa}$	$0 = \frac{\partial\phi_2}{\partial x} + (\frac{t_+-t_-}{f})\frac{\partial \ln c}{\partial x} + \frac{i_2}{\kappa}$	$0 = \frac{\partial\phi_2}{\partial x} + (\frac{t_+-t_-}{f})\frac{\partial \ln c}{\partial x} + \frac{i_2}{\kappa}$
$0 = \frac{\partial\phi_1}{\partial x} + \frac{i-i_2}{\sigma}$	$\dots$	$0 = \frac{\partial\phi_1}{\partial x} + \frac{i-i_2}{\sigma}$

Table 2.1: The supercapacitor model equations as described by [163]. The electrode length is denoted L_{elec} and the separator length by L_{sep}.

Current Collector	Electrode-Separator Boundary	Electrode-Separator Boundary	Current Collector
$x = 0$	$x = L_{elec}$	$x = L_{elec} + L_{sep}$	$x = 2L_{elec} + L_{sep}$
$\frac{\partial \phi_1}{\partial x} = -\frac{i}{\sigma}$, $\phi_1 = 0$	$\frac{\partial \phi_1}{\partial x} = 0$	$\frac{\partial \phi_1}{\partial x} = 0$	$\frac{\partial \phi_1}{\partial x} = -\frac{i}{\sigma}$
$\frac{\partial \phi_2}{\partial x} = 0$	$\left[\kappa \frac{\partial \phi_2}{\partial x} + \kappa \left(\frac{t_+ - t_-}{f}\right) \frac{\partial \ln c}{\partial x}\right]_L = \left[\kappa \frac{\partial \phi_2}{\partial x} + \kappa \left(\frac{t_+ - t_-}{f}\right) \frac{\partial \ln c}{\partial x}\right]_R$	$\left[\kappa \frac{\partial \phi_2}{\partial x} + \kappa \left(\frac{t_+ - t_-}{f}\right) \frac{\partial \ln c}{\partial x}\right]_L = \left[\kappa \frac{\partial \phi_2}{\partial x} + \kappa \left(\frac{t_+ - t_-}{f}\right) \frac{\partial \ln c}{\partial x}\right]_R$	$\frac{\partial \phi_2}{\partial x} = 0$
$i_2 = 0$	$i_2 = i$	$i_2 = i$	$i_2 = 0$
$\frac{\partial c}{\partial x} = 0$	$D \frac{\partial c}{\partial x}\Big\|_L = D \frac{\partial c}{\partial x}\Big\|_R$	$D \frac{\partial c}{\partial x}\Big\|_L = D \frac{\partial c}{\partial x}\Big\|_R$	$\frac{\partial c}{\partial x} = 0$

Table 2.2: The supercapacitor model boundary conditions as described by [163].

The four equations (2.2), (2.5), (2.6) and (2.7), can be combined to reduce the dimension of the state-space. In this chapter, the reduction is achieved by differentiating (2.5) with respect to x

$$\frac{\partial i_2}{\partial x} = \sigma \frac{\partial^2 \phi_1}{\partial^2 x}, \tag{2.22}$$

and then substituting this expression into (2.6)

$$aC \frac{\partial(\phi_1 - \phi_2)}{\partial t} = \sigma \frac{\partial^2 \phi_1}{\partial x^2}. \tag{2.23}$$

Summing the two algebraic equations, (2.2) and (2.5), gives

$$0 = \sigma \frac{\partial \phi_1}{\partial x} + \kappa \frac{\partial \phi_2}{\partial x} + \kappa \left(\frac{t_+ - t_-}{f} \right) \frac{\partial \ln c}{\partial x} + i, \tag{2.24}$$

eliminating the algebraic variable i_2 from the equation system. This substitution transforms the four equation system of [163] into the system described by the three equations

$$\epsilon \frac{\partial c}{\partial t} = D \frac{\partial^2 c}{\partial x^2} - \frac{aC}{F} \left(t_- \frac{dq_+}{dq} + t_+ \frac{dq_-}{dq} \right) \frac{\partial(\phi_1 - \phi_2)}{\partial t} \tag{2.25a}$$

$$aC \frac{\partial(\phi_1 - \phi_2)}{\partial t} = \sigma \frac{\partial^2 \phi_1}{\partial x^2} \tag{2.25b}$$

$$0 = \sigma \frac{\partial \phi_1}{\partial x} + \kappa \frac{\partial \phi_2}{\partial x} + \kappa \left(\frac{t_+ - t_-}{f} \right) \frac{\partial \ln c}{\partial x} + i \tag{2.25c}$$

which for each electrode can be written as

$$\begin{bmatrix} \epsilon & \frac{aC}{F}(t_- \frac{dq_+}{dq} + t_+ \frac{dq_-}{dq}) & 0 \\ 0 & aC & 0 \\ 0 & 0 & 0 \end{bmatrix} \begin{bmatrix} \dot{c} \\ \dot{\phi}_1 - \dot{\phi}_2 \\ \dot{\phi}_2 \end{bmatrix} = \begin{bmatrix} D\frac{\partial^2}{\partial x^2} & 0 & 0 \\ 0 & \sigma \frac{\partial^2}{\partial x^2} & \sigma \frac{\partial^2}{\partial x^2} \\ 0 & \sigma \frac{\partial}{\partial x} & \kappa \frac{\partial}{\partial x} + \sigma \frac{\partial}{\partial x} \end{bmatrix} \begin{bmatrix} c \\ \phi_1 - \phi_2 \\ \phi_2 \end{bmatrix} + \begin{bmatrix} 0 \\ 0 \\ \kappa \left(\frac{t_+ - t_-}{f} \right) \frac{\partial}{\partial x} \end{bmatrix} \ln c + \begin{bmatrix} 0 \\ 0 \\ 1 \end{bmatrix} i. \tag{2.26}$$

The state-space representation of the separator domain remains unchanged from (2.9). Table 2.3 expresses these equations in the domain.

Electrode	Separator	Electrode
$0 < x < L_{elec}$	$L_{elec} < x < L_{elec} + L_{sep}$	$L_{elec} + L_{sep} < x < 2L_{elec} + L_{sep}$
$\frac{aC}{F}\left(t_- \frac{dq_+}{dq} + t_+ \frac{dq_-}{dq}\right)\frac{\partial(\phi_1-\phi_2)}{\partial t} + \epsilon\frac{\partial c}{\partial t} = D\frac{\partial^2 c}{\partial x^2}$	$\epsilon\frac{\partial c}{\partial t} = D\frac{\partial^2 c}{\partial x^2}$	$\frac{aC}{F}\left(t_- \frac{dq_+}{dq} + t_+ \frac{dq_-}{dq}\right)\frac{\partial(\phi_1-\phi_2)}{\partial t} + \epsilon\frac{\partial c}{\partial t} = D\frac{\partial^2 c}{\partial x^2}$
$aC\frac{\partial(\phi_1-\phi_2)}{\partial t} = \sigma\frac{\partial^2\phi_1}{\partial x^2}$	...	$aC\frac{\partial(\phi_1-\phi_2)}{\partial t} = \sigma\frac{\partial^2\phi_1}{\partial x^2}$
$0 = \sigma\frac{\partial\phi_1}{\partial x} + \kappa\frac{\partial\phi_2}{\partial x} + \kappa\left(\frac{t_+-t_-}{f}\right)\frac{\partial \ln c}{\partial x} + i$	$0 = \kappa\frac{\partial\phi_2}{\partial x} + \kappa\left(\frac{t_+-t_-}{f}\right)\frac{\partial \ln c}{\partial x} + i$	$0 = \sigma\frac{\partial\phi_1}{\partial x} + \kappa\frac{\partial\phi_2}{\partial x} + \kappa\left(\frac{t_+-t_-}{f}\right)\frac{\partial \ln c}{\partial x} + i$

Table 2.3: Supercapacitor model equations.

One of the most fundamental assumptions of the model equations is that the electrolytic concentration does not vary significantly during charging so that the electrolytic conductivity κ can be treated as a constant, as described by (2.4). This assumption can be made more realistic using the substitution

$$\kappa = \beta c \tag{2.27}$$

that accounts for the linear relationship between electrolyte conductivity and concentration, as mentioned in [163]. Incorporating (2.27) into the model transforms the logarithmic non-linearity in the algebraic equations of (2.9) and (2.26) into a coupled quadratic non-linearity, as described by

$$\begin{bmatrix} \epsilon & \frac{aC}{F}(t_- \frac{dq_+}{dq} + t_+ \frac{dq_-}{dq}) & 0 \\ 0 & aC & 0 \\ 0 & 0 & 0 \end{bmatrix} \begin{bmatrix} \dot{c} \\ \dot{\phi}_1 - \dot{\phi}_2 \\ \dot{\phi}_2 \end{bmatrix} = \begin{bmatrix} D\frac{\partial^2}{\partial x^2} & 0 & 0 \\ 0 & \sigma\frac{\partial^2}{\partial x^2} & \sigma\frac{\partial^2}{\partial x^2} \\ \beta\left(\frac{t_+ - t_-}{f}\right)\frac{\partial}{\partial x} & \sigma\frac{\partial}{\partial x} & \beta c\frac{\partial}{\partial x} + \sigma\frac{\partial}{\partial x} \end{bmatrix} \begin{bmatrix} c \\ \phi_1 - \phi_2 \\ \phi_2 \end{bmatrix} + \begin{bmatrix} 0 \\ 0 \\ 1 \end{bmatrix} i. \tag{2.28}$$

in the electrodes and

$$\begin{bmatrix} \epsilon & 0 \\ 0 & 0 \end{bmatrix} \begin{bmatrix} \dot{c} \\ \dot{\phi}_2 \end{bmatrix} = \begin{bmatrix} D\frac{\partial^2}{\partial x^2} & 0 \\ \beta\left(\frac{t_+ - t_-}{f}\right)\frac{\partial}{\partial x} & \beta c\frac{\partial}{\partial x} \end{bmatrix} \begin{bmatrix} c \\ \phi_2 \end{bmatrix} + \begin{bmatrix} 0 \\ 1 \end{bmatrix} i \tag{2.29}$$

in the separator.

2.4 Spectral Methods

In general, non-linear PDE systems such as (2.28) or (2.29) are too complex to be solved analytically, so numerical methods are used. Numerical methods discretise the spatial domain and then use interpolation to obtain approximate solutions to the PDE, transforming the PDE into a set of ordinary differential equations (ODEs). The manner in which the discretisation is carried out is known to have a significant influence upon the accuracy of the numerical method [12]. The most basic method to increase the accuracy of the numerical solution is to refine the numerical mesh. However, doing so increases the number of ODEs in the model, increasing computational complexity and memory requirements. This results in a trade-off between solution accuracy and computational complexity, with the desired discretisation being such that a low-order model can be established that provides a sufficiently accurate solution.

Within numerical methods, the three most common techniques for spatial discretisation are the spectral method (SM), finite difference method (FDM) and finite element method (FEM) [12]. All three of these methods approximate the derivative of an unknown function by differentiating an 'approximating function', which is constructed by interpolating the known function values at the domain nodes. The main difference between the FDM, FEM and SM is the domain region used for the interpolation. Both the FDM and FEM can be considered local methods, as they only use information at nodes close to the node of interest where the derivative is to be approximated. This is done either through Taylor expansions for the FDM, or a calculus of variations approach across a sub-domain, known as an element, for the FEM. By contrast, spectral methods represent a global approximation to the derivative, involving a sum of known orthogonal basis functions that traverse the entire domain, with these functions generally chosen to be sinusoids for periodic solutions and polynomials for non-periodic solutions.

Given a suitable spatial grid with a smooth function distributed across it, spectral methods are an accurate numerical method for approximating derivatives. Improving the accuracy in this manner can lead to a significant reduction in computational complexity, as fewer grid points are needed to achieve a set solution accuracy. The fundamental building block of any spectral method is a set of orthogonal basis functions $\psi(x)$ whose sum forms an interpolating polynomial $\bar{p}(x)$ of order N that approximates the solution in the spatial domain of the differential equation $p(x)$ by

$$p(x) \approx \bar{p}(x) = \sum_{j=1}^{N+1} \psi_j(x)\bar{p}(\boldsymbol{x}_j). \tag{2.30}$$

In this chapter, Chebyshev polynomials of the first kind are used [156] as the solution $p(x)$ is assumed to be smooth in each of the model domains. The choice of basis function enforces the condition that the approximating polynomial exactly equals the true solution at the collocation points $\boldsymbol{x}_j$, i.e $\bar{p}(\boldsymbol{x}_j) = p(\boldsymbol{x}_j)$.

Approximating the solution to the differential equations through the sum of known polynomial functions in such a manner enables a simple expression for the derivative to be obtained by differentiating the interpolating polynomial

$$\frac{\partial^l}{\partial x^l} p(x) \approx \frac{\partial^l}{\partial x^l} \bar{p}(x) = \sum_{j=1}^{N+1} \frac{d^l}{dx^l} \psi_j(x)\bar{p}(\mathbf{x}_j). \tag{2.31}$$

The differentiation operation in (2.31) is linear and can be represented by a differentiation matrix $\boldsymbol{D}$. The accuracy of the spectral differentiation matrix is exponential

[12], which is superior to the accuracy of the differentiation matrices of both the FDM and FEM. The exponential error convergence rate of spectral methods is because increasing the order of their global interpolation functions improves the accuracy at each grid point in the domain simultaneously. In contrast, increasing the order of the interpolation function of local approximating methods such as FDM only increases the accuracy of each element separately. All of the spectral differentiation matrices required for the supercapacitor model proposed in this chapter were constructed with the MATLAB differentiation suite [169].

Spectral methods can give an order of magnitude increase in accuracy for the differentiation of a smooth function. However, it is known that spectral methods are only applicable for the interpolation of smooth solutions, as the fundamental basis of the method is a global interpolation function, which is itself smooth. For the supercapacitor equations outlined in (2.2), (2.5), (2.6) and (2.7), a discontinuity occurs at the electrode/separator boundary. For this reason, the supercapacitor domain of the presented model is split into three smaller sub-domains, one sub-domain for each of the electrodes and another for the separator, as shown in Figure 1.3, with the three sub-domains being connected by the boundary conditions using patching [12]. Partitioning the domain in this manner means that the applied spectral method resembles a finite element, albeit one with an interpolating polynomial of very high order. For this reason, the method is commonly known as the spectral element method (SEM).

The accuracy of spectral methods is affected by the Runge phenomenon, where the solution is found to oscillate at the extremal points of the domain as described in [156]. This problem can be minimised by discretising the nodes in terms of Chebyshev points $\hat{\mathbf{x}} \in [-1, 1]$

$$\hat{\mathbf{x}}_k = \cos\left(\frac{(k-1)\pi}{N}\right), \quad k = 1, 2, 3, \ldots, N+1, \tag{2.32}$$

with $\hat{\mathbf{x}}$ being the Chebyshev distribution corresponding to the maximal points of the Chebyshev polynomials. The Chebyshev distribution of (2.32) is irregular, with a greater density of points being clustered at the domain boundaries, and is defined across the local domain $[-1, 1]$. For implementation purposes, the transformation from $\hat{\mathbf{x}}$ to $\mathbf{x} \in [0, L]$ must be carried out to scale for the true domain [156], and the differentiation matrices must be scaled accordingly.

In this chapter, the SEM, FDM and FEM methods were used to discretise the model equations and Neumann boundary conditions described in section 2.3. The applied

FDM uses a second-order Runge-Kutta method as outlined in [162], the SEM implements a similar approach to [8], involving Chebyshev polynomials, while the FEM solutions were obtained using the 'Coefficient Form PDE' module from the commercially available software COMSOL [105].

2.5 Differential Algebraic Equations

The discrete form of the logarithmic non-linear equations given in (2.9) and (2.26) is respectively given by

$$\begin{bmatrix} \epsilon & \frac{aC}{F}\left(t_- \frac{dq_+}{dq} + t_+ \frac{dq_-}{dq}\right) & 0 \\ 0 & aC & 0 \\ 0 & 0 & 0 \end{bmatrix} \begin{bmatrix} \dot{\boldsymbol{c}} \\ \dot{\boldsymbol{\phi}}_{\mathbf{1}} - \dot{\boldsymbol{\phi}}_{\mathbf{2}} \\ \dot{\boldsymbol{\phi}}_{\mathbf{2}} \end{bmatrix} = \begin{bmatrix} D\boldsymbol{D}_c^2 & 0 & 0 \\ 0 & \sigma \boldsymbol{D}_{\phi_1}^2 & \sigma \boldsymbol{D}_{\phi_1}^2 \\ 0 & \sigma \boldsymbol{D}_{\phi_1} & \kappa \boldsymbol{D}_{\phi_2} + \sigma \boldsymbol{D}_{\phi_1} \end{bmatrix} \begin{bmatrix} \boldsymbol{c} \\ \boldsymbol{\phi}_{\mathbf{1}} - \boldsymbol{\phi}_{\mathbf{2}} \\ \boldsymbol{\phi}_{\mathbf{2}} \end{bmatrix} + \begin{bmatrix} 0 \\ 0 \\ \kappa\left(\frac{t_+ - t_-}{f}\right) \boldsymbol{D}_{\ln c} \end{bmatrix} \ln \boldsymbol{c} + \begin{bmatrix} 0 \\ 0 \\ 1 \end{bmatrix} i, \tag{2.33}$$

$$\begin{bmatrix} \epsilon & 0 \\ 0 & 0 \end{bmatrix} \begin{bmatrix} \dot{\boldsymbol{c}} \\ \dot{\boldsymbol{\phi}}_{\mathbf{2}} \end{bmatrix} = \begin{bmatrix} D\boldsymbol{D}_c^2 & 0 \\ 0 & \kappa \boldsymbol{D}_{\phi_2}^2 \end{bmatrix} \begin{bmatrix} \boldsymbol{c} \\ \boldsymbol{\phi}_{\mathbf{2}} \end{bmatrix} + \begin{bmatrix} 0 \\ \kappa\left(\frac{t_+ - t_-}{f}\right) \boldsymbol{D}_{\ln c} \end{bmatrix} \ln \boldsymbol{c} + \begin{bmatrix} 0 \\ 1 \end{bmatrix} i \tag{2.34}$$

where the states are now vectors of a size related to the number of grid points, e.g. $\boldsymbol{c} = [\boldsymbol{c}_1,\ \boldsymbol{c}_2,\ \ldots,\ \boldsymbol{c}_n]^T$. Similarly, the discrete form of the quadratically non-linear model of (2.28) and (2.29) is

$$\begin{bmatrix} \epsilon & \frac{aC}{F}\left(t_- \frac{dq_+}{dq} + t_+ \frac{dq_-}{dq}\right) & 0 \\ 0 & aC & 0 \\ 0 & 0 & 0 \end{bmatrix} \begin{bmatrix} \dot{\boldsymbol{c}} \\ \dot{\boldsymbol{\phi}}_{\mathbf{1}} - \dot{\boldsymbol{\phi}}_{\mathbf{2}} \\ \dot{\boldsymbol{\phi}}_{\mathbf{2}} \end{bmatrix} = \begin{bmatrix} D\boldsymbol{D}_c^2 & 0 & 0 \\ 0 & \sigma \boldsymbol{D}_{\phi_1}^2 & \sigma \boldsymbol{D}_{\phi_1}^2 \\ \beta\left(\frac{t_+ - t_-}{f}\right) \boldsymbol{D}_c & \sigma \boldsymbol{D}_{\phi_1} & \beta \boldsymbol{c}_{diag} \boldsymbol{D}_{\phi_2} + \sigma \boldsymbol{D}_{\phi_1} \end{bmatrix} \begin{bmatrix} \boldsymbol{c} \\ \boldsymbol{\phi}_{\mathbf{1}} - \boldsymbol{\phi}_{\mathbf{2}} \\ \boldsymbol{\phi}_{\mathbf{2}} \end{bmatrix} + \begin{bmatrix} 0 \\ 0 \\ 1 \end{bmatrix} i, \tag{2.35}$$

$$\begin{bmatrix} \epsilon & 0 \\ 0 & 0 \end{bmatrix} \begin{bmatrix} \dot{\boldsymbol{c}} \\ \dot{\boldsymbol{\phi}}_{\mathbf{2}} \end{bmatrix} = \begin{bmatrix} D\boldsymbol{D}_c^2 & 0 \\ \beta\left(\frac{t_+ - t_-}{f}\right) \boldsymbol{D}_c & \beta \boldsymbol{c}_{diag} \boldsymbol{D}_{\phi_2} \end{bmatrix} \begin{bmatrix} \boldsymbol{c} \\ \boldsymbol{\phi}_{\mathbf{2}} \end{bmatrix} + \begin{bmatrix} 0 \\ 1 \end{bmatrix} i. \tag{2.36}$$

In this notation, the differentiation matrix $\boldsymbol{D}_\zeta$ incorporates the boundary conditions of ζ. In the finite dimensional form, the parameters appearing in the matrices of the

model equations should be multiplied by the identity matrix, although this was not done here so as to have a cleaner representation. Due to the point-wise variation of electrode conductivity with ionic concentration, the quadratic nonlinearity of (2.35), (2.36) is defined using $\boldsymbol{c}_{diag} = diag(\boldsymbol{c})$.

Similarly, the discretised version of the output voltage

$$v = \boldsymbol{\phi}_1|_{x=0} - \boldsymbol{\phi}_1|_{x=L}. \tag{2.37}$$

is represented by

$$v = \begin{bmatrix} 0 & \boldsymbol{C}_1 \end{bmatrix} \begin{bmatrix} \boldsymbol{c} \\ \boldsymbol{\phi_1} - \boldsymbol{\phi_2} \end{bmatrix} + \boldsymbol{C}_1\boldsymbol{\phi_2} + \boldsymbol{D}_1 i. \tag{2.38}$$

when the boundary conditions on ϕ_1 are considered.

Equations (2.33), (2.34), (2.35) and (2.36) can be considered as semi-explicit differential algebraic equations (DAEs), of the form

$$\boldsymbol{M}\dot{\boldsymbol{y}} = \boldsymbol{f}(\boldsymbol{y}, \boldsymbol{z}), \tag{2.39a}$$

$$0 = \boldsymbol{g}(\boldsymbol{y}, \boldsymbol{z}, \boldsymbol{u}). \tag{2.39b}$$

where the dynamics of (2.39a) evolve along a manifold described by the algebraic equation (2.39b). It is noted that DAEs often appear in electrical systems, such as in applying Kirchoff's laws for circuit analysis [110]. In the electrodes, defining $\boldsymbol{y} := [\boldsymbol{c}^T, \boldsymbol{\phi}_1^T - \boldsymbol{\phi}_2^T]^T$, $\boldsymbol{z} := \boldsymbol{\phi_2}$, $\boldsymbol{u} := i$, and

$$\boldsymbol{M} := \begin{bmatrix} \epsilon & \frac{aC}{F}\left(t_- \frac{dq_+}{dq} + t_+ \frac{dq_-}{dq}\right) \\ 0 & aC \end{bmatrix}, \tag{2.40}$$

$$\boldsymbol{f}(\boldsymbol{y}, \boldsymbol{z}) := \begin{bmatrix} D\boldsymbol{D}_c^2 & 0 & 0 \\ 0 & \sigma\boldsymbol{D}_{\phi_1}^2 & \sigma\boldsymbol{D}_{\phi_1}^2 \end{bmatrix} \begin{bmatrix} \boldsymbol{c} \\ \boldsymbol{\phi_1} - \boldsymbol{\phi_2} \\ \boldsymbol{\phi_2} \end{bmatrix} = \left[\begin{array}{cc|c} D\boldsymbol{D}_c^2 & 0 & 0 \\ 0 & \sigma\boldsymbol{D}_{\phi_1}^2 & \sigma\boldsymbol{D}_{\phi_1}^2 \end{array}\right] \begin{bmatrix} \boldsymbol{y} \\ \boldsymbol{z} \end{bmatrix} \tag{2.41}$$

allows the dynamics to be expressed in the form of (2.39a). For the logarithmic model, the algebraic equation $\mathbf{g}(\mathbf{y}, \mathbf{z}, \mathbf{u})$ is defined as

$$\boldsymbol{g}(\boldsymbol{y}, \boldsymbol{z}, \boldsymbol{u}) := \left[\begin{array}{c|c} 0 & \sigma\boldsymbol{D}_{\phi_1} \end{array}\right. \left.\begin{array}{c} \kappa\boldsymbol{D}_{\phi_2} + \sigma\boldsymbol{D}_{\phi_1} \end{array}\right] \begin{bmatrix} \boldsymbol{c} \\ \boldsymbol{\phi_1} - \boldsymbol{\phi_2} \\ \boldsymbol{\phi_2} \end{bmatrix} + \kappa\left(\frac{t_+ - t_-}{f}\right) \boldsymbol{D}_{\ln c} \ln \boldsymbol{c} + i, \tag{2.42}$$

while for the quadratic nonlinearity

$$\boldsymbol{g}(\boldsymbol{y},\boldsymbol{z},\boldsymbol{u}) := \left[\begin{array}{cc|c} \beta\left(\frac{t_+-t_-}{f}\right)\boldsymbol{D}_c & \sigma\boldsymbol{D}_{\phi_1} & \beta\boldsymbol{c}_{diag}\boldsymbol{D}_{\phi_2}+\sigma\boldsymbol{D}_{\phi_1} \end{array}\right] \begin{bmatrix} \boldsymbol{c} \\ \boldsymbol{\phi_1}-\boldsymbol{\phi_2} \\ \boldsymbol{\phi_2} \end{bmatrix} + i. \quad (2.43)$$

Equivalently, in the separator, $\boldsymbol{y} := \boldsymbol{c}$, $\boldsymbol{z} := \boldsymbol{\phi_2}$, $\boldsymbol{u} := i$,

$$\boldsymbol{M} := \epsilon, \quad (2.44)$$

$$\boldsymbol{f}(\mathbf{y},\boldsymbol{z}) := \begin{bmatrix} D\boldsymbol{D}_c^2 & 0 \end{bmatrix} \begin{bmatrix} \boldsymbol{c} \\ \boldsymbol{\phi_2} \end{bmatrix} = \left[\begin{array}{c|c} D\boldsymbol{D}_c^2 & 0 \end{array}\right] \begin{bmatrix} \boldsymbol{c} \\ \boldsymbol{\phi_2} \end{bmatrix} \quad (2.45)$$

and $\boldsymbol{g}(\boldsymbol{y},\boldsymbol{z},\boldsymbol{u})$ is respectively as

$$\boldsymbol{g}(\boldsymbol{y},\boldsymbol{z},\boldsymbol{u}) := \begin{bmatrix} 0 & \kappa\boldsymbol{D}_{\phi_2} \end{bmatrix} \begin{bmatrix} \boldsymbol{c} \\ \boldsymbol{\phi_2} \end{bmatrix} + \kappa\left(\frac{t_+-t_-}{f}\right)\boldsymbol{D}_{\ln\, c}\ln\, \boldsymbol{c} + i, \quad (2.46)$$

$$\boldsymbol{g}(\boldsymbol{y},\boldsymbol{z},\boldsymbol{u}) := \begin{bmatrix} \beta\left(\frac{t_+-t_-}{f}\right)\boldsymbol{D}_c & \beta\boldsymbol{c}_{diag}\boldsymbol{D}_{\phi_2} \end{bmatrix} \begin{bmatrix} \boldsymbol{c} \\ \boldsymbol{\phi_2} \end{bmatrix} + i, \quad (2.47)$$

for the logarithmic and quadratic models.

A key parameter for solving any DAE system is its index, defined as the number of derivatives needed to transform the DAE into an ODE. DAEs of index 1 are of particular interest, as they are significantly simpler to solve. To solve an index 1 DAE system, the temporal derivative of the algebraic equation (2.39b) is taken

$$0 = \frac{d\boldsymbol{g}}{d\boldsymbol{y}}\dot{\boldsymbol{y}} + \frac{d\boldsymbol{g}}{d\boldsymbol{z}}\dot{\boldsymbol{z}} + \frac{d\boldsymbol{g}}{d\boldsymbol{u}}\dot{\boldsymbol{u}}, \quad (2.48)$$

such that an expression to propagate the algebraic variable $\boldsymbol{z}$ in time can be obtained by

$$\dot{\boldsymbol{z}} = -\left[\frac{d\boldsymbol{g}}{d\boldsymbol{z}}\right]^{-1}\left(\frac{d\boldsymbol{g}}{d\boldsymbol{y}}\dot{\boldsymbol{y}} + \frac{d\boldsymbol{g}}{d\boldsymbol{u}}\dot{\boldsymbol{u}}\right). \quad (2.49)$$

A solution to (2.49) only exists if $d\boldsymbol{g}/d\boldsymbol{z}$ is non-singular. For the logarithmically nonlinear model of (2.33) and (2.34), the derivative of $\mathbf{g}$ with respect to the algebraic variable $\boldsymbol{\phi_2}$ in the electrodes is given by

$$\frac{d\boldsymbol{g}}{d\boldsymbol{z}} = \kappa\boldsymbol{D}_{\phi_2} + \sigma\boldsymbol{D}_{\phi_1} \quad (2.50)$$

and in the separator by

$$\frac{d\boldsymbol{g}}{d\boldsymbol{z}} = \kappa\boldsymbol{D}_{\phi_2}. \quad (2.51)$$

The derivative $d\boldsymbol{g}/d\boldsymbol{z}$ for the quadratically non-linear model of (2.35) and (2.36) is given by

$$\frac{d\boldsymbol{g}}{d\boldsymbol{z}} = \beta \mathbf{c}_{diag} \boldsymbol{D}_{\phi_2} + \sigma \boldsymbol{D}_{\phi_1} \tag{2.52}$$

in the electrodes and by

$$\frac{d\boldsymbol{g}}{d\boldsymbol{z}} = \beta \boldsymbol{c}_{diag} \boldsymbol{D}_{\phi_2}. \tag{2.53}$$

in the separator. The matrices (2.50), (2.51), (2.52) and (2.53) are generally all invertible, and as such (2.33), (2.34), (2.36) and (2.35) are DAEs of index 1. This means that the evolution of the models can be considered as an initial value problem, which can be integrated using a solver such as MATLAB's ode15s routine, where a Newton iteration method is used to solve the algebraic equations and an implicit numerical differentiation formula (NDF) to carry out the integration [135, 136]. This solver is suitable for stiff systems and those with algebraic constraints, as encountered with the supercapacitor model.

2.6 Results

Experimental data of typical charging profiles of a supercapacitor from SAFT America [28] is presented in [163]. Most of the parameters of the supercapacitor are given in Tables 2.4 and 2.5, with the rest being calculated using equations (2.4), (2.11) and (2.12). In [163], the supercapacitor was first charged from an initial voltage of 1.63 V at a constant current of 100 A for 23.2 s whereupon the voltage was then held for 6 s at a constant value of 1.41 V, a constant-current, constant-voltage (CC-CV) charging profile. In this chapter, this CC-CV profile is labelled the standard charging profile.

Figure 2.1 compares the model outputs from (2.33) and (2.34) solved using the SEM and FDM with the experimental data presented in [163]. Both models can be seen to match well with the experimental data, validating the model assumptions for this typical charging profile. Furthermore, the size of the FDM and SEM models are small, using only 5 elements in each domain. This contrasts with the generalised finite element method of [3], which also compares its results against the data of [163], that used 1200 and 2500 finite elements. This shows that accurate results can be obtained using low order models.

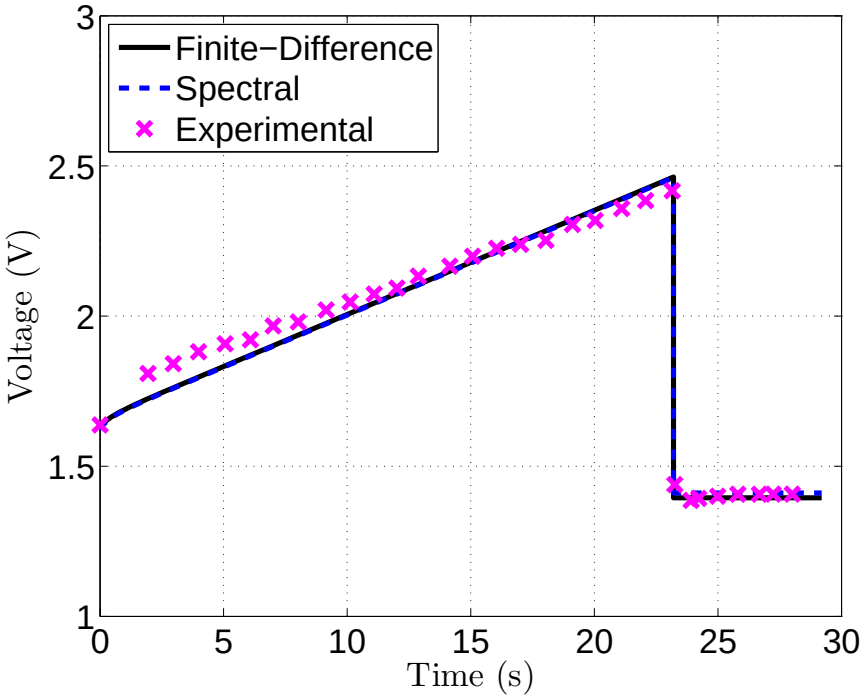
Parameter	Value	Units
L_{elect}	50	μ m
L_{sep}	25	μ m
aC	42 $\times 10^6$	F/m^3
c_0	930	mol/m^3
κ_∞	0.067	S/m
t_+	0.5	
I	100	A
S	2.747	m^2
$i := I/S$	36.403	A/m^2
$\frac{dq_+}{dq} = \frac{dq_-}{dq}$	-0.5	
T	298	K
Characteristic Time Constant	7.4	s

Table 2.4: Parameters for the supercapacitor model [163].

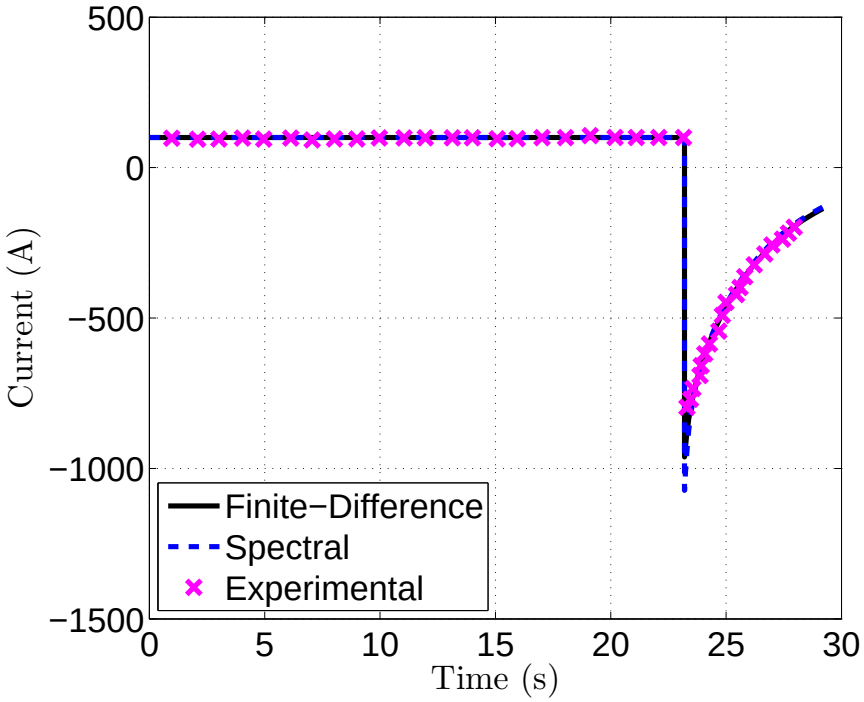
Electrode Region Parameters		
Parameter	Value	Units
ϵ	0.67	
σ	0.0521	S/m
Γ	2.3	
Separator Region Parameters		
Parameter	Value	Units
ϵ	0.6	
Γ	1.29	

Table 2.5: Separate parameters for both the separator and electrode regions [163].

The accuracy of the states of the model, rather than the model outputs, is investigated in Figure 2.2. In this figure, the error convergence rates with respect to the number of elements in each domain for the logarithmic model (2.33) and (2.34) discretised using the FDM and SEM are shown. For this comparison, the FEM solution with a high number of nodes (41 in each electrode and 18 in the separator) obtained from COMSOL is taken to be the reference numerical solution. The error of the figure is defined as the 2-norm of the absolute error between the solver and the reference solutions, normalised with respect to the number of time steps and spatial



(a) Voltage.

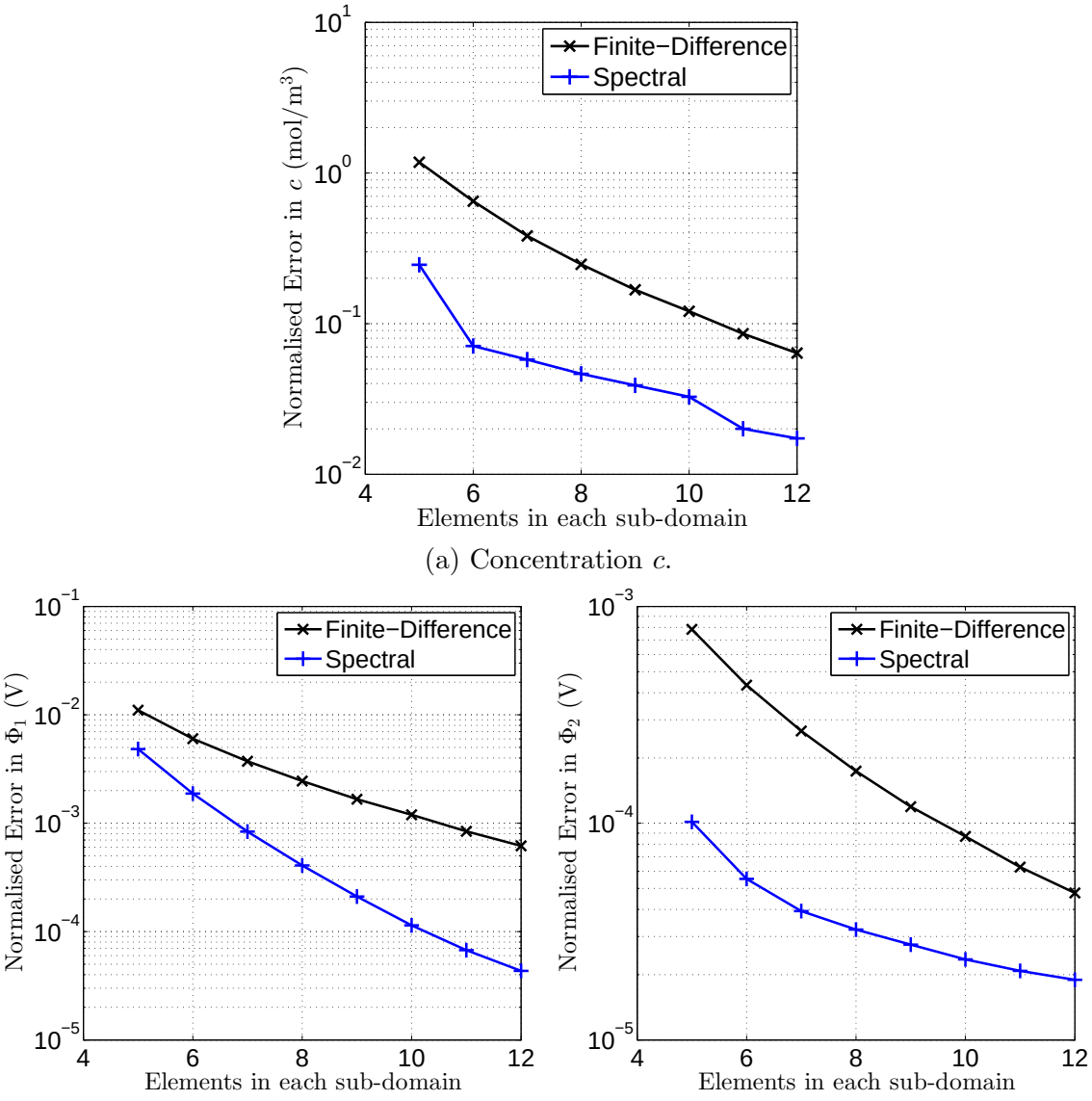


(b) Current.

Figure 2.1: The voltage/current responses of (2.33) and (2.34) for the standard charging profile discretised using the FDM and SEM with the experimental data of [163].

elements. Figure 2.2 shows that the error of the SEM converges much faster than the FDM, indicating that a given level of accuracy can be obtained with fewer nodes using the SEM. In Figure 2.3, simulation computing times for the standard charging profile of (2.33) and (2.34) discretised using the FDM and SEM are recorded using the MATLAB 'tictoc' command. The solution accuracies for both simulations are intended to be kept approximately the same and this is achieved by respectively using 6 and 12 elements in each domain for the SEM and FDM discretised models. It is shown that, for a similar level of solution accuracy, the simulation computing time of the SEM model is approximately 52% that of the FDM model. This implies that the SEM discretised model would be superior when used for accurate state estimation with an observer and as the basis for an online controller. Whilst only giving a relatively moderate speed up in simulation computing time, the compact form of the SEM discretisation has other benefits. For example, in chapter 5, optimisation problems are solved whose solutions gives bounds on energy properties of the supercapacitor model. The computational complexity of these optimisation problems was found to scale rapidly with the number of discretisation elements, with the compact form of the SEM making this analysis tractable.

The effect of the logarithmic and quadratic model non-linearities is investigated in Figures 2.4, 2.5, 2.6 and 2.7. It is noted that the choice of $t_+ = 0.5$ from Table 2.4 eliminates the non-linear logarithmic term from (2.33) and (2.34). To show that the presented model is also applicable for the non-linear case, CC-CV simulations where t_+ is increased from 0.5 to 0.75 are run. Referring to the labels of Figures 2.4, 2.5, 2.6 and 2.7, the "Linear" model involves (2.33) and (2.34) with $t_+ = 0.5$, the "Logarithm" model involves (2.33) and (2.34) with $t_+ = 0.75$ and the "Quadratic" model uses (2.35) and (2.36) with $t_+ = 0.5$. For the standard CC-CV charging profile, the impact of the non-linearities can be seen to be neglible, as shown in Figures 2.4 and 2.5, with the numerical solutions being in close agreement with the linear model. However, in Figure 2.6, the ionic concentration is decreased from 930 mol/m^3 to 250 mol/m^3, while in Figure 2.7, an extended charging profile is implemented. This extended charging profile is identical to the standard charging profile except with the initial voltage being -2.37 V, the CC and CV charges being held for 130 s and 70 s respectively and the voltage drop at the CC-CV transition point at 130 s being -1.08 V. For both of these cases, a noticeable difference in the numerical solutions between the quadratic model and the linear model is observed. This implies that the quadratic model is applicable for simulations where there is a large relative change in the electrolyte concentration. However, for the charging profiles simulated in this



(a) Concentration c.

(b) Electrode Potential Φ_1.

(c) Electrolyte Potential Φ_2.

Figure 2.2: The normalised errors of (2.33) and (2.34) discretised using the SEM and FDM, with the reference solution being obtained from COMSOL.

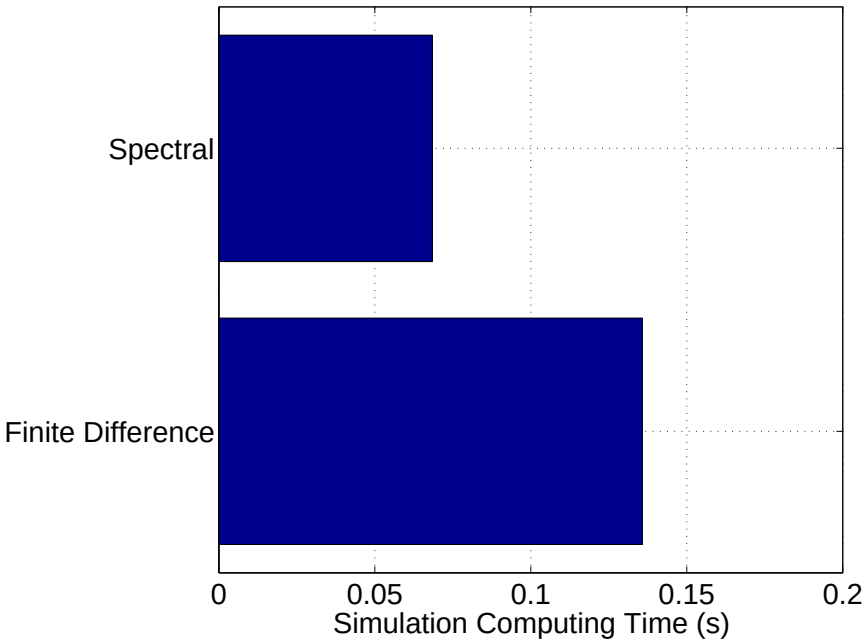
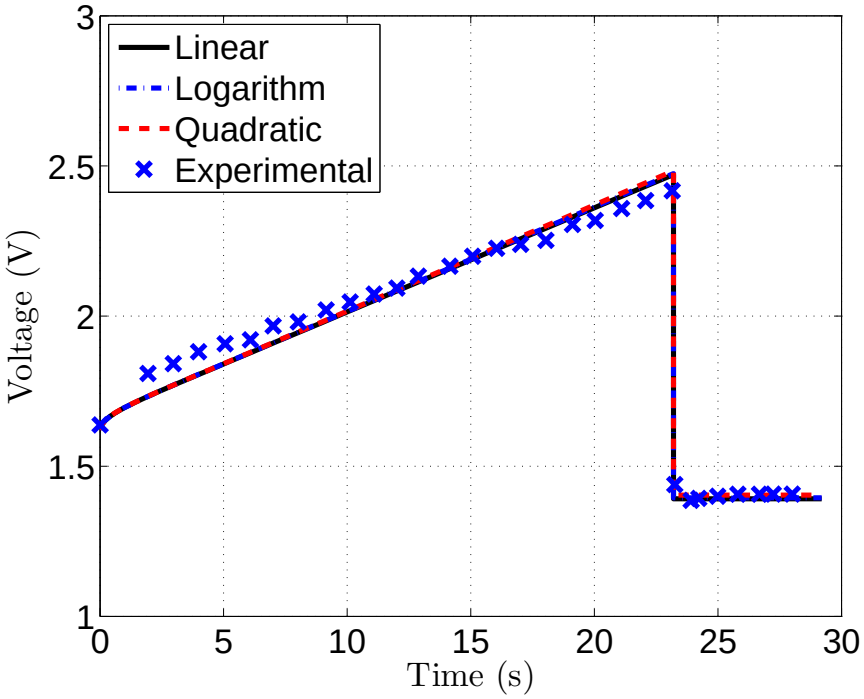


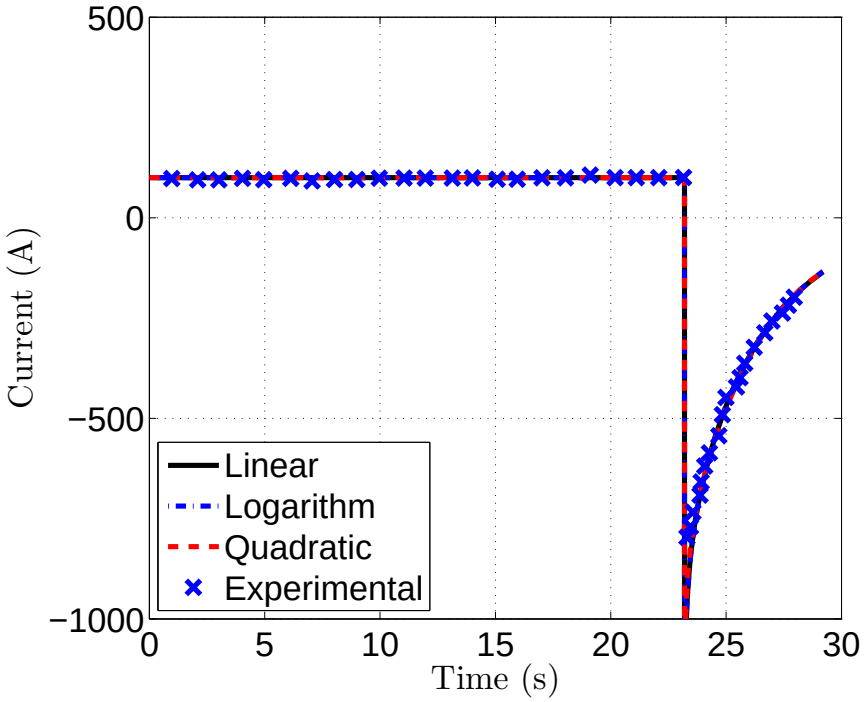
Figure 2.3: Simulation computing times for the standard charging profile of (2.33) and (2.34) discretised using the FDM and SEM. Computing times were recorded using the MATLAB 'tictoc' command.

chapter, the effect of the logarithmic non-linear term is neglible, with there being hardly any difference between its solution and that of the linear model. Due to the improved convergence properties of spectral methods outlined in Figure 2.2, all of the non-linear solutions of Figures 2.4, 2.5, 2.6 and 2.7 are discretised using the SEM. This means that the inclusion of the non-linear terms does not lead to a rapid rise in the number of elements, with the solutions of Figure 2.4 being obtained using 5 elements in each domain only.

Supercapacitors are often combined with fuel cells or batteries, forming a hybrid power system [176]. In this arrangement, the inclusion of the supercapacitor can act as a low-pass filter to reduce the stress on the fuel cell/battery and provide performance benefits, due to the high power density. A key property for the supercapacitor in this application is the variation of capacitance with frequency. Figure 2.8a shows simulated electrochemical impedance spectroscopy results using the procedure of [95] for an input current of 2 A overlaid with a small-amplitude 0.1 A sinusoidal signal. A rapid decrease in real capacitance due to diffusion limitations can be observed for all of the models above a certain frequency, known as the knee frequency. This indicates that the performance of the supercapacitor is poor in this operating regime. The knee frequency can be determined by inspecting the peak value of the complex capacitance

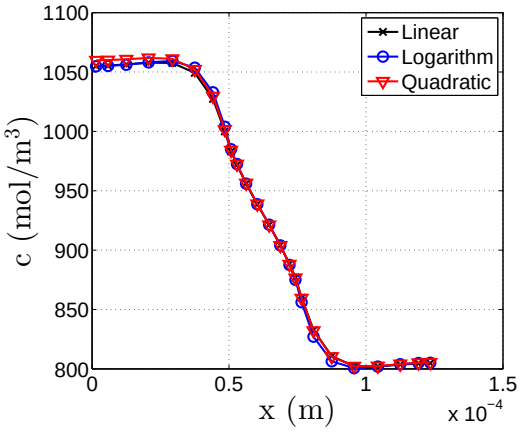


(a) Voltage.

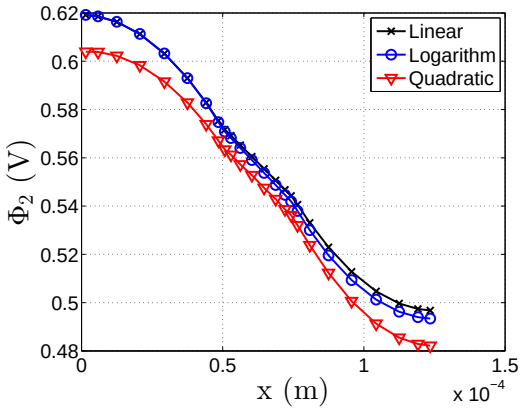


(b) Current.

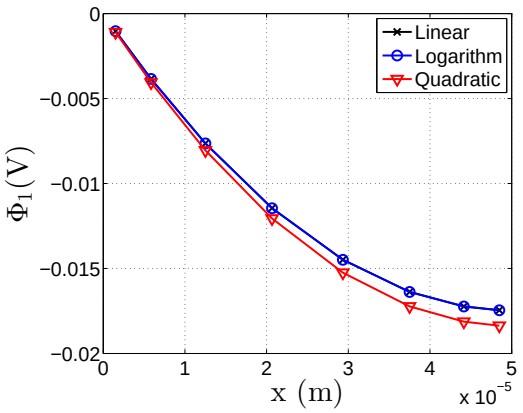
Figure 2.4: The voltage/current response of the non-linear models and experimental data of [163] for the standard CC-CV charging profile.



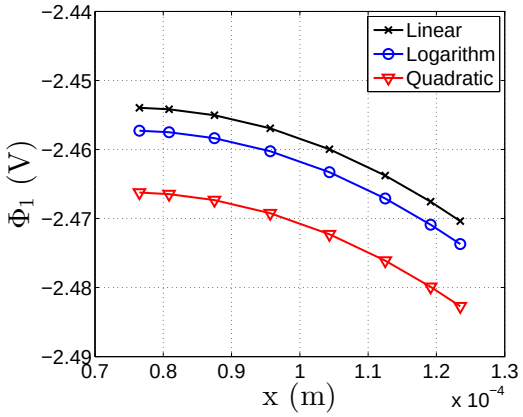
(a) Electrolyte concentration.



(b) Electrolyte potential.

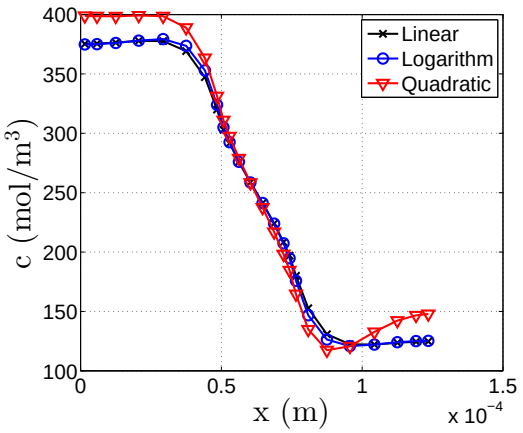


(c) Potential in the left electrode.

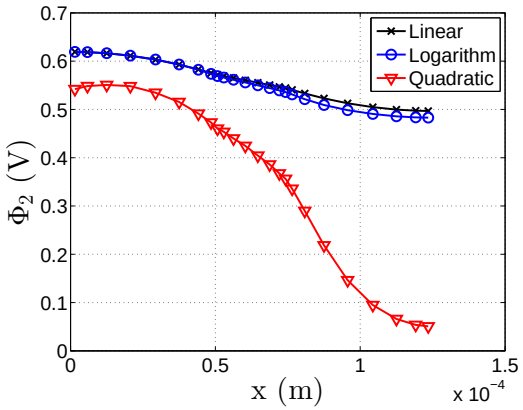


(d) Potential in the right electrode.

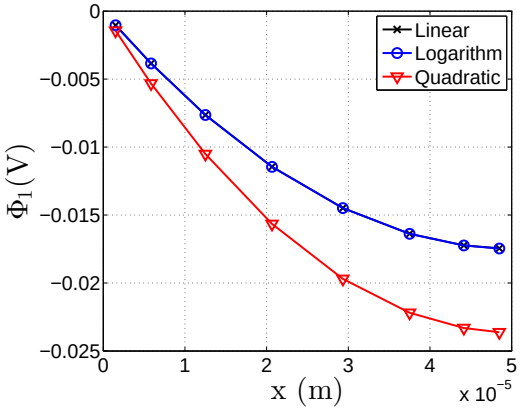
Figure 2.5: The state distribution of the non-linear models after 23.2 s of the standard charging profile.



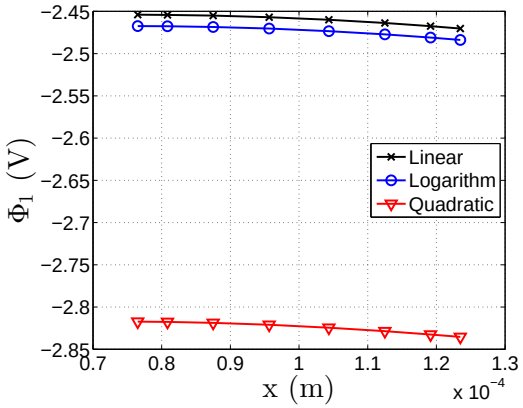
(a) Electrolyte concentration.



(b) Electrolyte potential.

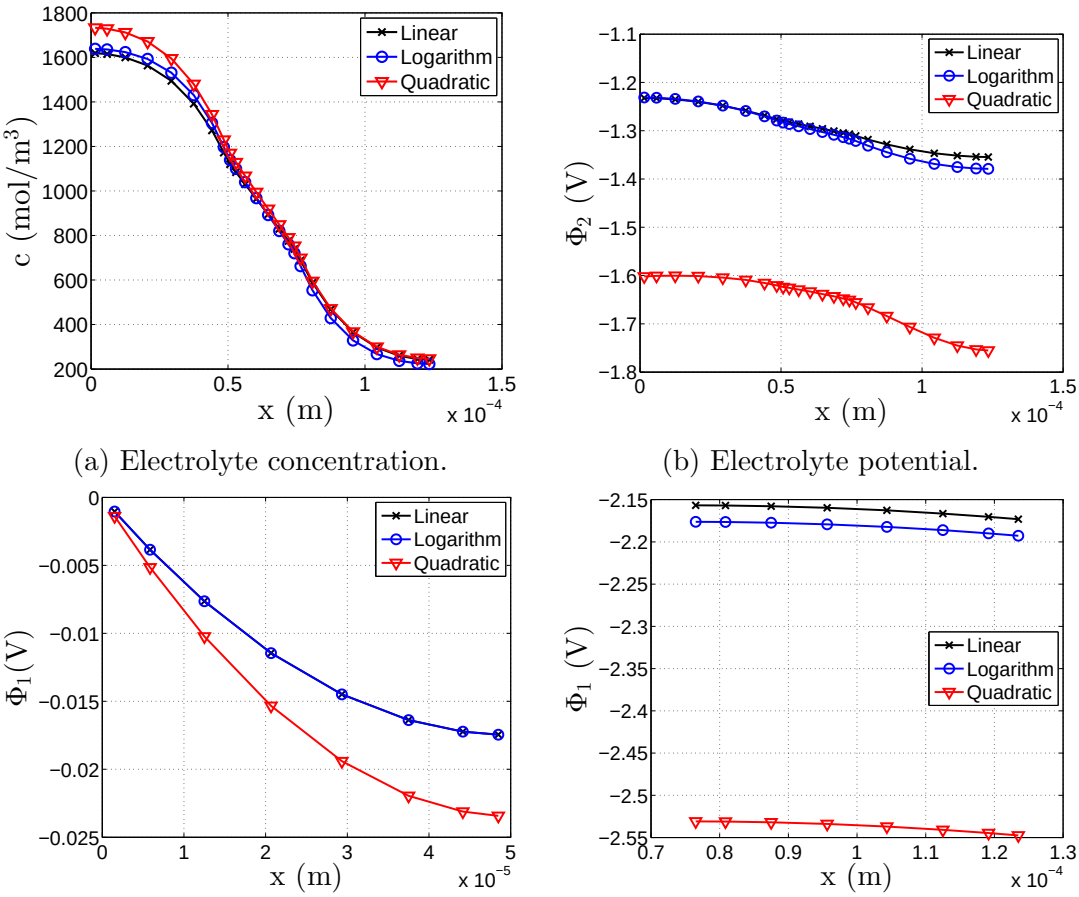


(c) Potential in the left electrode.



(d) Potential in the right electrode.

Figure 2.6: The state distribution of the non-linear models after 23.2 s of the standard charging profile with the electrolyte concentration reduced from 930 mol/m^3 to 250 mol/m^3.



(a) Electrolyte concentration.

(b) Electrolyte potential.

(c) Potential in the left electrode.

(d) Potential in the right electrode.

Figure 2.7: The state distribution of the non-linear models after 130 s of the extended charging profile.

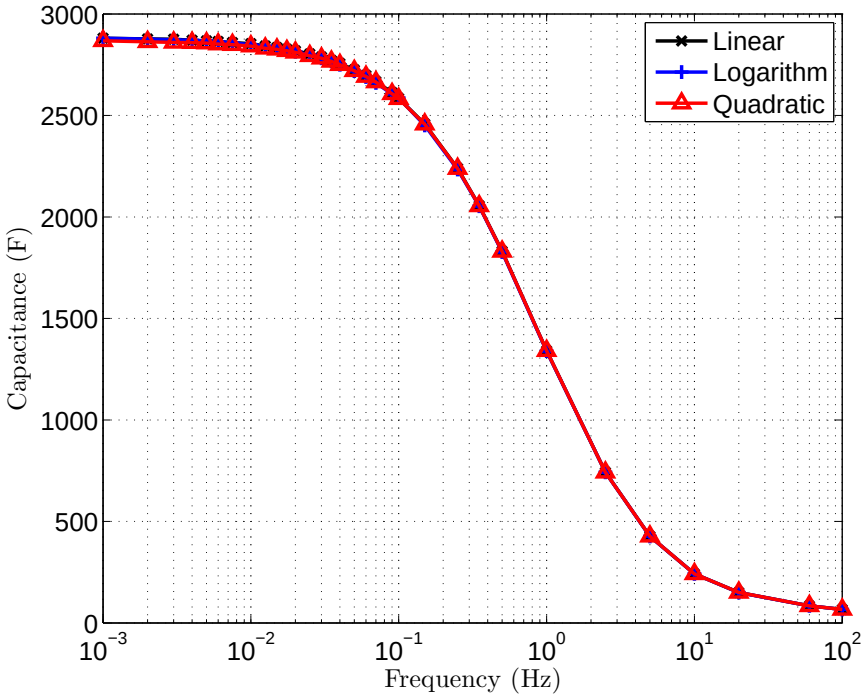
[95], as shown in Figure 2.8b. In the models used in this study, the capacitance is set as a fixed parameter that is independent of voltage whereas in real supercapacitors, capacitance varies with voltage [176]. The model could be extended to incorporate this effect, e.g. by implementing a Guoy-Chapman-Stern capacitance model [95], however, it is noted that the theoretical understanding of the relationship between double layer potential and capacitance is as yet too complex [95].

2.7 Conclusion

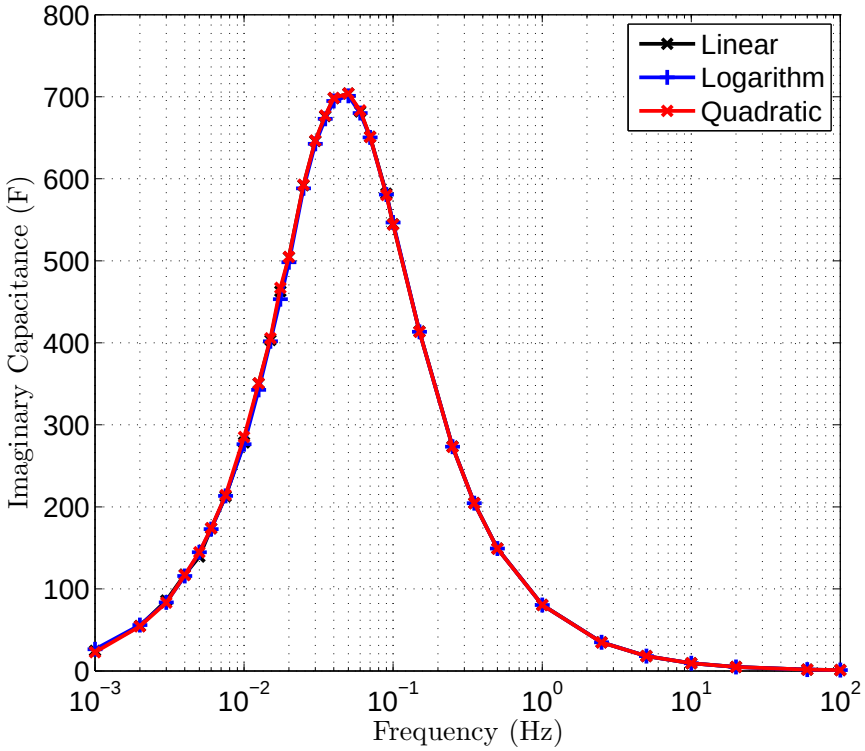
In this chapter, two non-linear physics-based supercapacitor models were implemented in a novel way using a spectral element method. The first model was based on the model presented in [163] while the second model accounted for the linear dependence between electrolyte conductivity and concentration. For a typical supercapacitor CC-CV charging profile, the numerical solutions from both models were found to be in close agreement with experimental data. However, for other conditions, such as the electrolyte concentration diluted or the charge duration of the supercapacitor extended, a noticeable difference between the numerical solutions of the two models was observed. This was due to the large relative change in electrolyte concentration affecting the conductivity. Electrical impedance spectroscopy simulations were also carried out on the models, and it was found that the capacitance of the supercapacitor models decreased rapidly when the frequency of the input current exceeded an upper threshold, as expected.

The normalised error of the model numerical solutions discretised using the spectral element method was found to converge faster as the number of domain elements was increased compared to the finite difference method of [162]. An accurate solution could also be obtained using fewer elements than the finite element 3D model of [3]. As a result, discretising the models using the spectral element method reduced the number of nodes needed to obtain a specified solution tolerance and resulted in a lower order model that was faster to implement. This implies that the models could be appropriate for a real-time implementation as well as for accurate state estimation with an observer.

In the rest of this thesis, the PB supercapacitor model with logarithmic nonlinearity developed in this chapter is analysed in detail. The following chapter considers how much information can be extracted regarding this model from sensor measurements.



(a) Real capacitance.



(b) Imaginary capacitance.

Figure 2.8: The variation of real and imaginary capacitance with input current frequency. Obtained using an electrochemical impedance spectroscopy simulation with an input current of 2 A overlaid with a small-amplitude 0.1 A sinusoidal signal.

More specifically, model observability, relating to whether the internal state of the supercapacitor can be estimated using an observer, is discussed as well as the problem of estimating the model parameters, such as the diffusion coefficient and electrode conductivity, from input-output data of current-voltage responses.

Chapter 3

Model Parameter Estimation and Observability

This chapter considers the extent to which information can be extracted about the supercapacitor model with a logarithmic nonlinearity presented in Chapter 2 using current/voltage experimental data. The topic of model observability is first addressed before the model parameters are estimated using experimental data. Observability is a key concept in control theory and describes the mapping from sensor measurements to the current value of the state. If a system is fully observable, then its states can be estimated using an "observer" that estimates the values of the states based on sensor measurements. In doing so, an observer corrects for the presence of noise in the dynamics and in the sensor, with the observer states giving a more accurate representation of the true state of the plant. In controllers, most complex systems are implemented along with an observer, and this includes electrochemical energy storage systems. Observer design for energy storage systems has been considered in numerous publications, including [106, 186] for supercapacitors and [9, 23, 104, 149] for lithium ion batteries. Many fundamental issues have been highlighted regarding observability of lithium ion batteries related to the flatness of the OCV curve, and similar issues are raised for the supercapacitor in this chapter. Parameter estimation aims to obtain accurate estimates of the parameters of a model with pre-described structure from the input output response. This enables the model to give accurate simulations of the plant, such that the analysis of the parameter estimated model relates to the true plant. Parameter estimation of supercapacitors using a systems theoretic approach, as in [94], has so far only involved circuits [118, 186], with the parameters of the PB models such as [162] being obtained through experimental techniques. The results of this chapter are used frequently in the rest of the thesis.

3.1 Observability Analysis

Observability of the discretised logarithmic index-1 DAE model of chapter 2 is considered. The majority of existing literature on observability analysis and parameter estimation involves ODE models, not DAEs [94, 165]. So, in order to use these developed tools for the supercapacitor model, the index-1 DAE of (2.33) is transformed into a ODE by first solving the algebraic equation (2.39b) for the algebraic variable $\boldsymbol{\phi_2}$

$$\boldsymbol{\phi_2} = -\left(\kappa\hat{\mathbf{D}}_{\phi_2} + \sigma\boldsymbol{D}_{\phi_1}\right)^{-1}\kappa\left(\frac{t_+ - t_-}{f}\right)\boldsymbol{D}_{\ln c}\ln\boldsymbol{c} + \sigma\boldsymbol{D}_{\phi_1}(\boldsymbol{\phi_1} - \boldsymbol{\phi_2}) + i \tag{3.1}$$

Solving (3.1) requires setting a reference potential as the model is only dependent upon the potential difference $\boldsymbol{\phi_1} - \boldsymbol{\phi_2}$. In the PB supercapacitor model, only potential gradients, rather than the potential values themselves, are used to describe the system dynamics and so an arbitrary reference can be set. Substituting this expression for the algebraic variable $\boldsymbol{\phi_2}$ back into the model dynamics gives

$$\begin{aligned}
&\begin{bmatrix}\epsilon & \frac{aC}{F}(t_-\frac{dq_+}{dq} + t_+\frac{dq_-}{dq}) \\ 0 & aC\end{bmatrix}\begin{bmatrix}\dot{\boldsymbol{c}} \\ \dot{\boldsymbol{\phi}}_{\mathbf{1}} - \dot{\boldsymbol{\phi}}_{\mathbf{2}}\end{bmatrix} = \\
&\begin{bmatrix}D\boldsymbol{D}_c^2 & 0 \\ 0 & \sigma\boldsymbol{D}_{\phi_1}^2 - \sigma\boldsymbol{D}_{\phi_1}^2(\kappa\hat{\mathbf{D}}_{\phi_2} + \sigma\boldsymbol{D}_{\phi_1})^{-1}\sigma\boldsymbol{D}_{\phi_1}\end{bmatrix}\begin{bmatrix}\boldsymbol{c} \\ \boldsymbol{\phi_1} - \boldsymbol{\phi_2}\end{bmatrix} \\
&+\begin{bmatrix}0 \\ -\sigma\boldsymbol{D}_{\phi_1}^2(\kappa\boldsymbol{D}_{\phi_2} + \sigma\boldsymbol{D}_{\phi_1})^{-1}\kappa\left(\frac{t_+ - t_-}{f}\right)\boldsymbol{D}_{\ln c}\end{bmatrix}\ln\boldsymbol{c} \\
&+\begin{bmatrix}0 \\ -\sigma\boldsymbol{D}_{\phi_1}^2(\kappa\boldsymbol{D}_{\phi_2} + \sigma\boldsymbol{D}_{\phi_1})^{-1}\end{bmatrix} i,
\end{aligned} \tag{3.2}$$

and back into the output voltage gives

$$\begin{aligned}
v = &\begin{bmatrix}0 & \boldsymbol{C_1} - \boldsymbol{C_1}(\kappa\boldsymbol{D}_{\phi_2} + \sigma\boldsymbol{D}_{\phi_1})^{-1}\sigma\boldsymbol{D}_{\phi_1}\end{bmatrix}\begin{bmatrix}\boldsymbol{c} \\ \boldsymbol{\phi_1} - \boldsymbol{\phi_2}\end{bmatrix} \\
&+ (-C_1(\kappa\boldsymbol{D}_{\phi_2} + \sigma\boldsymbol{D}_{\phi_1})^{-1}\kappa\left(\frac{t_+ - t_-}{f}\right)\boldsymbol{D}_{\ln c})\ln\boldsymbol{c} \\
&+ (\boldsymbol{D_1} - \boldsymbol{C_1}(\kappa\boldsymbol{D}_{\phi_2} + \sigma\boldsymbol{D}_{\phi_1})^{-1})i.
\end{aligned} \tag{3.3}$$

The algebra of (3.2) and (3.3) can be simplified by introducing the structure

$$\begin{bmatrix}\boldsymbol{M_{11}} & \boldsymbol{M_{12}} \\ 0 & \boldsymbol{M_{22}}\end{bmatrix}\begin{bmatrix}\dot{\boldsymbol{c}} \\ \dot{\boldsymbol{\phi}}_{\mathbf{1}} - \dot{\boldsymbol{\phi}}_{\mathbf{2}}\end{bmatrix} = \begin{bmatrix}\hat{\boldsymbol{A}}_{\mathbf{11}} & 0 \\ 0 & \hat{\boldsymbol{A}}_{\mathbf{22}}\end{bmatrix}\begin{bmatrix}\boldsymbol{c} \\ \boldsymbol{\phi_1} - \boldsymbol{\phi_2}\end{bmatrix} + \begin{bmatrix}0 \\ \boldsymbol{B_1}\end{bmatrix}\ln\boldsymbol{c} + \begin{bmatrix}0 \\ \boldsymbol{B_2}\end{bmatrix} i \tag{3.4}$$

$$v = \begin{bmatrix}0 & \tilde{\boldsymbol{C}}\end{bmatrix}\begin{bmatrix}\boldsymbol{c} \\ \boldsymbol{\phi_1} - \boldsymbol{\phi_2}\end{bmatrix} + \tilde{\boldsymbol{D}}_{\mathbf{1}}\ln\boldsymbol{c} + \tilde{\boldsymbol{D}}_{\mathbf{2}} i \tag{3.5}$$

where

$$\begin{bmatrix} \boldsymbol{M_{11}} & \boldsymbol{M_{12}} \\ \boldsymbol{0} & \boldsymbol{M_{22}} \end{bmatrix} = \begin{bmatrix} \epsilon & \frac{aC}{F}(t_- \frac{dq_+}{dq} + t_+ \frac{dq_-}{dq}) \\ 0 & aC \end{bmatrix} \tag{3.6}$$

$$\begin{bmatrix} \hat{\boldsymbol{A}}_{\boldsymbol{11}} & \boldsymbol{0} \\ \boldsymbol{0} & \hat{\boldsymbol{A}}_{\boldsymbol{22}} \end{bmatrix} = \begin{bmatrix} D\mathbf{D}_c^2 & 0 \\ 0 & \sigma\mathbf{D}_{\phi_1}^2 \left(I - (\kappa\mathbf{D}_{\phi_2} + \sigma\mathbf{D}_{\phi_1})^{-1} \sigma\mathbf{D}_{\phi_1}\right) \end{bmatrix} \tag{3.7}$$

$$\begin{bmatrix} 0 \\ \boldsymbol{B_1} \end{bmatrix} = \begin{bmatrix} 0 \\ -\left(\sigma\kappa\frac{t_+ - t_-}{f}\right) \mathbf{D}_{\phi_1}^2 \left(\kappa\mathbf{D}_{\phi_2} + \sigma\mathbf{D}_{\phi_1}\right)^{-1} \mathbf{D}_{\ln c} \end{bmatrix}$$

$$\begin{bmatrix} 0 \\ \boldsymbol{B_2} \end{bmatrix} = \begin{bmatrix} 0 \\ -\sigma\mathbf{D}_{\phi_1}^2 \left(\kappa\mathbf{D}_{\phi_2} + \sigma\mathbf{D}_{\phi_1}\right)^{-1} \end{bmatrix}. \tag{3.8}$$

The general form of this equation system is

$$\boldsymbol{M}\dot{\boldsymbol{x}} = \boldsymbol{A}\boldsymbol{x} + \tilde{\boldsymbol{B}}_{\boldsymbol{1}} \ln \boldsymbol{c} + \tilde{\boldsymbol{B}}_{\boldsymbol{2}} i \tag{3.9}$$

$$v = \boldsymbol{C}\boldsymbol{x} + \tilde{\boldsymbol{D}}_{\boldsymbol{1}} \ln \boldsymbol{c} + \tilde{\boldsymbol{D}}_{\boldsymbol{2}} i \tag{3.10}$$

having states $\boldsymbol{x} := [\boldsymbol{c}^T, \boldsymbol{\phi}_{\boldsymbol{1}}^T - \boldsymbol{\phi}_{\boldsymbol{2}}^T]^T$. The "mass" matrix $\boldsymbol{M}$ can be inverted as it is constant and full rank to give

$$\dot{\boldsymbol{x}} = \boldsymbol{A}_{\boldsymbol{m}}\boldsymbol{x} + \boldsymbol{B}_{\boldsymbol{1},\boldsymbol{m}} \ln \boldsymbol{c} + \boldsymbol{B}_{\boldsymbol{2},\boldsymbol{m}} i. \tag{3.11}$$

where $\boldsymbol{A}_{\boldsymbol{m}} = \boldsymbol{M}^{-1}\boldsymbol{A}$, $\boldsymbol{B}_{\boldsymbol{1},\boldsymbol{m}} = \boldsymbol{M}^{-1}\tilde{\boldsymbol{B}}_{\boldsymbol{1}}$ and $\boldsymbol{B}_{\boldsymbol{2},\boldsymbol{m}} = \boldsymbol{M}^{-1}\tilde{\boldsymbol{B}}_{\boldsymbol{2}}$. In essence, this model describes the evolution of the states in a lower-order state-space, with these states being implicitly constrained to the manifold described by the algebraic equation. It is noted that the finite dimensional approximation introduced by discretisation means that higher order dynamic modes of the PDEs are not captured. As such, only *approximate*, not *exact*, observability can be shown [33].

3.1.1 Local Nonlinear Observability

Observability is defined in [165] as:

Definition 3.1. *Consider a system such as (3.10), (3.11). States $\boldsymbol{x_1}$ and $\boldsymbol{x_2}$ are said to be distinguishable if there exists an input function $\boldsymbol{u}$ such that $\boldsymbol{y}(\boldsymbol{x_1}, \boldsymbol{u}) \neq \boldsymbol{y}(\boldsymbol{x_2}, \boldsymbol{u})$ where $\boldsymbol{y}(\boldsymbol{x_i}, \boldsymbol{u})$, $j = 1, 2$ is the output function corresponding to the input $\boldsymbol{u}$ and initial condition $\boldsymbol{x}(0) = \boldsymbol{x_j}$. The system is said to be locally observable at $\boldsymbol{x_0} \in X$ if there exists a neighbourhood $\mathcal{N}$ of $\boldsymbol{x_0}$ such that $\forall \boldsymbol{x} \in \mathcal{N}$ other than $\boldsymbol{x_0}$ is distinguishable from $\boldsymbol{x_0}$.*

When a model is fully observable, a unique solution for the states can be obtained solely from measurements of the output. If the model contains unobservable states, then those states cannot be estimated by an observer. The observability of a linear system is independent of the applied input, but this is not the case for nonlinear systems [165]. In the following nonlinear observability analysis, the current will be set to zero $i = 0$ A and the distinguishability argument from Definition 1 will be used to verify observability.

Observability of the logarithmic nonlinear ODE equation system given in (3.10), (3.11) will now be studied. Consider the nonlinear system

$$\dot{\boldsymbol{x}} = \boldsymbol{f}(\boldsymbol{x}) \tag{3.12}$$

$$\boldsymbol{y} = \boldsymbol{h}(\boldsymbol{x}) \tag{3.13}$$

which is a generalisation of the model in (3.10), (3.11). Observability of this system is shown by analysing the evolution of the output along the system trajectories. The Lie derivative of $\boldsymbol{h}$ with $\boldsymbol{f}$ enables this computation [165]. The first Lie derivative is defined by

$$L_{\boldsymbol{f}}^{0}\boldsymbol{h} = \boldsymbol{h}(\boldsymbol{x}) \tag{3.14}$$

with higher-order Lie derivatives being defined by the recursive relation

$$L_{\boldsymbol{f}}^{N}\boldsymbol{h} = \frac{d}{d\boldsymbol{x}}(L_{\boldsymbol{f}}^{N-1}) \cdot \boldsymbol{f}. \tag{3.15}$$

Lie derivatives offer the mathematical tools for computing the observability matrix $\boldsymbol{O}$

$$\boldsymbol{O} = \frac{d}{d\boldsymbol{x}} \begin{bmatrix} \boldsymbol{h}(\boldsymbol{x}) \\ \frac{d\boldsymbol{h}}{\partial \boldsymbol{x}} \cdot \boldsymbol{f}(\boldsymbol{x}) \\ \frac{d}{d\boldsymbol{x}} \left(\frac{d\boldsymbol{h}}{d\boldsymbol{x}} \cdot \boldsymbol{f}(\boldsymbol{x}) \right) \cdot \boldsymbol{f}(\boldsymbol{x}) \\ \vdots \\ \dots \end{bmatrix} = \frac{d}{d\boldsymbol{x}} \begin{bmatrix} L_{\boldsymbol{f}}^{0}\boldsymbol{h} \\ L_{\boldsymbol{f}}^{1}\boldsymbol{h} \\ L_{\boldsymbol{f}}^{2}\boldsymbol{h} \\ \vdots \\ L_{\boldsymbol{f}}^{n-1}\boldsymbol{h} \end{bmatrix} \tag{3.16}$$

with n being the state dimension of (3.11). If this matrix is full column rank, the model exhibits local nonlinear observability around the point $\boldsymbol{x}$ [165].

To compute $\boldsymbol{O}$, the $(n-1)^{th}$ Lie derivative is needed, which requires the $(n-1)^{th}$ derivatives of $\boldsymbol{f}(\boldsymbol{x})$ and $\boldsymbol{h}(\boldsymbol{x})$. These derivatives are the building blocks of $\boldsymbol{O}$ and for $\boldsymbol{f}$, these derivatives are defined by

$$\frac{d\boldsymbol{f}(\boldsymbol{x})}{d\boldsymbol{x}} = \frac{d}{d\boldsymbol{x}}(\boldsymbol{A_m}\boldsymbol{x} + \boldsymbol{B_{1,m}} \ln \boldsymbol{c}) = \boldsymbol{A_m} + \boldsymbol{B_{1,m}}\boldsymbol{c_{diag}^{-1}} \tag{3.17}$$

$$\frac{d^k\boldsymbol{f}(\boldsymbol{x})}{d\boldsymbol{x}^k} = \frac{d^k}{d\boldsymbol{x}^k}(\boldsymbol{A_m}\boldsymbol{x} + \boldsymbol{B_{1,m}} \ln \boldsymbol{c}) = (k-1)!\,\boldsymbol{B_{1,m}}\boldsymbol{c_{diag}^{-k}} \quad \text{for } k > 2, 3, \dots. \tag{3.18}$$

where $\boldsymbol{c_{diag}} = diag(\boldsymbol{c})$. A similar relation can be obtained for $\boldsymbol{h}(\boldsymbol{x})$ by exchanging the matrices $\boldsymbol{A_m}$ and $\boldsymbol{B_{1,m}}$ with $\boldsymbol{C}$ and $\tilde{\boldsymbol{D}}_{\boldsymbol{1}}$. The derivatives (3.17) and (3.18) are required for the computation of the Lie derivatives and appear in product rule combinations. Due to the product rule, the total number of terms that form the Lie derivative scales rapidly with its order. This makes the analysis limited to fairly small systems (typically $n < 10$) with the Lie derivatives being computed symbolically. To overcome this limitation, the observability analysis was carried out on a discretisation of the supercapacitor model PDEs with the fewest number of grid points necessary for a feasible solution.

In Fig 3.1, the singular values of $\boldsymbol{O}$ for a nine state discretisation of (3.10) and (3.11) are shown. The model parameters are the same as those given in Table 2.4, except with the transference number being $t_+ = 0.75$, so that the model is nonlinear. Local observability was checked for a "flat" distribution of $\boldsymbol{c}$, with $\boldsymbol{c} = 930\,\text{mol m}^{-3}$ everywhere, and a "step" distribution, where $\boldsymbol{c}$ was set to $100\,\text{mol m}^{-3}$ in the left electrode, $500\,\text{mol m}^{-3}$ in the separator and $1000\,\text{mol m}^{-3}$ in the right electrode. In both of these cases, the rank of $\boldsymbol{O}$ equaled the dimension of the state space system, so local nonlinear observability could be shown.

3.1.2 Unobservable Concentration States

When the two transference numbers are equal, i.e. $t_+ = t_-$, the model becomes linear and loses observability as shown in Fig 3.1 for the linear system. In this figure, the rank of $\boldsymbol{O}$ does not equal $n = 9$. Most transference number combinations appropriate for supercapacitor electrolytes are in general not equivalent, as different ions have different sizes [175]. However, in many models described in the literature, for example in [163], setting $t_+ = t_-$ is a commonly adopted parameter choice as it makes the model linear, eliminating the coefficient of the logarithmic term in (3.10) and (3.11).

When $t_+ = t_-$, the system matrices (3.4) can be written as

$$\begin{aligned}\begin{bmatrix}\dot{\boldsymbol{c}}\\ \dot{\bar{\boldsymbol{\phi}}}\end{bmatrix} &= \begin{bmatrix}\boldsymbol{M_{11}^{-1}} & -\boldsymbol{M_{11}^{-1}M_{12}M_{22}}\\ 0 & \boldsymbol{M_{22}^{-1}}\end{bmatrix}\begin{bmatrix}\hat{\boldsymbol{A}}_{\boldsymbol{11}} & 0\\ 0 & \hat{\boldsymbol{A}}_{22}\end{bmatrix}\begin{bmatrix}\boldsymbol{c}\\ \bar{\boldsymbol{\phi}}\end{bmatrix} \\ &= \begin{bmatrix}\boldsymbol{M_{11}^{-1}}\hat{\boldsymbol{A}}_{\boldsymbol{11}} & -\boldsymbol{M_{11}^{-1}M_{12}M_{22}}\hat{\boldsymbol{A}}_{\boldsymbol{22}}\\ 0 & \boldsymbol{M_{22}^{-1}}\hat{\boldsymbol{A}}_{\boldsymbol{22}}\end{bmatrix}\begin{bmatrix}\boldsymbol{c}\\ \bar{\boldsymbol{\phi}}\end{bmatrix} \\ &= \begin{bmatrix}\bar{\boldsymbol{A}}_{\boldsymbol{11}} & \bar{\boldsymbol{A}}_{\boldsymbol{12}}\\ 0 & \bar{\boldsymbol{A}}_{\boldsymbol{22}}\end{bmatrix}\begin{bmatrix}\boldsymbol{c}\\ \bar{\boldsymbol{\phi}}\end{bmatrix} = \bar{\boldsymbol{A}}\begin{bmatrix}\boldsymbol{c}\\ \bar{\boldsymbol{\phi}}\end{bmatrix}\end{aligned} \tag{3.19}$$

$$\boldsymbol{y} = \begin{bmatrix}0 & \tilde{\boldsymbol{C}}\end{bmatrix}\begin{bmatrix}\boldsymbol{c}\\ \bar{\boldsymbol{\phi}}\end{bmatrix} = \boldsymbol{C}\begin{bmatrix}\boldsymbol{c}\\ \bar{\boldsymbol{\phi}}\end{bmatrix} \tag{3.20}$$

where the substitution $\bar{\boldsymbol{\phi}} = \boldsymbol{\phi_1} - \boldsymbol{\phi_2}$ has been used. The observability matrix of this linear system is

$$\boldsymbol{O}_{lin} = \begin{bmatrix}\boldsymbol{C}\\ \boldsymbol{C}\bar{\boldsymbol{A}}\\ \boldsymbol{C}\bar{\boldsymbol{A}}^{\boldsymbol{2}}\\ \vdots\\ \boldsymbol{C}\bar{\boldsymbol{A}}^{n}\end{bmatrix}. \tag{3.21}$$

Global observability of the linear model (3.19), (3.20) can be deduced if $\boldsymbol{O}_{lin}$ is full column rank [165]. The computation of $\boldsymbol{O}_{lin}$ requires the computation of the n^{th} power of the system dynamic matrix $\bar{\boldsymbol{A}}$. The n^{th} power of an upper-triangular matrix, such as (3.19), is also upper-triangular in structure, following the general relation

$$\begin{bmatrix}\bar{\boldsymbol{A}}_{\boldsymbol{11}} & \bar{\boldsymbol{A}}_{\boldsymbol{12}}\\ 0 & \bar{\boldsymbol{A}}_{\boldsymbol{22}}\end{bmatrix}^{n} = \begin{bmatrix}\bar{\boldsymbol{A}}_{\boldsymbol{11}}^{n} & *\\ 0 & \bar{\boldsymbol{A}}_{\boldsymbol{22}}^{n}\end{bmatrix}. \tag{3.22}$$

Using (3.22), the observability matrix $\boldsymbol{O}_{lin}$ for (3.19) and (3.20) can be expressed as

$$\boldsymbol{O}_{lin} = \begin{bmatrix}0 & \tilde{\boldsymbol{C}}\\ 0 & \tilde{\boldsymbol{C}}\bar{\boldsymbol{A}}_{\boldsymbol{22}}\\ 0 & \tilde{\boldsymbol{C}}\bar{\boldsymbol{A}}_{\boldsymbol{22}}^{\boldsymbol{2}}\\ \vdots & \vdots\\ 0 & \tilde{\boldsymbol{C}}\bar{\boldsymbol{A}}_{\boldsymbol{22}}^{n}\end{bmatrix}. \tag{3.23}$$

The column of zeros in the observability matrix (3.23) reveals that the concentrations $\boldsymbol{c}$ are unobservable model states when the transference numbers are equal. The reason for these unobservable states is that the output (3.20) is solely dependent upon the potentials $\bar{\boldsymbol{\phi}}$ and the dynamics of $\bar{\boldsymbol{\phi}}$ can be described independently of $\boldsymbol{c}$ through the equation $\dot{\bar{\boldsymbol{\phi}}} = \bar{\boldsymbol{A}}_{\boldsymbol{22}}\bar{\boldsymbol{\phi}}$. This implies that the dynamics of the output v are independent

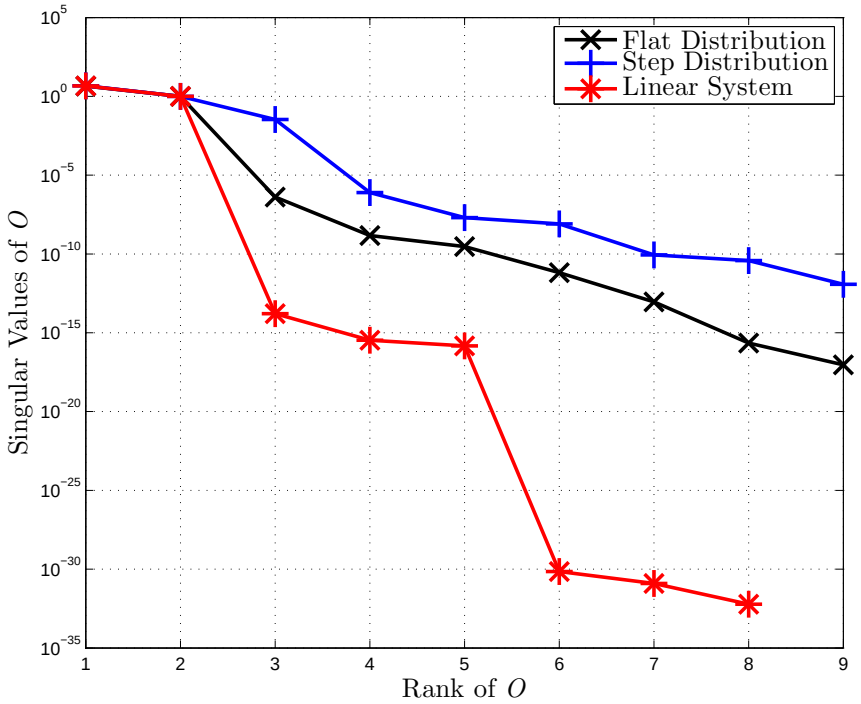


Figure 3.1: Singular values of the observability matrix $\boldsymbol{O}$ for two different linearisation points and for when the transference numbers are chosen such that the model is linear.

of the concentration states which means that from measurements of v, an estimate of the potentials can be gained, but not the concentration.

In Fig 3.2, the voltage difference when the model equations (5.9b) and (5.9a) were charged with a constant current of $i = 100\,A$ from two initial conditions is shown. The first initial condition had a flat distribution of $\boldsymbol{c} = 930\,\text{mol m}^{-3}$, while the other had a flat distribution of $200\,\text{mol m}^{-3}$. For the nonlinear model, a difference between the voltage across the model for two initial conditions was observed, however, this was not the case for the linear model with $t_+ = t_-$, which contradicts the definition of observability given by Definition 1. The presence of unobservable states means that an observer cannot be applied to correct these states for modelling and output noise.

A physical explanation for the unobservable concentration states can be obtained by returning to the fundamental PDEs. The problem originates from the algebraic equation (2.2), which is a nonlinear concentration dependent variation of Ohm's Law. When the transference numbers are equal, $D_+ = D_-$ and the ionic flux is only affected by migration due to the potential and not diffusion. One of the assumptions of the model is electro-neutrality of the electrolyte in the bulk solution, which is the important region for transport phenomenon. If the ions diffuse at different rates, a

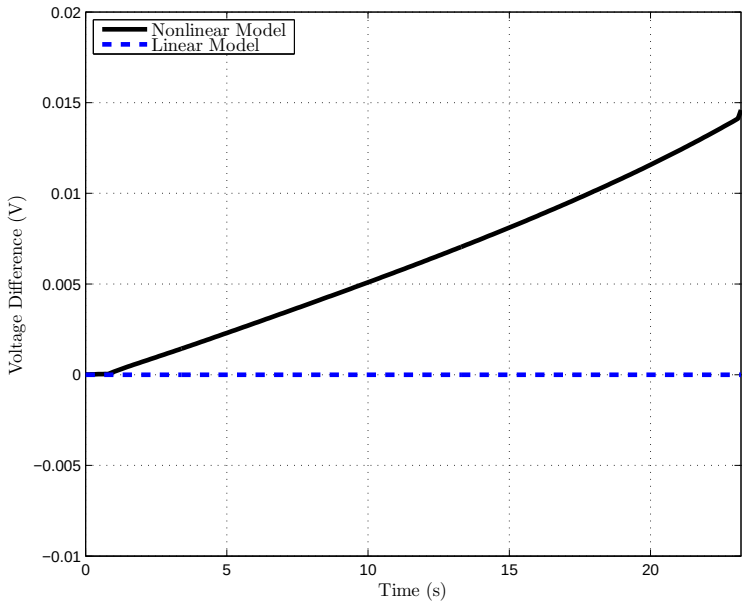


Figure 3.2: Differences between the voltages from simulations of the linear and nonlinear models starting from two different initial conditions, $\boldsymbol{c} = 200$ mol m^{-3} and $\boldsymbol{c} = 930$ mol m^{-3}.

potential difference is formed that pulls the ions together and enforces this assumption. This provides a link between concentration and potential, leading to full model observability.

3.1.3 Integrator Dynamics

As well as model observability issues, the supercapacitor model dynamics also limit the performance of the observer. For both the linear and nonlinear models, three dynamic modes were found to be integrators. A physical reason for the existence of the integrators lies with the energy storage characteristic of supercapacitors. Supercapacitors absorb energy provided by the current, and this energy is stored through charge separation across the double layer. The absorption of energy corresponds to an integrator dynamical system. In reality, supercapacitors exhibit self-discharge over time due to electrical field relaxation in the double layer, but this effect was not modelled.

An example of the impact of the integrator dynamics on the implementation of a Kalman filter with (3.19), (3.20) will now be discussed. The Kalman filter assumes that the true state $\boldsymbol{x}$ of the system evolves according to

$$\boldsymbol{x_{k+1}} = \bar{\boldsymbol{A}}\boldsymbol{x_k} + \hat{\boldsymbol{w}}_{\boldsymbol{k}} \tag{3.24}$$

where the system matrix $\bar{\boldsymbol{A}}$ is in discrete time with the sampling time chosen to be $\Delta t = 1s$. Noisy measurements $\boldsymbol{z_k}$ are obtained by

$$\boldsymbol{z_k} = \boldsymbol{C}\boldsymbol{x_k} + \hat{\boldsymbol{v}}_{\boldsymbol{k}}. \tag{3.25}$$

The noise signals $\hat{\boldsymbol{w}} \sim N(0, \boldsymbol{Q})$ and $\hat{\boldsymbol{v}} \sim N(0, \boldsymbol{R})$ are taken to be zero mean normally distributed signals with the co-variance matrices $\boldsymbol{Q}$ and $\boldsymbol{R}$ defined as

$$\boldsymbol{Q} = \begin{bmatrix} 100\,\boldsymbol{I_5} & 0 \\ 0 & 0.1\,\boldsymbol{I_4} \end{bmatrix} \quad \boldsymbol{R} = 0.1 \quad \boldsymbol{P_0} = \boldsymbol{Q}. \tag{3.26}$$

The Kalman filter smoothes this noise through an update stage

$$\hat{\boldsymbol{x}}_{\boldsymbol{k+1}} = \bar{\boldsymbol{A}}\hat{\boldsymbol{x}}_{\boldsymbol{k}} \tag{3.27}$$

$$\boldsymbol{P}_{\boldsymbol{k+1}} = \bar{\boldsymbol{A}}\boldsymbol{P}_{\boldsymbol{k}}\bar{\boldsymbol{A}}^{\boldsymbol{T}} + \boldsymbol{Q} \tag{3.28}$$

and a corrector stage

$$\boldsymbol{y}_{\boldsymbol{k+1}} = \boldsymbol{z}_{\boldsymbol{k+1}} - \boldsymbol{C}\hat{\boldsymbol{x}}_{\boldsymbol{k+1}} \tag{3.29}$$

$$\boldsymbol{K}_{\boldsymbol{k+1}} = \boldsymbol{C}\boldsymbol{P}_{\boldsymbol{k+1}}(\boldsymbol{C}\boldsymbol{P}^{-}_{\boldsymbol{k+1}}\boldsymbol{C}^{\boldsymbol{T}} + \boldsymbol{R})^{-1} \tag{3.30}$$

$$\hat{\boldsymbol{x}}^{+}_{\boldsymbol{k+1}} = \hat{\boldsymbol{x}}_{\boldsymbol{k+1}} + \boldsymbol{K}_{\boldsymbol{k+1}}\boldsymbol{y}_{\boldsymbol{k+1}} \tag{3.31}$$

$$\boldsymbol{P}_{\boldsymbol{k+1}} = (\boldsymbol{I} - \boldsymbol{K}_{\boldsymbol{k+1}}\boldsymbol{C})\boldsymbol{P}_{\boldsymbol{k+1}}. \tag{3.32}$$

where $\boldsymbol{P_k}$ is the evolving state co-variance matrix. The integrator dynamics mean that the introduction of noise into the system, as in (3.24), results in random walk trajectories. As $t \to \infty$, the deviation of the states is normally distributed with increasing variance, a flattening of the Gaussian distribution. This causes the noisy trajectories to "wander" and the corrected Kalman states follow this wandering trajectory.

In Fig 3.3, a Kalman filter simulation of the noisy model described by (3.24) and (3.25) is shown. The corrected Kalman output was shown to match up well with the true noisy measurements. However, the random walk trajectories of the noisy states can be clearly seen as the simulation progressed. This limitation means that a Kalman filter implementation is only appropriate for short simulation times. Both the linear and nonlinear models have integrator dynamics and so both follow random walk trajectories when subject to external inputs.

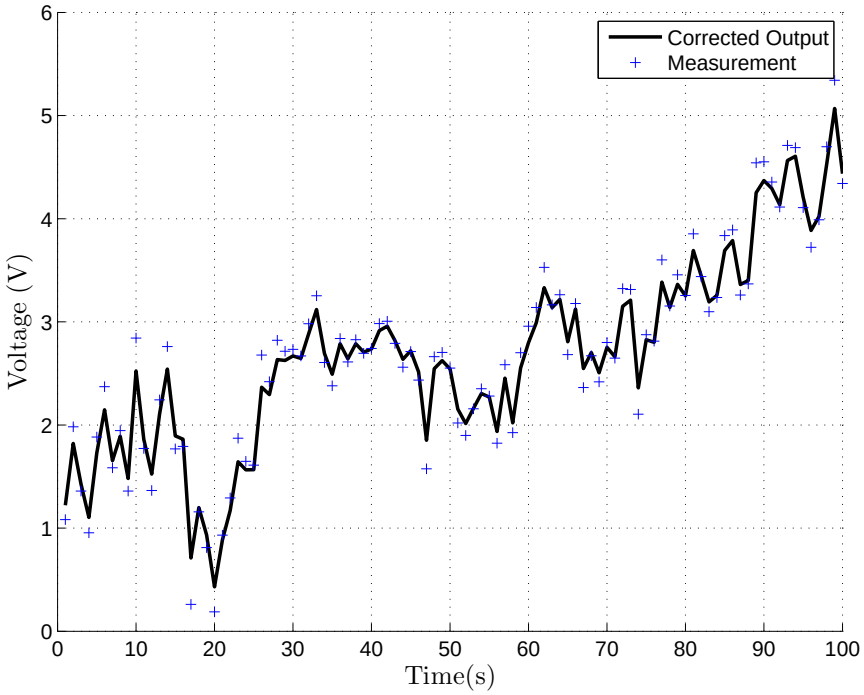


Figure 3.3: Random walk dynamics of the model output v with a Kalman filter implementation of (3.19) and (3.20).

3.2 Parameter Estimation of Electrochemical Supercapacitor Model

In this section, the parameters of the PB supercapacitor with logarithmic nonlinearity of chapter 2 are estimated. Experimental data in both the frequency and time domains of a commercially available Maxwell supercapacitor are used to estimate the parameters. The performance of the estimated PB model is compared against a 3^{rd} order "dynamic" circuit (EC) model from [185] with the dynamics

$$\begin{bmatrix} \dot{\boldsymbol{x}}_1 \\ \dot{\boldsymbol{x}}_2 \\ \dot{\boldsymbol{x}}_3 \end{bmatrix} = \begin{bmatrix} 0 & 0 & 0 \\ 0 & -\frac{1}{R_1 C_1} & 0 \\ 0 & 0 & -\frac{1}{R_2 C_2} \end{bmatrix} \begin{bmatrix} \boldsymbol{x}_1 \\ \boldsymbol{x}_2 \\ \boldsymbol{x}_3 \end{bmatrix} + \begin{bmatrix} \frac{1}{C} \\ \frac{1}{C_1} \\ \frac{1}{C_2} \end{bmatrix} i \tag{3.33a}$$

$$v = \boldsymbol{x}_1 + \boldsymbol{x}_2 + \boldsymbol{x}_3 + \boldsymbol{R}_s i \tag{3.33b}$$

3.2.1 Experimental Setup

Data were obtained on a commercially available supercapacitor produced by Maxwell with part number BCA P0100 P270T01. Testing was carried out on the Biologic SP-150 machine in the Energy and Power Group, Dept of Engineering Science, Univ of

Parameter	Identified Parameters				Units
		Frequency Domain			
	Time Domain	$0.5V_{ss}$	$1.5V_{ss}$	$2.5V_{ss}$	
κ_e	5.78×10^{-5}	1.018×10^{-4}	9.89×10^{-5}	9.09×10^{-5}	S m^{-1}
aC	1.91×10^{5}	1.08×10^{6}	1.27×10^{6}	1.35×10^{6}	F m^{-2}
σ	0.002	4.07×10^{-4}	4.58×10^{-4}	4.84×10^{-4}	S m^{-1}

Table 3.1: Identified parameters of the PB model for different steady state voltages V_{ss}.

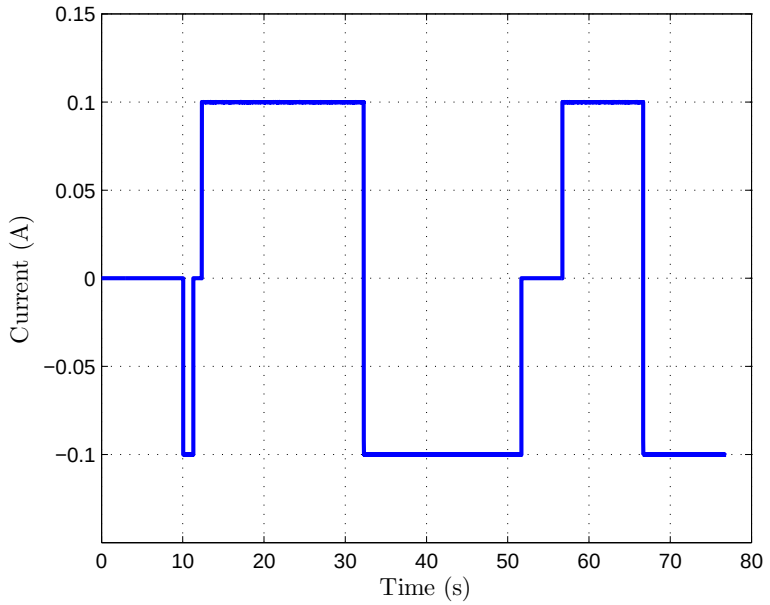
Parameter	Identified Parameters				Units
		Frequency Domain			
	Time Domain	$0.5V_{ss}$	$1.5V_{ss}$	$2.5VV_{ss}$	
R_1	1.04	0.0015	0.0017	0.0018	Ω
C_1	13.78	0.142	0.123	0.124	F
R_2	0.154	1.688	1.865	1.832	Ω
C_2	0.838	0.156	0.169	0.194	F
R_s	0.275	6.695	7.821	8.299	Ω
C	1.265	0.0987	0.0977	0.0984	F

Table 3.2: Identified parameters of the EC for different steady state voltages V_{ss}.

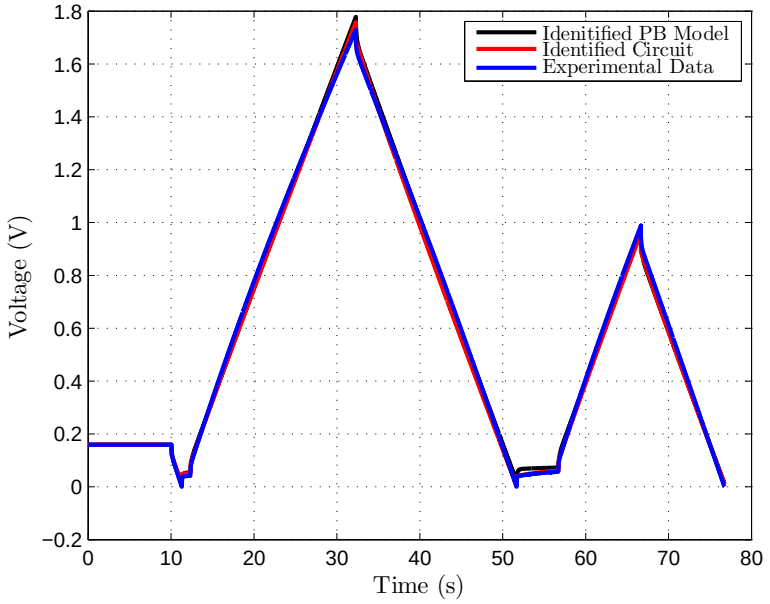
Oxford. The sampling time of the data logger was 0.01s and the machine could supply a maximum current of 400mA. Data were obtained both in the frequency domain with electrical impedance spectroscopy (EIS) [95] which shows the magnitude and phase of the impedance function $G(j\omega)$ at steady state voltages at which the supercapacitor is held (V_{ss}) 0.5V, 1.5V and 2.5V and in the time domain. The charging profile of the time domain data is composed of square waves of irregular frequency as shown in Figure 3.4a. This profile was chosen to introduce excitation frequencies into the supercapacitor in a manner that was convenient with regards to the testing equipment since these machines are orientated towards constant current charges/discharges.

3.3 Parameter Estimation

Parameter estimation was carried out by considering the model as a grey box model. Estimates of the model parameters were obtained using the MATLAB 'Systems Iden-



(a) Experimental square wave current charging profile.



(b) Voltage responses for the EC, the PB model and experimental data.

Figure 3.4: Identification in the time domain.

Parameter	Value	Units
ϵ_e	0.67	
ϵ_s	0.6	
κ_s	0.0259	S m^{-1}
t_+	0.55	
c_0	500	mol m^{-3}
S_A	2	m^2
L_e	2.5 $\times 10^{-5}$	m
L_s	1 $\times 10^{-5}$	m

Table 3.3: Fixed parameters of the PB model.

tification Toolbox' by solving the optimisation problem

$$\boldsymbol{\theta}^* = \arg\min_{\boldsymbol{\theta}} \|\boldsymbol{y} - \hat{\boldsymbol{y}}(\boldsymbol{\theta})\|_2 \tag{3.34}$$

$$\text{subject to } \boldsymbol{\theta} \in \Theta \subset \mathbb{R}^n \tag{3.35}$$

which minimises the norm of the error between the output from the experimental data output $\boldsymbol{y}$ and the simulated output from the model $\hat{\boldsymbol{y}}$ that is a function of the model parameters $\boldsymbol{\theta}$ [94], with the set of feasible parameters constrained to Θ. The subscripts $\boldsymbol{pb}$ and $\boldsymbol{ec}$ respectively define parameters for the logarithmic PB supercapacitor model and the equivalent circuit of (3.33).

By introducing the definition of the diffusion coefficient

$$D = \frac{2\kappa(t_+(1-t_+))RT}{F^2 c_0} \tag{3.36}$$

given in [163], the number of parameters required by the PB model can be reduced to the following eleven: ϵ_e, ϵ_s, κ_e, κ_s, aC, σ, t_+, L_e, L_s, S_A, c_0 where the subscripts e and s respectively define parameters in the electrode and separator domains. It was found that only the parameters $\boldsymbol{\theta_{pb}} = \{\kappa_e, aC, \sigma\}$, which were constrained to the set $\Theta_{pb} := \{\boldsymbol{\theta_{pb}} : \boldsymbol{\theta_{pb}} \geq 0\}$, were identifiable from the data. To improve the accuracy of the overall estimation, only these parameters were estimated in the identification of the PB model, with the rest of the parameters being fixed to values given in Table 3.3. This is a similar approach to [133] for lithium ion batteries. Due to their physical interpretation, these fixed parameters can be measured directly. The parameters of the EC model given in (3.33) were defined as $\boldsymbol{\theta_{ec}} := \{C_1, R_1, C_2, R_2, C, R_s\}$ which were constrained to be positive $\Theta_{ec} := \{\boldsymbol{\theta_{ec}} : \boldsymbol{\theta_{ec}} \geq 0\}$.

The simulated results from the square wave time domain data are shown in Figure 3.4. It was found that the added complexity of the PB model resulted in a slightly

less accurate simulation for this charging profile when compared to the EC, with the two models having error norms

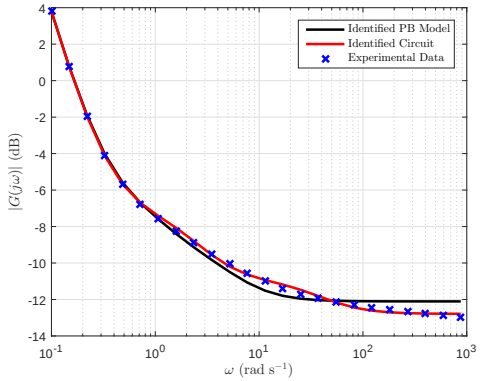
$$\|\boldsymbol{y} - \hat{\boldsymbol{y}}_{ec}(\boldsymbol{\theta_{ec}})\|_2 = 1.71 \tag{3.37}$$

$$\|\boldsymbol{y} - \hat{\boldsymbol{y}}_{\boldsymbol{pb}}(\boldsymbol{\theta_{pb}})\|_2 = 2.08. \tag{3.38}$$

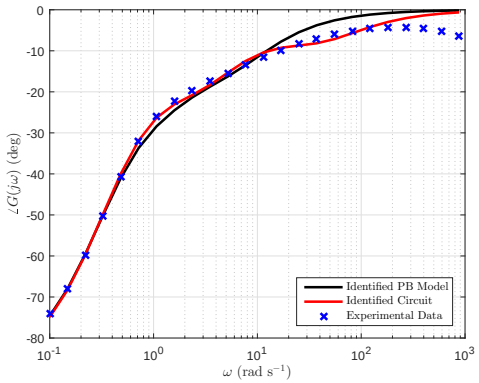
The identified model parameters for this charging profile are shown in Tabs 3.1 & 3.2.

The majority of existing studies on parameter estimation of batteries have fitted the parameters of ECs to EIS data and have shown that EIS varies with effects such as temperature, state-of-charge and steady-state voltage where the supercapacitor is held V_{ss} [187]. Figures 3.5, 3.6 and 3.7 compare simulated EIS results of the EC and a linearised version of the PB model with experimental data for different steady state voltages. The errors introduced by the linearisation should not be too significant for the small amplitude signals of EIS since the logarithm of the PB model is fairly benign when the concentration is far away from 0 mol m^{-3}. The parameters of the fitted models are shown in Tables 3.1, 3.2 and 3.3 . Both the PB model and the EC can be parameterised to give reasonably accurate representations of the EIS data, but the EC is more accurate. This was due to the simplicity of the EC being more suitable for the parameter estimation method. The accuracy of both model types was found to drop off at high frequencies which could be due to a Faradaic current [95], with high frequency accuracy loss also being mentioned in [184] for circuits. The slow diffusion process of the ions is directly modelled in the PB model, which suggests that this model should be more accurate at very low frequencies, below those sampled in the data. The variances of the parameter estimates obtained using the frequency domain data were significantly lower than those obtained from the time domain data. This was because the time domain identification process had noise entering the state's integrator dynamics, a similar problem as found for the observer design.

As predicted by the electrochemistry [95], the EIS response of the data changed at different steady state voltages, resulting in different model parameterisations. The identified parameters were found to vary with steady state voltage for both the EC and the PB model, suggesting that the models only describe the local dynamics. This implies that the PB model is missing some physical relationships that account for this variation, but it is noted that the addition of more physical relationships, such as temperature dependence, will result in even more complex and possibly nonlinear models.

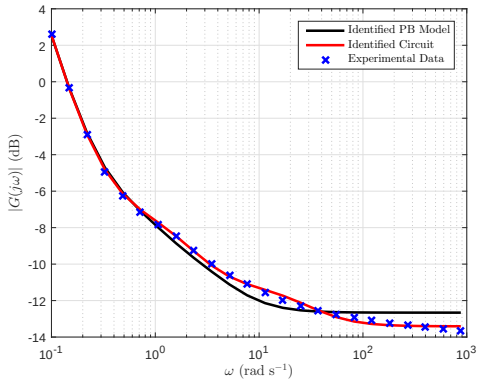


(a) Impedance function magnitude at 0.5 V_{ss}.

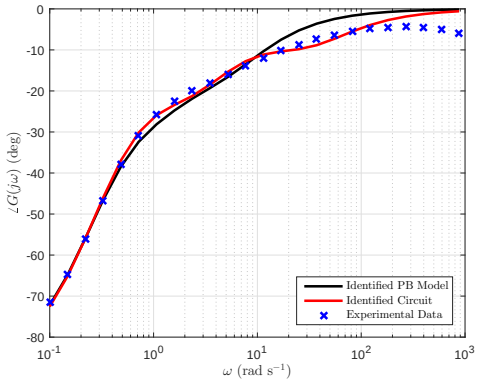


(b) Impedance function phase at 0.5 V_{ss}.

Figure 3.5: EIS data at a steady state voltage of 0.5 V.

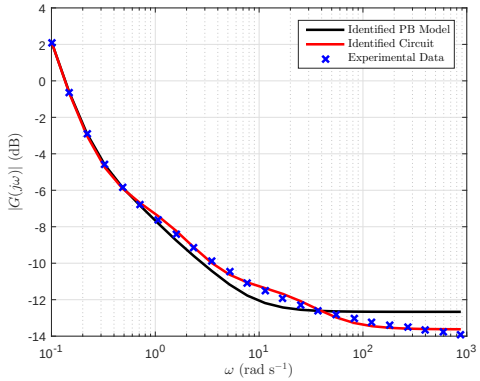


(a) Impedance function magnitude at 1.5 V_{ss}.

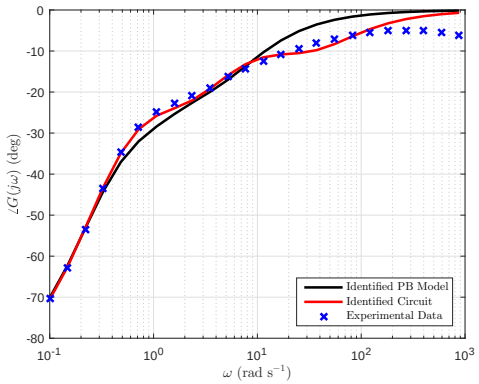


(b) Impedance function phase at 1.5 V_{ss}.

Figure 3.6: EIS data at a steady state voltage of 1.5 V.



(a) Impedance function magnitude at 2.5 V_{ss}.



(b) Impedance function phase at 2.5 V_{ss}.

Figure 3.7: EIS data at a steady state voltage of 2.5 V.

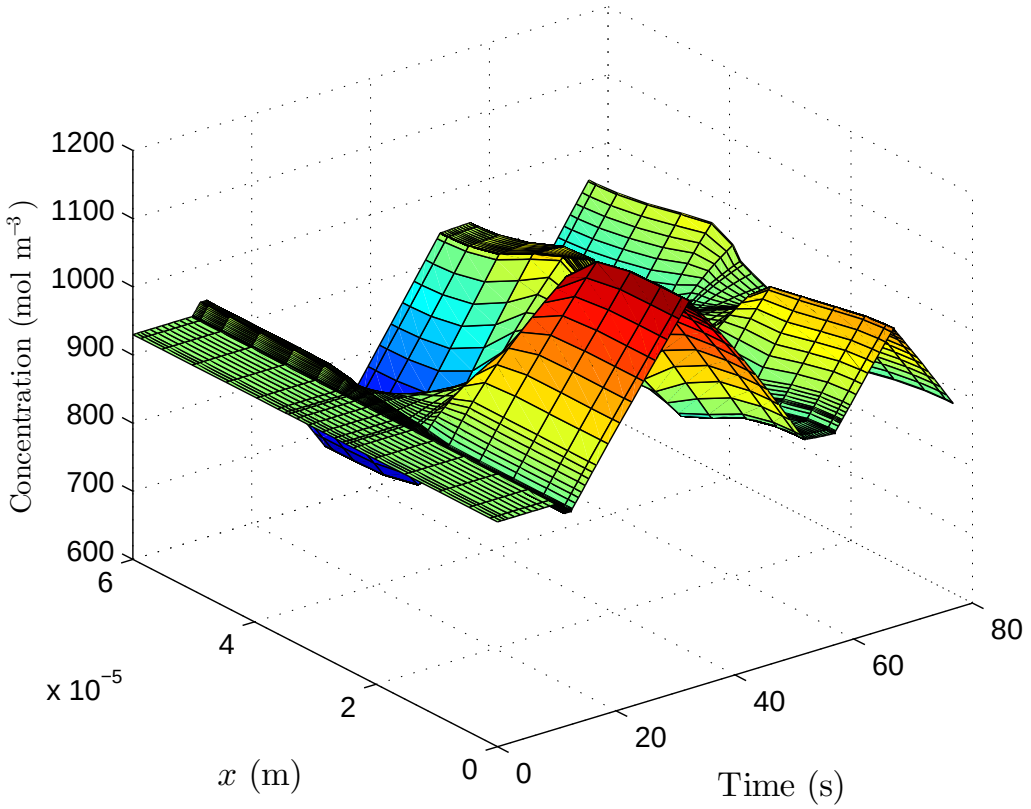


Figure 3.8: The simulated diffusion of the ionic concentration during the square wave input charging profile.

The two models differed in their complexity, with the 3 state linear EC being simpler to analyse than the nonlinear PB model which needed a 20 state discretisation of the PDEs for suitable accuracy. However, this added complexity had powerful implications since the PB model could make predictions about the internal state of the system. This is shown in Figure 3.8 where the evolution of the ionic concentration during the square wave charging profile of Figure 3.4a is shown. Utilisation of this information could lead to the battery management system reducing the effect of degradation by predicting ionic depletion and by helping designers to construct improved electrodes that account for the movement of the ions in a more meaningful way. It will also allow physically constrained (e.g. on the the concentration and potential) control of high current charging and discharging, which should allow higher performance than an EC. The optimal choice of supercapacitor model would therefore depend upon the particular application, if speed and simplicity is desired then an EC should be implemented, but if more detail about the internal state of the device is required, then a PB model would be more desirable.

3.4 Conclusions

This chapter has analysed the question of how much information can be extracted from an electrochemical model of a supercapacitor from voltmeter readings. The two topics addressed were observability and parameter estimation. Local nonlinear observability of the model was shown using Lie derivatives. When the two transference numbers of the model were equal, the model became linear and lost observability of the states related to ionic concentration. Furthermore, the model was shown to exhibit integrator dynamics and this meant that the concentration states were not detectable. The impact of the integrator dynamics with a Kalman filter was also studied and it was shown to lead to random walk state trajectories. This problem could be corrected by using a more suitable observer or by introducing a control system to make the model asymptotically stable. The estimation of the model parameters for a PB supercapacitor model was also studied. The accuracy of this model was compared to that of a 2^{nd} order circuit. The simulated output of the identified model was shown to accurately describe experimental data both in the frequency domain with electrical impedance spectroscopy (EIS) results and in the time domain with charge/discharge current profiles composed of square waves. At different steady state voltages, the supercapacitor gave different EIS readings and this resulted in

different parameterisations of the physical model and the circuit, implying they could only describe the local dynamics. The benefits and disadvantages of physical models and circuits are discussed, with the circuits being simpler while physical models are more descriptive and enable predictions to be made about the internal state of the supercapacitor, not simply its input/output response.

The following chapter proposes a method to synthesize equivalent circuits from the PB model. The procedure is structured and considers how closely the current-voltage responses of the circuits represents the PB model. In some sense, the following chapter presents a mathematical framework for obtaining the circuit parameters of a general class of circuits from a PB model parameters, giving a new physical intuition to the circuit components.

Chapter 4

Circuit Synthesis of Electrochemical Supercapacitor Models

This chapter presents a mathematical framework for the synthesis of a general class of equivalent circuits from a given PB model of a supercapacitor. The aim of the chapter is to link, in a mathematical sense, the PB models and equivalent circuits, such as to provde an improved phsyical interpretation of the terms of the circuits. Even though both EC and PB supercapacitor models describe the same physical device, there has not been much overlap between the two methods and they are often treated as two separate approaches. The efforts that have been made to link the approaches tend to give a qualitative, rather than quantitative, relationship between the two. The purpose of this chapter is to bridge this gap by linking the two approaches using a mathematical transformation, such that equivalent circuits can be synthesized from the physical PDEs. This mathematical transformation uses balanced model order reduction [48] and passive network synthesis [60]. In order for circuits to be realised, it is necessary to give a state-space realisation of the impedance function. State-space realisations of analytic impedance functions using model order reduction and Taylor series expansion for PB lithium ion models was studied by Smith *et al.* in [85, 141] and this chapter is concerned with the circuit synthesis of similar realisations. The work of this chapter could be said to generalise [122], where a specific circuit is designed to describe a PB lithium ion model, since the goal of this chapter is show that a wide *class* of PB models can be synthesised into a wide *class* of circuits. This work also generalises [119], which obtains a transmission line model from molecular simulations.

The circuits developed by this approach have a physical basis and should be more robust than those which simply fit an impedance function to data.

It is stressed that the presented method does not give analytic expressions for the various components of the synthesized circuits in terms of the physical parameters of the device. Instead, a numerical procedure is introduced that allows the circuit synthesize to be efficiently carried out. The reason no analytic expression can be obtained is because the model order reduction results in a loss of model information. It should be noted that this work does not focus on model *development*, but instead on PB model *analysis* in terms of electrical components. For this reason, the models considered in this chapter are not validated against experimental data although this validation was considered in [47, 163] amongst others.

4.1 Equivalent Circuit Models

A large number of equivalent circuits have been proposed in the literature to model supercapacitors, but to make the circuit synthesis problem tractable, the class of circuits is restricted to the *classical*, *ladder* and *dynamic* circuits that have seen widespread application and are compared in [185]. The classical circuit with added series capacitance term, shown in Fig. 4.1, is the simplest model and has dynamics

$$\begin{bmatrix} \dot{\boldsymbol{x}}_1 \\ \dot{\boldsymbol{x}}_2 \end{bmatrix} = \begin{bmatrix} 0 & 0 \\ 0 & -\frac{1}{R_1 C_1} \end{bmatrix} \begin{bmatrix} \boldsymbol{x}_1 \\ \boldsymbol{x}_2 \end{bmatrix} + \begin{bmatrix} \frac{1}{C} \\ \frac{1}{C_1} \end{bmatrix} i \tag{4.1a}$$

$$v = \boldsymbol{x}_1 + \boldsymbol{x}_2 + Ri. \tag{4.1b}$$

Incorporating additional time constants to this circuit by the inclusion of more RC branches results in the dynamic circuit, shown in Fig. 4.2, with dynamics

$$\begin{bmatrix} \dot{\boldsymbol{x}}_1 \\ \dot{\boldsymbol{x}}_2 \\ \dot{\boldsymbol{x}}_3 \\ \dot{\boldsymbol{x}}_4 \end{bmatrix} = \begin{bmatrix} 0 & 0 & 0 & 0 \\ 0 & -\frac{1}{R_1 C_1} & 0 & 0 \\ 0 & 0 & -\frac{1}{R_2 C_2} & 0 \\ 0 & 0 & 0 & -\frac{1}{R_3 C_3} \end{bmatrix} \begin{bmatrix} \boldsymbol{x}_1 \\ \boldsymbol{x}_2 \\ \boldsymbol{x}_3 \\ \boldsymbol{x}_4 \end{bmatrix} + \begin{bmatrix} \frac{1}{C} \\ \frac{1}{C_1} \\ \frac{1}{C_2} \\ \frac{1}{C_3} \end{bmatrix} i \tag{4.2a}$$

$$V = \boldsymbol{x}_1 + \boldsymbol{x}_2 + \boldsymbol{x}_3 + \boldsymbol{x}_4 + R_s i. \tag{4.2b}$$

The third circuit which will be studied is the ladder circuit of Fig. 4.3

$$\begin{bmatrix} \dot{\boldsymbol{x}}_1 \\ \dot{\boldsymbol{x}}_2 \\ \dot{\boldsymbol{x}}_3 \end{bmatrix} = \begin{bmatrix} -\frac{1}{R_2 C_1} & \frac{1}{R_2 C_1} & 0 \\ \frac{1}{R_2 C_2} & -\frac{R_2 + R_3}{R_3 R_2 C_2} & \frac{1}{R_3 C_2} \\ 0 & \frac{1}{R_3 C_3} & -\frac{1}{R_3 C_3} \end{bmatrix} \begin{bmatrix} \boldsymbol{x}_1 \\ \boldsymbol{x}_2 \\ \boldsymbol{x}_3 \end{bmatrix} + \begin{bmatrix} \frac{1}{C_1} \\ 0 \\ 0 \end{bmatrix} i \tag{4.3a}$$

$$V = \boldsymbol{x}_1 + R_1 i. \tag{4.3b}$$

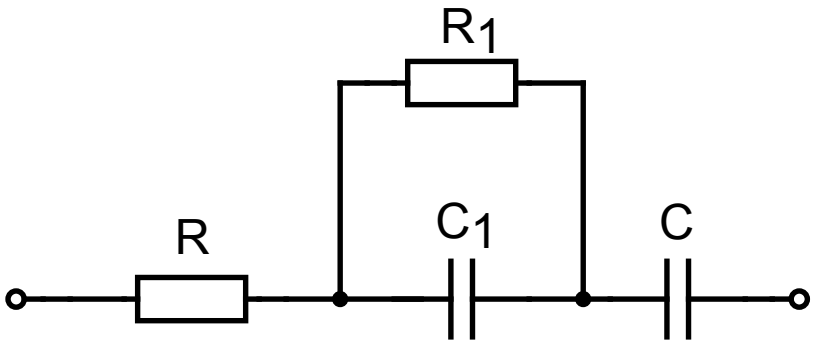


Figure 4.1: Classical circuit.

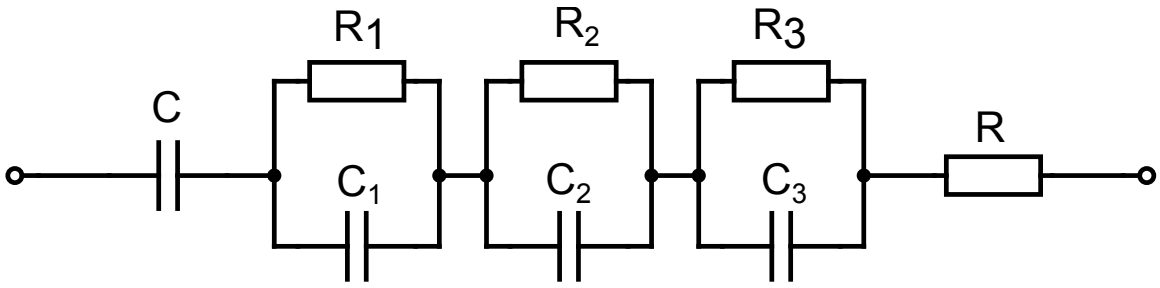


Figure 4.2: Dynamic circuit.

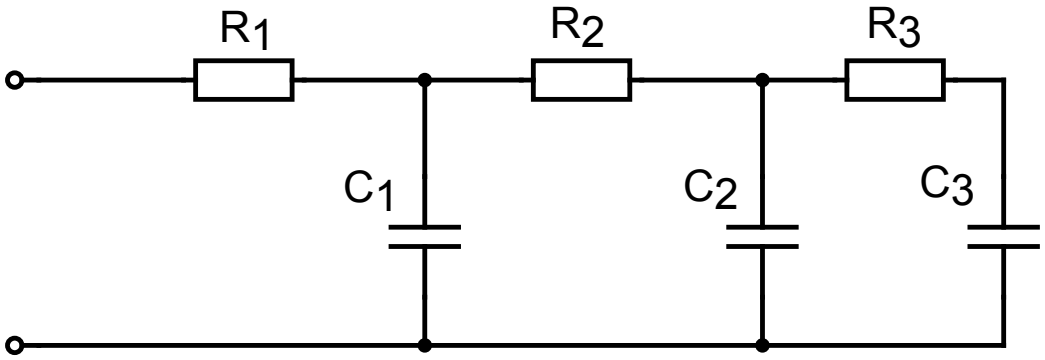


Figure 4.3: Ladder circuit.

4.2 Circuit Synthesis

In order to synthesize the three circuits of Figs. (4.1), (4.2) and (4.3), the logarithmic PB supercapacitor model is linearised around an equilibrium concentration $\boldsymbol{c_e}$ where the concentration has diffused to a flat distribution, which results in the following dynamic model

$$\dot{\boldsymbol{x}} = \left(\boldsymbol{A_m} + [\boldsymbol{B_{1,m}}\boldsymbol{c_{ed}^{-1}}\ 0]\right)\boldsymbol{x} + \boldsymbol{B_{2,m}}i \tag{4.4a}$$

$$\boldsymbol{y} = \left(\boldsymbol{C} + [\tilde{\boldsymbol{D}}_{\boldsymbol{1}}\boldsymbol{c_{ed}^{-1}}\ 0]\right)\boldsymbol{x} + \tilde{\boldsymbol{D}}_{\boldsymbol{2}}i. \tag{4.4b}$$

where $\boldsymbol{c_{ed}} = diag(\boldsymbol{c_e})$. The logarithmic nonlinearity is relatively benign when $\boldsymbol{c_e} \gg 0$ and only becomes significant when the concentration approaches zero. The near linear voltage-current dynamics of supercapacitors makes them more suitable for circuit realisation than other electrochemical devices such as lithium ion batteries, which exhibit highly nonlinear behaviour, due to the Butler-Volmer equation and OCV curve [8].

The dimensionality n of the discretised physical state-space system (4.4) is, in general, greater than the number of RC branches of typical equivalent circuit models, which most commonly have 2 or 3 branches [185]. In order for the boundary conditions to be implemented in (4.4), it was found that the electrode domain required a minimum of three discretisation elements and the separator required a minimum of two elements. This meant that the minimum dimensionality for the PB model in (4.4) was nine and, for circuit synthesis, the order of the model in (4.4) needed to be reduced. There are a number of methods for model order reduction [4] with the balanced truncation method being implemented in this work [48].

Let us first define the space of signals under consideration. A signal $\theta(t)$ is said to be in $\mathcal{L}_2[0, t_1]$ if

$$\sqrt{\int_0^{t_1} \theta(t)^T\theta(t)dt} < \infty. \tag{4.5}$$

The reason for this selection of spaces instead of the classical Hilbert space $\mathcal{L}_2$, with $\theta \in \mathcal{L}_2$ if

$$\sqrt{\int_0^{\infty} \theta(t)^T\theta(t)dt} < \infty, \tag{4.6}$$

is due to the integrators. The first stage of the circuit synthesis is to introduce the observability operator $\boldsymbol{\Psi_o} : \mathbb{R}^n \to \mathcal{L}_2[0, t_1]$ where

$$\|\boldsymbol{y}\|_2^2 = \langle \boldsymbol{x_0^* \Psi_o^*}, \boldsymbol{\Psi_o x_0} \rangle \tag{4.7}$$

such that the observability grammian $\boldsymbol{Y_o}$ can be defined by

$$\boldsymbol{Y_o} = \boldsymbol{\Psi_o^* \Psi_o} = \int_0^{t_1} e^{\boldsymbol{A^*}\tau} \boldsymbol{C^* C} e^{\boldsymbol{A}\tau} d\tau. \tag{4.8}$$

This self-adjoint operator maps the initial conditions to the outputs lying in $\mathcal{L}_2[0, t_1]$. Similarly, the controllability operator $\boldsymbol{\Psi_c} : \mathcal{L}_2[-t_2, 0] \to \mathbb{R}^n$

$$\boldsymbol{x_0} = \boldsymbol{\Psi_c u} \tag{4.9}$$

defines the controllability grammian $\boldsymbol{X_c}$

$$\boldsymbol{X_c} = \boldsymbol{\Psi_c^* \Psi_c} = \int_{-t_2}^{0} e^{\boldsymbol{A^*}\tau} \boldsymbol{B^* B} e^{\boldsymbol{A}\tau} d\tau \tag{4.10}$$

which maps all inputs $\boldsymbol{u} \in \mathcal{L}_2[-t_2, 0]$ to the initial condition $\boldsymbol{x_0} \in \mathbb{R}^n$. If a linear system is Hurwitz stable, controllable and observable, with system matrices $(\boldsymbol{A}, \boldsymbol{B}, \boldsymbol{C}, \boldsymbol{D})$, then it has a balanced realisation meaning that there exists a transformation matrix $\boldsymbol{T}$ such that the equivalent system $(\tilde{\boldsymbol{A}}, \tilde{\boldsymbol{B}}, \tilde{\boldsymbol{C}}, \tilde{\boldsymbol{D}}) = (\boldsymbol{T}\tilde{\boldsymbol{A}}\boldsymbol{T}^{-1}, \boldsymbol{T}\tilde{\boldsymbol{B}}, \tilde{\boldsymbol{C}}\boldsymbol{T}^{-1}, \boldsymbol{D})$ satisfies

$$\tilde{\boldsymbol{X}}_{\boldsymbol{c}} = \tilde{\boldsymbol{Y}}_{\boldsymbol{o}} = \boldsymbol{\Sigma} \tag{4.11}$$

with diagonal $\boldsymbol{\Sigma > 0}$. The states that are least controllable in this equivalent system are also least observable. The error between a balanced system $G(s)$ and a reduced order system $G_r(s)$ is bounded by

$$\|G(s) - G_r(s)\|_\infty \geq \boldsymbol{\sigma_{r+1}} \tag{4.12}$$

where $\boldsymbol{\sigma_1} \geq \boldsymbol{\sigma_2} \geq \cdots \geq \boldsymbol{\sigma_r} \geq \boldsymbol{\sigma_{r+1}} \geq \cdots \geq \boldsymbol{\sigma_n}$ are the singular values of the Hankel operator $\boldsymbol{\Gamma_G} = \boldsymbol{\Psi_o \Psi_c} : \mathcal{L}_2[-t_2, 0] \to \mathcal{L}_2[0, t_1]$ which maps the model input to the output [48]. In this truncation method, the (balanced) state-space matrices are partitioned by

$$\boldsymbol{A} = \begin{bmatrix} \boldsymbol{A_{11}} & \boldsymbol{A_{12}} \\ \boldsymbol{A_{21}} & \boldsymbol{A_{22}} \end{bmatrix} \quad \boldsymbol{B} = \begin{bmatrix} \boldsymbol{B_1} \\ \boldsymbol{B_2} \end{bmatrix} \quad \boldsymbol{C} = \begin{bmatrix} \boldsymbol{C_1} & \boldsymbol{C_2} \end{bmatrix} \tag{4.13}$$

and the resulting reduced order model $(\boldsymbol{A_{11}}, \boldsymbol{B_1}, \boldsymbol{C_1}, \boldsymbol{D})$ has frequency domain form

$$G_r(s) = \boldsymbol{C_1}(sI - \boldsymbol{A_{11}})^{-1}\boldsymbol{B_1} + \boldsymbol{D} \tag{4.14}$$

which is balanced with Hankel singular values $\boldsymbol{\sigma_1}, \ldots, \boldsymbol{\sigma_r}$ [48]. Reducing the order of the system in this manner means that the error of the input/output response of the reduced order model depends on the model order and can be lower bounded by $\boldsymbol{\sigma_{r+1}}$.

The requirement that the system matrix $\boldsymbol{A}$ be Hurwitz for the balanced truncation method is violated by (4.4a) since n_i of the dynamic modes of this system are integrators. This problem was overcome by removing the integrators from the system, performing the model order reduction on the remaining Hurwitz subsystem and then combining this reduced order system back with the integrators. This means that the size of the reduced order system can never be less than $n_i + 1$. However, in synthesis, the n_i integrator states combine to form a single lumped capacitor. This is shown by considering the dynamics of the integrator states $\boldsymbol{x_i} \in \mathbb{R}^{n_i}$

$$\dot{\boldsymbol{x}}_{\boldsymbol{i}} = \boldsymbol{B_{int}} i \tag{4.15a}$$

$$\boldsymbol{y_i} = \boldsymbol{C_{int}} \boldsymbol{x_i} \tag{4.15b}$$

where $\boldsymbol{B_{int}} \in \mathbb{R}^{n_i \times 1}, \boldsymbol{C_{int}} \in \mathbb{R}^{1 \times n_i}$ such that the integrator capacitance $\mathfrak{C}$ is given by

$$\mathfrak{C} = \left(\boldsymbol{C_{int}} \boldsymbol{B_{int}}\right)^{-1}. \tag{4.16}$$

In addition to the Hurwitz condition, the system is also required to be both observable and controllable for a balanced realisation. These properties were studied in chapter 3, where it was found that the nonlinear model was fully controllable but lost observability when the two transference numbers, t_+ and t_- in (2.2), were equal. To avoid this problem for this model, t_+ and t_- were chosen as 0.75 and 0.25.

The transfer function $G(s)$ of the reduced order system (4.4) is known as the impedance function, giving the s-domain gain from current to voltage. When (4.4) was reduced to a three state system using the parameters from Table 2.4 the impedance function was

$$G(s) = \frac{V(s)}{I(s)} = \frac{(s + 6.56)(s + 1.59)(s + 0.29)}{s(s + 5.62)(s + 1.4)}. \tag{4.17}$$

Equivalent circuit realisations of the impedance function (4.17) can now be obtained using passive network synthesis. Passive network synthesis was studied extensively in the electrical engineering community in the 1930s [11, 17] with the goal being to understand and simulate complex dynamical systems using electrical components [22]. Interest in this field died down in the 1960s even though many problems still remained open. Network synthesis has recently witnessed a revival due to the application

of modern mathematical tools to the classical methods [24] and its application to mechanical systems through the discovery of the inerter [142].

The key requirement for circuit synthesis of an impedance function is that $G(s)$ must be a positive real function. Positive real functions satisfy:

1. $G(s)$ is real for real s.
2. Real $G(s) \geq 0$ for real $s \geq 0$.

Positive realness is equivalent to showing that the system is passive, i.e. non energy generating [171]. Passivity of the supercapacitor model has been shown for both the nonlinear discretised system and for the underlying nonlinear partial differential algebraic equations [45]. This implies that the PDE model could be realised by a RC circuit of infinite dimension, but this is beyond the scope of this chapter.

The positive-real conditions are satisfied by (4.17). Realising a transfer function in terms of a circuit is equivalent to realising it in terms of a state-space system that has a particular structure. State transformation operations imply that transfer functions have a non-unique state-space representation and this explains the vast array of circuit models that can be found in the literature. By restricting the class of circuits to the classical, dynamic and ladder circuits of [185], circuit realisations can be obtained, although it is pointed out that there exists a much wider class of circuits that could be realised by the proposed approach, but are not considered here.

The methodology of network synthesis is to expand the positive real impedance function $G(s)$ around some point, such as a pole at $s = 0$. The various components of this expansion can then be realised by passive electrical components such as resistors, capacitors and inductors [166]. The realisation of the impedance function (4.17) in terms of the dynamic circuit (4.2) is known as the Foster form of the first kind [166] and is obtained by continuously removing a pole of $G(s)$ at $s = 0$. This is similar to performing a partial fraction expansion

$$G(s) = \frac{1}{k_0} + \frac{k_1}{s + \sigma_1} + \cdots + \frac{k_i}{s + \sigma_i} + \cdots + k_\infty. \tag{4.18}$$

The resistances and capacitances of the circuit can then be obtained by the following rules

$$C = \frac{1}{k_0} \quad C_i = \frac{1}{k_i} \quad R_i = \frac{k_i}{\sigma_i} \quad R = k_\infty. \tag{4.19}$$

By reducing the order of the reduced system to one, the classical circuit of (4.1) is realised. An alternative method for obtaining the RC components for the dynamic circuit would be to take the eigen-decomposition of the reduced order physical system (4.4) and then match up the system matrix coefficients to that of (4.2), since both would have diagonal structures.

The ladder circuit (4.3) can be realised from the impedance function by the continuous removal of poles at $s = \infty$. This representation is known as the Cauer form of the first kind [166] and can be obtained by taking a continuous fraction expansion of the impedance function

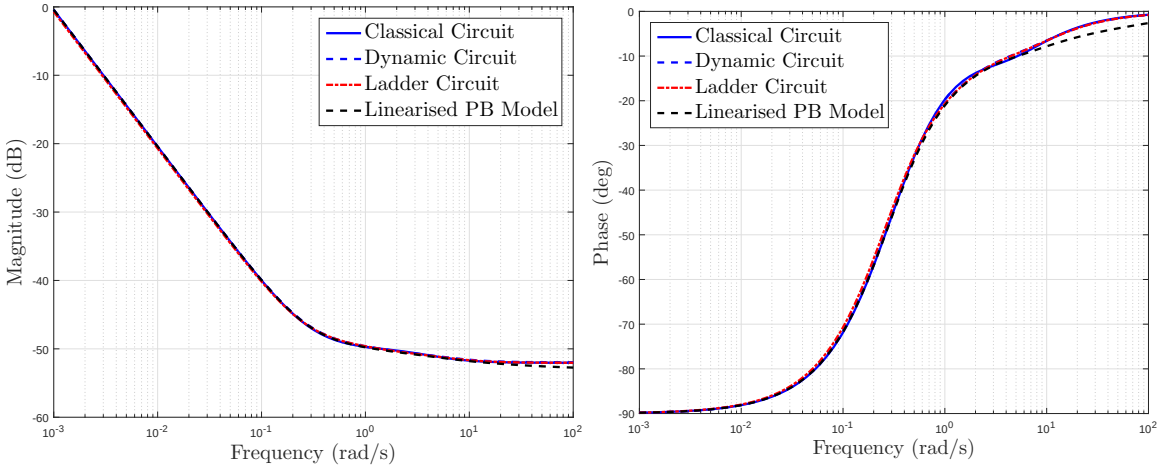
$$G(s) = \alpha_1 + \cfrac{1}{\alpha_2 s + \cfrac{1}{\alpha_3 + \cfrac{1}{\alpha_4 s + \cfrac{1}{\alpha_5 + \ddots \\ \alpha_{r-1} + \frac{1}{\alpha_r s}}}}}. \tag{4.20}$$

The resistors and capacitors of the circuit can then be obtained with

$$R_i = \alpha_{2i-1} \quad C_i = \alpha_{2i} \quad \text{for } i = 1, \ldots, r/2. \tag{4.21}$$

The Cauer form of the second kind [166] of (4.17) has the resistors and capacitors swapped around in Fig. 4.3. The values of the resistors and capacitors for the three circuits obtained by the synthesis procedure are given in Table 4.1 for the SAFT America supercapacitor described by the parameters from Table 2.4. It is noted that the proposed synthesis method allows a wide class of circuits to be synthesized, with this class not being restricted to the three circuits described. The Bode plots for the three circuits match the full order linearised PB model as shown in Fig 4.4. This is to be expected since the circuits are simply reduced order realisations of the physical impedance function.

Using this approach, quantitative estimates for the the errors introduced at each step of the synthesis process (discretisation, linearisation and model order reduction) can be obtained when the full order PB model is treated as describing the true dynamics of the system. This contrasts with the rather qualitative errors discussed with fitted EC circuits. The singular values of the Hankel norm describe the error bound for the reduced order system and are shown for a 20 state discretisation of (4.4) in Fig. 4.5. The first three singular values in this plot have been removed since they relate to the



(a) Magnitude of $G(s)$.

(b) Phase of $G(s)$.

Figure 4.4: Bode plot of the three synthesized circuits and full order linearised physical model.

Component	Classical	Dynamic	Ladder
R_1	$6.2 \times 10^{-4}\ \Omega$	$3.75 \times 10^{-4}\ \Omega$	$2.5 \times 10^{-3}\ \Omega$
R_2		$3.15 \times 10^{-4}\ \Omega$	$9.8 \times 10^{-4}\ \Omega$
R_3		$2.52 \times 10^{-4}\ \Omega$	$4 \times 10^{-3}\ \Omega$
R	$2.52 \times 10^{-3}\ \Omega$	$2.52 \times 10^{-3}\ \Omega$	
C_1	$431\ F$	$475\ F$	$285.9\ F$
C_2		$2.26 \times 10^{3}\ F$	$549.6\ F$
C_3		$1.3 \times 10^{6}\ F$	$249.6 \times 10^{-6}\ F$
C	$1.05 \times 10^{3}\ F$	$1.05 \times 10^{3}\ F$	

Table 4.1: Resistor and capacitor values for the synthesized classical, dynamic and ladder circuits.

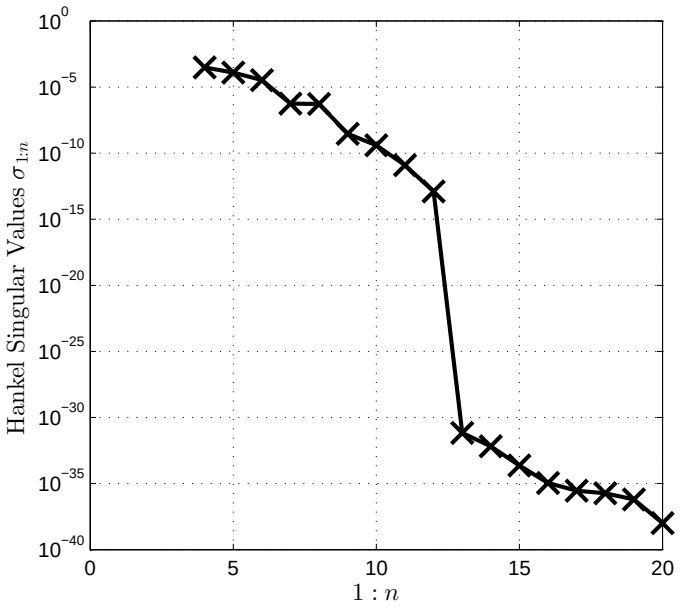


Figure 4.5: Singular values of the Hankel operator Γ_G.

integrator states. For this discretisation, 12 states were related to the concentration c with the remaining eight being related to the potential difference $\phi_1 - \phi_2$. This shows that the concentration states have a greater impact on the input/output dynamics of (4.4) than the potential states. This is because the concentration states evolve by a diffusion process, which is much slower than the rapidly decaying, fast dynamics associated with the potentials. This suggests that there is no advantage gained in increasing the number of RC branches beyond the number of concentration states $n_c - n_i$ when this synthesis process is used.

Recently, circuits have been developed for specific charging conditions such as charge relaxation [155]. With the proposed PB approach, there should be a much broader range of dynamics that are considered in forming the impedance functions. This should result in more generalised synthesized circuits that are designed for a broader range of charging conditions. The ability to realise the physical dynamics in terms of both the ladder and the dynamic circuits contrasts with the view in the literature that gives each of these circuits a distinct physical interpretation; the ladder circuit is said to describe ion movement within a pore while the dynamic circuit is said to model double layer effects [185]. The analysis of this chapter suggests that the physical interpretation of these circuits is not as well defined as that, with each of the modelled phenomenon contributing to the components of each branch. The admittance function

$F(s)$, which is the inverse of the impedance function $G(s)$, can also be synthesized in terms of resistors and inductors [166]. The PB model is transformed into a circuit and it is believed that this transformation cannot occur in the opposite direction, i.e. going from the circuit equations to the model PDEs. However, it is pointed out that developing PB models by considering the physics would be a better approach than reverse synthesizing circuits.

The proposed circuit synthesis method is flexible since it can be applied to general PB models describing additional physical phenomena. For example, including the linear dependence of electrolyte conductivity with concentration

$$\kappa = \kappa_0 \boldsymbol{c}, \tag{4.22}$$

gives the linearised impedance function

$$G(s) = \frac{V(s)}{I(s)} = \tag{4.23}$$

$$\frac{(s+4.76)(s+0.3)(s+2.95\times10^{-5})(s+3.27\times10^{-5})}{s(s+3.74)(s+2.9\times10^{-5})(s+3.27\times10^{-6})}. \tag{4.24}$$

As well as electrolyte conductivity, the capacitance aC has also been shown to vary during charging. Several models have been proposed to account for this relationship, with the most popular being the Guoy-Chapman-Stern model [95]. In the region of low voltage, this relationship can be approximated by a linear fit

$$aC = \alpha + \beta(\boldsymbol{\phi_1} - \boldsymbol{\phi_2}). \tag{4.25}$$

This relationship changes the state-space system to

$$\begin{bmatrix} \epsilon & \frac{\alpha+\beta(\boldsymbol{\phi_{1,d}}-\boldsymbol{\phi_{2,d}})}{F}\left(t_-\frac{dq_+}{dq}+t_+\frac{dq_-}{dq}\right) & 0 \\ 0 & \alpha+\beta(\phi_1-\phi_2) & 0 \\ 0 & 0 & 0 \end{bmatrix} \begin{bmatrix} \dot{c} \\ \dot{\boldsymbol{\phi}}_{\boldsymbol{1,d}} - \dot{\boldsymbol{\phi}}_{\boldsymbol{2,d}} \\ \dot{\phi}_2 \end{bmatrix} =$$

$$\begin{bmatrix} D\frac{\partial^2}{\partial x^2} & 0 & 0 \\ 0 & \sigma\frac{\partial^2}{\partial x^2} & \sigma\frac{\partial^2}{\partial x^2} \\ 0 & \sigma\frac{\partial}{\partial x} & \kappa\frac{\partial}{\partial x}+\sigma\frac{\partial}{\partial x} \end{bmatrix} \begin{bmatrix} c \\ \phi_1-\phi_2 \\ \phi_2 \end{bmatrix} + \begin{bmatrix} 0 \\ 0 \\ \kappa\left(\frac{RT(t_+-t_-)}{F}\right)\frac{\partial}{\partial x} \end{bmatrix} \ln(c) + \begin{bmatrix} 0 \\ 0 \\ 1 \end{bmatrix} i. \tag{4.26}$$

where $\boldsymbol{\phi_{1,d}} = diag(\boldsymbol{\phi_1})$ and $\boldsymbol{\phi_{2,d}} = diag(\boldsymbol{\phi_2})$. The impedance for this system with $\alpha = 42\times10^6$ and $\beta = 10\times10^6$ is

$$G(s) = \frac{V(s)}{I(s)} = \frac{(s+6.04)(s+1.46)(s+0.27)(s+0.0031)}{s(s+5.17)(s+1.29)(s+0.003)}. \tag{4.27}$$

Both impedance functions (4.23) and (4.27) are positive real functions, so can be synthesized by passive circuit elements. The method can also be easily updated to generate local circuits applicable to any operating region besides the equilibrium concentration by changing the linearisation point of the model.

Circuits approximate the local dynamics of a nonlinear supercapacitor model in a given operating region. During a charging profile, the state of the supercapacitor may leave this region, necessitating the need for a new circuit to be generated, typically using parameter estimation methods [187]. This parameter estimation problem for the circuit components can be re-cast as a synthesis problem of the PB model. Fig. 4.6 shows the percentage deviation from their original values of the three time constants of the dynamic circuit (4.2) that were synthesized from the logarithmic PB supercapacitor model using an input current of $i = 10 + 10\sin(0.1t)$ A m^{-2}. Unlike Fig. 4.4, Fig. 4.6 does not describe the accuracy of the circuit realisation, but instead analyses how the components of the dynamic circuit realisation would vary during a charge to account for the nonlinearity of the PB model. The three RC branches shown in Fig. 4.6 relate to different time constants with $C_1R_1 < C_2R_2 < C_3R_3$. It was found that only the time constant C_3R_3, which is related to long term dynamics, changed significantly during this charging profile. This is because the localised component of the PB model dynamics that changes during the charging profile is due to the $\ln(\boldsymbol{c})$ nonlinearity, which is solely a function of the concentration. Since the concentration exhibits slow diffusion dynamics via (2.2), only the long term time constants are local. If the electrochemical equations were linear, then the circuit component values would be fixed. However, the circuit component values would still be dependent upon the parameters of the PB model, such as temperature and porosity factor, as these parameters affect the impedance function. The proposed method can easily accommodate this dependency. Since no analytic expression was obtained for the circuit components in terms of the physical parameters, the synthesis process was carried out at each time step of the simulation. Although, since the numerical procedure for the synthesis was fairly efficient, this process was not computationally exhaustive. The trajectory based synthesis method proposed here should be more accurate than circuits synthesized around an equilibrium point.

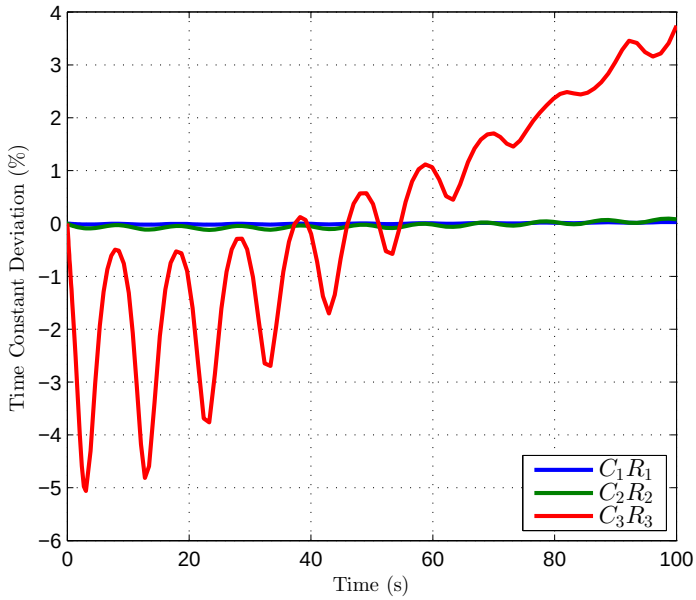


Figure 4.6: Variation of the time constants of the dynamic circuit during a charge with sinusoidal current.

4.3 Conclusion

In this chapter, a method for synthesising electrical circuits from physical supercapacitor models has been proposed. This method uses model discretisation, linearisation, balanced model order reduction and passive network synthesis. The method is flexible since a wide class of circuits can be realised from a wide class of physical models. The circuits were validated by comparing their frequency responses to that of a linearised physical model. The aim of this chapter is to give a greater understanding to the physical interpretation of equivalent circuit models and also to enable the synthesis of more general circuits whose impedance function would be generated by considering the device physics, not by experimental fitting.

The following chapter uses the PB supercapacitor model for the purpose of design. Using a local absolute stability theory framework, a method is proposed that links the parameters of the electrochemical supercapacitor model, such as the electrode conductivity and the diffusion coefficient, to energy storage properties. These properties include the resistance, capacitance, dissipated energies and maximum voltages. The main idea is to use advanced techniques from control theory to help make cheaper, better supercapacitors that can be tailored for particular applications.

Chapter 5

Design Tools for Electrochemical Supercapacitors Using Local Absolute Stability Theory

This chapters uses the logarithmic electrochemical supercapacitor model developed in chapter 2 for the purpose of design and the proposed approach uses Lyapunov analysis to obtain bounds on the energy dissipation properties of the supercapacitor model. The variation of these bounds as functions of the model physical parameters is investigated and compared to the experimental results given in [163] and [47]. The methods introduced in this chapter are valuable tools for designers, as they directly relate the impact of changes in the physical parameters, such as porosity and diffusion coefficient, to the electrical properties that describe the performance of the device. These properties determine the energy, power and safety of the supercapacitor, which are important to users. Introducing a systematic method for computing these properties, based upon the ideas of systems theory, provides a new methodical approach for supercapacitor design.

Improvements in supercapacitor performance have generally been achieved through advancements in electrochemistry, for example through the design of more advanced electrodes [178]. This approach requires exhaustive electrochemical testing to iterate towards a design with potentially long rest periods between tests to redesign the device. Recently, systems theory, based on electrochemical models, has been applied to energy storage devices to improve this design process by making predictions about the system properties so that an improved design can be achieved with fewer experiments [125]. Compared to an optimisation approach based upon experimental testing, this 'model based' approach is faster and considers more potential designs.

In this chapter, methods from systems analysis and control theory [14, 89] are applied to a PB supercapacitor model, whose PDEs are discretised in space using the spectral collocation method [46]. Since the goal of this chapter is to relate the supercapacitor's physical parameters to its performance, only PB models are considered. Bounds for the following system properties of the model are given:

- Model stability, characterising the limits of the model for safe use.
- Estimates of reachable sets for the states describing the ionic concentration and electropotential. These reachable sets are also related to safety as they characterise the maximum deviation in the states due to a unit impulse in energy via the current.
- Dissipated and stored energies for a charging profile to give more accurate predictions for the state-of-charge of the supercapacitor, which is one of the key design metrics for an electrical energy storage device.
- Gains from current to voltage that describe the capacitance and the resistance.
- Safe maximum voltages such that electrolyte degradation is avoided. This property impacts the maximum stored energy of a supercapacitor which is proportional to the maximum voltage squared.

The bounds are computed using absolute stability theory and the solution of optimisation problems involving linear matrix inequalities (LMIs) and semi-definite programming. Absolute stability theory is a classical control problem, which considers the stability properties of nonlinear systems that can be expressed as the feedback interconnection of a linear system with a nonlinearity that is bounded around the origin by a cone [89]. A key result of the theory is that the results are applicable to all nonlinearities satisfying the cone condition. As such, it allows a wide class of nonlinear systems to be analysed using the well understood concepts of feedback developed for linear systems. Numerous solutions have been proposed for the absolute stability problem, with these solutions in general being posed either in the frequency domain or in the time domain. Frequency domain results include some of the original results of Kalman, Popov and Yakubovich, who showed that if a "multiplier" could be found that shifted the phase of the transfer function of the linear system in a suitable manner, then it implied the existence of a particular Lyapunov function and hence stability could be verified [126]. This result sparked considerable attention with numerous different forms of multipliers then being proposed [182]. The frequency domain integral quadratic constraint framework was proposed in [100] for

studying robust problems such as this, which has seen extensive use due to its general nature. Time domain solutions to the absolute stability problem generally involve the search for suitable Lyapunov functions and for particular classes of such functions, this search can be solved numerically using fast semi-definite programming solvers [14].

Generally speaking, the solutions to absolute stability that are posed in the frequency domain tend to be less conservative than those posed in the time domain. However, the time domain conditions have two main advantages. The first is that they permit a local analysis as they exploit the geometric conditions of the positively invariant level sets of the Lyapunov functions. Secondly, they can easily be extended to the case of the feedback being multi-input/multi-output (MIMO). Even though MIMO frequency domain stability methods have been developed, it is not as intuitive to work with these methods compared to Lyapunov functions. In this work, a local analysis of a MIMO nonlinear feedback system that describes the electrochemistry of a supercapacitor is considered, so the time domain approach is used. Local absolute stability theory was developed in [34, 69] for an application to saturating systems where it was shown that tighter results could be obtained than those obtained for a global analysis. A recent extension of these results was developed in [160] for the case of the nonlinearity being slope-restricted.

5.1 State Transformed Electrochemical Supercapacitor Model

In order for the electrochemical supercapacitor model with logarithmic nonlinearity to be amenable to absolute stability theory [89], the nonlinearity has to be translated into a sector bounded form. To do this, a co-ordinate transformation on the concentration is introduced with $c = c_0 + \tilde{c}$, where c_0 is the flat equilibrium concentration and $\tilde{c}$ is the deviation from this equilibrium. This transformation changes (2.2) and (2.6) into

$$\epsilon\frac{\partial\tilde{c}}{\partial t} = D\frac{\partial^2\tilde{c}}{\partial x^2} - \frac{aC}{F}\left(t_-\frac{dq_+}{dq} + t_+\frac{dq_-}{dq}\right)\frac{\partial(\phi_1-\phi_2)}{\partial t}, \tag{5.1a}$$

$$\frac{\kappa\ RT}{F}(t_+ - t_-)\frac{\partial}{\partial x}\ln\left(1+\frac{\tilde{c}}{c_0}\right) + \sigma\frac{\partial(\phi_1-\phi_2)}{\partial x} + \left(\kappa\frac{\partial}{\partial x} + \sigma\frac{\partial}{\partial x}\right)\phi_2 + i = 0 \tag{5.1b}$$

since $\ln(c) = \ln(1 + \tilde{c}/c_0) + \ln(c_0)$ and

$$\frac{\partial c_0}{\partial t} = \frac{\partial c_0}{\partial x} = \frac{\partial^2 c_0}{\partial x^2} = \frac{\partial \ln(c_0)}{\partial x} = 0. \tag{5.2}$$

The PDE state-space form of the electrode dynamics in this new co-ordinate frame is given in (5.3a) with that of the separator is given in (5.3b). This transformation of the concentration makes the origin the equilibrium point of the system, hence making the model amenable to a Lyapunov based analysis. The discretised version of the state transformed PDEs for the electrode and separator domains are respectively given in (5.4a) and (5.4b).

$$\begin{bmatrix} \epsilon & \frac{aC}{F}(t_- \frac{dq_+}{dq} + t_+ \frac{dq_-}{dq}) & 0 \\ 0 & aC & 0 \\ 0 & 0 & 0 \end{bmatrix} \begin{bmatrix} \dot{\tilde{c}} \\ \dot{\phi}_1 - \dot{\phi}_2 \\ \dot{\phi}_2 \end{bmatrix} = \begin{bmatrix} D\frac{\partial^2}{\partial x^2} & 0 & 0 \\ 0 & \sigma\frac{\partial^2}{\partial x^2} & \sigma\frac{\partial^2}{\partial x^2} \\ 0 & \sigma\frac{\partial}{\partial x} & \kappa\frac{\partial}{\partial x} + \sigma\frac{\partial}{\partial x} \end{bmatrix} \begin{bmatrix} \tilde{c} \\ \phi_1 - \phi_2 \\ \phi_2 \end{bmatrix} + \begin{bmatrix} 0 & 0 \\ 0 & 0 \\ \kappa\left(\frac{t_+ - t_-}{f}\right)\frac{\partial}{\partial x} & 1 \end{bmatrix} \begin{bmatrix} \ln\left(1 + \frac{\tilde{c}}{c_0}\right) \\ i \end{bmatrix} \tag{5.3a}$$

$$\begin{bmatrix} \epsilon & 0 \\ 0 & 0 \end{bmatrix} \begin{bmatrix} \dot{\tilde{c}} \\ \dot{\phi}_2 \end{bmatrix} = \begin{bmatrix} D\frac{\partial^2}{\partial x^2} & 0 \\ 0 & \kappa\frac{\partial}{\partial x} \end{bmatrix} \begin{bmatrix} \tilde{c} \\ \phi_2 \end{bmatrix} + \begin{bmatrix} 0 & 0 \\ \kappa\left(\frac{t_+ - t_-}{f}\right)\frac{\partial}{\partial x} & 1 \end{bmatrix} \begin{bmatrix} \ln\left(1 + \frac{\tilde{c}}{c_0}\right) \\ i \end{bmatrix} \tag{5.3b}$$

$$\begin{bmatrix} \epsilon & \frac{aC}{F}(t_- \frac{dq_+}{dq} + t_+ \frac{dq_-}{dq}) & 0 \\ 0 & aC & 0 \\ 0 & 0 & 0 \end{bmatrix} \begin{bmatrix} \dot{\tilde{\boldsymbol{c}}} \\ \dot{\boldsymbol{\phi}}_1 - \dot{\boldsymbol{\phi}}_2 \\ \dot{\boldsymbol{\phi}}_2 \end{bmatrix} = \begin{bmatrix} D\hat{\mathbf{D}}_c^2 & 0 & 0 \\ 0 & \sigma\hat{\mathbf{D}}_{\phi_1}^2 & \sigma\hat{\mathbf{D}}_{\phi_1}^2 \\ 0 & \sigma\hat{\mathbf{D}}_{\phi_1} & \kappa\hat{\mathbf{D}}_{\phi_2} + \sigma\hat{\mathbf{D}}_{\phi_1} \end{bmatrix} \begin{bmatrix} \tilde{\boldsymbol{c}} \\ \boldsymbol{\phi_1} - \phi_{\mathbf{2}} \\ \boldsymbol{\phi_2} \end{bmatrix} + \begin{bmatrix} 0 & 0 \\ 0 & 0 \\ \kappa\left(\frac{t_+ - t_-}{f}\right)\hat{\mathbf{D}}_{\ln c} & 1 \end{bmatrix} \begin{bmatrix} \ln\left(1 + \frac{\tilde{\boldsymbol{c}}}{\mathbf{c_0}}\right) \\ i \end{bmatrix} \tag{5.4a}$$

$$\begin{bmatrix} \epsilon & 0 \\ 0 & 0 \end{bmatrix} \begin{bmatrix} \dot{\tilde{\boldsymbol{c}}} \\ \dot{\boldsymbol{\phi}}_{\mathbf{2}} \end{bmatrix} = \begin{bmatrix} D\hat{\mathbf{D}}_c^2 & 0 \\ 0 & \kappa\hat{\mathbf{D}}_{\phi_2}^2 \end{bmatrix} \begin{bmatrix} \tilde{\boldsymbol{c}} \\ \boldsymbol{\phi_2} \end{bmatrix} + \begin{bmatrix} 0 & 0 \\ \kappa\left(\frac{t_+ - t_-}{f}\right)\hat{\mathbf{D}}_{\ln c} & 1 \end{bmatrix} \begin{bmatrix} \ln\left(1 + \frac{\tilde{\boldsymbol{c}}}{\mathbf{c_0}}\right) \\ i \end{bmatrix} \tag{5.4b}$$

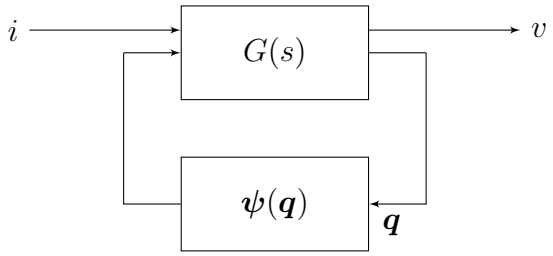


Figure 5.1: The supercapacitor model expressed in a feedback loop with the logarithmic nonlinearity being treated as an input.

Equation (5.4b) can be embedded into the structure of (5.4a) by expanding the state dimension so only the form from (5.4a) will be considered in the following analysis. When the boundary conditions on ϕ_1 are considered [163], the discretised model output in the new co-ordinate frame becomes

$$v = \begin{bmatrix} \mathbf{0} & \tilde{\boldsymbol{C}} \end{bmatrix} \begin{bmatrix} \tilde{\boldsymbol{c}} \\ \boldsymbol{\phi_1} - \boldsymbol{\phi_2} \end{bmatrix} + \tilde{\boldsymbol{C}}\boldsymbol{\phi_2} + \tilde{\boldsymbol{D}}_{\boldsymbol{i}} i. \tag{5.5}$$

An expression for the algebraic variable $\boldsymbol{\phi_2}$ in this new state co-ordinate frame is obtained by solving the algebraic equation of (2.33)

$$\boldsymbol{\phi_2} = -\left(\kappa \hat{\mathbf{D}}_{\phi_2} + \sigma \hat{\mathbf{D}}_{\phi_1}\right)^{-1} \left(\kappa \left(\frac{t_+ - t_-}{f}\right) \hat{\mathbf{D}}_{\ln c} \ln\left(1 + \frac{\tilde{\boldsymbol{c}}}{\boldsymbol{c_0}}\right) + \sigma \hat{\mathbf{D}}_{\phi_1} (\boldsymbol{\phi_1} - \boldsymbol{\phi_2}) + i\right). \tag{5.6}$$

As before, a solution of (5.6) can only be obtained if a reference potential is set, in this case being $\boldsymbol{\phi_1}|_{\boldsymbol{x}=0} = 0$. This expression for $\boldsymbol{\phi_2}$ allows (2.33) to be expressed as an ordinary differential equation (ODE) with structure

$$\begin{bmatrix} \boldsymbol{M_{11}} & \boldsymbol{M_{12}} \\ \mathbf{0} & \boldsymbol{M_{22}} \end{bmatrix} \begin{bmatrix} \dot{\tilde{\boldsymbol{c}}} \\ \dot{\boldsymbol{\phi}}_1 - \dot{\boldsymbol{\phi}}_2 \end{bmatrix} = \begin{bmatrix} \hat{\boldsymbol{A}}_{\boldsymbol{11}} & \mathbf{0} \\ \mathbf{0} & \hat{\boldsymbol{A}}_{\boldsymbol{22}} \end{bmatrix} \begin{bmatrix} \tilde{\boldsymbol{c}} \\ \boldsymbol{\phi_1} - \boldsymbol{\phi_2} \end{bmatrix} + \begin{bmatrix} 0 \\ \hat{\boldsymbol{B}}_{\boldsymbol{1}} \end{bmatrix} \ln\left(1 + \frac{\tilde{\boldsymbol{c}}}{\boldsymbol{c_0}}\right) + \begin{bmatrix} \mathbf{0} \\ \hat{\boldsymbol{B}}_{\boldsymbol{2}} \end{bmatrix} i \tag{5.7a}$$

$$v = \begin{bmatrix} \mathbf{0} & \hat{\boldsymbol{C}} \end{bmatrix} \begin{bmatrix} \tilde{\boldsymbol{c}} \\ \boldsymbol{\phi_1} - \boldsymbol{\phi_2} \end{bmatrix} + \hat{\mathbf{D}} \ln\left(1 + \frac{\tilde{\boldsymbol{c}}}{\boldsymbol{c_0}}\right) + \hat{D}_i i. \tag{5.7b}$$

The dynamical equation (5.7a) can be expressed in the form

$$\boldsymbol{M}\dot{\boldsymbol{x}} = \hat{\boldsymbol{A}}\,\boldsymbol{x} + \hat{\boldsymbol{B}} \ln\left(1 + \frac{\tilde{\boldsymbol{c}}}{\boldsymbol{c_0}}\right) + \hat{\boldsymbol{B}}_{\boldsymbol{i}} i \tag{5.8a}$$

with state vector $\boldsymbol{x} := [\tilde{\boldsymbol{c}}^T \quad \boldsymbol{\phi_1}^T - \boldsymbol{\phi_2}^T]^T \in \mathbb{R}^n$ and inverting the "mass" matrix $\boldsymbol{M}$ leads to

$$\dot{\boldsymbol{x}} = \hat{\boldsymbol{A}}_{\boldsymbol{M}}\, \boldsymbol{x} + \hat{\boldsymbol{B}}_{\boldsymbol{M}} \ln\left(1 + \frac{\tilde{\boldsymbol{c}}}{\boldsymbol{c_0}}\right) + \hat{\boldsymbol{B}}_{\boldsymbol{i,M}} i \tag{5.9a}$$

$$v = \boldsymbol{C}\boldsymbol{x} + \hat{\boldsymbol{D}} \ln\left(1 + \frac{\tilde{\boldsymbol{c}}}{\boldsymbol{c_0}}\right) + \hat{\boldsymbol{D}}_{\boldsymbol{i}} i. \tag{5.9b}$$

Matrices $\boldsymbol{M_{11}}$, $\boldsymbol{M_{22}}$ are diagonal with non-zero entries and hence invertible. This system has the feedback structure of Figure 5.1 where $\boldsymbol{q} = \tilde{\boldsymbol{c}} = \boldsymbol{C_c x}$, $\boldsymbol{\psi(q)} = \ln(1+\tilde{\boldsymbol{c}}/\boldsymbol{c_0})$ and $G(s)$ is a MIMO transfer function described by the linear fractional transform

$$G(s) = \left[\begin{array}{c|cc} \hat{\boldsymbol{A}}_{\boldsymbol{M}} & \hat{\boldsymbol{B}}_{\boldsymbol{M}} & \hat{\boldsymbol{B}}_{\boldsymbol{i,M}} \\ \hline \boldsymbol{C_c} & \boldsymbol{0} & \boldsymbol{0} \\ \boldsymbol{C} & \hat{\boldsymbol{D}} & \hat{\boldsymbol{D}}_{\boldsymbol{i}} \end{array}\right]. \tag{5.10}$$

Due to the supercapacitor being an energy *storage* device that absorbs the energy supplied by the current, its transfer function has n_i poles at $s = 0$, corresponding to n_i integrator states. For stability analysis, the presence of these integrators states is problematic as they are unbounded and do not exist in the $\mathcal{L}_2$ Hilbert space. The absolute stability of such critically stable systems was considered in [83] where the unbounded integrator dynamics are handled by encapsulating the integrator via a transformation of the system feedback loop. This encapsulation operation is not required for the analysis of both supercapacitor models as the concentration $\boldsymbol{q}$ is independent of the integral of the current for both supercapacitors analysed in this chapter, which are described by the parameters in Table 2.4.

To show this independence, the eigen-decomposition of the system (5.9) was taken by defining $\tilde{\boldsymbol{x}} = \boldsymbol{Q}^{-1}\boldsymbol{x}$, where $\boldsymbol{Q}$ is the eigenvector matrix of $\hat{\boldsymbol{A}}_{\boldsymbol{M}}$ such that the state space can be separated into $\tilde{\boldsymbol{x}} = [\boldsymbol{x_d}^T, \boldsymbol{x_i}^T]^T$ with dynamical states $\boldsymbol{x_d} \in \mathbb{R}^{n-n_i}$ and integrator states $\boldsymbol{x_i} \in \mathbb{R}^{n_i}$. The dynamics of this transformed system are

$$\dot{\boldsymbol{x}}_{\boldsymbol{d}} = \boldsymbol{A_d x_d} + \boldsymbol{B_d} \ln\left(1 + \frac{\tilde{\boldsymbol{c}}}{\boldsymbol{c_0}}\right) + \boldsymbol{B_{d,i}} i \tag{5.11a}$$

$$y_d = \boldsymbol{C_d x_d} + \boldsymbol{D_d} \ln\left(1 + \frac{\tilde{\boldsymbol{c}}}{\boldsymbol{c_0}}\right) + \boldsymbol{D_{d,i}} i \tag{5.11b}$$

$$\tilde{\boldsymbol{c}} = \boldsymbol{C_c x} = \begin{bmatrix} \boldsymbol{C_{c,1}} & \boldsymbol{C_{c,2}} \end{bmatrix} \begin{bmatrix} \boldsymbol{x_d} \\ \boldsymbol{x_i} \end{bmatrix} = \boldsymbol{C_{c,1} x_d} \tag{5.11c}$$

$$\dot{\boldsymbol{x}}_i = \boldsymbol{B_i} i \tag{5.12a}$$

$$y_i = \boldsymbol{C_i x_i} \tag{5.12b}$$

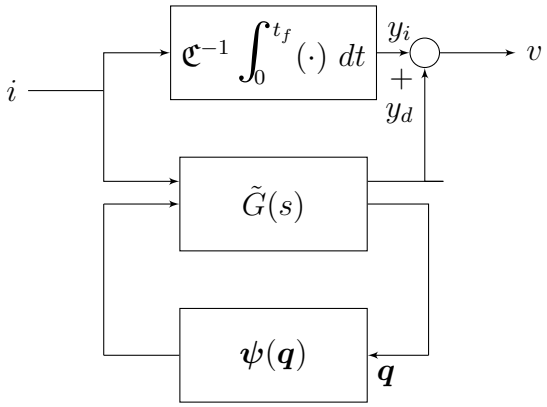


Figure 5.2: The reformulated supercapacitor model loop structure with the separation of the integrator and dynamical subsystems.

$$v = y_d + y_i. \tag{5.13}$$

Evaluating the integrator of (5.12a) means that (5.11c) can be expressed as

$$\tilde{\boldsymbol{c}} = \boldsymbol{C_c}\tilde{\boldsymbol{x}} = \boldsymbol{C_{c,1}}\boldsymbol{x_d} + \boldsymbol{C_{c,2}}\boldsymbol{B_i}\int_0^T i\;dt. \tag{5.14}$$

For both sets of supercapacitor parameters considered in this chapter, the matrices $\boldsymbol{C_{c,2}}\boldsymbol{B_i} = 0$ and so the concentration could be expressed solely in terms of the dynamical states and independently of the integral of the current, i.e. $\tilde{\boldsymbol{c}} = \boldsymbol{C_{c,1}}\boldsymbol{x_d}$. This means that the integrator states are unobservable with respect to the concentration, so there is not a unique mapping $\tilde{\boldsymbol{c}} \to \boldsymbol{x_i}$. The system can be expressed as Figure 5.2 with transfer function $\tilde{G}(s)$

$$\tilde{G}(s) = \left[\begin{array}{c|cc} \boldsymbol{A_d} & \boldsymbol{B_d} & \boldsymbol{B_{d,i}} \\ \hline \boldsymbol{C_{c,1}} & \boldsymbol{0} & \boldsymbol{0} \\ \boldsymbol{C_d} & \boldsymbol{D_d} & \boldsymbol{D_i} \end{array}\right]. \tag{5.15}$$

The upper subsystem of Figure 5.2 is labelled the *integrator* subsystem and the lower system involving $\tilde{G}(s)$ and the feedback loop of $\boldsymbol{\psi}(\boldsymbol{q})$ is labelled the *dynamical* subsystem. The independence on $\tilde{\boldsymbol{c}}$ from the integral of $i(t)$ greatly simplifies the stability analysis of the following section, as the dynamical and integrator systems can be decoupled and analysed separately.

By returning to the underlying PDEs of the model, a physical reason for the independence of the integrator dynamics is now given. The model has two sets of dynamics: those for the concentration (2.2) and those for the potentials (2.5). It is now shown that the integrator dynamics come from the electropotential dynamics (2.5) and not

from the concentration dynamics in (2.2). By differentiating in space the expression for Ohm's law in the solid phase [163]

$$\sigma \frac{\partial \phi_1}{\partial x} = i - i_2, \tag{5.16}$$

where i_2 is the current carried by the electrolyte, the dynamics of the potential difference across the double layer (2.5) can be expressed as

$$aC \frac{\partial(\phi_1 - \phi_2)}{\partial t} = \frac{\partial i_2}{\partial x}. \tag{5.17}$$

Integrating (5.17) with respect to x across an electrode and noting that all the current is carried in the solid phase at the current collector boundary ($i_2 = 0$) and all the current in the separator is carried by the electrolyte phase ($i_2 = i$) [163] gives

$$aC \frac{\partial}{\partial t} \int_0^{L_{elec}} (\phi_1 - \phi_2) dx = -i, \tag{5.18a}$$

$$aC \frac{\partial}{\partial t} \int_{L_{elec}+L_{sep}}^{L} (\phi_1 - \phi_2) dx = i. \tag{5.18b}$$

A set of integrator states is obtained from (5.18), with these states being the total potential difference across the double layer. In contrast, the diffusion operator in (2.2) means that the concentration dynamics are not pure integrators. This agrees with the numerical result that $\boldsymbol{C_{c,2}B_i} = 0$ implying that the dynamics of the concentration are independent of the integral of the current. Interestingly, (5.18) can be recognised as the typical dynamics of a capacitor consisting of two flat plates separated by an insulator, although (5.18) is in infinite dimensions.

5.2 System Properties

In this section, bounds on the system properties for the PB model (5.11) are computed, including model stability, the reachable set with unit energy impulse current, stored and dissipated energies for a charging profile, current to voltage gains corresponding to the capacitance and resistance and the maximum voltage without the potential difference across the double layer exceeding the electrolyte overpotential.

The intention of the following pages is to formulate an optimisation problem whose solution gives bounds for energy and stability properties of the supercapacitor model. To achieve this, the discretised version of the supercapacitor model is first put into the form of a Lur'e system and then the techniques of absolute stability theory are

applied. This approach allows for a rigorous characterisation of the supercapacitor model properties and includes the nonlinearity inherently within the analysis. These properties are then linked back to the electrochemical parameters of the model, such as to provide a systematic supercapacitor design procedure.

The discretised version of the dynamic state-space model (5.11) can be considered as a Lur'e system. Using the notation of [14], the Lur'e system has the form

$$\dot{\boldsymbol{x}}_{\boldsymbol{d}} = \boldsymbol{A}\boldsymbol{x}_{\boldsymbol{d}} + \boldsymbol{B}_{\boldsymbol{p}}\boldsymbol{p} + \boldsymbol{B}_{\boldsymbol{w}}w \tag{5.19a}$$

$$\boldsymbol{p}_{\boldsymbol{j}}(t) = \boldsymbol{\psi}_{\boldsymbol{j}}(\boldsymbol{q}_{\boldsymbol{j}}(t)), \quad \boldsymbol{j} = 1, \ldots, n_p \tag{5.19b}$$

$$\boldsymbol{q} = \boldsymbol{C}_{\boldsymbol{q}}\boldsymbol{x}_{\boldsymbol{d}} \tag{5.19c}$$

$$z = \boldsymbol{C}_{\boldsymbol{z}}\boldsymbol{x}_{\boldsymbol{d}} + \boldsymbol{D}_{\boldsymbol{p}}\boldsymbol{p} + \boldsymbol{D}_{\boldsymbol{w}}w. \tag{5.19d}$$

where $\boldsymbol{A} = \boldsymbol{A}_{\boldsymbol{d}}$ is Hurwitz, $\boldsymbol{B}_{\boldsymbol{p}} = \boldsymbol{B}_{\boldsymbol{d}}$, $\boldsymbol{B}_{\boldsymbol{w}} = \boldsymbol{B}_{\boldsymbol{d,i}}$, $\boldsymbol{C}_{\boldsymbol{z}} = \boldsymbol{C}_{\boldsymbol{d}}$, $\boldsymbol{D}_{\boldsymbol{w}} = \boldsymbol{D}_{\boldsymbol{d,i}}$, $w = i \in \mathbb{R}$ is the external input, n_p is the number of Lur'e system outputs, $z = y_d \in \mathbb{R}$ from (5.11b) is the dissipated voltage output, $\boldsymbol{q} = \tilde{\boldsymbol{c}}/\boldsymbol{c}_{\boldsymbol{0}} \in \mathbb{R}^{n_p}$ which includes boundary values. The nonlinearity $\boldsymbol{\psi}(\boldsymbol{q}) = \ln(1 + \boldsymbol{q}) : \mathbb{R}^{n_p} \to \mathbb{R}^{n_p}$ is static, memoryless, locally Lipschitz in $\boldsymbol{q}$, locally sector bounded

$$\frac{\boldsymbol{\psi}_{\boldsymbol{j}}(\boldsymbol{q}_{\boldsymbol{j}})}{\boldsymbol{q}_{\boldsymbol{j}}} \in [\underline{\boldsymbol{\delta}_{\boldsymbol{j}}}, \overline{\boldsymbol{\delta}_{\boldsymbol{j}}}] \quad \forall \boldsymbol{q} \in \mathcal{Q} \subseteq \mathbb{R}^{n_p} \tag{5.20}$$

and decentralised

$$\boldsymbol{\psi}(\boldsymbol{q}) = \left[\boldsymbol{\psi}_{\boldsymbol{1}}(\boldsymbol{q}_{\boldsymbol{1}}),\ \boldsymbol{\psi}_{\boldsymbol{2}}(\boldsymbol{q}_{\boldsymbol{2}}), \quad \ldots, \boldsymbol{\psi}_{\boldsymbol{n_p}}(\boldsymbol{q}_{\boldsymbol{n_p}})\right]^T. \tag{5.21}$$

The shifted logarithmic nonlinearity of Fig. 5.3 is an unbounded nonlinearity, i.e. $\overline{\boldsymbol{\delta}_{\boldsymbol{j}}} \to \infty$ as $\tilde{\boldsymbol{c}}_j \to -\boldsymbol{c}_0$. To make the Lyapunov analysis of the following section tractable, the sector $\overline{\boldsymbol{\delta}}_{\boldsymbol{j}}$ is constrained to a finite value with the level sets of the Lyapunov function being contained within the set detailed by the sector condition $\mathcal{Q} = \{\boldsymbol{q} : \underline{\boldsymbol{q}}_{\boldsymbol{j}} < \boldsymbol{q}_{\boldsymbol{j}} < \overline{\boldsymbol{q}}_{\boldsymbol{j}},\ \boldsymbol{j} = 1, \ldots, n_p\}$ where $\underline{\boldsymbol{q}}_{\boldsymbol{j}} > -1$ and $\overline{\boldsymbol{q}}_{\boldsymbol{j}} < \infty$. This means the analysis is only appropriate for a finite domain where $\boldsymbol{q} \in \mathcal{Q}$ [89]. The set of values of $\boldsymbol{x}_{\boldsymbol{d}}$ for which the local conditions hold is defined as $\mathcal{X}_q = \{\boldsymbol{x}_{\boldsymbol{d}} : \boldsymbol{q}(\boldsymbol{x}_{\boldsymbol{d}}) \in \mathcal{Q}\}$.

In order to compute bounds for the system properties, a positive definite Lyapunov function $V(\boldsymbol{x}_{\boldsymbol{d}}) > 0$ whose temporal derivative is negative definite

$$\frac{d\,V(\boldsymbol{x}_{\boldsymbol{d}})}{dt} < 0 \ \forall \boldsymbol{x}_{\boldsymbol{d}} \neq 0 \tag{5.22}$$

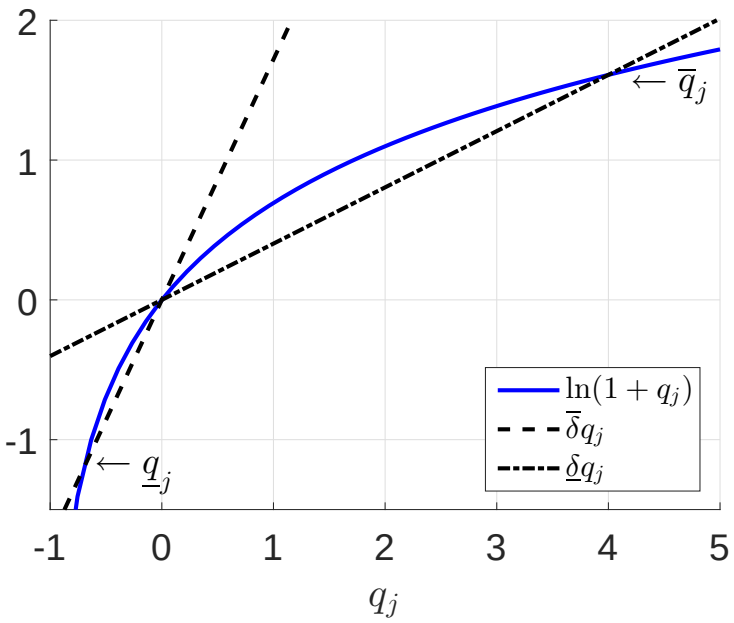


Figure 5.3: The locally sector bounded nature of the shifted logarithm.

is defined. In this chapter, the Lur'e-type Lyapunov function [14]

$$V(\boldsymbol{\theta}) = \boldsymbol{\theta}^T \boldsymbol{P} \boldsymbol{\theta} + \sum_{\boldsymbol{j}=1}^{n_p} \boldsymbol{\lambda_j} \int_0^{\boldsymbol{C_{q,j}\theta}} \boldsymbol{\psi_j}(v) dv \tag{5.23}$$

will be used where $\boldsymbol{P} > 0$, $\boldsymbol{\lambda_j} > 0$ and $\boldsymbol{C_{q,j}}$ denotes the $\boldsymbol{j}^{th}$ row of $\boldsymbol{C}_q$ [14].

Due to the sector conditions only holding locally, a modified version of the local absolute stability theory method of [69] that allows for asymmetric domains and generic level sets and which was inspired by [160] is implemented. When $\mathbf{q} \in \mathcal{Q}$, the following inequality is satisfied

$$\boldsymbol{\beta_j}(\overline{\boldsymbol{c}}_{\boldsymbol{j}} - \boldsymbol{q_j})(\boldsymbol{q_j} - \underline{\boldsymbol{c}}_{\boldsymbol{j}}) \geq 0, \quad \boldsymbol{j} = 1, \dots n_p \tag{5.24}$$

with $\boldsymbol{\beta_j} > 0$. If also the following inequality holds

$$\boldsymbol{\beta_j}(\overline{\boldsymbol{q}}_{\boldsymbol{j}} - \boldsymbol{q_j})(\boldsymbol{q_j} - \underline{\boldsymbol{q}}_{\boldsymbol{j}}) \geq \boldsymbol{\alpha_j} - V(\boldsymbol{x_d}), \quad \boldsymbol{j} = 1, \dots n_p \tag{5.25}$$

then the sublevel sets of $V(\boldsymbol{x_d})$ defined by $\mathcal{E}(V, \underline{\alpha})$ where $\mathcal{E}(V, \underline{\alpha}) = \{\boldsymbol{x_d} \in \mathbb{R}^{n-n_i} \mid \underline{\alpha} - V(\boldsymbol{x_d}) \geq 0\}$ and $\underline{\alpha} = \min_{\boldsymbol{j}=1,\dots,n_p} \boldsymbol{\alpha_j}$ are contained within the local domain with $\mathcal{E}(V, \underline{\alpha}) \subseteq \mathcal{Q}$.

To obtain a LMI representation for the inclusion conditions of (5.25), a quadratic lower bound for $V(\boldsymbol{x_d})$ will be used

$$\tilde{V}(\boldsymbol{\theta}) = \boldsymbol{\theta^T P \theta}. \tag{5.26}$$

Since $V(\boldsymbol{x_d}) \geq \tilde{V}(\boldsymbol{x_d})$ in the region where the sector conditions hold, if

$$\boldsymbol{\beta_j}(\overline{\boldsymbol{q}}_{\boldsymbol{j}} - \boldsymbol{q_j})(\boldsymbol{q_j} - \underline{\boldsymbol{q}}_{\boldsymbol{j}}) \geq \boldsymbol{\alpha_j} - \tilde{V}(\boldsymbol{x_d}), \quad \boldsymbol{j} = 1, \ldots n_p \tag{5.27}$$

holds, then (5.25) holds with (5.27) being defined by the n_p LMIs

$$\boldsymbol{\pi_j} = \begin{bmatrix} -\boldsymbol{\beta_j}\overline{\boldsymbol{c}}_{\boldsymbol{j}}\underline{\boldsymbol{c}}_{\boldsymbol{j}} - \boldsymbol{\alpha_j} & \frac{\boldsymbol{\beta_j}}{\boldsymbol{2}}(\overline{\boldsymbol{c}}_{\boldsymbol{j}} + \underline{\boldsymbol{c}}_{\boldsymbol{j}})\boldsymbol{C_{q,j}} \\ \boldsymbol{C_{q,j}^T}(\overline{\boldsymbol{c}}_{\boldsymbol{j}} + \underline{\boldsymbol{c}}_{\boldsymbol{j}})\frac{\boldsymbol{\beta_j}}{\boldsymbol{2}} & \boldsymbol{P} - \boldsymbol{\beta_j}\boldsymbol{C_{q,j}^T}\boldsymbol{C_{q,j}} \end{bmatrix} \geq 0, \quad \boldsymbol{j} = 1, \ldots n_p. \tag{5.28}$$

Satisfying these LMIs means that the local domain of the Lyapunov analysis is defined as $\mathcal{Q}_0 = \mathcal{E}(\tilde{V}, \underline{\alpha})$ since $\mathcal{E}(\tilde{V}, \underline{\alpha}) \subseteq \mathcal{E}(V, \underline{\alpha}) \subseteq \mathcal{Q}$.

The time derivative of the Lyapunov function (5.23) has quadratic form

$$\dot{V}(\boldsymbol{x_d}, \boldsymbol{p}, w) = \begin{bmatrix} \boldsymbol{x_d^T} & \boldsymbol{p}^T & w^T \end{bmatrix} \begin{bmatrix} \boldsymbol{A}^T\boldsymbol{P} + \boldsymbol{P}\boldsymbol{A} & \boldsymbol{P}\boldsymbol{B_p} + \boldsymbol{A}^T\boldsymbol{C_q^T}\boldsymbol{\Lambda} & \boldsymbol{P}\boldsymbol{B_w} \\ \boldsymbol{B_p^T}\boldsymbol{P} + \boldsymbol{\Lambda}\boldsymbol{C_q}\boldsymbol{A} & \boldsymbol{\Lambda}\boldsymbol{C_q}\boldsymbol{B_p} + \boldsymbol{B_p^T}\boldsymbol{C_q^T}\boldsymbol{\Lambda} & \boldsymbol{\Lambda}\boldsymbol{C_q}\boldsymbol{B_w} \\ \boldsymbol{B_w^T}\boldsymbol{P} & \boldsymbol{B_w^T}\boldsymbol{C_q^T}\boldsymbol{\Lambda} & 0 \end{bmatrix} \begin{bmatrix} \boldsymbol{x_d} \\ \boldsymbol{p} \\ w \end{bmatrix} \leq 0 \tag{5.29}$$

with $\boldsymbol{\Lambda} = \mathbf{diag}(\boldsymbol{\lambda_1}, \ldots, \boldsymbol{\lambda_{n_p}}) \geq 0$. The sector condition of (5.20) satisfies the inequality

$$-(\boldsymbol{p_j} - \underline{\boldsymbol{\delta}}_{\boldsymbol{j}}\boldsymbol{q_j})(\boldsymbol{p_j} - \overline{\boldsymbol{\delta}}_{\boldsymbol{j}}\boldsymbol{q_j}) \geq 0 \;\forall\; \boldsymbol{j} = 1, \ldots, n_p, \; \forall \boldsymbol{q} \in \mathcal{Q} \tag{5.30}$$

which is satisfied if

$$s_1(\boldsymbol{x_d}, \boldsymbol{p}, \boldsymbol{T}) = \begin{bmatrix} \boldsymbol{x_d^T} & \boldsymbol{p^T} \end{bmatrix} \begin{bmatrix} -\boldsymbol{C^T}\underline{\boldsymbol{\Delta}}\boldsymbol{T}\overline{\boldsymbol{\Delta}}\boldsymbol{C} & \boldsymbol{C_q^T}\frac{\underline{\boldsymbol{\Delta}}+\overline{\boldsymbol{\Delta}}}{\boldsymbol{2}}\boldsymbol{T} \\ \boldsymbol{T}\frac{\underline{\boldsymbol{\Delta}}+\overline{\boldsymbol{\Delta}}}{\boldsymbol{2}}\boldsymbol{C_q} & -\boldsymbol{T} \end{bmatrix} \begin{bmatrix} \boldsymbol{x_d} \\ \boldsymbol{p} \end{bmatrix} \geq 0 \tag{5.31}$$

where $\overline{\boldsymbol{\Delta}} = \mathbf{diag}(\overline{\boldsymbol{\delta}}_{\mathbf{1}}, \ldots, \overline{\boldsymbol{\delta}}_{\boldsymbol{n_p}})$, $\underline{\boldsymbol{\Delta}} = \mathbf{diag}(\underline{\boldsymbol{\delta}}_{\mathbf{1}}, \ldots, \underline{\boldsymbol{\delta}}_{\boldsymbol{n_p}})$ and $\boldsymbol{T} = \mathbf{diag}(\boldsymbol{\tau_1}, \ldots, \boldsymbol{\tau_{n_p}}) > 0$. Inequality constraints such as (5.29) and (5.31) are combined using the S-procedure [14, 82].

The following proposition gives a general semi-definite optimisation problem structure that allows the computations of the various system properties to be compactly described.

Proposition 5.1. *Consider a cost function* Π *to be minimised and a quadratic* $\boldsymbol{M} = \dot{V}(\tilde{\boldsymbol{x}}_{\boldsymbol{d}}, \boldsymbol{p}, w) + s_1(\tilde{\boldsymbol{x}}_{\boldsymbol{d}}, \boldsymbol{p}, \boldsymbol{T}) + \Omega(z, w)$ *where* $\dot{V}(\boldsymbol{x_d}, \boldsymbol{p}, w)$ *is the time derivative of* $V(\boldsymbol{x_d})$ *along the trajectories of* (5.19) *as given in* (5.29) *and* $\Omega(w, z)$ *characterises a current/voltage property of interest. Feasible solutions to the semidefinite programme*

$$\min \quad \Pi \tag{5.32a}$$

$$\text{s.t.} \quad \boldsymbol{P} > 0, \, \boldsymbol{T} > 0, \, \boldsymbol{M} \leq 0, \, \boldsymbol{\pi_j} \geq 0 \text{ for } \boldsymbol{j} = 1, \ldots n_p \tag{5.32b}$$

give bounds on particular system properties of the supercapacitor model relating to stability and current/voltage criteria. Each of these criteria is discussed separately in the rest of this section. Standard semidefinite program solvers such as MOSEK [103] can be used to solve the optimisation problem. The formulations of these problems for the Lur'e system are described in [14] with a key difference being that the analysis presented here is local.

5.2.1 Case 1: Stability

With $\Pi = \{\}$, $\Omega(z, w) = 0$ and $w = 0$, the solution of Problem 5.1 gives a sufficient condition on locally stability of the model. Increasing the bounds $\underline{\boldsymbol{q}}$ and $\overline{\boldsymbol{q}}$, and hence the sector conditions, until no solution exists, defines the limits on how far the supercapacitor can theoretically be pushed.

Solving Problem 5.1 for this case implies that the dynamic subsystem (5.11) is passive when $\tilde{\boldsymbol{c}} \in (-\boldsymbol{c_0}, \infty)$. Passivity implies that the sub-system is non-energy generating and gives a weak condition for model stability [89]. Since the integrator subsystem is also non-energy generating, and therefore passive, the whole system can then be said to be passive, as the interconnection of two passive systems is itself passive. This reflects the known passive nature of capacitor circuit devices [60].

5.2.2 Case 2: Maximum Reachable Set with Unit Energy Impulse

With $\Pi = \mathbf{trace}(\boldsymbol{P})$, $\underline{\alpha} = 1$ and $\Omega(z, w) = -w^2$, the solution of Problem 5.1 gives an outer approximation to the local maximal reachable set with unit energy impulse of current $R_{ue} \triangleq \left\{\boldsymbol{x_d}(t_f) : \boldsymbol{x_d}(0) = 0, \int_0^{t_f} w^2\, dt \leq 1\right\}$ for all $\{\boldsymbol{x_d}, w\}$ satisfying (5.19), (5.27). The outer approximation of this set is defined by $\Xi = \{\boldsymbol{\xi} : \boldsymbol{\xi}^T \boldsymbol{P} \boldsymbol{\xi} \leq 1\}$ with $\Xi \supseteq R_{ue}$. The trajectories of the integrator subsystem can be obtained analytically by integrating (5.12a) such that

$$\boldsymbol{x_i}(t_f) - \boldsymbol{x_i}(0) = \boldsymbol{B_i} \int_0^{t_f} i(t)\, dt \tag{5.33}$$

where $\boldsymbol{x_i}(t_f)$ and $\boldsymbol{x_i}(0)$ are the integrator states at times t_f and 0.

The physical interpretation of this set is that it gives an upper bound for the maximum deviation from steady-state of the concentration and potentials with the current

supplying 1 Joule of energy. Input charging signals of arbitrary energy can similarly be analysed by scaling. Knowledge of this set is useful for safety purposes, i.e. if the physical states have to remain within some limit when power is supplied to the supercapacitor.

5.2.3 Case 3: Bounds on Stored and Dissipated Energy

With $\Pi = \boldsymbol{x}_{\boldsymbol{d},\boldsymbol{0}}^T \boldsymbol{P} \boldsymbol{x}_{\boldsymbol{d},\boldsymbol{0}}$, $w = 0$, $\underline{\alpha} = V(\boldsymbol{x}_{\boldsymbol{d},\boldsymbol{0}})$ and $\Omega(z, w) = z^2$, the energy dissipated by the system in returning to the steady-state from some initial condition $\boldsymbol{x}_{\boldsymbol{d},\boldsymbol{0}} \in \mathcal{X}_q$

$$J_d = \int_0^\infty z^2 \, dt \tag{5.34}$$

is upper bounded by $\boldsymbol{x}_{\boldsymbol{d},\boldsymbol{0}}^T \boldsymbol{P} \boldsymbol{x}_{\boldsymbol{d},\boldsymbol{0}}$. No energy from the integrator subsystem is dissipated, so (5.34) defines the dissipated energy of the whole system. The energy stored in the integrator subsystem after a charge of time t_f is

$$J_i = \int_0^{t_f} i(t) \, dt \; \boldsymbol{B}_{\boldsymbol{i}}^T \boldsymbol{C}_{\boldsymbol{i}}^T \boldsymbol{C}_{\boldsymbol{i}} \boldsymbol{B}_{\boldsymbol{i}} \int_0^{t_f} i(t) \, dt. \tag{5.35}$$

After charging, the energy stored in the supercapacitor is given by J_i while the energy that is subsequently dissipated is upper bounded by J_d. Energy storage is achieved by the separation of charge across the double layer, while the dissipated energy is related to the diffusion of the concentration. The stored energy can be drawn from the supercapacitor at any time and should be the property that is used to compare the energy storage performance of different supercapacitors. The dissipated energy is an often overlooked phenomenon and improvements to state-of-charge estimation and device safety can be made by considering its effect.

Figure 5.4 shows a simulation of the model with the parameters of a SAFT America supercapacitor obtained from [163]. The charging profile is as follows; the supercapacitor is at rest for 5s before a 100A constant current (CC) charge is applied for 23s whereupon the current is removed and the device returns to near steady-state. Experimental data for the CC charging period up to the point where the current was turned off, which was also obtained from [163], is shown. The upper bound on J_d for the rest period after 25s of the charge obtained by solving Problem 5.1 was 1.46×10^{-4} and the value obtained by numerically integrating the simulation output signal was 1.38×10^{-4}.

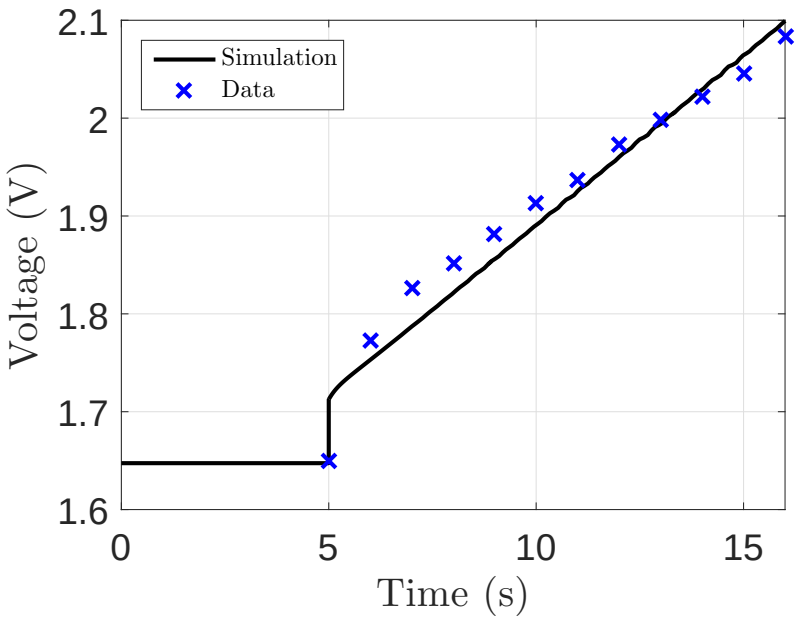


Figure 5.4: Simulation results and experimental data of the SAFT America supercapacitor. The data and the model parameters were obtained from [163]. The supercapacitor was rested for 5s before a 100A current was applied for 23s. After this charge, the current was removed and the voltage returned to an steady-state.

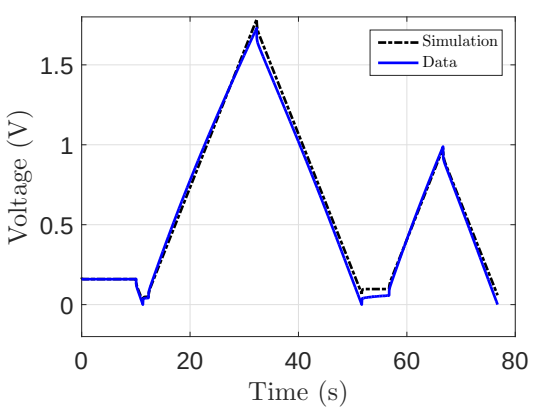
5.2.4 Case 4: Capacitance and Resistance

With $\Pi = {\gamma_d}^2$, $\underline{\alpha} = \|w\|_2$ and $\Omega(z, w) = z^2 - {\gamma_d}^2 w^2$, the $\mathcal{L}_2$ gain of the dynamic subsystem is upper bounded by γ_d. The gain γ_d has the physical representation of bounding the resistance of the supercapacitor. The gain from $i(t)$ to $\boldsymbol{y_i}(t)$ of the integrator subsystem is defined by

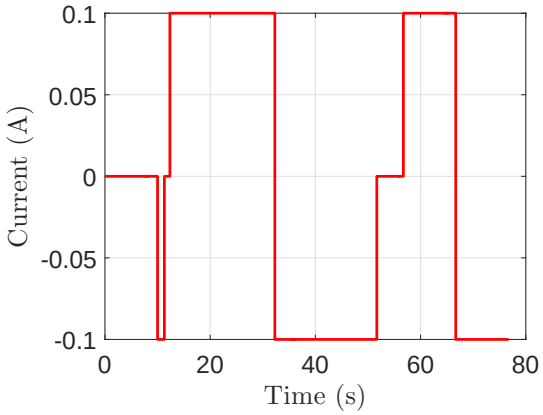
$$\boldsymbol{y_i}(t_f) - \boldsymbol{y_i}(0) = \boldsymbol{C_i B_i} \int_0^{t_f} i(t)\, dt \tag{5.36}$$

where $\boldsymbol{y_i}(t_f)$, $\boldsymbol{y_i}(0)$ are the values of $\boldsymbol{y_i}$ at times t_f and 0. Defining the capacitance $\mathfrak{C}$ by $Q = \mathfrak{C} v_s$ where $Q = \int_0^{t_f} i(t)\, dt$ is the transferred charge and $v_s = \boldsymbol{y_i}(t_f) - \boldsymbol{y_i}(0)$ is the voltage stored, the capacitance can be represented by $\mathfrak{C} = (\boldsymbol{C_i B_i})^{-1}$ upon consideration of (5.36).

One of the main advantages of EC models is that expressions for their capacitance and resistance can be easily obtained by resolving the circuit. Obtaining bounds for these electrical properties as functions of the physical parameters will help designers of supercapacitors, since it provides a design method for constructing supercapacitors with certain resistance and capacitance properties.

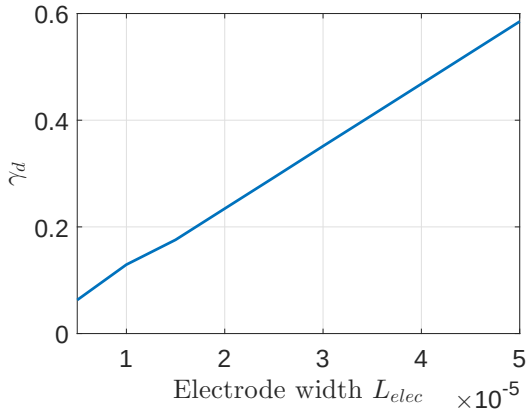


(a) Voltage response.

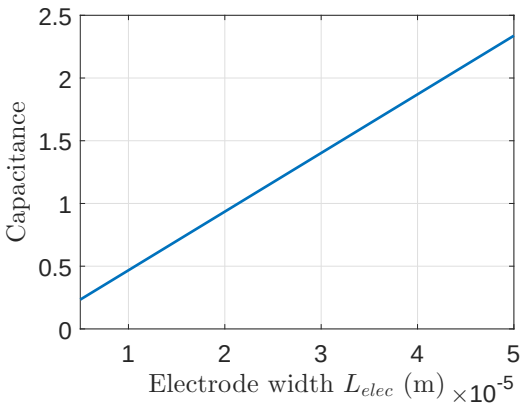


(b) Current profile.

Figure 5.5: Simulation results and experimental data from [47] for the square wave charging of the Maxwell Technologies supercapacitor.



(a) Gain of the dynamic subsystem describing resistance.



(b) Capacitance.

Figure 5.6: Variation in the $\mathcal{L}_2$ gain of the dynamical subsystem, describing resistance, and the capacitance as functions of the electrode lengths for the Maxwells Technologies supercapacitor.

Figure 5.5a shows experimental data and simulation results of the voltage response of a supercapacitor from Maxwell Technologies with part number P0100 P270T01, when subjected to the square wave charging profile of Figure 5.5b. To evaluate the method, γ_d and $\mathfrak{C}$ are used as metrics. The experimental data was obtained from [47] and the bounds $\overline{\boldsymbol{q}}$, $\underline{\boldsymbol{q}}$ characterising the local domain were obtained from the simulation. The $\mathcal{L}_2$ gain from the simulation was $\gamma_{d,sim} = 0.3065$ while the upper bound obtained by computing Problem 5.1 with a 15 state discretisation of the model PDEs was $\gamma_d = 0.3108$. The value of the capacitance was $\mathfrak{C} = 1/0.86 = 1.16$.

The conservatism of the computed bound for γ_d is due to the inherent conservatism of absolute stability theory and the satisfaction of the local inclusion conditions. Increasing the limits $\overline{\boldsymbol{q}}$ and $\underline{\boldsymbol{q}}$ where the local sector conditions hold leads to a larger sector condition that gives a less accurate representation of the logarithm, and hence increases conservatism. However, increasing the bounds also leads to less stringent conditions on the geometry of the Lyapunov function imposed by the local set inclusion conditions, reducing conservatism.

The variation of the the resistance γ_d and capacitance $\mathfrak{C}$ as functions of the electrode length L_{elec} are shown in Figure 5.6 for the Maxwell Technologies supercapacitor. This figure shows that conflicting design objectives have to be considered when designing supercapacitors, with devices that have low resistances but high capacitances being desired. This ability to link changes in physical parameters to electrical properties may lead to an improvement in the supercapacitor design process.

5.2.5 Maximum Voltage Limits

The final system property that will be computed is an upper bound on the supercapacitor voltage such that the potential difference across the double layer does not exceed the overpotential [95]. The main limitation holding back the implementation of supercapacitors is their low energy densities, defined as

$$E = \frac{1}{2}\mathfrak{C}v^2. \tag{5.37}$$

Low maximum operating voltages, enforced to prevent decomposition of the electrolyte, are a significant reason why this energy density is low [95]. However, in comparison to lithium-ion batteries, the reason for the low energy density of supercapacitors is that ions are only stored at the surface of the electrodes, while in a battery, the ions can be stored within the volume of the material. For aqueous electrolytes,

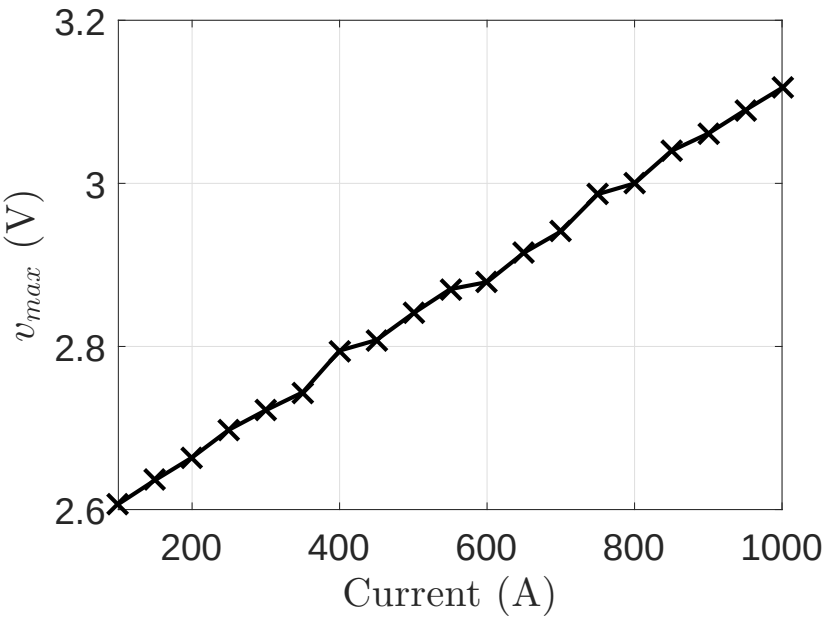


Figure 5.7: The maximum voltage of the SAFT America supercapacitor such that potential across the double layer never exceeds the overpotential as a function of current I.

such as that used in [163], if the potential difference between the electrode and the solvated ion is greater than 1.27 V, then the solvated ions undergo the overall reaction

$$2\mathrm{H_2O(l)} \rightarrow 2\mathrm{H_2(g)} + \mathrm{O_2(g)} \tag{5.38}$$

transitioning from a liquid to a gas. This causes the charges in the electrolyte and the electrode to no longer be separated and a short circuit occurs.

To compute this maximum voltage, the term $\kappa\,\partial\phi_1/\partial x$ is added and subtracted to the algebraic constraint (2.6) such that it can be expressed as

$$\frac{\partial \phi_1}{\partial x} = -\frac{\kappa}{\sigma+\kappa}\frac{\partial(\phi_2-\phi_1)}{\partial x} - \frac{\kappa(t_+-t_-)}{f(\kappa+\sigma)}\frac{\partial \ln(c)}{\partial x} - \frac{i}{\sigma+\kappa}. \tag{5.39}$$

Substituting this expression into the definition of the voltage gives

$$v = \phi_1|_{x=0} - \phi_1|_{x=L} \tag{5.40a}$$

$$= -\int_0^L \frac{\partial \phi_1}{\partial x} dx \tag{5.40b}$$

$$= \int_0^L \frac{\kappa}{\sigma+\kappa}\frac{\partial(\phi_2-\phi_1)}{\partial x} + \frac{\kappa(t_+-t_-)}{f(\kappa+\sigma)}\frac{\partial \ln(c)}{\partial x} + \frac{i}{\sigma+\kappa} dx \tag{5.40c}$$

$$= \underbrace{\frac{\kappa}{\sigma+\kappa}(\phi_2-\phi_1)\Big|_{x=0}^{x=L}}_{(a)} + \underbrace{\frac{\kappa(t_+-t_-)}{f(\kappa+\sigma)}\ln(c)\Big|_{x=0}^{x=L}}_{(b)} + \underbrace{\frac{2iL_{elec}}{\sigma+\kappa}}_{(c)}. \tag{5.40d}$$

This algebraic relation for the voltage expressed in terms of the boundary values of the states has been split into three components; (a) the potential difference across the double layer, (b) the charge carried by the ions and (c) the series resistance term. This expression shows that the voltage is linearly dependent upon the maximum potential difference across the double layer and the current i. The maximum value of (b) depends upon the extremal values of the interval $c \in [\underline{c}, \overline{c}]$, since the image of this set under the function $\ln(c)$ is concave when $\underline{c} > 0$. The following optimisation problem computes the maximum voltage with a limit on the double layer potential difference

$$v_{max} = \max_{c,\phi_1,\phi_2} \quad v \tag{5.41a}$$

$$\text{subject to (5.6)}, \ |\phi_1 - \phi_2| \leq 1.27, \ c \in [\underline{c}, \overline{c}], \ BCs(\tilde{c}, \phi_1, \phi_2). \tag{5.41b}$$

To ensure that the optimisation searches over the physically real subset of the state-space, the algebraic equation (5.6) and state boundary conditions $BCs(\tilde{c}, \phi_1, \phi_2)$, are included into (5.41) as equality constraints and an inequality condition is enforced to ensure that the potential difference across the double layer never exceeds $1.27\ V$ at any point in the domain. This constrained, nonlinear optimisation problem can be solved for the discretised problem using standard MATLAB solvers such as "fmincon" and Figure 5.7 shows the variation of this maximum voltage as a function of the current I for the case of the SAFT America supercapacitor. The quoted maximum voltage of the supercapacitor given by the manufacturers is 2.8 V [163]. The results of (5.41) are close to this manufacturing limit, but it shows that this is a conservative limit as the maximum voltage is actually dependent upon the current profile, suggesting that more reasonable limits could be implemented for known charging conditions. It is pointed out that the PDE model does not have a detailed description of the double layer, but instead uses porous electrode theory, which assumes that the electrode can be treated

as a single homogenised phase. The double layer is a physical phenomenon that is not well understood, especially in complex geometries such as porous media [95], which means that the analysis of (5.41) may not capture local effects occurring in the double layer. The benefits of increasing the maximum voltage of the supercapacitor are significant as a doubling of the voltage results in a quadrupling of the maximum energy, as described by (5.37).

5.2.6 Absolute Stability Theory for Energy Storage Devices

Although this work has considered electrochemical supercapacitor models, the approach has many features that make it attractive for analysing and understanding other forms of electrochemical energy storage systems. Firstly, it is noted that absolute stability theory was partly inspired by the notion of passivity in circuit analysis, and the presented approach links these two classic approaches through the electrochemistry. Robustness is a core concept in absolute stability theory which can accommodate the approximations and parameterisations of the complex PB electrochemical models. This robustness comes at the expense of conservatism which could be overcome by using more advanced Lyapunov functions such as [160]. The choice of Lyapunov function also allows time-varying systems to be analysed, making the method applicable for models which incorporate degradation. Lastly, since most energy storage devices are known to be passive, the proposed approach can be applied to models of other devices such as the Newman model for Li-ion batteries [44] whose main nonlinearities are the OCV curve and the Butler Volmer equation, which can both be represented by sector conditions.

5.3 Conclusion

This chapter described a method for bounding the system properties of a physics-based supercapacitor model. By treating the model as a Lur'e system, bounds for the dissipated and stored energies after charging, $\mathcal{L}_2^e$ gains from current to voltage corresponding to the capacitance and the resistance, model stability, maximum reachable set with unit energy impulse current and limits on the maximum voltage such that the potential difference across the double layer never exceeded the electrolyte overpotential were computed. These bounds were obtained by solving several optimisation problems involving linear matrix inequalities and semi-definite programmes.

The following chapter extends these results to supercapacitors with structured electrodes. Structured electrodes introduce layers of different materials into the electrode such that it no longer has homogeneous properties. Experimental data are used to develop and verify a model of these electrodes and also to investigate how the real and imaginary capacitances of the supercapacitors are affected by the presence of these layers.

Chapter 6

Supercapacitors With Structured Electrodes

This chapter considers the analysis of supercapacitors with "structured" electrodes. Typically, commercial supercapacitor electrodes are composed of a single medium of porous carbon and are assumed to have an equivalent homogenised property throughout the electrode. These electrodes are typically produced by slurry casting [73]. It is standard that both the positive and negative electrodes are equivalent, although recently, the introduction of pseudo-capacitance has led to some supercapacitors with asymmetric electrodes [93], as in batteries [111]. These devices are known as "supercapatteries", with this name highlighting the combination of supercapacitor and battery properties in a single device [179]. An alternative electrode structure has recently been proposed involving structured electrodes [73], which purposefully remove the single phase nature of the electrode, with the electrodes instead being formed of distinct layers composed of different materials, as illustrated in Figure 6.1. Experimental studies have shown the benefits of structuring the electrodes in this manner, with exceptional specific capacitance values being recorded [73]. Even with such atypical constructions, manufacturing processes exist for structured electrodes with the different layers being applied using a spray forming process [75]. This process sprays carbon nanotubes embedded in droplets to form the layers, with the vapour in the droplets then evaporating leaving a porous structure, as shown in Figure 6.2 [73]. In terms of design, the variable for structured electrodes is the configuration (lengths and placement) of the different layers. Splitting the electrode into a finite number of layers in this manner makes the resulting design problem both more tractable and the solutions more verifiable than for a continuous electrode porosity distribution,

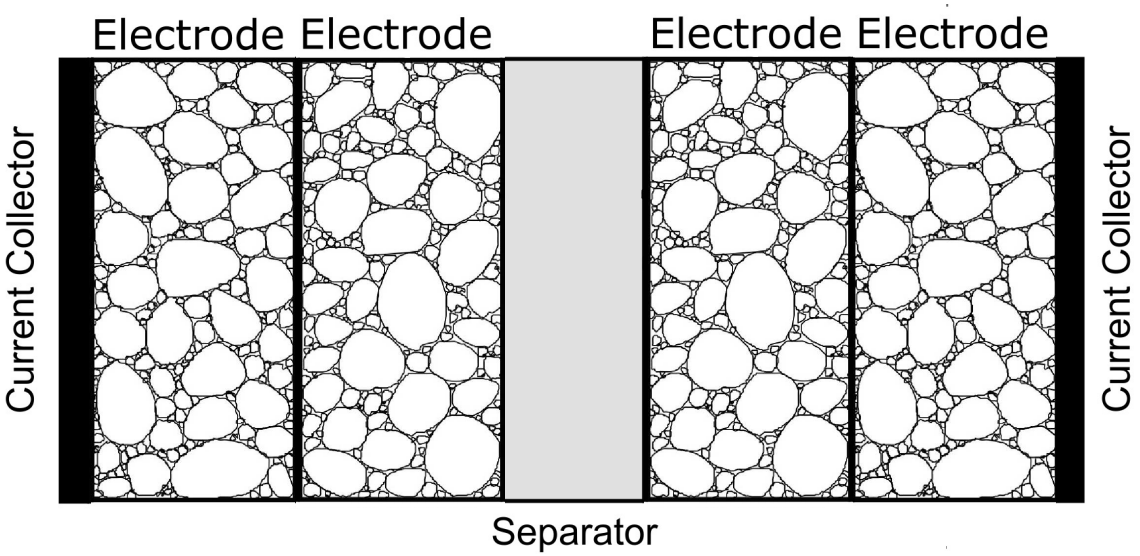


Figure 6.1: A supercapacitor with structured electrodes. The porous electrodes are formed of two layers with different material properties and thicknesses.

as adopted in [15, 101, 124]. This is because with structured electrodes, issues regarding spatial homogenisation in varying domains [16] do not need to be addressed and a manufacturing process exists to build the resulting optimal designs. As well as classical supercapacitors, structured electrodes have also been applied to lithium ion batteries [74] and solid-state supercapacitors [75].

6.1 Design Metrics: Real and Imaginary Capacitance

Even though structured electrodes have been shown to perform well in experiments [73], obtaining the optimal configuration of the various layers for a particular application is currently obtained in a rather ad-hoc manner. This chapter proposes a modelling and optimisation approach to configure the electrode layers that is both cheaper and less time consuming than carrying out a physical experiments. The previous chapter considered the design of supercapacitors using design objectives derived from control theory [14]. These objectives were originally constructed for the analysis of passive systems in general, not particularly energy storage. By contrast, the supercapacitor design objectives considered in this chapter stem from a dialogue with Prof. Patrick Grant and Dr. Ann Huang from the Material Science Department at Oxford University, whose research is currently directly involved with the manufacture and

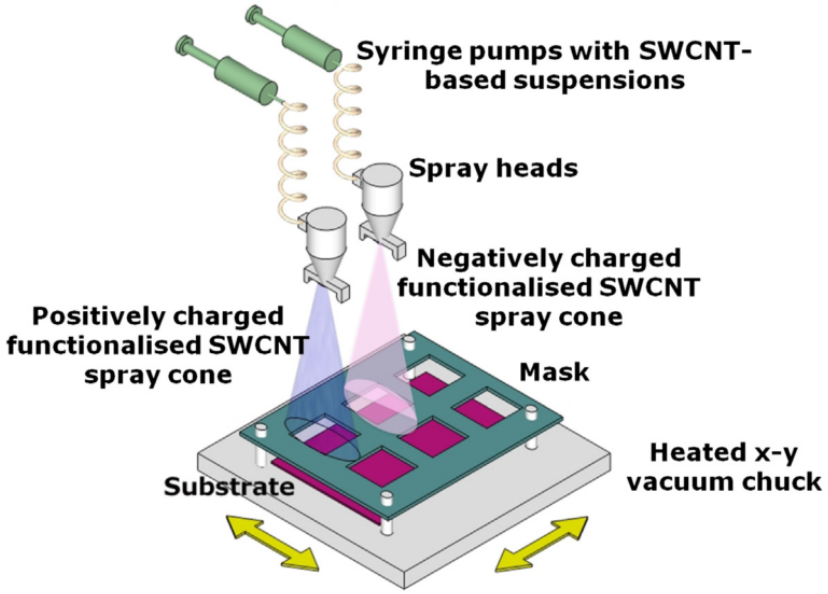


Figure 6.2: Schematic of the structured electrode spray forming process. Image obtained from [73].

design of structured electrode supercapacitors from a materials science perspective [73–75]. The design objectives that were selected to be optimised over were the real and imaginary capacitances described in chapter 2 [95, 151]. These capacitance values are obtained from EIS data, which is a frequency domain measurement relating the gain from small sinusoidal currents to the voltage, in essence, allowing the impedance function to be generated for the supercapacitor

$$G(jw) = \frac{V(j\omega)}{I(j\omega)}. \tag{6.1}$$

The impedance function can be decomposed into real and imaginary parts as

$$G(j\omega) = G'(\omega) + jG''(\omega). \tag{6.2}$$

where primes denote real components and double primes denote imaginary components. This function can be represented as a *supercapacitance* $C(j\omega)$ such that

$$G(j\omega) = \frac{1}{j\omega C(w)}. \tag{6.3}$$

The reason for expressing $G(j\omega)$ in this manner is to obtain a frequency domain form of the capacitance equation $Q = \mathfrak{C}v$

$$\frac{1}{j\omega C(w)} = \frac{V(j\omega)}{I(j\omega)} \tag{6.4}$$

$$\frac{1}{j\omega} I(j\omega) = C(w)V(j\omega) \tag{6.5}$$

$$Q(j\omega) = C(w)V(j\omega). \tag{6.6}$$

Through some re-arranging, it follows that the *supercapacitance* has the form

$$C(\omega) = C'(\omega) - jC''(\omega) \tag{6.7}$$

where $C'(\omega)$ is the real capacitance

$$C'(\omega) = -\frac{G''(\omega)}{\omega|G(\omega)|^2} \tag{6.8}$$

and $C''(\omega)$ is the imaginary capacitance

$$C'(\omega) = \frac{G'(\omega)}{\omega|G(\omega)|^2}. \tag{6.9}$$

According to [151], the low frequency value of $C'(\omega)$ is the supercapacitor's capacitance under a constant current charge and the imaginary capacitance $C''(\omega)$ corresponds to energy dissipated by irreversible losses. To show this, [151] obtains analytic expressions of $C'(\omega)$ and $C''(\omega)$ for the classical equivalent circuit (see Figure 4.1) and notices that the resistance term only appears in the numerator of $C''(\omega)$. In the material science community, optimising over these capacitances is equivalent to optimising over the Pareto front of the Ragone plot [26]. The Ragone plot expresses the trade-off between energy density and power density, with these properties generally being inversely proportional to each other. This trade-off occurs because high energy density supercapacitors ideally require a large concentration of ions, and hence charge, concentrated at the double layer, but this increased ion density limits their movement, hence decreasing the power. Other design objectives that were proposed include optimising the energy stored for a particular charging profile as in [37]. This approach would not be generalisable to different charging conditions, although it would consider the nonlinearity in a more fundamental manner.

The work of this chapter is not yet complete with further experimental validation of the model being needed to ensure its suitability for the optimisation procedure and the design objectives need to be further refined. Therefore, this chapter represents an

initial contribution to an interesting supercapacitor design problem, which has already shown great potential to improve supercapacitor performance using a radically new electrode construction.

6.2 Structured Electrode Supercapacitor Model

Similarly to the previous chapter, a model based optimisation approach is adopted for the design of structured electrodes. However, such an approach requires a suitable PB model, with (to the author's knowledge) the first such model being introduced in this chapter. The model is similar to [163] that was presented in Chapter 2 and is again formed of a set of PDEs describing electrochemical phenomena and boundary conditions (BCs) connecting the different domains. The structured supercapacitor model again has both electrode and separator domains, with new internal BCs connecting the different layers of the electrode and with different electrochemical parameter values for each layer. The PDEs governing the dynamics of the structured electrode domains are shown in Table 6.1 for a two layer electrode. It should be straight forward to extend this model to n-layer electrodes, as the electrode dynamics have the same form in each layer, albeit with different parameter values.

The boundary conditions connecting the current collectors to the extremal electrode layers and those connecting the most internal electrode layers to the separator are the same as for the unstructured electrode model, as in Table 2.2. However, three new boundary conditions are proposed for the interconnection of the different layers. The first boundary condition conserves the flux of the ionic concentration via

$$D\frac{\partial c}{\partial x}\bigg|_L = D\frac{\partial c}{\partial x}\bigg|_R. \tag{6.10}$$

The second boundary condition requires that the current in the solid phase is conserved across the boundary, i.e. $i_1|_L = i_1|_R$. This is enforced using the relation for solid phase current given in (2.5) so that

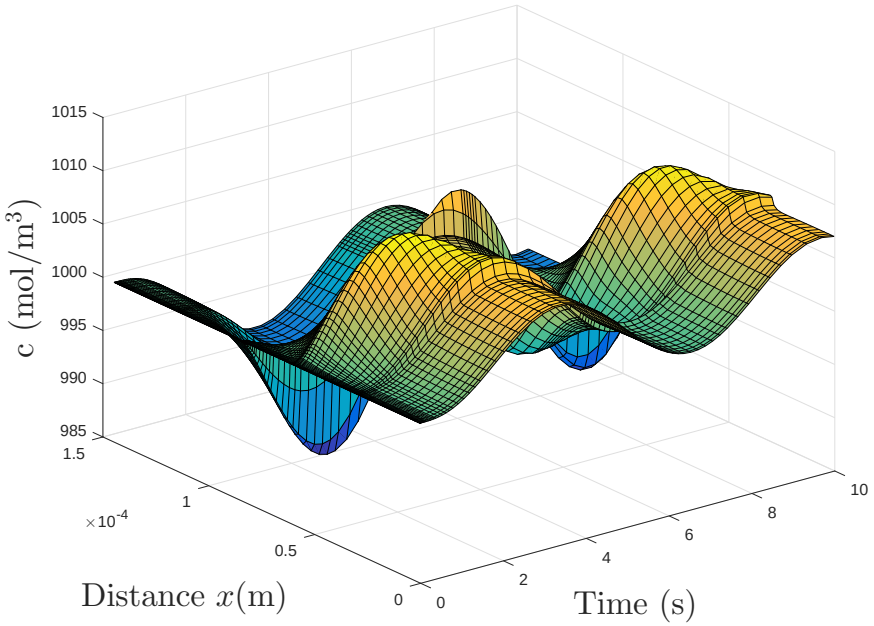
$$\sigma\frac{\partial \phi_1}{\partial x}\bigg|_L = \sigma\frac{\partial \phi_1}{\partial x}\bigg|_R. \tag{6.11}$$

The final boundary condition enforces conservation of current in the electrolyte across the boundary, with $i_2|_L = i_2|_R$

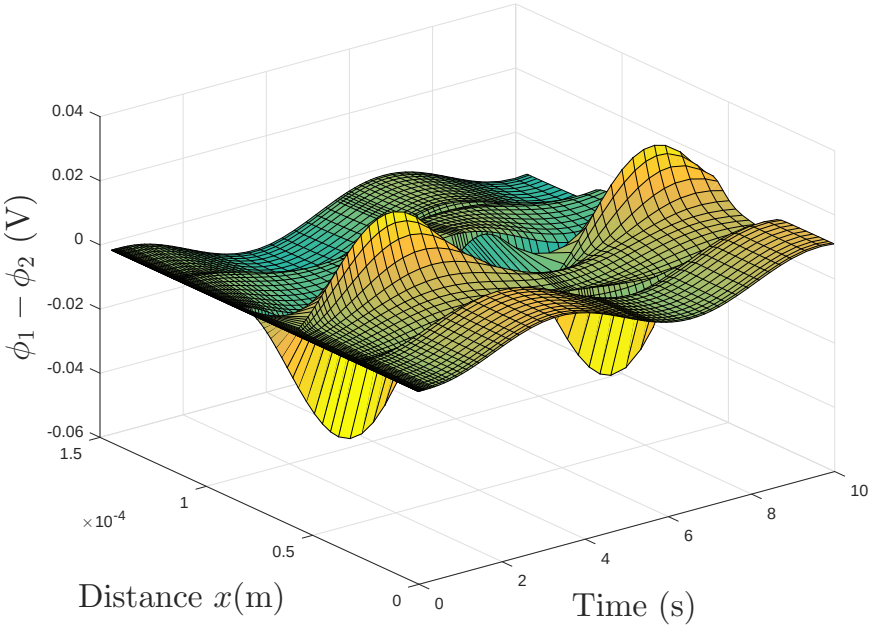
$$\left[\kappa\frac{\partial \phi_2}{\partial x} + \kappa\left(\frac{t_+ - t_-}{f}\right)\frac{\partial \ln\, \mathrm{c}}{\partial x}\right]_L = \left[\kappa\frac{\partial \phi_2}{\partial x} + \kappa\left(\frac{t_+ - t_-}{f}\right)\frac{\partial \ln\, \mathrm{c}}{\partial x}\right]_R \tag{6.12}$$

which is derived from (2.2). These boundary conditions are expressed in Table 6.2.

The evolution of the structured electrode model states for a sinusoidal input charging current $i = \sin(t)$ is shown in Figure 6.3. The supercapacitor described in this simulation had electrodes composed of two layers of equal thicknesses and was characterised by the parameters in Table 6.3 and 6.4. Figure 6.3a plots the evolution of the ionic concentration while Figure 6.3b plots the potential difference across the double layer. A clear discrepancy between the state trajectories in each layer can be seen from these plots, with the trajectories forming complex shapes.



(a) Ionic concentration.



(b) Double layer potential difference.

Figure 6.3: Evolution of the ionic concentration and potential difference across the double layer with a sinusoidal charging current $i = \sin(t)$ for the structured layer supercapacitor with two equal length layers in the electrode.

Electrode Layer 1	Electrode Layer 2	Separator
$0 \leq x < L_1$	$L_1 < x < L_{elec}$	$L_{elec} < x < L_{elec} + L_{sep}$
$\frac{aC}{F}\left(t_- \frac{dq_+}{dq} + t_+ \frac{dq_-}{dq}\right)\frac{\partial(\phi_1-\phi_2)}{\partial t} + \epsilon\frac{\partial c}{\partial t} = \mathrm{D}\frac{\partial^2 c}{\partial x^2}$	$\frac{aC}{F}\left(t_- \frac{dq_+}{dq} + t_+ \frac{dq_-}{dq}\right)\frac{\partial(\phi_1-\phi_2)}{\partial t} + \epsilon\frac{\partial c}{\partial t} = \mathrm{D}\frac{\partial^2 c}{\partial x^2}$	$\epsilon\frac{\partial c}{\partial t} = \mathrm{D}\frac{\partial^2 c}{\partial x^2}$
$aC\frac{\partial(\phi_1-\phi_2)}{\partial t} = \sigma\frac{\partial^2\phi_1}{\partial x^2}$	$aC\frac{\partial(\phi_1-\phi_2)}{\partial t} = \sigma\frac{\partial^2\phi_1}{\partial x^2}$	$\ldots$
$0 = \sigma\frac{\partial\phi_1}{\partial x} + \kappa\frac{\partial\phi_2}{\partial x} + \kappa\left(\frac{t_+-t_-}{f}\right)\frac{\partial \ln c}{\partial x} + i$	$0 = \sigma\frac{\partial\phi_1}{\partial x} + \kappa\frac{\partial\phi_2}{\partial x} + \kappa\left(\frac{t_+-t_-}{f}\right)\frac{\partial \ln c}{\partial x} + i$	$0 = \kappa\frac{\partial\phi_2}{\partial x} + \kappa(\frac{t_+-t_-}{f})\frac{\partial \ln c}{\partial x} + i$

Table 6.1: Electrochemical model equations for a supercapacitor with two layer structured electrodes.

Current Collector	Electrode Layer-Electrode Layer Boundary	Electrode-Separator Boundary
$\frac{\partial\phi_1}{\partial x} = -\frac{i}{\sigma}, \phi_1 = 0$	$\sigma\frac{\partial\phi_1}{\partial x}\Big\vert_L = \sigma\frac{\partial\phi_1}{\partial x}$	$\frac{\partial\phi_1}{\partial x}\Big\vert_R = 0$
$\frac{\partial\phi_2}{\partial x} = 0$	$\left[\kappa\frac{\partial\phi_2}{\partial x} + \kappa\left(\frac{t_+-t_-}{f}\right)\frac{\partial \ln c}{\partial x}\right]_L = \left[\kappa\frac{\partial\phi_2}{\partial x} + \kappa\left(\frac{t_+-t_-}{f}\right)\frac{\partial \ln c}{\partial x}\right]_R$	$\left[\kappa\frac{\partial\phi_2}{\partial x} + \kappa\left(\frac{t_+-t_-}{f}\right)\frac{\partial \ln c}{\partial x}\right]_L = \left[\kappa\frac{\partial\phi_2}{\partial x} + \kappa\left(\frac{t_+-t_-}{f}\right)\frac{\partial \ln c}{\partial x}\right]_R$
$\frac{\partial c}{\partial x} = 0$	$\mathrm{D}\frac{\partial c}{\partial x}\Big\vert_L = \mathrm{D}\frac{\partial c}{\partial x}\Big\vert_R$	$\mathrm{D}\frac{\partial c}{\partial x}\Big\vert_L = \mathrm{D}\frac{\partial c}{\partial x}\Big\vert_R$

Table 6.2: Boundary conditions for a supercapacitor with two layer structured electrodes.

6.3 Model Experimental Verification and Capacitances

EIS model simulation results were compared with experimental data for a supercapacitor with structured electrodes composed of two layers in Figures 6.4a to 6.5c. The experimental data were received from Dr. Ann Huang from the Material Science Department of Oxford University. The electrodes of the tested supercapacitor were composed of an outer layer of length L_1 made from TiO_2-nanoparticles and an inner layer of length L_2 formed by carbon nanotubes, see [75] for further details about these materials. The values of the electrochemical parameters for this structured electrode supercapacitor are given in Table 6.3 and 6.4. In general, carbon nanotubes have better electrochemical properties than the TiO_2-nanoparticles, having higher electrode conductivity for example, but they are also much more expensive, representing another trade-off in design. The majority of the parameters of the supercapacitor model were measured via experimental techniques, but others including the diffusion coefficients, transference number, porosity factors and tortuosity factors were estimated using the methods from chapter 3. In order to obtain the EIS response of the supercapacitor model, it was linearised around the equilibrium point as in chapter 4, giving the impedance function.

Figures 6.4a -6.4c compare EIS results from the model with experimental data for a supercapacitor with the ratio of electrode layer lengths being $8L_1 = L_2$. Figure 6.4a shows real and imaginary components of the identified impedance function as an Argand diagram. Real and imaginary values of the impedance as functions of frequency are respectively shown in Figures 6.4b and 6.4c.

The model was then verified on a new data set for a structured supercapacitor with an electrode ratio of $L_1 = L_2$. The only parameters that were changed in the model for this new data set were the lengths L_1 and L_2. Experimental and model simulations results for this configuration are shown in Figures 6.5a to 6.5c, where Figure 6.5a is the Argand diagram of the impedance plot, Figure 6.5b shows the real component of the impedance as a function of frequency and Figure 6.5c shows the imaginary component.

These figures show that the proposed model can capture the frequency response of the structured electrode supercapacitor. Not only was the identified model's frequency response close to the first identified dataset, but also the second dataset, reinforcing the

model accuracy. Note that the impedance function of the model has values at frequencies, both low and high, that are beyond those that can be measured experimentally. It is also worth noting the difference in the parameter values for the supercapacitors described in Tables 2.4, 2.5 and 6.3, 6.4. The supercapacitors of Tables 2.4, 2.5 are both commercially available while that of Table 6.3, 6.4 is a state-of-the-art research project, highlighting the gap in performance between research devices and devices that are readily available in the market.

Figures 6.6a- 6.6b respectively show real and imaginary capacitance values as functions of frequency for various supercapacitors. Experimental data is shown in black for the structured electrodes with a layer ratio of $L_1 = L_2$. Capacitances of the structured electrode model are shown in blue, with configuration 1 having an inner layer made of carbon nanotubes and an outer layer of TiO_2 nano-particles. Configuration two has the order of these layers swapped around. Values for single layer supercapacitors are shown in red.

There are several noticeable similarities and discrepancies in the curves of these figures. First, notice that swapping the order of the layers gives different results, so the spatial organisation of the electrode affects its performance. The most noticeable feature in the capacitances plots of structured electrodes are the presence of several bumps, with these bumps being more exaggerated in the model results than the experimental data. Such bumps are not as prevalent in the plots for the single layer supercapacitors, suggesting that a new dynamic storage mechanism is introduced with the layers, possibly due to a resonance effect, that may be exploited. The maximum real capacitance for structured electrode lay between that of the two single layer electrodes, so they could not store as much energy for a DC charge as the single layer of carbon nanotubes. The knee frequency is defined as the frequency when the real capacitance rapidly drops. The knee frequency for structured electrodes is below that of single layered electrodes, at approximately 10^{-3} rad s^{-1} instead of 10^{-1} rad s^{-1} for the single layer case. This equates to a drop in stored energy at low frequencies. However, at frequencies between 10^0 rad s^{-1} and 10^2 rad s^{-1}, the real capacitance of the structured electrodes was actually greater than that of the single layer. This result gives encouraging signs for the use of structured electrodes at high frequency applications, an example being the British electrical grid which operates at 50 Hz. Looking at the imaginary capacitances, the peak value of the structured supercapacitors is lower than that of the single layer, implying that structured electrodes exhibit lower peak losses.

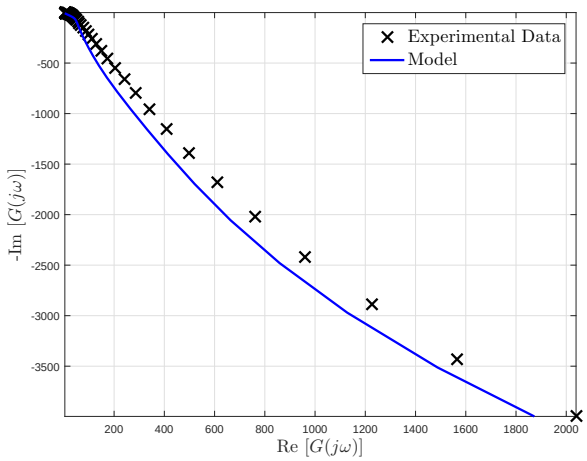
Parameter	Value	Units
L_{elec}	37	μ m
κ_∞	0.1	S/m
c_0	1000	mol/m^3
t_+	0.625	
S	1.13 $\times 10^{-4}$	m^2
$\frac{dq_+}{dq} = \frac{dq_-}{dq}$	-0.5	
T	298	K

Table 6.3: Global parameters for the supercapacitor model with structured electrodes.

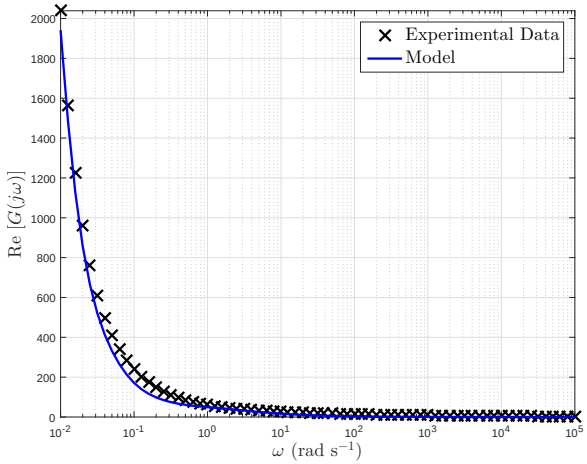
The benefit of using a PB model for design is that it links changes in the electrochemical parameters to energy storage performance. Figures 6.7a and 6.7b explore this idea by showing the obtained capacitances during a sweep of the ratios of the electrode layer lengths, where L_{elec} is the total electrode length satisfying $L_{elec} = L_1 + L_2$. Noticeably, for all ratios of the lengths of the layers, the form of the capacitance plots were fairly similar. This insensivity of the capacitance plots was also observed in Figures 6.4 and 6.5 for both the experimental data and the simulation results, with different relative layer lengths not giving significantly different capacitance plots. In fact, a bigger difference in the capacitances was observed when the layers were the same size but swapped around, as in Figures 6.6a and 6.6b. This suggests that it is the mere presence of layers in the electrodes that has the biggest impact upon the capacitances, with the capacitances being insensitive to the layer lengths. This result also suggests that the inclusion of even more layers into the electrode will result in even more varied capacitance responses with more bumps, that may be optimised over.

TiO_2 Nano-particles Parameters		
Parameter	Value	Units
ϵ_1	0.26	
Γ_1	0.5	
σ_1	22	S/m
aC_1	3.28×10^{7}	F m^{-3}
D_1	2.25×10^{-13}	m^2 s^{-1}
Carbon Nanotube Parameters		
Parameter	Value	Units
ϵ_2	0.083	
Γ_2	1.65	
σ_2	340	S/m
aC_2	2.30×10^{7}	F m^{-3}
D_2	8.39×10^{-12}	m^2 s^{-1}
Separator Parameters		
Parameter	Value	Units
L_{sep}	80	μ m
ϵ_s	0.05	
Γ	3.5	
D_s	1×10^{-11}	m^2 s^{-1}

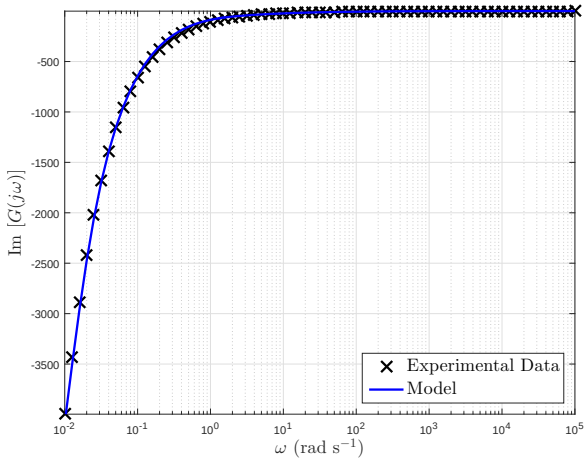
Table 6.4: Local parameters for the different domains of the supercapacitor model with structured electrodes.



(a) Argand diagram of $G(j\omega)$.

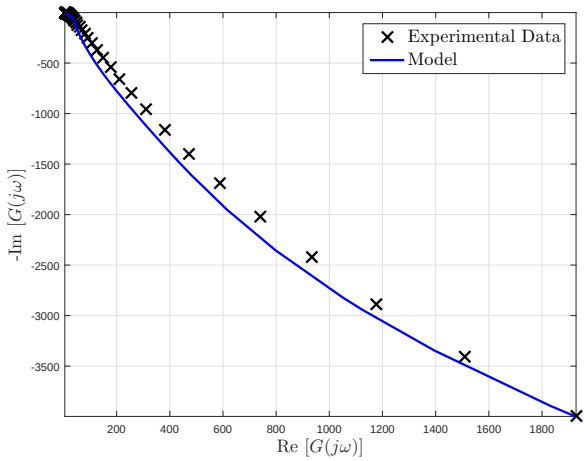


(b) Real component of $G(j\omega)$ as a function of frequency.

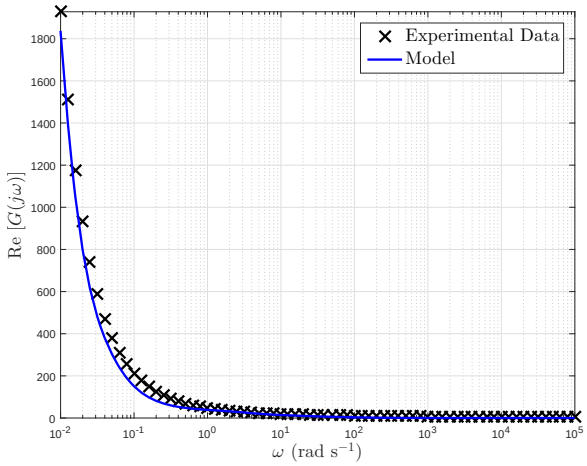


(c) Imaginary component of $G(j\omega)$ as a function of frequency.

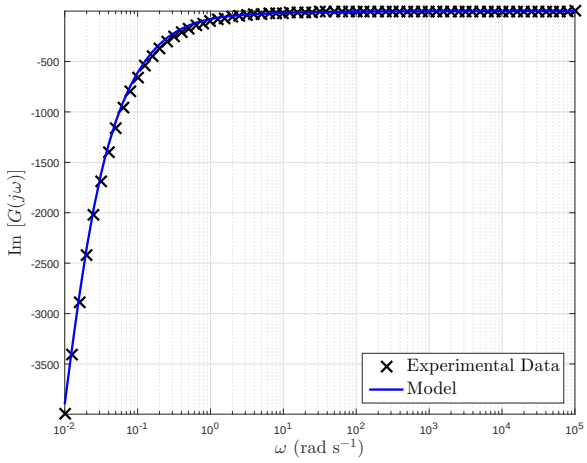
Figure 6.4: Impedance function plots for a supercapacitor with a structured electrode layer length ratio of $8L_1 = L_2$. Both Experimental and model simulation results are shown.



(a) Argand diagram of $G(j\omega)$.

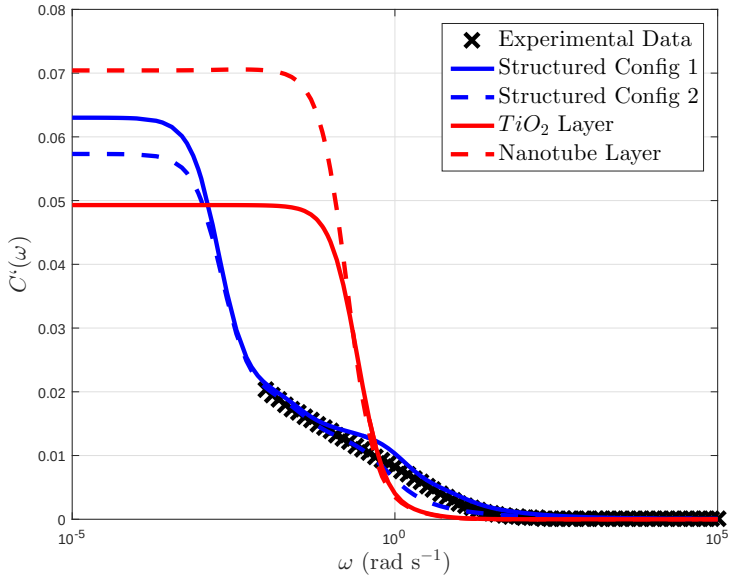


(b) Real component of $G(j\omega)$ as a function of frequency.

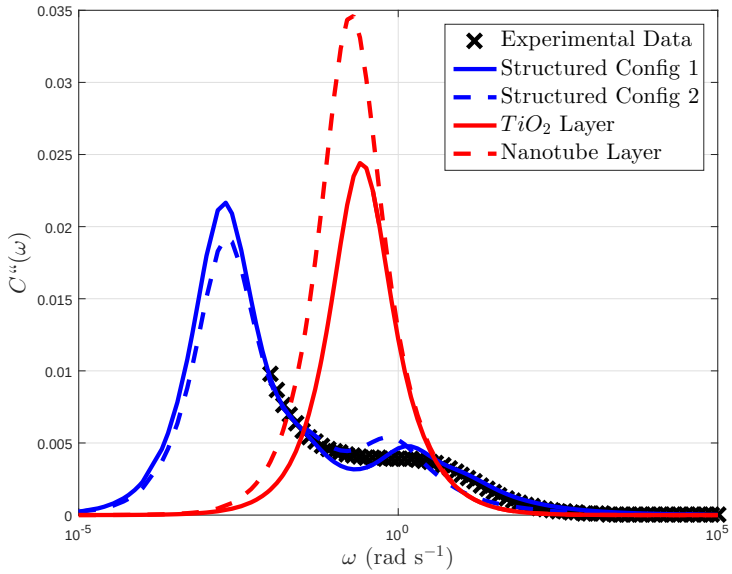


(c) Imaginary component of $G(j\omega)$ as a function of frequency.

Figure 6.5: Impedance function plots for a supercapacitor with a structured electrode layer length ratio of $L_1 = L_2$. Both Experimental and model simulation results are shown.

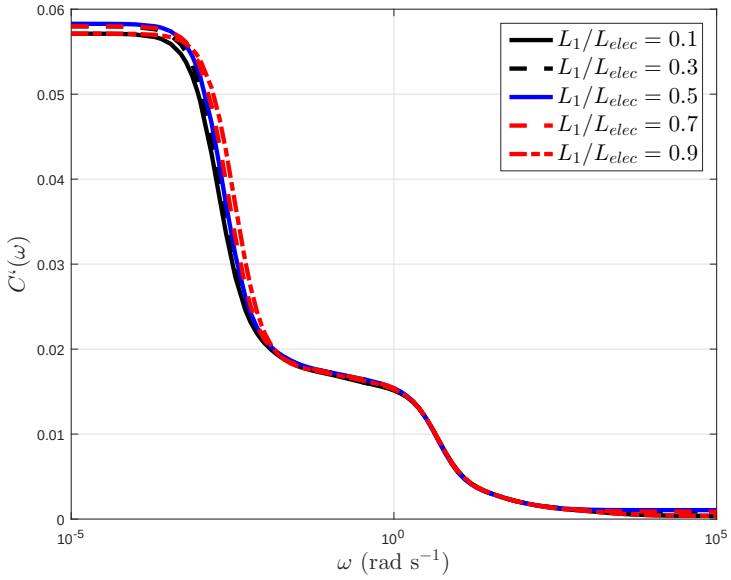


(a) Real capacitance.

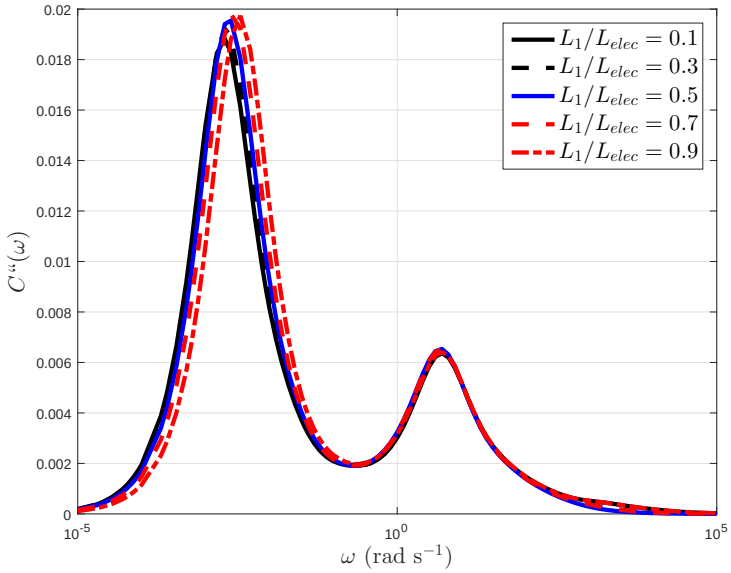


(b) Imaginary capacitance.

Figure 6.6: Capacitances as a function of frequency. Model simulation results are shown for the structured electrodes with a layer length ratio of $L_1 = L_2$. Both spatial configurations of the electrode layers are plotted as well as single layer electrodes composed of each layer material. Experimental data is also shown for the first structured electrode configuration.



(a) Sweep of real capacitance.



(b) Sweep of imaginary capacitance.

Figure 6.7: A sweep of real and imaginary capacitances over the ratio of the structured electrode layers.

6.4 Circuit Representation of Structured Electrodes

To help explain these results, a circuit representation of the structured electrodes is considered. The circuit describes the flow of current through the electrodes, as expressed by Figure 6.8a. The simplest model of a supercapacitor is the "classical" circuit used in Chapter 4 (see Figure 4.1), which has a resistor and capacitor in series with a single RC branch. This circuit is now used as the building block for structured electrode circuits.

6.4.1 Series Circuit

The voltage across a 2-layer structured electrode is the sum of the potential differences across both layers $V_{elec} = V|_{x=0} - V|_{x=L} = V|_{x=0} - V|_{x=L_1} + V|_{x=L_1} - V|_{x=L}$, with a constant current flowing through the electrode. In a circuit notation, this is the series interconnection of two classical circuits, as expressed in Figure 6.8b. The impedance function of a such a series circuit is

$$G(j\omega) = G_1(j\omega) + G_2(j\omega), \tag{6.13}$$

with $G_1(j\omega)$ and $G_2(j\omega)$ being the impedances of each layer, as

$$\frac{V(j\omega)}{I(j\omega)} = \frac{(V|_{x=0} - V|_{x=L_1})(j\omega)}{I(j\omega)} + \frac{(V|_{x=L_1} - V|_{x=L})(j\omega)}{I(j\omega)}. \tag{6.14}$$

6.4.2 Parallel Circuit

A new electrode spatial layering configuration is now proposed, which has not yet been experimentally validated. In this approach, the layering is done in the second spatial dimension, with the layers being perpendicular to those of the original layers. This layer configuration is expressed in Figure 6.9a with its circuit representation being a parallel connection of classical circuits, as expressed by Figure 6.9b. In this parallel configuration, the potential difference across each layer is the same, however the current passing through each layer depends upon the layer's conductivity, with the summation of the layer currents being I, according to $\sum_{k=1}^{m} I_k = I$ where I_k is the current in the k^{th} layer. The impedance function for a 2-layer parallel configuration is

$$G(j\omega) = \frac{G_1(j\omega)G_2(j\omega)}{G_1(j\omega) + G_2(j\omega)} \tag{6.15}$$

when the layer currents are considered.

6.4.3 Circuit Realisations

Using equivalent circuits, the overall resistances and capacitances of these circuits can be obtained. The resistances and capacitances of a series circuit are

$$R_{ser} = R_1 + R_2 \tag{6.16a}$$

$$\frac{1}{C_{ser}} = \frac{1}{C_1} + \frac{1}{C_2} \tag{6.16b}$$

while those of a parallel circuit are

$$\frac{1}{R_{par}} = \frac{1}{R_1} + \frac{1}{R_2} \tag{6.17a}$$

$$C_{par} = C_1 + C_2. \tag{6.17b}$$

Note that the inverse relation, as in (6.16b) and (6.17b), are never greater than their sums. This implies that the parallel layer configuration should be better for a supercapacitor, as it will lead to lower resistances for given values of capacitances.

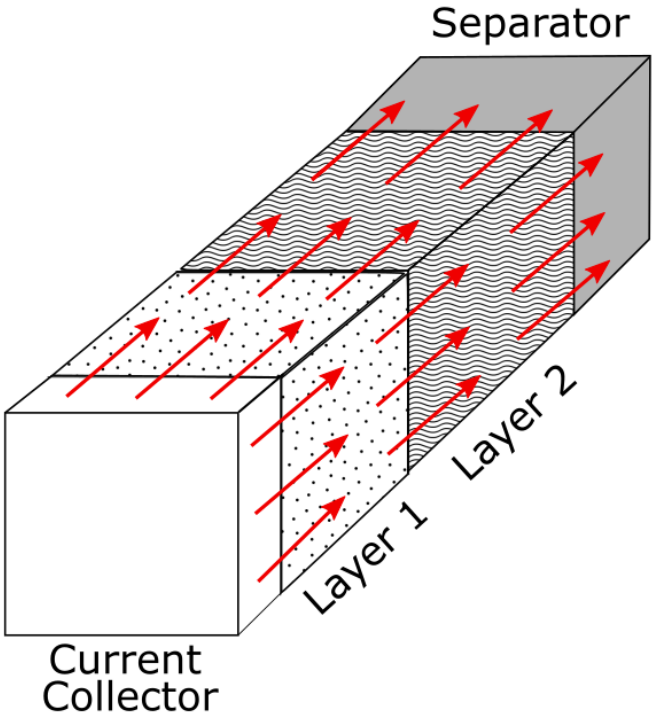
However, this simplified circuit analysis does not explain the experimental data. The real and imaginary capacitances of series and parallel connections of classical circuits are plotted in Figures 6.10a and 6.10b, with the bumps recorded in Figures 6.6a and 6.6b not being captured. The circuit analysis is therefore too simple to fully characterise structured electrodes, with timescales not being captured. The reason for this discrepancy is that the introduction of layers fundamentally changes the distribution profile of ϕ_1 in the electrode and so the impedances $G_1(j\omega)$ and $G_2(j\omega)$ from (6.13) and (6.15) are not the same as the single layer case.

Spatial solutions of $\phi_1(x)$ are now proposed for both the single layer and structured electrodes to highlight this discrepancy. The proposed solutions satisfy the boundary conditions of ϕ_1 but have not yet been verified to be the solutions of the electrochemical PDEs. For the single layer case, the solution

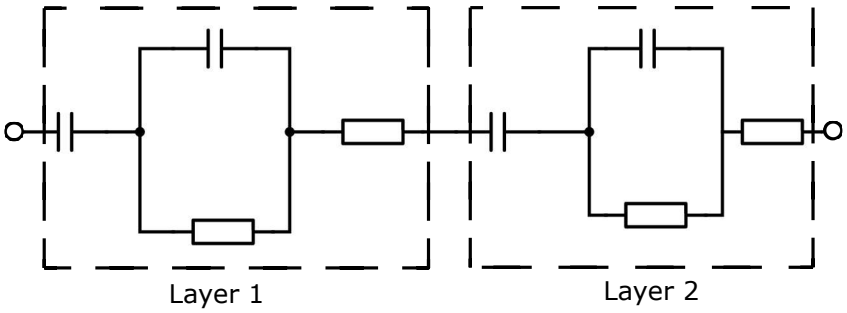
$$\frac{\partial \phi_1(x)}{\partial x} = \frac{i}{\sigma L_{elec}}(x - L_{elec}) \tag{6.18}$$

satisfies the boundary conditions on ϕ_1 given in Table 2.2. Integrating this function with respect to the spatial variable x gives a quadratic distribution of $\phi_1(x)$

$$\phi_1(x) = \frac{i}{2\sigma L_{elec}}x^2 - \frac{i}{\sigma}x + \text{ constant}. \tag{6.19}$$

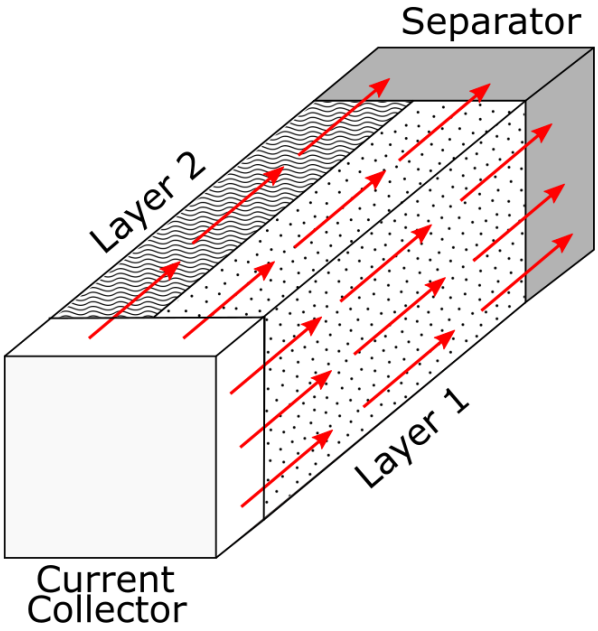


(a) A schematic of a 2-layer structured electrode. Current flow is represented by red arrows.

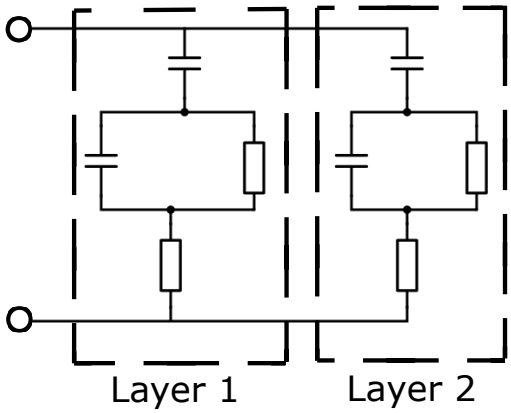


(b) Series circuit representation of the structured electrodes of 6.8a.

Figure 6.8: The circuit realisation of the structured electrode supercapacitor.

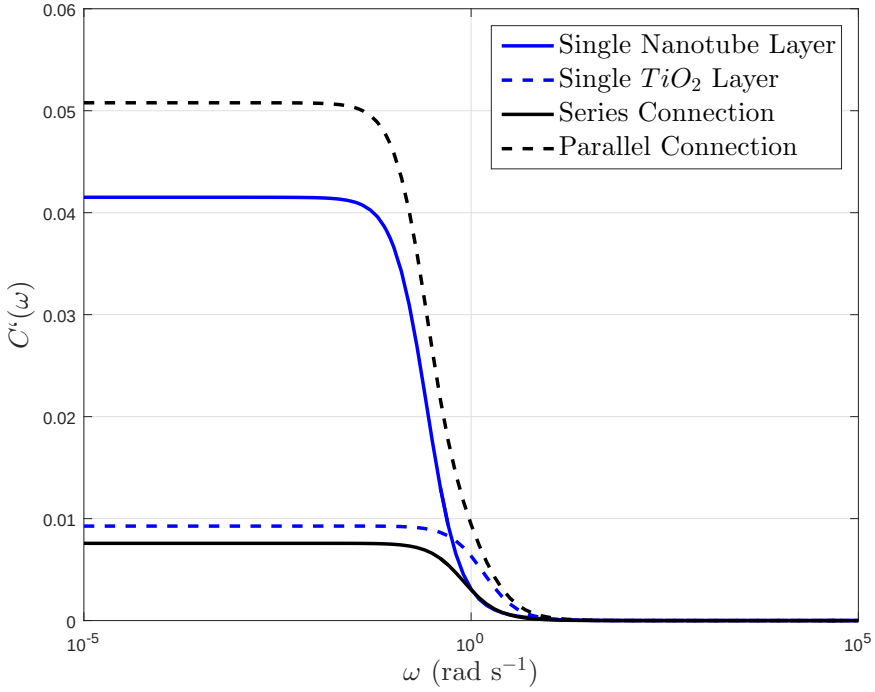


(a) Proposed electrode layers that are perpendicular to those of 6.8a. The flow of current is expressed by red arrows.

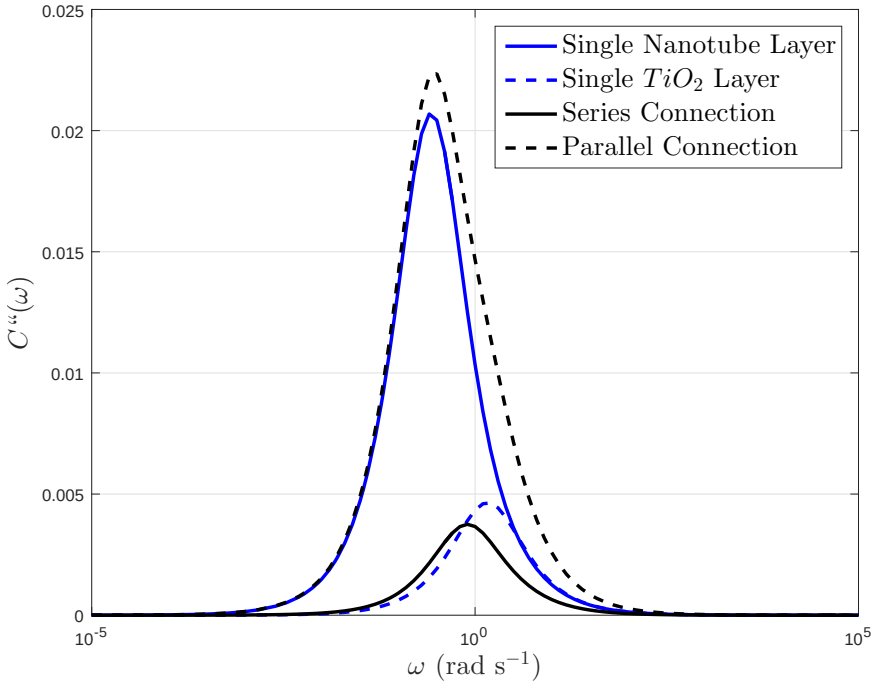


(b) Parallel circuit representation of the structured electrodes of 6.9a.

Figure 6.9: The circuit realisation of the proposed structured electrode supercapacitor with the newly proposed layering.



(a) Real capacitance.



(b) Imaginary capacitance.

Figure 6.10: Real and imaginary capacitances of single layer supercapacitors and their parallel and series interconnections.

For the case of the structured electrodes, the following electropotential gradient distributions satisfy the boundary conditions of Table. 6.2

$$\frac{\partial \phi_{11}(x)}{\partial x} = \frac{i}{\sigma_1 L_1}(x - L_1) + \frac{\sigma_2}{\sigma_1}\frac{x}{L_1}\frac{\partial \phi_{12}(x)}{\partial x}, \tag{6.20a}$$

$$\frac{\partial \phi_{12}(x)}{\partial x} = \frac{\sigma_1}{\sigma_2}\frac{x}{L_1}\left(\frac{L_{elec} - x}{L_{elec} - L_1}\right)\frac{\partial \phi_{11}(x)}{\partial x}, \tag{6.20b}$$

with ϕ_{11} and ϕ_{12} respectively being ϕ_1 in layers one and two. These expressions can be combined to give

$$\frac{\partial \phi_{11}(x)}{\partial x} = \left(1 - \frac{x^2}{L_1^2}\left(\frac{L_{elec} - x}{L_{elec} - L_1}\right)\right)^{-1}\left(\frac{i}{\sigma_1 L_1}(x - L_1)\right), \tag{6.21a}$$

$$\frac{\partial \phi_{12}(x)}{\partial x} = \left(1 - \frac{x^2}{L_1^2}\left(\frac{L_{elec} - x}{L_{elec} - L_1}\right)\right)^{-1}\left(\frac{\sigma_1}{\sigma_2}\frac{i(x - L_1)x}{\sigma_1 L_1}\frac{(L_{elec} - x)}{L_{elec} - L_1}\right). \tag{6.21b}$$

with both terms in the numerator and denominator approaching 0 as $x \to L_1$. This reinforces the notion that the simple action of introducing layers into the electrode fundamentally changes its characteristics and potential distribution. However, these proposed solutions are only spatial distributions of ϕ_1 that satisfy the boundary conditions and do not consider its temporal evolution, and hence it is not immediately clear how they impact upon the impedance function.

The implication of the circuit representation is that introducing layers into the electrode structure is equivalent to connecting different supercapacitors together in a circuit. Moreover, the resulting impedance function of the structured electrode will be proper with degree of the order of the number of layers. In principle, through the appropriate choice of materials, any n^{th} order proper impedance function can then be realised through a structured electrode. This has implications for filter design amongst other applications. By combining many supercapacitors together in the one device through layering might lead to overall weight savings, as less packaging and wiring might, for example, not be required. Also, it implies any combination of parallel and series first order circuits can be realised by a supercapacitor with suitably structured electrodes.

6.5 Conclusion

This chapter has explored the analysis and design of supercapacitors with structured electrodes. A model was proposed for electrodes with such structure, with the main

contribution being the introduction of inter-layer boundary conditions that enforce conservation of current in the electrode and electrolyte as well as flux of ionic concentration. The model parameters were identified using EIS measurements before the model was verified on another set of EIS meaurements for an electrode with a different ratio of electrode layer lengths. Experimental and model predicted real and imaginary capacitances were plotted and compared to those of a single layered electrode. It was found that the introduction of layers via structured electrodes led to "bumps" in the capacitance plots which were not observed in the single layer results. Circuit models based upon parallel and series interconnections of "classical" supercapacitor models were then proposed, however, these circuits could not replicate the form of the experimental results.

This chapter completes the first past of the thesis on the analysis and design of supercapacitors. The remaining part has a shift in tone and develops less conservative conditions for the local analysis of general slope restricted nonlinear systems. An application of these results is the supercapacitor design problem of chapter 5, as the logarithmic nonlinearity of the supercapacitor model satisfies the class of functions considered. Developing less conservative conditions might allow smarter predictions to be made concerning the dissipation of the supercapacitor, giving designers an improved and more representative picture of the true dynamics of the supercapacitor. This will once more speed up the design process, making the design process both smarter and more effective.

Part B

Notation

A new set of notation is introduced for this part so as not to clash with the previous definitions. Adopting the format of control theory, vectors and matrices are no longer denoted in bold. The set of non-negative numbers is denoted $\mathbb{R}_{\geq 0}$. The interior of a set $\mathcal{D} \subset \mathbb{R}^m$ is denoted $\mathcal{D}^\circ$ The norm of a signal is denoted $\|z\| = \sqrt{\int_0^\infty z^T(\theta) z(\theta) \mathrm{d}\theta}$. We define the ρ sublevel set of V by $\mathcal{E}(V, \rho) = \{x \in \mathbb{R}^n \mid V(x) \leq \rho\}$ for $\rho \geq 0$. The interior of a set $\mathcal{D} \subseteq \mathbb{R}^n$ is denoted $\mathcal{D}^\circ$. We drop the arguments of some functions when it is clear from the context. We denote the time-derivative of a function of time, x by $\dot{x}$ and ∂ is used to denote the sub-differential operator.

The set of real valued matrices of dimensions $n \times m$ is denoted $\mathbb{R}^{n \times m}$, the set of symmetric matrices of dimension n is denoted $\mathbb{S}^n$. The set of diagonal matrices is denoted $\mathbb{D}$. The sets of positive semidefinite and positive diagonal matrices are respectively denoted $\mathbb{S}_{\geq 0}$ and $\mathbb{D}_{\geq 0}$. The equivalent positive definite matrices are $\mathbb{S}_{>0}$ and $\mathbb{D}_{>0}$. The Hermitian of a matrix is $He(A) := A + A^T$. I_m denotes the identity matrix of dimension m.The i^{th} row of matrix C will be denoted C_i and the i^{th} element of vector y is denoted y_i.

The ring of polynomials of real coefficients in variables x and ϕ of dimension is denoted $\mathcal{R}^n[x, \phi]$ and the ring of positive sum-of-squares polynomials of dimension n is denoted $\Sigma^n[x, \phi]$. The ring of diagonal sum-of-squares polynomials is $\Sigma_n^{diag}[x, \phi]$. The ring of positive polynomials of dimension n are denoted $\mathcal{R}_{>0}^n[x, \phi]$. For $f \in \mathcal{R}[x]$, $deg(f, x)$ stands for the degree of f on variable x.

Chapter 7

Regional Analysis of Slope Restricted Lur'e Systems

This chapter begins the second part of the thesis, which is concerned with the local stability analysis of general slope restricted nonlinear systems. The supercapacitor model analysed in chapter 5 is a special case of the systems considered here, with the inspiration of the upcoming results being the desire to develop less conservative bounds on the resistance of this model. Developing less conservative resistance bounds will lead to an even more effective design process, with the design predictions being closer to those of the true dynamics. The presented conditions are expressed within the framework of absolute stability theory, a classical problem in control theory. The original problem of absolute stability was formulated by Lur'e and Postnikov [96] which considered the feedback interconnection of a linear system with a generic passive nonlinear operator characterised by sector bounds. The basic idea was to study a wide class of linear systems using tools derived from linear systems theory. This problem inspired a rich body of literature, which is summarised in [61], that broadened the analysis of such systems and reduced the conservatism of the results. A major result in the field is the in the celebrated KYP-lemma [86, 126] that gave stability conditions in terms of the transfer function of the linear system. This condition was equivalent to the existence of a Lyapunov function that was quadratic on the states and also had an integral term on the nonlinearity. The quadratic element of this Lyapunov function characterises the energy of the states while the integral term describes the work down by the nonlinearity. An alternative method was proposed in [182], leading to the Zames-Falb multiplier approach, which guaranteed stability if a suitable multiplier that appropriately shifted the phase of the linear system could be found. For a class of second order multipliers, known as the Park multipliers [42, 177], this search could be

formulated as a convex programming problem that could be efficiently solved [13, 116]. This was achieved by casting the problem as the search for a suitable Lyapunov function that was quadratic with respect to the states and the nonlinearity.

7.1 The Sector Bounded Approach to Absolute Stability

The stability analysis of feedback loops consisting of linear time-invariant systems and sector bounded nonlinearities can be studied via the passivity properties of the elements in the interconnection. These properties can be verified via a graphical approach using the Circle and Popov criteria [89] for SISO systems, where the key assumption is that the nonlinearity exists in a sector. The assumption that the nonlinearity is sector bounded might be overly conservative whenever the nonlinearities are known or their slopes can be bounded. The study of the class of slope-restricted nonlinear systems using the framework of absolute stability theory was first proposed in two papers; a frequency domain condition given in [41] and a geometrical condition based upon the construction of a Lyapunov function (LF) in [177]. It is noted that several positivity conditions on the LF were relaxed in [177]. Approaches that study these class of nonlinearities have been recently proposed in [20, 54, 116, 158].

In addition to the Lyapunov functions associated with the Circle and Popov criteria, different LF's have been proposed for studying Lur'e systems: composite LFs [70]; LFs with the quadratic components with respect to both the nonlinearities and the states and Lur'e terms were studied in [116, 150, 158]. For quadratic LFs associated with the Circle criterion, the positivity of the LF is enforced with a positive-definite Lyapunov matrix [89]. In the case of LF's with a Lur'e type term, which are associated with the Popov criterion, the positivity of the LF requires the positivity of the Lyapunov matrix, but does not necessarily impose the positivity of the Lur'e integral terms coefficients [66, 115].

For the case of nonlinearities that are sector and slope bounded in a set containing the origin, it is often of interest to obtain *local* certificates for gains, reachable sets and estimates of the basin of attraction. This provides tighter results and allows unbounded nonlinearities to be studied. Examples of systems modeled with unbounded nonlinearities include the driven Stirling engine [64] and the logarithmic supercapacitor model [46]. Estimates of region of attraction for sector bound nonlinear systems

obtained with the Popov criterion have been considered in [132, 167, 170], and more recently in [69] using Semi-Definite Programming (SDP).

For global stability analysis, frequency domain methods that include a multiplier into the feedback loop, have been shown to improve results at the expense of computational complexity. The most famous example of such frequency-based methods are the multipliers of Zames and Falb [182] and their computational implementation [131]. A recent review on the contribution of the works of O'Shea [113] and Zames & Falb [182] is given in [21]. For systems with multiple slope restricted nonlinearities, a frequency domain criterion generalizing previous results for SISO systems and the associated multipliers has been presented in [62].

7.1.1 Contribution

The results of this chapter focus on the local analysis of Lur'e type systems with slope-restricted nonlinearities. LFs that are quadratic in both the state and the nonlinear terms and contain a Lur'e integral term are developed. Conditions are presented for the positivity of the LF that *do not impose* the positivity of the Lur'e terms coefficients nor require that the quadratic terms on the nonlinearities are positive definite. Connections between these results and recent results in the literature that use similar LF structures are also presented.

The conditions verify dissipation inequalities that rely on inequalities associated with the sector and the slope bounds. In cases where the sector inequalities hold only locally, inclusion conditions are given to guarantee the inclusion of level sets in the region where the sector inequalities hold. These inclusion conditions allow an estimate of the region of attraction to be obtained using contractive and invariant sets defined by the level sets of the computed LF. This enables the effect of additive exogenous inputs and outputs to be studied, allowing us to derive conditions for the computation of reachable sets and local induced gains. The constraints of the convex optimization formulation are highlighted and the results are evaluated with numerical examples.

7.2 Problem statement

Consider the linear time-invariant (LTI) system with input nonlinearities

$$\begin{cases} \dot{x} &= Ax + B\phi(y) + B_w w \\ y &= Cx + D\phi(y) + D_w w \\ z &= C_z x + D_z \phi(y) + D_{zw} w \end{cases} \tag{7.1}$$

with $x \in \mathbb{R}^n$, $y \in \mathbb{R}^m$, $w \in \mathbb{R}^{m_w}$.

The nonlinearity $\phi : \mathcal{Y} \to \mathbb{R}^m$, $\mathcal{Y} \subseteq \mathbb{R}^m$, is assumed to be *time-invariant*, Lipschitz on $\mathcal{Y}^\circ$, *decentralized*

$$\phi(y) = [\phi_1(y_1) \quad \phi_2(y_2) \quad \dots \phi_m(y_m)]^T, \tag{7.2a}$$

sector bounded

$$\frac{\phi_i(y_i)}{y_i} \in [\underline{\delta}_i, \overline{\delta}_i] \quad \forall y \in \mathcal{Y}_0 \subseteq \mathcal{Y} \tag{7.2b}$$

which implies $\phi(0) = 0$, and *slope restricted*

$$\partial\phi_i(y_i) \in [\underline{\gamma}_i, \overline{\gamma}_i] \quad \forall y \in \mathcal{Y}_0 \subseteq \mathcal{Y}. \tag{7.2c}$$

where $\underline{\gamma}_i \leq \underline{\delta}_i$ and $\overline{\delta}_i \leq \overline{\gamma}_i$. We also introduce the matrices $\underline{\Delta} := diag(\underline{\delta}_1, \dots, \underline{\delta}_m)$, $\overline{\Delta} := diag(\overline{\delta}_1, \dots, \overline{\delta}_m)$ $\underline{\Gamma} := diag(\underline{\gamma}_1, \dots, \underline{\gamma}_m)$, $\overline{\Gamma} := diag(\overline{\gamma}_1, \dots, \overline{\gamma}_m)$ to compactly express the sector and slope bounds. The Lipschitz assumption on ϕ implies that $\partial\phi_i(y_i) = \frac{d\phi_i}{dy_i}$ almost everywhere, relaxing the requirement for the nonlinearity to be continuously differentiable [158, Section 2].

The well posedness of the algebraic loop in (7.1) is guaranteed if there exists a unique solution to the implicit equation $F(\mu) := \mu - D\phi(\mu) = \nu$, that is, a mapping $\mu(\nu)$ satisfying $F(\mu(\nu)) = \nu$. Following [180, Claim 1], for functions ϕ that are differentiable almost everywhere, the well-posedness of the loop is obtained if $JF(\mu)$, the Jacobian of F, belongs to a compact and convex set of invertible matrices for almost all values of μ (see [180, Proposition 2]). If the assumption below holds, then the above conditions on the Jacobian are satisfied.

Assumptions 7.1 (Well-posedness)**.** *There exists a matrix* $W \in \mathbb{D}^m_{\geq 0}$ *such that*

$$2W - He(W(I - D\underline{\Gamma})^{-1}D(\overline{\Gamma} - \underline{\Gamma})) > 0. \tag{7.3}$$

The assumption clearly holds for $D = 0$. For the special case of the deadzone nonlinearity, with $\phi(y) = dz(y)$, conditions to verify whether the above assumption holds

were presented in [71]. We now show that the general condition that well-posedness of Lur'e systems of the form (7.1) exists provided (7.3) holds. The only difference to the reasoning presented in [180, Proposition 2] is given by conditions related to the non-singularity of the Jacobian of $F(\mu)$.

The Jacobian of $F(\mu)$ is given by $JF(\mu) = I - D\partial\phi(\mu)$ a.e.. Thanks to the slope restriction of $\phi(\mu)$ in (7.2c), for almost all μ, $JF(\mu) \in \mathcal{M} := \overline{co}(\{I - D\Gamma, \Gamma \in \mathcal{G}\})$, where

$$\mathcal{G} := \left\{\Gamma \in \mathbb{D} : \Gamma = diag(\gamma_1, \gamma_2, \ldots, \gamma_m), \gamma_i \in \left[\underline{\gamma}_i, \overline{\gamma}_i\right], \forall i\right\}$$

and $\overline{co}(\mathcal{A})$ denotes the closed convex hull of the set $\mathcal{A}$. From the above description we have that the set $\mathcal{M}$ is convex and compact, the proposition below sets conditions for the matrices in the set $\mathcal{M}$ to be nonsingular, thus guaranteeing that the solution to the algebraic loop exists and is unique.

Proposition 7.1. *Given a matrix $D \in \mathbb{R}^{m\times m}$, if there exists a matrix $W \in \mathbb{D}^m_{\geq 0}$ such that $2W - W(I - D\underline{\Gamma})^{-1}D(\overline{\Gamma} - \underline{\Gamma}) - (\overline{\Gamma} - \underline{\Gamma})D^TW((I - D\underline{\Gamma})^{-1})^T > 0$ then $I - D\Gamma$ is nonsingular for all matrices Γ belonging to the set $\mathcal{G}$.*

Proof. If $(I - D\Gamma)$ is singular then there exists $z \in \mathbb{R}^m$, $z \neq 0$ such that $0 = (I - D\Gamma)z = ((I - D\underline{\Gamma}) - D(\Gamma - \underline{\Gamma}))z = (I - D\underline{\Gamma})z - D(\overline{\Gamma} - \underline{\Gamma})(\overline{\Gamma} - \underline{\Gamma})^{-1}(\Gamma - \underline{\Gamma}))z$. Define $\bar{z} = (\overline{\Gamma} - \underline{\Gamma})^{-1}(\Delta - \underline{\Gamma}))z$ to obtain

$$(I - D\underline{\Gamma})\left[z - (I - D\underline{\Gamma})^{-1}D(\overline{\Gamma} - \underline{\Gamma})\bar{z}\right] = 0.$$

Multiply the above expression on the left by $\bar{z}^TW(I - D\underline{\Gamma})^{-1}$, to obtain

$$\bar{z}^TWz - \bar{z}^TW(I - D\underline{\Gamma})^{-1}D(\overline{\Gamma} - \underline{\Gamma})\bar{z} = 0.$$

Since $1 \geq (\overline{\gamma}_i - \underline{\gamma}_i)^{-1}(\delta_i - \underline{\gamma}_i) \geq 0$ we have $\bar{z}^TWz = z^T(\overline{\Gamma} - \underline{\Gamma})^{-1}(\Gamma - \underline{\Gamma})Wz \geq z^T(\overline{\Gamma} - \underline{\Gamma})^{-2}(\Gamma - \underline{\Gamma})^2Wz = \bar{z}^TW\bar{z}$. Thus, if $(I - D\Gamma)$ is singular we must have

$$\bar{z}^T\left(W - \frac{1}{2}He(\bar{z}^TW(I - D\underline{\Gamma})^{-1}D(\overline{\Gamma} - \underline{\Gamma}))\right)\bar{z} \leq 0,$$

which contradicts the inequality of the claim. Hence if the inequality in the claim holds the matrix $(I - D\Gamma)$ is non-singular for any $\Gamma \in \mathcal{G}$. □

Provided Assumption 7.1 holds, the following set can be defined

$$\mathcal{X}_0 := \{x \in \mathbb{R}^n \mid y(x) \in \mathcal{Y}_0\}, \tag{7.4}$$

where $\mathcal{Y}_0 \subseteq \mathcal{Y} \subseteq \mathbb{R}^m$ corresponds to the set where the sector and the slope restrictions hold, as defined in (7.2). Under Assumption 7.1, this chapter provides a solution to the following problem:

Problem 7.1. *For system* (7.1) *with* ϕ *satisfying* (7.2)*:*

a) certify the stability of the origin with an estimate of the region of attraction (ERA) contained in $\mathcal{X}_0$*;*

b) compute reachable sets for bounded disturbances satisfying $\|w\|_2 \leq \rho^{\frac{1}{2}}$*;*

c) compute the (local) induced $\mathcal{L}_2$ *gains between* w *and* z*.*

Global properties will be obtained by setting $\mathcal{X}_0 = \mathbb{R}^n$.

7.3 Sector inequalities

In this section, inequalities related to the sector and slope bounds of the nonlinearities in system (7.1) are presented. These inequalities are required for assessing the positivity of quadratic-like expressions.

Define $s_1 : \mathbb{R}^{m\times m} \times \mathbb{R}^m \times \mathbb{R}^m \to \mathbb{R}$, $s_2 : \mathbb{R}^{m\times m} \times \mathbb{R}^m \times \mathbb{R}^m \to \mathbb{R}$, $s_3 : \mathbb{R}^{m\times m} \times \mathbb{R}^m \times \mathbb{R}^m \times \mathbb{R}^m \times \mathbb{R}^m \to \mathbb{R}$ as

$$\begin{aligned} s_1(T,\phi,\theta) &:= (\phi - \underline{\Delta}\theta)^T T \left(\overline{\Delta}\theta - \phi\right) \\ s_2(T,\phi,\theta) &:= (\phi - \underline{\Gamma}\theta)^T T \left(\overline{\Gamma}\theta - \phi\right) \\ s_3(T,\phi_1,\phi_2,\theta_1,\theta_2) &:= \left((\phi_1-\phi_2) - \underline{\Gamma}\left(\theta_1-\theta_2\right)\right)^T \times T \left(\overline{\Gamma}\left(\theta_1-\theta_2\right) - (\phi_1-\phi_2)\right). \end{aligned}$$

The following lemma is associated with the sector boundedness of the functions ϕ_i.

Lemma 7.1. *If* $T_1 \in \mathbb{D}^m_{\geq 0}$ *is a diagonal matrix of size* m *with strictly non-negative terms and* $\phi : \mathbb{R}^m \to \mathbb{R}^m$ *satisfies* (7.2)*, then*

$$s_1(T_1, \phi(\theta), \theta) \geq 0 \tag{7.5}$$

for all $\theta \in \mathcal{Y}_0$.

Proof. For $T_1 \in \mathbb{D}^m$ we have $s_1(T_1,\phi(\theta),\theta) = \sum_{i=1}^m T_{1(i,i)} \left(\phi_i(\theta) - \underline{\delta}_i\theta_i(x)\right)\left(\overline{\delta}_i\theta_i(x) - \phi_i(\theta_i)\right)$. If ϕ satisfies (7.2a), (7.2b), we have $\left(\frac{\phi_i(\theta)}{\theta} - \underline{\delta}_i\right)\left(\overline{\delta}_i - \frac{\phi_i(\theta)}{\theta}\right) \geq 0$, which, when multiplied by θ^2 gives $\left(\phi_i(\theta) - \underline{\delta}_i\theta\right)\left(\overline{\delta}_i\theta - \phi_i(\theta)\right) \geq 0$, $i = 1,\ldots,m$ for $\theta \in \mathcal{Y}_0$. Since $T_{1(i,i)} \geq 0$, and (7.2) hold then (7.5) holds for all $\theta \in \mathcal{Y}_0$. □

In the following two lemmas, $\theta : [0,\infty) \to \mathcal{Y}_0$, $\theta(t) \in \mathcal{C}^1(t)$ is used to obtain inequalities for the slope restrictions of ϕ.

Lemma 7.2. *If $T_2 \in \mathbb{D}^m_{\geq 0}$ and $\phi : \mathbb{R}^m \to \mathbb{R}^m$ satisfies* (7.2)*, then*

$$s_2(T_2, \dot{\phi}(\theta), \dot{\theta}) \geq 0 \tag{7.6}$$

for all $\theta \in \mathcal{Y}_0$.

Proof. From (7.2c), it follows that $(\partial\phi_i(\theta) - \underline{\gamma}_i)(\overline{\gamma}_i - \partial\phi_i(\theta)) \geq 0$. Multiplying this expression by $\dot{\theta}^2$, gives

$$\begin{aligned} 0 &\leq \dot{\theta}^2 \left(\partial\phi_i(\theta) - \underline{\gamma}_i\right)(\overline{\gamma}_i - \partial\phi_i(\theta)) \\ &= \left(\partial\phi_i(\theta)\dot{\theta} - \underline{\gamma}_i\dot{\theta}\right)\left(\overline{\gamma}_i\dot{\theta} - \partial\phi_i(\theta)\dot{\theta}\right) \\ &= \left(\dot{\phi}_i(\theta) - \underline{\gamma}_i\dot{\theta}\right)\left(\overline{\gamma}_i\dot{\theta} - \dot{\phi}_i(\theta)\right). \end{aligned} \tag{7.7}$$

For $T_2 \in \mathbb{D}^m_{\geq 0}$ we have $s_2(T_2, \dot{\phi}(\theta), \dot{\theta}) = \sum_{i=1}^m T_{2(i,i)}\left(\dot{\phi}_i(\theta) - \underline{\gamma}_i\dot{\theta}_i(x)\right)\left(\overline{\gamma}_i\dot{\theta}_i(x) - \dot{\phi}_i(\theta_i)\right)$, and, from (7.7) then (7.6) holds. □

Lemma 7.3. *If $T_3 \in \mathbb{D}^m_{\geq 0}$ and $\phi : \mathbb{R}^m \to \mathbb{R}^m$ satisfies* (7.2c)*, then*

$$s_3(T_3, \phi(\theta_1), \phi(\theta_2), \theta_1, \theta_2) \geq 0 \tag{7.8}$$

for all $\theta_1, \theta_2 \in \mathcal{Y}_0$.

Proof. For $i = 1, \ldots, m$, define $\hat{\phi}_{i1}(u) := (\phi_i(\theta) - \underline{\gamma}_i\theta)$, $\hat{\phi}_{i2}(\theta) := (\overline{\gamma}_i\theta - \phi_i(\theta))$. Provided (7.2c) holds, then $\hat{\phi}_{1i}$, $\hat{\phi}_{2i}$ satisfy $\partial_\theta\hat{\phi}_{1i}(\theta) \geq 0$, $\partial_\theta\hat{\phi}_{2i}(\theta) \geq 0$, so that, for any $\theta_1, \theta_2 \in \mathcal{Y}_0$,

$$\frac{\hat{\phi}_{ji}(\theta_1) - \hat{\phi}_{ji}(\theta_2)}{\theta_1 - \theta_2} \geq 0. \tag{7.9}$$

For $T_3 \in \mathbb{D}^m_{\geq 0}$ we have

$$\begin{aligned} &s_3(T_3, \phi(\theta_1), \phi(\theta_2), \theta_1, \theta_2) \\ &\quad= \sum_{i=1}^m T_{3(i,i)}\left((\phi_i(\theta_1) - \phi_i(\theta_2)) - \underline{\gamma}_i(\theta_{1i} - \theta_{2i})\right) \\ &\qquad\qquad \times (\overline{\gamma}_i(\theta_{1i} - \theta_{2i}) - (\phi_i(\theta_1) - \phi_i(\theta_2))) \\ &\quad= \sum_{i=1}^m T_{3(i,i)}\left(\hat{\phi}_{1i}(\theta_1) - \hat{\phi}_{1i}(\theta_2)\right)\left(\hat{\phi}_{2i}(\theta_1) - \hat{\phi}_{2i}(\theta_2)\right) \\ &\quad= \sum_{i=1}^m T_{3(i,i)}(\theta_{1i} - \theta_{2i})^2\left(\tfrac{\hat{\phi}_{1i}(\theta_1) - \hat{\phi}_{1i}(\theta_2)}{\theta_{1i} - \theta_{2i}}\right) \\ &\qquad\qquad \times \left(\tfrac{\hat{\phi}_{2i}(\theta_1) - \hat{\phi}_{2i}(\theta_2)}{\theta_{1i} - \theta_{2i}}\right). \end{aligned}$$

Since $T_{3(i,i)} \geq 0$ and (7.9) hold, then (7.8) holds. □

The above lemma shows that the slope restriction with non-negative bounds satisfies the *incremental sector boundedness property* [183, Definition 1].

7.4 Main results

This section is concerned with Lyapunov functions of the form

$$V(x) = V_0(x) + \sum_{i=1}^{m} \lambda_i \int_0^{\tilde{y}_i(x)} (\phi_i(s) - \underline{\delta}_i s)\ ds, \tag{7.10a}$$

where

$$V_0(x) = \begin{bmatrix} x \\ \phi(\tilde{y}(x)) \end{bmatrix}^T \begin{bmatrix} P_{11} & P_{12} \\ P_{12}^T & P_{22} \end{bmatrix} \begin{bmatrix} x \\ \phi(\tilde{y}(x)) \end{bmatrix}. \tag{7.10b}$$

and $\tilde{y}$ is the the solution of

$$\tilde{y}(x) = Cx + D\phi(\tilde{y}(x)). \tag{7.11}$$

The integral terms in (7.10a) are referred to as the Lur'e terms. For the sake of compactness of notation, $\tilde{\phi}$ is used to denote $\phi(\tilde{y}(x))$. One way to enforce the positivity of $V(x)$ is to impose $P := \left[\begin{smallmatrix} P_{11} & P_{12} \\ P_{12}^T & P_{22} \end{smallmatrix}\right] > 0$ and $\lambda_i \geq 0$, as discussed in [158] and also in [165] for the case $P_{12} = 0$, $P_{22} = 0$. When $P_{12} = 0$, $P_{22} = 0$, the relaxation of the non-negativity of the coefficients λ_i was considered in [1, 66, 115].

Define $\Lambda := diag(\lambda_1, \ldots, \lambda_m)$ which is used in the following lemma that gives conditions for the positivity of V without imposing positive-definiteness of P, nor the non-negativity of the coefficients λ_i.

Lemma 7.4. *Consider V in (7.10) where ϕ satisfies (7.2a)-(7.2b) and Assumption 7.1 holds. If there exists a matrix $\tilde{\Lambda} \in \mathbb{D}_{\geq 0}^m := diag(\tilde{\lambda_1}, \ldots, \tilde{\lambda_m})$ such that*

$$\Lambda \geq -\tilde{\Lambda} \tag{7.12a}$$

$$V_0(x) - \frac{1}{2}\tilde{y}^T(x)(\overline{\Delta} - \underline{\Delta})\tilde{\Lambda}\tilde{y}(x) > 0,\ \forall x \in \mathcal{X}_0, \tag{7.12b}$$

then $V(x) > 0$, $\forall x \in \mathcal{X}_0 \subset \mathbb{R}^n$.

Proof. Use (7.12a) to obtain a positive-definite lower bound for (7.10a) as follows. If Assumption 7.1 holds, the mapping $\tilde{y} : \mathcal{X}_0 \to \mathcal{Y}_0$ is well defined. We can then prove that $V(x)$ is positive-definite in $\mathcal{X}_0$ by obtaining a positive-definite lower bound as

follows

$$
\begin{aligned}
V(x) &= V_0(x) + \textstyle\sum_{i=1}^m \lambda_i \int_0^{\tilde{y}_i(x)} (\phi_i(s) - \underline{\delta}_i s) ds \\
&\geq V_0(x) - \textstyle\sum_{i=1}^m \tilde{\lambda}_i \int_0^{\tilde{y}_i(x)} (\phi_i(s) - \underline{\delta}_i s) ds \\
&= V_0(x) - \tfrac{1}{2}\tilde{y}^T(x)(\overline{\Delta} - \overline{\Delta})\tilde{\Lambda}\tilde{y}(x) \\
&\qquad - \textstyle\sum_{i=1}^m \tilde{\lambda}_i \int_0^{\tilde{y}_i(x)} (\phi_i(s) - \underline{\delta}_i s) ds \\
&= V_0(x) - \tfrac{1}{2}\tilde{y}^T(x)(\overline{\Delta} - \overline{\Delta} - \underline{\Delta})\tilde{\Lambda}\tilde{y}(x) \\
&\qquad - \textstyle\sum_{i=1}^m \tilde{\lambda}_i \int_0^{\tilde{y}_i(x)} \phi_i(s) ds \\
&= V_0(x) - \tfrac{1}{2}\tilde{y}^T(x)(\overline{\Delta} - \underline{\Delta})\tilde{\Lambda}\tilde{y}(x) \\
&\qquad + \textstyle\sum_{i=1}^m \tilde{\lambda}_i \int_0^{\tilde{y}_i(x)} ((\overline{\delta}_i s - \phi_i(s)) ds \\
&= \underbrace{V_0(x) - \frac{1}{2}\tilde{y}^T(x)(\overline{\Delta} - \underline{\Delta})\tilde{\Lambda}\tilde{y}(x)}_{>0 \text{ from (7.12b)}} \\
&\qquad + \underbrace{\sum_{i=1}^m \tilde{\lambda}_i \int_0^{\tilde{y}_i(x)} (\overline{\delta}_i s - \phi_i(s)) ds}_{\geq 0 \text{ from } \tilde{\Lambda} \geq 0 \text{ and (7.2b)}}.
\end{aligned}
\tag{7.13}
$$

□

The following theorem presents conditions for the stability of the origin of Lur'e system (7.1) with slope-restricted nonlinearities:

Theorem 7.1. *For nonlinearities ϕ satisfying* (7.2) *if there exists a matrix $P \in \mathbb{R}^{(n+m)\times(n+m)}$, matrices $\Lambda \in \mathbb{D}^m$, $\tilde{\Lambda}$, $T_j \in \mathbb{D}^m_{\geq 0}$, $j \in \{0, \ldots, 4\}$, and a scalar $\rho > 0$ such that* (7.12a) *holds,*

$$
V_0(x) - \frac{1}{2}\tilde{y}^T(x)(\overline{\Delta} - \underline{\Delta})\tilde{\Lambda}\tilde{y}(x) - s_1(T_0, \tilde{\phi}, \tilde{y}(x)) > 0 \tag{7.14a}
$$

$\forall x \in \mathbb{R}^n,\ \tilde{\phi} \in \mathbb{R}^m,$

$$
\begin{aligned}
-\left\langle \begin{bmatrix} \nabla_x V \\ \nabla_{\tilde{\phi}} V \end{bmatrix}, \begin{bmatrix} \dot{x} \\ \dot{\tilde{\phi}} \end{bmatrix} \right\rangle &- \Psi(z, w) - s_1(T_1, \tilde{\phi}, \tilde{y}(x)) \\
&- s_1(T_2, \phi, y(x, w)) - s_2(T_3, \dot{\tilde{\phi}}, \dot{\tilde{y}}(\dot{\tilde{\phi}}, x, \phi, w)) \\
&- s_3(T_4, \tilde{\phi}, \phi, \tilde{y}(x), y(x, w)) > 0
\end{aligned}
\tag{7.14b}
$$

$\forall x \in \mathbb{R}^n,\ \phi \in \mathbb{R}^m,\ \tilde{\phi} \in \mathbb{R}^m,\ \dot{\tilde{\phi}} \in \mathbb{R}^m,\ w \in \mathbb{R}^{m_w}$ *and*

$$
\mathcal{E}(V, \rho) \subseteq \mathcal{X}_0 \tag{7.14c}
$$

hold with

a) $\Psi \equiv 0$ *and* $w \equiv 0$ *(which gives* $\tilde{\phi} = \phi$ *so that* $s_3 \equiv 0$ *and allows us to set* $T_2 = 0$*);*

b) $\Psi(z,w) = -w^T w$;

c) $\Psi(z,w) = -w^T w + \eta^2 z^T z$;

then

a) (stability) the origin of (7.1) *is locally asymptotically stable and* $\mathcal{E}(V,\rho)$ *is an estimate of its region of attraction. In the case* $\mathcal{X}_0 = \mathbb{R}^n$*, the origin is globally asymptotically stable.*

b) (reachable set) $x_0 = 0$ *and* $\|w\|_2 \leq \rho^{\frac{1}{2}}$ *so that* $x(t) \in \mathcal{E}^\circ(V,\rho)$ *for all* $t \geq 0$;

c) (local finite $\mathcal{L}_2$*-gain)* $x_0 = 0$ *and* $\|w\|_2 \leq \rho^{\frac{1}{2}}$ *imply* $\|w\|_2 \leq \eta\|z\|_2$*, that is, the induced* $\mathcal{L}_2$ *gain from* w *to* z *is bounded by* η *for every input satisfying* $\|w\|_2 \leq \rho^{\frac{1}{2}}$.

Proof. If (7.14a) holds,

$$V_0(x) - \frac{1}{2}\tilde{y}^T(x)(\overline{\Delta} - \underline{\Delta})\tilde{\Lambda}\tilde{y}(x) > s_1(T_0, \tilde{\phi}, \tilde{y}(x))$$

from Lemma 7.1 and $s_1(T_0, \phi(\tilde{y}), \tilde{y}) \geq 0$ holds for all $x \in \mathcal{X}_0$, thus (7.12b) holds. Following Lemma (7.4) if (7.12a) also holds, then $V(x) \geq 0,\ \forall x \in \mathcal{X}_0$.

$\dot{V}(x, \tilde{\phi}, \dot{\tilde{\phi}}, \phi, w)$ is used to express the time-derivative of $V(x)$ along the trajectories of (7.1)

$$\dot{V}(x, \tilde{\phi}, \dot{\tilde{\phi}}, \phi, w) = \left\langle \begin{bmatrix} \nabla_x V \\ \nabla_{\tilde{\phi}} V \end{bmatrix}, \begin{bmatrix} Ax + B\phi + B_w w \\ \dot{\tilde{\phi}} \end{bmatrix} \right\rangle.$$

From (7.14b) we have

$$\begin{aligned} -\dot{V}(x, \tilde{\phi}, \dot{\tilde{\phi}}, \phi, w) - \Psi(z,w) > s_1(T_1, \tilde{\phi}, \tilde{y}(x, \tilde{\phi})) \\ + s_1(T_2, \phi, y(x, \phi, w)) + s_2(T_3, \dot{\tilde{\phi}}, \dot{\tilde{y}}(x, \dot{\tilde{\phi}}, \phi, w)) \\ + s_3(T_4, \tilde{\phi}, \phi, \tilde{y}(x, \tilde{\phi}), y(x, \phi, w)). \end{aligned}$$

If (7.2) holds, the relations in Lemmas 7.1-7.3 give

$$-\dot{V}(x, \tilde{\phi}, \dot{\tilde{\phi}}, \phi, w) - \Psi(z,w) > 0,\ \forall x \in \mathcal{X}_0. \tag{7.15}$$

Thus if

a) $\Psi(z,w) \equiv 0$, we have that $\dot{V}$ is negative for all $x \in \mathcal{X}_0$. Since from (7.14c) the time-derivative of V is negative along the trajectories of system (7.1) provided the sector inequalities hold, that is, provided the trajectories belong to the set $\mathcal{X}_0$ which, from (7.14c) contains the set $\mathcal{E}(V,\rho)$. Following [89, Theorem 4.1],

with (7.14a) and (7.14b) that hold in the sublevel set, $\mathcal{E}(V,\rho)$ is an invariant and contractive set and hence provides an estimate of the region of attraction of (7.1).

b) $\Psi(z,w) = -w^T w$, $x_0 = 0$, integrate (7.15) from 0 to t^* to obtain $\int_0^{t^*} w^T(\tau)w(\tau)\mathrm{d}\tau > V(t^*)$ since $V(0) = 0$. Hence, provided $\|w\|_2^2 = \int_0^{t^*} w^T(\tau)w(\tau)\mathrm{d}\tau \leq \rho$ we have that $x(t^*) \in \mathcal{E}^\circ(V(x),\rho)$. From (7.14c) the sector inequalities hold so (7.14a) and (7.14b) hold.

c) $\Psi(z,w) = -w^T w + \eta z^T z$ and $x_0 = 0$, integrate from 0 to t^* to obtain $\int_0^{t^*} w^T(\tau)w(\tau)\mathrm{d}\tau > \int_0^{t^*} \eta z^T(\tau)z(\tau)\mathrm{d}\tau + V(x(t^*))$. Since $V(t^*) \geq 0$, then $\|w\|_2^T \leq \eta \|z\|_2^T$ for any $t^* \in [0,\infty)$. From $\|w\|_2 \leq \rho^{\frac{1}{2}}$ and $\int_0^{t^*} \eta z^T(\tau)z(\tau)\mathrm{d}\tau \geq 0$ the above inequality implies $V(x(t^*)) < \rho$, thus from (7.14c) we have $x(t^*) \in \mathcal{X}_0$ for any $t^* \in [0,\infty)$, hence (7.14a) and (7.14b) hold for $\|w\|_2 \leq \rho^{\frac{1}{2}}$.

□

Note that the set inclusion (7.14c) is required to guarantee that the sector inequalities in Lemmas 7.1-7.3 hold so that (7.14b) implies (7.15). However, for $D_w \neq 0$ and disturbances w only assumed to satisfy $\|w\|_2^2 \leq \rho$, the fact that $\tilde{y} \in \mathcal{Y}_0$, solution to (7.11), for all $t \geq 0$ does not necessarily imply that the solution $y(t)$ to $y(x(t)) = Cx(t) + D\phi(y(x(t))) + D_w w(t)$ satisfies $y(t) \in \mathcal{Y}_0$ for all $t \geq 0$ (thus the sector inequalities may not hold). For $D_w = 0$, we have $\tilde{y} \equiv y$ and (7.14c) implies that $y(t) \in \mathcal{Y}_0$, for all $t \geq 0$. Note also that for the case $\mathcal{Y}_0 = \mathbb{R}^m$, the sector inequalities from Lemmas 7.1-7.3 hold globally so (7.14c) is trivially satisfied.

A convenient property of the quadratic inequalities (7.14a)-(7.14b) is that their representation is affine on P, Λ, $\tilde{\Lambda}$, T_i, $i = \{0,\ldots,4\}$. Whenever the inclusion (7.14c) is also formulated in terms of affine inequalities on these variables, and the system matrices (A,B,C,D) and the sector bounds $\underline{\Delta}$, $\overline{\Delta}$, $\underline{\Gamma}$, $\overline{\Gamma}$ are given, we can formulate the problem of computing these variables as a convex semi-definite program. Numerical examples illustrate the solution to these convex semi-definite programs in Section 7.5 and the corresponding linear matrix inequalities (LMIs) are detailed in (7.23).

7.4.1 Inclusion conditions

To satisfy local properties of (7.1) with Theorem 7.1, the inclusion (7.14c) has to be guaranteed. For sets of the form

$$\mathcal{X}_0 = \left\{ x \in \mathbb{R}^n \mid (\tilde{y}_j(x) - \underline{\tilde{y}}_j)(\tilde{y}_j(x) - \overline{\tilde{y}}_j) \leq 0, j = 1 \ldots m \right\}, \tag{7.16}$$

a condition for the set inclusion is provided by the following lemma.

Lemma 7.5. *If there exist scalars $\alpha_j > 0$ such that*

$$-\alpha_j(\tilde{y}_j(x) - \underline{\tilde{y}}_j)(\tilde{y}_j(x) - \overline{\tilde{y}}_j) \geq (\rho - V(x)) \tag{7.17}$$

$j = 1, \ldots, m$ then (7.14c) *holds.*

Proof. If the above inequality holds, then for all x satisfying $(\rho - V(x)) \geq 0$ the inequality $-(\tilde{y}_j(x) - \underline{\tilde{y}}_j)(\tilde{y}_j(x) - \overline{\tilde{y}}_j) \geq 0$ holds and $x \in \mathcal{X}_0 \; \forall x \in \mathcal{E}(V, \rho)$, hence the set inclusion. □

For the function $V(x)$ in (7.10), the inequalities (7.17) become

$$\begin{aligned} -\alpha_j \underline{\tilde{y}}_j \overline{\tilde{y}}_j - \rho + \alpha_j(\underline{\tilde{y}}_j + \overline{\tilde{y}}_j)\tilde{y}_j(x) - \alpha_j \tilde{y}_j^2(x) \\ + V_0(x) + \sum_{i=1}^{m} \lambda_i \int_0^{\tilde{y}_i} \phi_i(s) - \underline{\delta}_i s \; \mathrm{d}s \geq 0. \end{aligned} \tag{7.18}$$

$j = 1, \ldots, m$. The reason for expressing nonlinearities in quadratic-like forms is to frame the inclusion condition of Theorem 7.1 as a set of affine matrix inequalities on the unknown coefficients λ_i. Whenever only its bounds are given, as in (7.2a), consider $\tilde{\lambda}_i$ satisfying $\lambda_i \geq -\tilde{\lambda}_i$ to obtain the following lower bound for the Lur'e terms in (7.18) (see (7.13))

$$\sum_{i=1}^{m} \lambda_i \int_0^{\tilde{y}_i} \phi_i(s) - \underline{\delta}_i s \; \mathrm{d}s \geq -\frac{1}{2}\tilde{y}^T(x)(\overline{\Delta} - \underline{\Delta})\tilde{\Lambda}\tilde{y}(x) \geq 0. \tag{7.19}$$

Provided the inequalities

$$\begin{aligned} -\alpha_j \underline{\tilde{y}}_j \overline{\tilde{y}}_j - \rho + \alpha_j(\underline{\tilde{y}}_j + \overline{\tilde{y}}_j)\tilde{y}_j(x) - \alpha_j \tilde{y}_j^2(x) \\ + V_0(x) - \frac{1}{2}\tilde{y}^T(x)(\overline{\Delta} - \underline{\Delta})\tilde{\Lambda}\tilde{y}(x) \geq 0, \end{aligned} \tag{7.20}$$

$j = 1, \ldots, m$, hold, we have that (7.18) holds and hence guarantees set inclusion (7.14c). A lower bound on the Lur'e terms that guarantee inclusion conditions for sector nonlinearities similar to (7.19), was proposed in [69].

When the nonlinearity that satisfies the sector condition is known, in some cases it is possible to explicitly write the Lur'e term in a quadratic-like form. As an example, consider the nonlinearities $\ln(1 + \tilde{y}_i)$ and $\frac{\tilde{y}_i}{1+\tilde{y}_i}$

$$\begin{array}{rcl} \int_0^{\tilde{y}_i} \ln(1+s) - \underline{\delta}_i s \; \mathrm{d}s & = & \ln(1+\tilde{y}_i)(1+\tilde{y}_i) - \tilde{y}_i - \frac{1}{2}\underline{\delta}_i \tilde{y}_i^2 \\ \int_0^{\tilde{y}_i} \frac{s}{1+s} - \underline{\delta}_i s \; \mathrm{d}s & = & -\ln(1+\tilde{y}_i) + \tilde{y}_i - \frac{1}{2}\underline{\delta}_i \tilde{y}_i^2, \end{array} \tag{7.21}$$

$\phi(\tilde{y}_j)$	$\underline{\delta}$	$\overline{\delta}$	$\underline{\gamma}$	$\overline{\gamma}$
$\ln(1+\tilde{y}_j)$	$\frac{\ln\ (1+\overline{\tilde{y}}_j)}{\overline{\tilde{y}}_j}$	$\frac{\ln\ (1+\underline{\tilde{y}}_j)}{\underline{\tilde{y}}_j}$	$\frac{1}{1+\overline{\tilde{y}}_j}$	$\frac{1}{1+\underline{\tilde{y}}_j}$
$\frac{\tilde{y}_j}{1+\tilde{y}_j}$	$\frac{1}{1+\overline{\tilde{y}}_j}$	$\frac{1}{1+\underline{\tilde{y}}_j}$	$\frac{\overline{\tilde{y}}_j}{(1+\overline{\tilde{y}}_j)^2}$	$\frac{\underline{\tilde{y}}_j}{(1+\underline{\tilde{y}}_j)^2}$

Table 7.1: Local sector and slope bounds for the nonlinearities .

which can be expressed as quadratic-like forms in the vector $[1 \quad \tilde{y}_i \quad \ln(1+\tilde{y}_i)]^T$. These nonlinearities present sector and slope bounds that hold only in the interval $\left[\underline{\tilde{y}}_j, \overline{\tilde{y}}_j\right]$ as detailed in the table below: note that for both $\ln(1+\tilde{y}_j)$ and $\frac{\tilde{y}_j}{1+\tilde{y}_j}$, (7.2) holds with $\mathcal{Y} = (-1, \infty)$ thus $\mathcal{Y}_0 = \left[\underline{\tilde{y}}_j, \overline{\tilde{y}}_j\right]$ is defined with $-1 < \underline{\tilde{y}}_j < 0$ and $0 < \overline{\tilde{y}}_j$.

7.4.2 Discussion on the proposed LF

The function (7.10) was introduced in [177] to study single-input single-output (SISO) systems with slope-restricted nonlinearities satisfying $\underline{\gamma} = -\infty$ or $\overline{\gamma} = \infty$, yielding a graphical criterion involving the frequency response of the linear part. A main feature of the result presented in this chapter is that neither the Lur'e coefficient λ nor the corresponding P_{22} block (scalar in the SISO case) are required to be positive definite. The same Lyapunov structure was used in [84] where the extension of the frequency domain criteria of [177] to the MIMO case was presented.

Convex optimization based approaches using the quadratic-like term in (7.10) have also been proposed [116, 150, 158], although none of these references addresses the positivity of the LF as proposed by Lemma 7.4. In [150], the positivity of (7.10) is obtained by imposing $P > 0$ and $\Lambda > 0$ and the slope restriction is addressed by considering a norm-bounded inequality. In [116] and [158], the slope restriction is studied with the inequality of Lemma 7.2 and the proposed Lyapunov functions contain additional Lur'e type terms with non-negative coefficients and impose $P \geq 0$ ($P > 0$ in [158]). The history of the use of variants of $V(x, \phi(y(x))$ for Lyapunov analysis is expressed in Figure 7.1. Initial results were interpreted in the frequency domain [41, 177] with a KYP-type lemma being proposed in [177]. These results were rediscovered in the modern literature in [150] which framed the search for a suitable LF as a matrix inequality. A convex search for a LF was proposed in [116], with this result being extended and simplified in [158, 160]. The application of the convex search method to saturated systems was considered in [35].

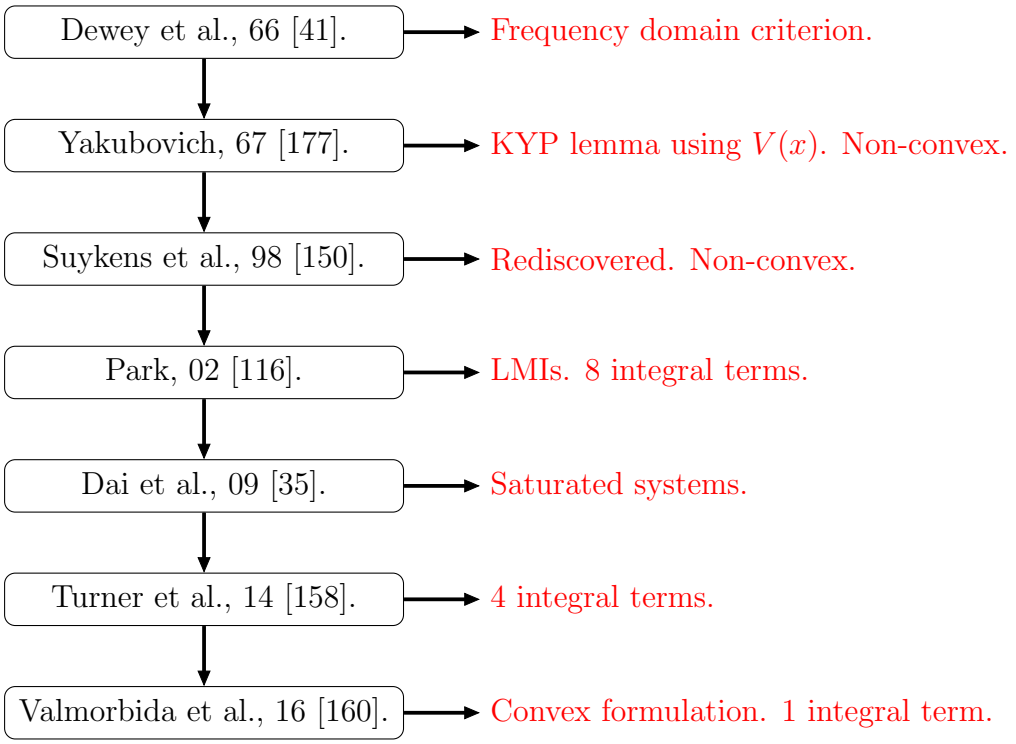


Figure 7.1: History of the piecewise quadratic Lyapunov function for stability analysis of slope-restricted nonlinear systems.

The remark below shows that the additional terms on these papers can be recast in the form (7.10) where the block P_{22} is allowed to be negative definite.

Remark 7.1. *(Additional Lur'e terms for slope-restricted nonlinearities) In [116] and [158], Lyapunov functions structures containing the term* $V_0(x)$ *as in* (7.10b) *were studied for the stability and induced* $\mathcal{L}_2$ *gain analysis for system* (7.1) *with additive disturbance terms. When compared to* (7.10a) *the structures in [116] and [158] use additional integral terms. It is shown in [158] that some of the additional Lur'e terms in [116] were redundant. We now discuss how* (7.10a) *with a single Lur'e term compares with the LF of [158], which can be written as*

$$\bar{V}(x) = \begin{bmatrix} x \\ \tilde{\phi} \end{bmatrix}^T \bar{P} \begin{bmatrix} x \\ \tilde{\phi} \end{bmatrix} + \sum_{j=1}^{4} \sum_{i=1}^{m} \mu_{1,i} \int_0^{\tilde{y}_i(x)} \bar{g}_{j,i}(s) \mathrm{d}s \tag{7.22}$$

where $\bar{g}_{1,i}(s) = \phi_i(s)$, $\bar{g}_{2,i}(s) = \overline{\delta}_i s - \phi_i(s)$, $\bar{g}_{3,i} = (\overline{\gamma}_i - \partial\phi_i(s))\, s$, $\bar{g}_{4,i} = \partial\phi_i(s)\left(\overline{\delta}_i s - \phi_i(s)\right)$ *and* $\bar{P} > 0$ *and* $\mu_{j,i} \geq 0$, $i = 1, \ldots, m$, $j = 1, \ldots, 4$. *For* ϕ *satisfying* (7.2) *with* $\underline{\delta}_i = \underline{\gamma}_i = 0$, $i = 1, \ldots, m$ *we clearly have* $g_{j,i}(x) \geq 0$ $i = 1, \ldots, m$, $j = 1, \ldots, 4$.

By using the relations

$$\int_0^{\tilde{y}_i} \phi_i(s)\partial\phi_i(s)\mathrm{d}s = \frac{1}{2}\phi_i^2(\tilde{y}_i)$$
$$\int_0^{\tilde{y}_i} \partial\phi_i(s)s\mathrm{d}s = \phi_i(\tilde{y}_i)\tilde{y}_i + \int_0^{\tilde{y}_i} \phi_i(s)\mathrm{d}s,$$

it is straightforward to obtain

$$\sum_{j=1}^{4}\sum_{i=1}^{m} g_{j,i}(x) = \begin{bmatrix} x \\ \phi(\tilde{y}(x)) \end{bmatrix}^T M \begin{bmatrix} x \\ \phi(\tilde{y}(x)) \end{bmatrix} + \sum_{i=1}^{m}(\mu_{1,i} - \mu_{2,i} + \mu_{3,i} - \overline{\delta}_i\mu_{4,i}) \int_0^{\tilde{y}_i(x)} \phi_i(s)\mathrm{d}s$$

with $M = \left[\begin{smallmatrix} C^T & 0 \\ D^T & I \end{smallmatrix}\right] \left[\begin{smallmatrix} \overline{\Delta}M_2+\overline{\Gamma}M_3 & \frac{1}{2}(\overline{\Delta}M_4-M_3) \\ \frac{1}{2}(\overline{\Delta}M_4-M_3) & -\frac{1}{2}M_4 \end{smallmatrix}\right] \left[\begin{smallmatrix} C & D \\ 0 & I \end{smallmatrix}\right]$ *where* $M_j = diag(\mu_{j,1}, \ldots, \mu_{j,m})$, $j = 1, \ldots, 4$. *Thus* (7.10a) *is obtained from* (7.22) *by setting* $P = \bar{P} + M$ *and* $\lambda_i = (\mu_{1,i} - \mu_{2,i} + \mu_{3,i} - \overline{\delta}_i\mu_{4,i})$. *Note that the matrix* $\bar{P} + M$ *is not necessarily positive definite since its lower, right diagonal block* $\bar{P}_{22} - \frac{1}{2}M_4$ *may not be positive definite. Note also that the Lur'e term coefficients* $\bar{\mu}_i := (\mu_{1,i} - \mu_{2,i} + \mu_{3,i} - \overline{\delta}_i\mu_{4,i})$ *can also be negative since* $\mu_{j,i} \geq 0$ *does not imply* $\bar{\mu}_i \geq 0$.

For the specific case of saturation or deadzone nonlinearities, the integral terms can be incorporated to the quadratic-like term V_0. This fact has been observed in [35]. In [57], the slope restriction of the deadzone is accounted for (see [57, Fact 2]). In both [35] and [57], the positive definiteness of $V_0(x)$ is obtained by imposing $P > 0$.

7.5 Numerical Formulation and Examples

In this section, numerical solutions are presented for the inequalities presented in Theorem 7.1. The computation of the stability certificates, reachable sets and local induced $\mathcal{L}_2$-gains are based on the solution to the SDPs obtained from the inequalities of Theorem 7.1. The quadratic inequalities in Theorem 7.1 and the inequality (7.20), which is a sufficient condition for (7.14c), are equivalent to linear matrix inequalities presented in (7.23), where M_Ψ satisfies $\Psi(w, z) = \zeta^T M_\Psi \zeta$ with $\zeta = \left[x^T \ \tilde{\phi}^T \ \dot{\tilde{\phi}}^T \ \phi^T \ w^T\right]^T$. Whenever the nonlinearity is known and the Lur'e term is expressed as a quadratic form, *ad hoc* inequalities replace (7.23d).

$$\tilde{\Lambda} \geq 0,\ \Lambda \geq -\tilde{\Lambda},\ T_i \geq 0,\ i = 0, \ldots, 4, T_{c,j} \geq 0,\ j = 0, \ldots, m, \tag{7.23a}$$

$$\begin{bmatrix} P_{11} & P_{12} \\ P_{12}^T & P_{22} \end{bmatrix} - \frac{1}{2} \begin{bmatrix} C^T \\ D^T \end{bmatrix} (\overline{\Delta} - \underline{\Delta}) \tilde{\Lambda} \begin{bmatrix} C & D \end{bmatrix} + He \left(\frac{1}{2} \begin{bmatrix} (\underline{\Delta} C)^T \\ (\underline{\Delta} D^T - I_m)^T \end{bmatrix} T_0 \begin{bmatrix} \overline{\Delta} C & (\overline{\Delta} D^T - I_m) \end{bmatrix} \right) > 0, \tag{7.23b}$$

$$\begin{aligned} &- He \left(\left(\left(\begin{bmatrix} P_{11} & P_{12} \\ P_{12}^T & P_{22} \\ 0 & 0 \\ 0 & 0 \\ 0 & 0 \end{bmatrix} + \frac{1}{2} \begin{bmatrix} -(\underline{\Delta} C)^T \\ (I - \underline{\Delta} D)^T \\ 0 \\ 0 \\ 0 \end{bmatrix} \begin{bmatrix} \Lambda C & \Lambda D \end{bmatrix} \right) \begin{bmatrix} A & 0 & 0 & B & B_w \\ 0 & 0 & I_m & 0 & 0 \end{bmatrix} \right. \\ &\quad + \frac{1}{2} \begin{bmatrix} (\underline{\Delta} C)^T \\ (\underline{\Delta} D - I_m)^T \\ 0 \\ 0 \\ 0 \end{bmatrix} T_1 \begin{bmatrix} \overline{\Delta} C & (\overline{\Delta} D - I_m) & 0 & 0 & 0 \end{bmatrix} + \frac{1}{2} \begin{bmatrix} (\underline{\Delta} C)^T \\ 0 \\ 0 \\ (\underline{\Delta} D - I_m)^T \\ (\underline{\Delta} D_w)^T \end{bmatrix} T_2 \begin{bmatrix} \overline{\Delta} C & 0 & 0 & (\overline{\Delta} D - I_m) & \overline{\Delta} D_w \end{bmatrix} \\ &\quad + \frac{1}{2} \begin{bmatrix} A^T & 0 \\ 0 & 0 \\ 0 & I_m \\ B^T & 0 \\ B_w^T & 0 \end{bmatrix} \begin{bmatrix} (\underline{\Gamma} C)^T \\ (\underline{\Gamma} D - I_m)^T \end{bmatrix} T_3 \begin{bmatrix} \overline{\Gamma} C & (\overline{\Gamma} D - I_m) \end{bmatrix} \begin{bmatrix} A & 0 & 0 & B & B_w \\ 0 & 0 & I_m & 0 & 0 \end{bmatrix} \\ &\quad \left. + \frac{1}{2} \begin{bmatrix} 0 \\ (I - \underline{\Gamma} D) \\ 0 \\ -(I - \underline{\Gamma} D) \\ \underline{\Gamma} D_w \end{bmatrix} T_4 \begin{bmatrix} 0 & (I - \overline{\Gamma} D) & 0 & -(I - \overline{\Gamma} D) & \overline{\Gamma} D_w \end{bmatrix} + M_\Psi \right) > 0, \end{aligned} \tag{7.23c}$$

$$\begin{bmatrix} -(\tilde{\underline{y}}_j\tilde{\overline{y}}_j+\rho) & \frac{\tilde{\underline{y}}_j+\tilde{\overline{y}}_j}{2}C_j & \frac{\tilde{\underline{y}}_j+\tilde{\overline{y}}_j}{2}D_j \\ \frac{\tilde{\underline{y}}_j+\tilde{\overline{y}}_j}{2}C_j^T & -C_j^TC_j+P_{11}-\frac{1}{2}C^T(\overline{\Delta}-\underline{\Delta})\tilde{\Lambda}C & -C_j^TD_j+P_{12}-\frac{1}{2}C^T(\overline{\Delta}-\underline{\Delta})\tilde{\Lambda}D \\ \frac{\tilde{\underline{y}}_j+\tilde{\overline{y}}_j}{2}D_j^T & -D_j^TC_j+P_{12}^T-\frac{1}{2}D^T(\overline{\Delta}-\underline{\Delta})\tilde{\Lambda}C & -D_j^TD_j+P_{22}-\frac{1}{2}D^T(\overline{\Delta}-\underline{\Delta})\tilde{\Lambda}D \end{bmatrix}$$
$$+He\left(\frac{1}{2}\begin{bmatrix} 0 \\ (\underline{\Delta}C)^T \\ (\underline{\Delta}D^T-I_m)^T \end{bmatrix}T_{c,j}\begin{bmatrix} 0 & \overline{\Delta}C & (\overline{\Delta}D^T-I_m) \end{bmatrix}\right)\geq 0 \quad j=1,\ldots,m. \quad (7.23d)$$

For nonlinearities that yield sector and slope bounds that hold only locally, the set inclusion (7.14c) is guaranteed by solving the inequalities (7.18) for the case where the nonlinearity is known and has an explicit quadratic-like representation, or, if it is only known to satisfy sector bounds we use a lower bound to the integral term and solve (7.20) otherwise.

In the following example sector and slope bounds are optimised using different structures of the Lyapunov function (7.10).

Example 7.1. *This example computes the maximum sector and slope restriction for the SISO system described by* $G_1(s) = \frac{0.2s^2}{s^4+0.4s^3+6s^2+0.1s+1}$. *The sector and slope conditions are defined by a parameter* ϵ, *as* $\underline{\delta} = 0$, $\overline{\delta} = \epsilon$, $\underline{\gamma} = -0.5\epsilon$, $\overline{\gamma} = 1.5\epsilon$. *Via a bissection algorithm, bounds are obtained for the parameter* ϵ *such that the global stability of system* (7.1) *is guaranteed. Table 7.2 compares the bounds of* $V(x)$ *to the bounds obtained with* $V_0(x)$, *together with the special cases of* V *given by* $V_Q := x^T P_{11} x$ *and* $V_{LP} := x^T P_{11} x + \sum_{i=1}^{m} \lambda_i \int_0^{y_i} \phi(s)\mathrm{d}s$

	V_Q	V_{LP}	V_0	V
ϵ	0.730	1.272	0.730	2.422

Table 7.2: Maximum bound on ϵ for global stability of system $G_1(s)$. The bounds were obtained using the bisection algorithm.

Example 7.2. *Consider the system*

$$\begin{cases} \dot{x}_1 &= -x_2 + \ln(1+y_1) + 2\frac{y_2}{1+y_2} \\ \dot{x}_2 &= x_1 - 0.65x_2 + \ln(1+y_1) + \frac{y_2}{1+y_2} \\ y_1 &= 0.1(x_1+x_2) - 0.2\frac{y_2}{1+y_2} \\ y_2 &= 0.1(x_2 - x_1). \end{cases}$$

This can be readily put in the form (7.1) *with* $\phi_1(y_1) = \ln(1+y_1)$, $\phi_2(y_2) = \frac{y_2}{1+y_2}$. *In order to compute a region of attraction of its origin, the interval of interest* $y_1 \in [-.4, 50]$, $y_2 \in [-.5, 50]$ *is fixed thus defining the slope and sector bounds for the nonlinearities according to Table 7.1. The inclusion inequality* (7.18) *is obtained by explicitly computing the Lur'e terms as in* (7.21) *and fixing* $\rho = 1$. *An ERA is then obtained by solving the convex optimization problem that minimizes* $Trace(P_{11})$ *subject to* (7.23a)-(7.23c), (7.18). *The level sets obtained are depicted in Figure 7.2. Inner level sets of the LF are also depicted and show that incorporating the Lur'e terms and the nonlinearities in* V_0 *may yield an asymmetric ERA with respect to the origin. Note also that the innermost level set is indistinguishable from an ellipsoid, showing that close to the equilibrium point, the term* $x^T P_{11} x$ *dominates the non-quadratic terms of the LF.*

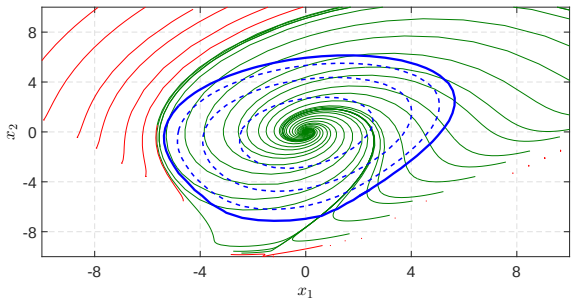


Figure 7.2: Estimate of the region of attraction with the Lyapunov function (7.10) (dark blue). Trajectories asymptotically converging to the origin are shown in green, while diverging trajectories are depicted in red .

Example 7.3. *This example computes upper bounds for the local induced $\mathcal{L}_2$ gain η of an idealised Stirling engine. The dynamic equations are obtained from (3) of [64] with damping factor $c = 50$ and nonlinearity $\phi(y) = y/(1+y)$*

$$\begin{aligned}\dot{x}_1 &= x_2 - cx_1 - cw\\ \dot{x}_2 &= -\frac{x_1}{1+x_1}\\ y &= x_1\\ z &= x_1.\end{aligned}$$

The gain depends upon both the local domain and the magnitude of the disturbance whose norm is upper bounded by $\|w\|_2 \leq \rho^{\frac{1}{2}}$. For this example, the upper bound on the domain is set as $\overline{\tilde{y}} = 0.5$ and η is computed for each $\{\underline{\tilde{y}},\ \rho\} = \{1,\ 2,\ 5,\ 6,\ 8\} \times 10^{\{-2,\ -1\}}$. Figure 7.3 shows minimal upper bounds for η searched over the values of $\underline{\tilde{y}}$ for fixed ρ. The bounds were computed using $V(x)$ subject to (7.23a)-(7.23c)*,* (7.18) *and a local Popov criterion obtained using $V_{LP}(x)$ and the substitution of a lower bound for the LF given by V_C into* (7.17)*, a similar method to [69]. Tighter bounds were obtained using $V(x)$ for all values.*

7.6 Conclusions

In this chapter, stability analysis of Lur'e type systems with slope-restricted nonlinearities was carried out for LFs that have a quadratic-like term on the state and the nonlinearity together with Lur'e type terms. Relaxed conditions for the positivity of the LF (cf. Lemma 7.4) have been proposed and have used sector inequalities to

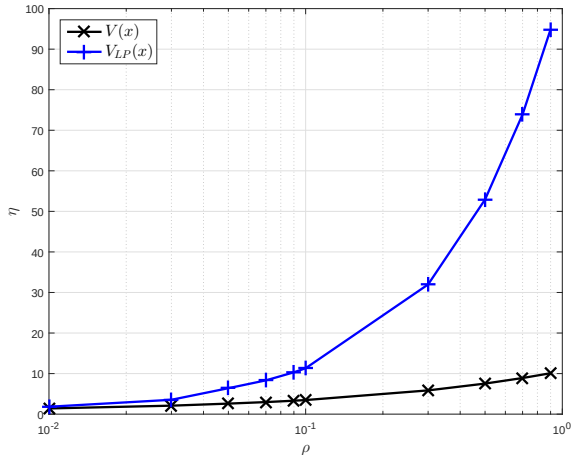


Figure 7.3: Induced $\mathcal{L}_2$ gain bounds for an idealised Stirling engine.

propose conditions for the global and local properties of solutions to Lur'e systems. Importantly, the LF structure allows for negative coefficients in the Lur'e term.

A numerical formulation to solve to dissipation inequalities presented in the main result (cf. Theorem 7.1) has been given. Due to the quadratic-like nature of these inequalities and an affine dependence on the Lyapunov/storage function coefficients and multipliers associated to sector conditions, a numerical solution can be obtained via the solution of SDPs. Examples illustrate the results and provide comparison between them to different LF structures. Gain curves for nonlinearities that satisfy sector and slope bounds globally are also given.

The next chapter broadens these results to generalised absolute stability theory, where the systems evolves along a vector field that is a rational function of the states and the slope restricted nonlinearities. Once more, stability conditions are derived with relaxed positivity requirements. However, instead of matrix positive definiteness condition being relaxed, the polynomials that form the Lyapunov functions for these systems are relaxed from being sum-of-squares.

Chapter 8

Generalised Absolute Stability using Lyapunov Functions that are not Sum-of-Squares

This chapter extends the results of the previous chapter to systems that evolve along vector fields that are rational functions of the state and the slope restricted nonlinearity. Less conservative stability and dissipitivity conditions are derived for the local analysis of such systems, with these conditions again including the sector information into the Lyapunov function's positivity condition. Once again, the supercapacitor model of chapter 5 is a particular example of the class of system considered here, and so the proposed conditions will again lead to less conservative bounds for the resistance, making the design predictions more accurate.

8.0.1 Introduction

Motivated by recent developments on polynomial optimization, a refinement of the absolute stability problem, labelled "generalised absolute stability thoery", was proposed in [63], with the nonlinearities assumed to be bounded by polynomials. This result extended the approach proposed in [68] that used a recasting transformation for the analysis. In a different vein, the advances on polynomial optimization also motivated the approximation of vector fields defined by (locally) analytic nonlinear functions by polynomials systems [25, 99].

The chapter gives a set of a convex conditions, in terms of semi-definite programmes (SDPs), for verifying stability and computing upper bounds on the induced $\mathcal{L}_2$ gain

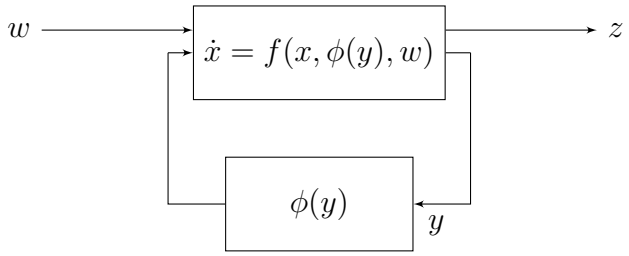


Figure 8.1: Feedback interconnection of sector bounded nonlinearity with a rational vector field.

from input to output for the considered class of system. The results use Lyapunov functions candidates that are polynomial with respect to both the states and the nonlinearity, and contain Lur'e type terms. The conditions for the positivity of such Lyapunov functions *do not* impose the positivity of the function with respect to the nonlinearities. This positivity result generalises [160] which considered quadratic Lyapunov functions. Another relevant aspect of the proposed condition is that the Lur'e term coefficients are polynomials rather than scalars. Moreover, for the class of nonlinearities studied, these terms are not required to be positive. The results are obtained for both global and local domains, where the local domains are characterised by the level sets of the Lyapunov function.

By allowing the terms of $V(x, \phi)$ to be general polynomials, not simply quadratic V_0 and scalar λ_i, as in [160], we generalise the class of candidate Lyapunov function but lose a frequency domain interpretation of the method. This makes it difficult to formally compare the proposed method in a general manner against frequency dependent criteria, such as Zames-Falb multipliers [21], which are generally considered to be the least conservative methods for the global analysis of absolute stability [21].

8.1 Problem Statement

Consider the dynamical system

$$\dot{x} = D_1(x, \phi(y)))^{-1} N_1(x, \phi(y)) + B_w w \tag{8.1a}$$

$$y = Cx \tag{8.1b}$$

$$z = C_z x \tag{8.1c}$$

with $x \in \mathbb{R}^n$, $\phi : \mathcal{Y}^m \to \mathbb{R}^m$, $\phi \in \mathcal{C}^1$, output $z \in \mathbb{R}^{n_z}$ and $w \in \mathbb{R}^{n_w}$ with rational functions $N_1(x, \phi) : \mathbb{R}^n \times \mathcal{Y}^m \to \mathcal{R}^n$, $D_1(x, \phi) : \mathbb{R}^n \times \mathcal{Y}^m \to \mathbb{R}\backslash\{0\}$. This system

can be represented by the feedback form of Figure 8.1. The nonlinearity $\phi(y(x))$ is defined on $\mathcal{Y}$ which contains the subset of interest for the local analysis $\mathcal{Y}_0 \subseteq \mathcal{Y}$.

We will restrict the considered class of nonlinearities to those which are decentralised

$$\phi(y) = \begin{bmatrix} \phi_1(y_1) & \phi_2(y_2) & \dots \phi_m(y_m) \end{bmatrix}^T, \tag{8.2}$$

sector bounded

$$\frac{\phi_i(y_i)}{y_i} \in [0, \overline{\delta_i}] \quad \forall y \in \mathcal{Y}_0 \subseteq \mathcal{Y} \tag{8.3}$$

and

$$\frac{\mathrm{d}\ \phi(y_i)}{\mathrm{d}y_i} = (D_{2i}(\phi(y_i), y_i)^{-1} N_{2i}(\phi(y_i), y_i) \tag{8.4}$$

where $N_2 : \mathbb{R} \times \mathbb{R} \to \mathbb{R}$, $D_2 : \mathbb{R}^n \times \mathbb{R} \to \mathbb{R}\backslash\{0\}$ and $\mathcal{X}_0 = \{x : y(x) \in \mathcal{Y}_0\}$.

The sector condition (8.3) implies that

$$s_1(y, \phi(y), T(x, \phi(y))) := (\phi(y))\, T(x, \phi(y)) \left(\overline{\Delta} y - \phi(y)\right) \geq 0 \tag{8.5}$$

where $T = diag(\tau_1,\ \tau_2, \dots,\ \tau_m)$ with $\tau_i \in \mathcal{R}_{>0}(x, \phi)$ for $i = 1,\ 2, \dots,\ m$ and $\overline{\Delta} = diag(\overline{\delta}_1, \dots, \overline{\delta}_m)$.

This chapter considers solutions to the following problems:
Problem 8.1 (Stability)**.** *Provide conditions that guarantee local stability of the origin of system* (8.1).
Problem 8.2 ($\mathcal{L}_2$ gain)**.** *Obtain upper bounds for the locally induced $\mathcal{L}_2$ gain from w to z of* (8.1).

8.2 Main Results

This section details a set of inequalities for solutions of Problems 8.1 and 8.2. The analysis is based upon Lyapunov functions of the form

$$V(x) = V_0(x, \phi(y(x))) + \sum_{i=1}^{m} \int_0^{y_i(x)} \lambda_i(\sigma)\ \phi(\sigma)\ d\sigma \tag{8.6}$$

where $V_0 : \mathbb{R}^n \to \mathbb{R}_{\geq 0}$, $V_0(0) = 0$, and $\lambda_i : \mathbb{R} \to \mathbb{R}$, $i = 1, \dots, m$. The term involving the integral in (8.12a) is called the Lur'e term. Allowing $\lambda_i(\sigma)$ to be polynomials can be interpreted as enabling the work done by the 'force' $\phi(y)$ to be scaled in the domain $\mathcal{Y}_0$.

Using (8.5), a polynomial lower bound for $V(x)$ is given by the following lemma:

Lemma 8.1. *Let V_0 and λ_i, $i = 1, \ldots, m$, defining* (8.12a) *be given and let $\mathcal{X}_0 \subseteq \mathbb{R}^n$, $0 \in \mathcal{X}_0$. If there exists $\tilde{\lambda}_i : \mathcal{R} \to \mathcal{R}_{\geq 0}$, $i = 1, \ldots, m$, such that*

$$\lambda_i(\sigma) \geq -\tilde{\lambda}_i(\sigma), \ i = 1, \ldots, m, \quad \forall x \in \mathcal{Y}_{0i} \tag{8.7a}$$

$$\underline{V}(x) = V_0(x, \phi(y(x))) - \sum_{i=1}^{m} \int_0^{y_i} \overline{\delta}_i \sigma \tilde{\lambda}_i(\sigma) \ d\sigma > 0 \quad \forall x \in \mathcal{X}_0 \tag{8.7b}$$

then $V(x) > 0, \ \forall x \in \mathcal{X}_0 \backslash \{0\}$.

Proof.

$$\begin{array}{rcl} V(x) & = & V_0(x) + \sum_{i=1}^m \int_0^{y_i(x)} \lambda(\sigma)\phi_i(\sigma)\mathrm{d}\sigma \\ & \geq & V_0(x) - \sum_{i=1}^m \int_0^{y_i(x)} \tilde{\lambda}(\sigma)\phi_i(\sigma)\mathrm{d}\sigma \\ & = & V_0(x) - \sum_{i=1}^m \int_0^{y_i(x)} \tilde{\lambda}(\sigma)\phi_i(\sigma)\mathrm{d}\sigma \\ & & - \sum_{i=1}^m \int_0^{y_i(x)} \overline{\delta}_i \sigma \tilde{\lambda}(\sigma)\mathrm{d}\sigma \\ & & + \sum_{i=1}^m \int_0^{y_i(x)} \overline{\delta}_i \sigma \tilde{\lambda}(\sigma)\mathrm{d}\sigma \\ & = & V_0(x) - \sum_{i=1}^m \int_0^{y_i(x)} \overline{\delta}_i \sigma \tilde{\lambda}(\sigma)\mathrm{d}\sigma \\ & & + \sum_{i=1}^m \int_0^{y_i(x)} \tilde{\lambda}(\sigma)(\overline{\delta}_i \sigma - \phi_i(\sigma))\mathrm{d}\sigma \\ & \geq & V_0(x) - \sum_{i=1}^m \int_0^{y_i(x)} \overline{\delta}_i \sigma \tilde{\lambda}(\sigma)\mathrm{d}\sigma \end{array} \tag{8.8}$$

□

The following gives a set of inequalities, which use the lower bound of Lemma 8.1, that verify solutions to Problems 8.1 and 8.2.

Theorem 8.1. *Suppose there exists functions V_0, $T = diag(\tau_1, \ \tau_2, \ldots, \ \tau_m)$ with $\tau_i \in \mathcal{R}_{>0}(x, \phi)$, polynomials $\tilde{\lambda}_i \in \mathcal{R}_{\geq 0}(\sigma)$, $\lambda_i \in \mathcal{R}(\sigma)$ for $i = 1, \ 2, \ldots, \ m$ and scalars $\eta \in \mathbb{R}_{\geq 0}$, if* (8.7a) *and*

$$\begin{aligned} & V_0(x, \phi(y(x))) - \sum_{i=1}^{m} \int_0^{y_i} \overline{\delta}_i \sigma \tilde{\lambda}_i(\sigma) \ d\sigma \\ & \qquad - s_1(x, \phi(y), T(x, \phi(y))) > 0 \end{aligned} \tag{8.9a}$$

$$\begin{aligned} & - \left\langle \begin{bmatrix} \nabla_x V \\ \nabla_\phi V \end{bmatrix}, \begin{bmatrix} \dot{x} \\ \dot{\phi} \end{bmatrix} \right\rangle \\ & \qquad - s_1(x, \phi(y), T(x, \phi(y))) - \Omega(z, w) > 0 \end{aligned} \tag{8.9b}$$

$$\mathcal{E}(V, \rho) \subseteq \mathcal{X}_0 \tag{8.9c}$$

hold for all $x \in \mathcal{X}_0$ with

a) $\Omega = 0$ and $w = 0$;

b) $\Omega(z, w) = -\eta w^T w + z^T z$;

then

a) The origin of (8.1) *is locally asymptotically stable with domain of attraction* $\mathcal{E}(V, \rho)$.

b) The induced $\mathcal{L}_2$ *gain from* w *to* z *is upper-bounded by* $\sqrt{\eta}$, *that is,* $\frac{\|z\|}{\|w\|} \leq \sqrt{\eta}$ *for all solutions of* (8.1) *satisfying* $x(0) = 0$ *and* $\|w\| \leq \rho^{\frac{1}{2}}$.

Proof. The proof is analagous to that of Theorem 7.1. □

Remark 8.1. *Note that Theorem 8.1 does not require strict positivity of the individual terms of* V_0 *or* λ_i. *Positivity of the terms of* V_0 *is relaxed by including the sector information into* (8.9a) *while the positivity of* λ_i *is relaxed by using the polynomial lower bound of the Lur'e term given in Lemma 8.1. Including the sector information in* (8.9a) *allows the monomials of the Lyapunov function to be related via the passivity of* ϕ, *defined by the sector.*

8.3 Numerical Formulation

In order to make the verification of the inequalities of Theorem 8.1 computational tractable, numerical relaxations on the polynomial inequalities are proposed. These relaxations use the SOS formulation for positive polynomials.

If the Lur'e term is polynomial, then the inclusion conditions of (8.9c) can be evaluated exactly. This is true for functions such as $\ln(1 + y)$, $\tan^{-1}(y)$ and $\sin(y)$. Otherwise, the inclusion conditions can be verified using a polynomial outer approximation of the level sets defined by $\underline{V}(x)$ from (8.7b):

Proposition 8.1. *If* $\mathcal{E}(\underline{V}, \rho) \subseteq \mathcal{X}_0$ *then* $\mathcal{E}(V, \rho) \subseteq \mathcal{X}_0$ *since* $\mathcal{E}(V, \rho) \subseteq \mathcal{E}(\underline{V}, \rho)$.

8.3.1 SOS Formulation

The following section briefly summarises the SOS relaxation. For a comprehensive analysis, see [117].

Definition 8.1. *A multivariate polynomial* p *is said to be a SOS polynomial if there exists a finite set of polynomials* $h_i \in \mathcal{R}[x]$ *satisfying*

$$p(x) = \sum_{i=1}^{M} h_i^2(x). \tag{8.10}$$

The search for a SOS decomposition of a polynomial was shown to be affine in the coefficients of h_i and as such could be expressed as a semi-definite programme (SDP) [117],

Proposition 8.2. *A polynomial $p(x) \in \mathcal{R}[x]$ of degree $2d$ is an SOS polynomial if and only if there exists $Q \in \mathbb{S}_{\geq 0}$ and a vector of monomials $Z(x) \in \mathcal{R}^M[x]$ such that*

$$p(x) = Z(x)^T Q Z(x) \tag{8.11}$$

then $p(x)$ is SOS.

The following proposition gives a convex formulation of Theorem 8.1, expressed as a SDP.

Proposition 8.3. *If there exists $V_0 \in \mathcal{R}[x, \phi]$, $V(0,0) = 0$, $T_1,\ T_2 \in \Sigma_m^{diag}[x, \phi]$, $\lambda_i \in \mathcal{R}(\sigma)$, $\tilde{\lambda}_i \in \Sigma(\theta)$, satisfying $\lambda_i \geq -\tilde{\lambda}_i$ $i = 1, \ldots, m$, $\eta \in \mathbb{R}_{\geq 0}$*

$$\begin{aligned} & V_0 - \sum_{i=1}^{m} \int_0^{y_i} \overline{\delta}_i \sigma \tilde{\lambda}_i(\sigma)\, d\sigma && \text{(8.12a)} \\ & - s_1(y(x), \phi, T_1) - \varepsilon x^T x \in \Sigma[x, \phi] \\ & \\ & - \left\langle \begin{bmatrix} \nabla_x V \\ \nabla_\phi V \end{bmatrix}, \begin{bmatrix} D_2(\phi, y)\left(N_1(\phi(y), y(x)) + D_1(\phi, y(x)) B_w w\right) \\ D_1(\phi, y(x)) N_2(\phi, y(x)) \dot{y}(x) \end{bmatrix} \right\rangle \\ & + D_1(\phi, y(x)) D_2(\phi, y(x)) \left(\eta w^T w - z^T(x) z(x)\right) \\ & - s_1(y(x), \phi, T_2) - \varepsilon x^T x \in \Sigma[x, \phi, w] && \text{(8.12b)} \\ & \\ & \mathcal{E}(V, \rho) \subseteq \mathcal{X}_0 && \text{(8.12c)} \end{aligned}$$

with $D_2(\phi, y(x)) = \Pi_{i=1}^m D_{2i}(\phi_i, y_i(x))$ and $N_2(\phi, y(x)) = diag(N_{21}(\phi_1, y_1(x), \ldots, N_{2m}(\phi_m, y_m(x))$ then the origin of (8.1) is locally asymptotically stable for $w \equiv 0$ and an upper-bound for the induced $\mathcal{L}_2$ gain of (8.1) is given by $\gamma = \sqrt{\eta}$ for all solutions of (8.1) satisfying $x(0) = 0$ and $\|w\| \leq \rho^{\frac{1}{2}}$.

Proposition 8.3 is obtained by replacing the positivity conditions of Theorem 8.1 with SOS requirements on the polynomials. Multiplying through by the denominators of the rational terms of the vector field and its Jacobian, convert the conditions into polynomials. Care has to be taken with this multiplication when the terms in the denominators are not positive.

Remark 8.2. *The level sets of $V(x)$, which may not be sum-of-squares, are not necessarily convex and may not be connected. This allows a wider class of candidate*

Lyapunov functions to be considered, but also introduces problems such as in maximising the volume of the level sets to estimate the domain of attraction. Typically, this procedure involves quadratic on the states Lyapunov functions and maximising the magnitude of the axes of an ellipse. An equivalent procedure which uses convex programming is not immediately obvious for V.

8.4 Examples

8.4.1 Nonlinearities

The arctangent nonlinearity is used in the following examples, with this nonlinearities locally satisfying the sector boundedness and slope restricted conditions of (7.2b) and (8.4) since

$$\frac{d\,\tan^{-1}(y)}{dy} = \frac{y}{1+y^2}. \tag{8.13}$$

8.4.2 Numerical Example 1: Switched Systems

In this first numerical example, we assess the global stability of the (linear) Lur'e system

$$\begin{bmatrix}\dot{x}_1\\ \dot{x}_2\end{bmatrix} = \begin{bmatrix}-0.05 & 1\\ -10 & -0.5\end{bmatrix}\begin{bmatrix}x_1\\ x_2\end{bmatrix} + \begin{bmatrix}0\\ 1\end{bmatrix}\tan^{-1}(y) \tag{8.14a}$$

$$y = \begin{bmatrix}9.9 & 0.495\end{bmatrix}\begin{bmatrix}x_1\\ x_2\end{bmatrix}. \tag{8.14b}$$

The function $\tan^{-1}$ can be regarded as a smooth approximation of the saturation function. The above system is adapted from [181, Example 4.3.1], where the authors illustrate that there does not exist a *common* quadratic function for the open-loop system and the linear closed loop system (i.e. the system obtained by replacing $\tan^{-1}(y)$ by y). However, using $V(x, \phi(y(x)))$, we can prove the global stability of the non-linear closed-loop system. Suitable level sets of $V(x, \phi(y(x)))$ depict the decrease of the function along the trajectories of the system in Figure 8.2.

8.4.3 Numerical Example 2: Vehicle Stability

The second example considers the application of the presented results to a physical system and involves the estimation of the maximal region of attraction of a vehicle

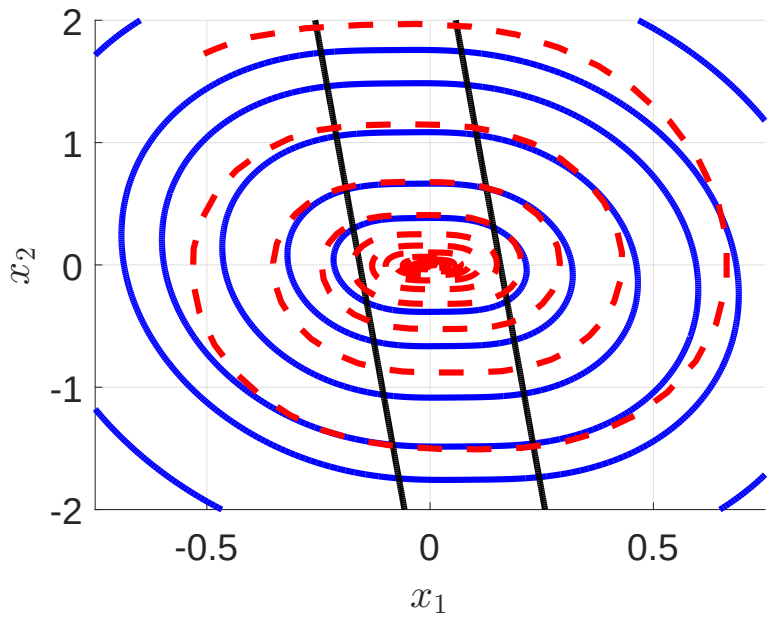


Figure 8.2: Trajectories of (8.14) from different initial conditions are depicted in red solid lines. Level sets of the computed function $V(x, \phi(y(x)))$ are depicted in solid blue lines. The black dashed lines correspond to the set $\{x \in \mathbb{R}^2 || \tan^{-1}(y(x))| = 0.8\}$.

model. Consider the following vehicle dynamics model from [98]

$$m\dot{v} = -mu_0\omega + F_{fy} + F_{ry} \tag{8.15a}$$

$$I\dot{\omega} = -aF_{fy} - bF_{ry} \tag{8.15b}$$

with states lateral velocity v and rotational velocity ω. The model parameters are mass $m = 2527$ kg, longitudinal speed $u_0 = 20$ m s^{-1}, moment of inertia $I = 6550$ kg m^2, mass centre from front axle $a = 1.37$ m, mass centre from rear axle $b = 1.86$. The nonlinearity of the model enters via the tyre forces F_{fy}, F_{fy}, F_{fy} and F_{fy} which are defined in [98] by

$$F_{fy} = -2C_f(\alpha_f - K_f\alpha_f^3) \tag{8.16a}$$

$$F_{ry} = -2C_r(\alpha_r - K_r\alpha_r^3) \tag{8.16b}$$

where $C_r = C_f = 57300$ N rad^{-1} are the cornering stiffnesses and $K_f = K_r = 4.87$ are tyre force parameters. Compared to the "Magic Formula Tire Models" of [114, Chapter 4], this definition of the tyre forces assumes that the tyre slips do not become large. Under the assumption of small steering angle deflection, the front and rear tyre

lateral slip angles are

$$\alpha_f = \tan^{-1}\left(\frac{v + a\omega}{u_0}\right), \tag{8.17a}$$

$$\alpha_r = \tan^{-1}\left(\frac{v - b\omega}{u_0}\right). \tag{8.17b}$$

This vehicle model can be expressed in the form of (7.1) by

$$\begin{bmatrix}\dot{v}\\ \dot{\omega}\end{bmatrix} = \begin{bmatrix}0 & -u_0\\ 0 & 0\end{bmatrix}\begin{bmatrix}v\\ \omega\end{bmatrix} \tag{8.18a}$$

$$+ \begin{bmatrix} -\frac{2C_f}{m} & \frac{2C_fK_f}{m} & -\frac{2C_r}{m} & \frac{2C_rK_r}{m} \\ \frac{2aC_f}{I} & -\frac{2aC_fK_f}{I} & -\frac{2bC_r}{I} & \frac{2bC_rK_r}{I}\end{bmatrix}\begin{bmatrix}\phi_1(y_1)\\ \phi_1(y_1)^3\\ \phi_2(y_2)\\ \phi_2(y_2)^3\end{bmatrix}$$

with output signals

$$\begin{bmatrix}y_1\\ y_2\end{bmatrix} = \begin{bmatrix}1/u_0 & a/u_0\\ 1/u_0 & -b/u_0\end{bmatrix}\begin{bmatrix}v\\ \omega\end{bmatrix} \tag{8.18b}$$

and nonlinearities

$$\begin{bmatrix}\phi_1(y_1)\\ \phi_2(y_2)\end{bmatrix} = \begin{bmatrix}\tan^{-1}(y_1)\\ \tan^{-1}(y_2)\end{bmatrix}. \tag{8.18c}$$

The region of attraction for this model obtained using Proposition 8.3 is shown in Figure 8.3. In this case, $deg(V_0(x,\phi),\phi) = 8$ and $deg(\lambda(\sigma),\sigma) = 2$. Including the nonlinearities of the model directly within the stability analysis of the system in this manner will give a more represenativite picture of the stability profile of the real system compared to using a linear analysis, as is commonly used [114, Chapter 11].

8.5 Conclusion

This chapter has considered the stability analysis of systems that evolve along a vector field that is a rational function of the states, and a nonlinearity that is slope restricted. To analyse this class of system, Lyapunov functions that are polynomial functions of both the states and the nonlinearity and included a Lur'e term with polynomial Lur'e scaling terms, were used. Analogous to chapter 7, a main result of this chapter was to relax the polynomial Lyapunov function and the scaling parameters of the Lur'e terms from being sum-of-squares. Only by including the sector information

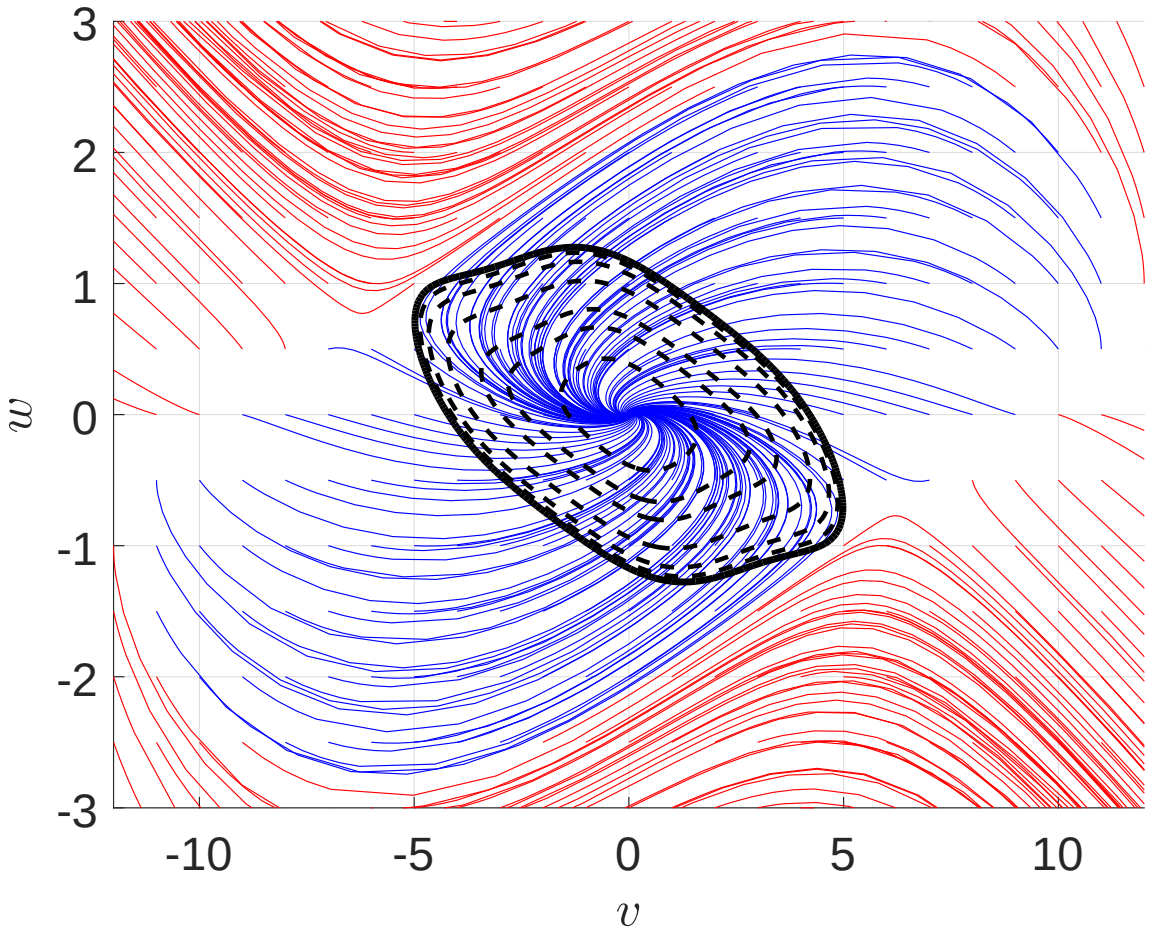


Figure 8.3: Estimate of the region of attraction (black solid) of the vehicle model of numerical example 4 obtained using the polynomial Lyapunov function of Proposition 8.3. Also shown are sublevel sets of the Lyapunov function (black dashed), stable trajectories of the system (blue) and unstable trajectories (red).

of the nonlinearity into the positivity condition of the Lyapunov function could the sum-of-squares requirements be relaxed. The stability conditions were formulated in a manner that allows them to be verified efficiently using convex programming. Numerical examples are used to highlight the benefits of the proposed conditions.

Chapter 9

Summary of Thesis

9.1 Review of Chapters

This thesis has developed methods for the analysis and design of electrochemical electrical energy storage devices known as supercapacitors. The contributions of this thesis extend to both the theory and application of systems and control theory. The foundation of the majority of the results in this thesis is a computationally efficient, yet accurate model of a supercapacitor. This model uses a set of partial differential equations to describe the electrochemistry within the energy storage device, giving greater insight into how these devices behave during charging. The model was rigorously analysed from a control systems perspective, with results obtained in parameter estimation, observability and energy dissipation and storage amongst others. An effective design procedure based on this model was proposed, which may reduce the number of expensive and time consuming physical experiments that have to implemented. A method was proposed to synthesize equivalent circuits from the electrochemical model, giving physical intuition into the components of the circuits and in doing so, linking the two main supercapacitor modeling approaches. The optimisation of electrodes with structured electrodes was also considered, with the results being compared to experimental data. Theoretical results were also obtained for the problem of absolute stability theory, more specifically, the local analysis of slope restricted nonlinear systems. This work simplified many of the existing results found in the modern literature and gave convex conditions for the set of stability conditions of [177]. Lastly, these results were extended to the case of generalised absolute stability theory, where the system dynamics are rational functions of the states and the nonlinearity.

Chapter 1 gave background information for the work presented in the thesis, allowing the results to be placed in a wider context. The importance of energy storage as a key technology for the upcoming century was stressed, both as a means to reduce the extent of fossil fuel combustion and to improve the capability of personal electronic technologies. Various solutions to the energy storage problem were discussed, including batteries, fuel cells, dielectric capacitors and supercapacitors. The charging mechanism of supercapacitors was described, with the impact upon the energy density caused by the porous electrodes and double layer being highlighted.

Chapter 2 introduced two electrochemical supercapacitor models, one being a reformulation of that presented in [163] and the other treating electrolyte conductivity as a linear function of ionic concentration. In order for the models to be computationally efficient to implement, the set of partial differential equations describing the electrochemical dynamics of ion movement and double layer potential difference from [163] were discretised in space using the spectral collocation method. This discrestisation method resulted in spectral accuracy of the numerical solution, meaning that an accurate numerical solution could be obtained with fewer grid points. It was shown that the model captured known phenomena occurring within the supercapacitor, including ionic movement and the drop in real and imaginary capacitance at high frequency charging.

Chapter 3 was concerned with improving the accuracy of the supercapacitor model and characterising how much information could be inferred about the internal state of the plant from sensor measurements. Two topics were covered, observability analysis and parameter estimation. The nonlinear electrochemical supercapacitor model was shown to be locally approximately observable through the computation of Lie derivatives. However, for the case of equal ionic transference numbers (corresponding to the relative charges carried by the positive and negative ions being equal), it was shown that the electrochemical model became linear but lost observability, with the ionic concentration becoming an an unobservable subspace. Moreover, a potential pitfall occurring in the naive implementation of an extended Kalman filter (or any observer) with the electrochemical model was highlighted, with the pitfall being that the integrator dynamics lead to a random walk drift of the states. The electrochemical model parameters were estimated from current/voltage experimental defined in the temporal and frequency domains. The temporal domain data consisted of a set of pulsed currents while the frequency domain data was in the form of electrical impedance spectroscopy (EIS) data. The identification was carried out for EIS data

at different open cell voltages, resulting in different parameter values being obtained. The accuracy of the identified electrochemical model was found to not be as accurate as an identified equivalent circuit, which had a much simpler form.

Chapter 4 proposed a method to synthesize equivalent circuits from PDE electrochemical models. This work linked the two main modeling approaches of supercapacitors and in doing so, gave a physical intuition behind the circuit components. The proposed procedure involved spatial discrestisation of the PDEs, linearisation, balanced model order reduction, checking for positive realness of the resulting impedance function and passive circuit synthesis. The synthesis method was general as a wide class of circuits with various topologies could be synthesized from a wide class of PDEs. This generality is due to the fact that the circuits are simply different state-space realisations of the impedance function. This point challenges the existing notion that each circuit has a distinct physical interpretation, with it instead being proposed that the physical interpretation of the circuit is derived from the governing electrochemical PDEs.

Chapter 5 developed supercapacitor design tools via the analysis of the electrochemical supercapacitor model. Currently, the design of supercapacitors is carried out by electrochemists and material scientists in a rather ad hoc manner, involving extensive experiments, which are both slow and expensive. This chapter explored a method to relate the electrochemical parameters of the supercapacitor to electrical energy storage performance. This may reduce the number of experiments that have to implemented, replacing them with the solution of a convex semi-definite programming optimisation problem. Local absolute stability theory was used to analyse the model, with convex conditions being obtained to bound reachable sets, energy dissipation, stability and $\mathcal{L}_2$ gains related to resistance and capacitance. It was also shown that the maximum voltage of the supercapacitor could be bounded by solving a convex nonlinear programming problem, with the obtained results being close to quoted manufacturer values.

Chapter 6 expanded upon the supercapacitor design problem of Chapter 5, but with a focus on structured electrodes. By introducing layers of different materials into the electrode, the so-called "structured" element, improved supercapacitor performance was achieved, especially at high frequency charging. This chapter explored optimising the configuration of the electrode layers with regards to real and imaginary capacitance. A model was proposed to incorporate the layering of the electrodes, with this model using the same basic PDEs as the original supercapacitor model from

[163] but with different boundary connections. The new boundary conditions enforced conservation of ionic flux across the layers and current in the solid and liquid phases. A set of parameters was identified for this model with the model being verified by experimental data.

Chapter 7 gave a set of convex conditions for verifying absolute stability theory of nonlinear Lur'e systems which are decentralised, sector bounded and slope restricted. A Lyapunov function was given that was quadratic on both the states and the nonlinearity and had a Lur'e term involving the integral of the nonlinearity. The main result of this chapter was to relax positive definiteness of the quadratic matrix defining the Lyapunov function and also the scaling terms of the Lur'e term. Positive definiteness of the quadratic matrix was relaxed by including information about the nonlinearity's sector into the positivity condition of the Lyapunov function and the scalars of the Lur'e terms were relaxed by using the sector conditions to bound the integral. The given stability conditions used the framework of LMIs to search for Lyapunov functions characterised by non-sign definite matrices. This work simplified many of the existing results in the literature including [20, 54, 116, 158], reducing the number of integral terms appearing in the Lyapunov functions from eight to one. Only by relaxing the positivity conditions of the Lyapunov functions could this simplified form be achieved. The presented conditions gave a convex formulation of the classical results of [177].

Chapter 8 extended the results of Chapter 7 to the case of generalised absolute stability theory. In this context, the system dynamics were allowed to be rational functions of the states and of the slope restricted nonlinearities. Sum-of-squares programming was used to construct Lyapunov functions for such systems, with the main result being that the class of Lyapunov function considered were not required to be sum-of-squares with respect to the nonlinearity.

The main contributions of this thesis were to give a richer understanding of the dynamic response of supercapacitors and to develop an efficient and effective methodology for their design. The outcomes of this research may allow better and cheaper supercapacitors to be developed which can have tailored energy storage properties. This will lead to an improvement in supercapacitor performance, driving their demand and making them applicable to a wider range of applications. It is hoped that many of the results developed in this thesis will be extended to lithium ion batteries, whose models exhibit some similar properties to supercapacitors, for example involving ionic diffusion and having sector bounded nonlinearities. Another key contribution of the

thesis was to give a novel set of convex conditions for the stability analysis of nonlinear systems, where the nonlinearity is both sector and slope restricted. This reduces the conservatism associated with nonlinear systems analysis, making its predictions more reasonable and giving a more informed idea of the dynamics of such systems.

9.2 Future Research

The following represent suggestions to further develop the results presented in this thesis as part of future research:

- The model developed in chapter 2 is derived using numerous electrochemical assumptions and simplifications from [163]. More accurate models could be constructed that remove many of these assumptions. Potential additional electrochemical phenomena that could be added include the voltage dependency of capacitance, side reactions, temperature dynamics and a leakage current. However, the inclusion of such phenomena into the model would add additional complexity, possibly making the model intractable to analyse.
- The developed supercapacitor model could be used for an actual physical application. A particular application where the use of such a high fidelity model would be of value is in a hybrid power source. The use of the PB model would enable the power management system to have a more detailed idea of the true state of the supercapacitor, allowing the system to be pushed further and to be safer. Another potential high impact application area is fault ride through, where the supercapacitor compensates for sudden power losses occurring in a wind turbine.
- Given a set of current and voltage data, it was impossible to identify all the parameters of the electrochemical model at once as many of the parameters were insensitive to the input. A rigorous identifiability analysis of the model should be applied to find the group of parameters that can theoretically be estimated from data. This may involve the non-dimensionalisation of the model which is given in [163]. This will result in a more effective identification process, with informed ideas about the limitations on what can be achieved by the parameter estimation method.
- The circuits synthesized from the electrochemical model in chapter 4 are linear, finite dimensional and passive. The literature on circuit synthesis extends to

both PDEs and nonlinear systems, with PDEs being realised by infinitely long transmission lines [67] and nonlinear resistors and circuits being used for the synthesis of nonlinear systems [29]. Synthesizing such circuits would give even more physically relevant circuits which would describe the pure electrochemical PDE relations. However, it is worth noting that the main point behind the equivalent circuit representation is the simplicity of the resulting models, and the use of such nonlinear and infinitely long circuits would destroy this simplicity. It would also be useful to obtain analytical expressions for the synthesized circuit components as functions of the electrochemical parameters. Currently, these are related numerically, as the model order reduction destroys the analytical nature of the results, but obtaining such a result would give an even greater physically intuitive interpretation of what the circuits represent.

- The work on supercapacitor design of chapter 5 is rather mathematical with the design objectives that are optimised being derived from the control literature [14]. A dialogue should be opened with electrochemists, materials scientists and those who apply supercapacitors to find out what design objective they care about the most. This may involve maximising the Pareto front on the Ragone plot or the real and imaginary capacitance as used in chapter 6 for structured electrodes. This will make the results of this analysis more relevant to engineers, driving forward the effective capability of supercapacitors for a wider range of applications.

- The analysis of chapter 5 was applicable for all input signals lying in a Hilbert space, but this work could be transformed from such a systems analysis approach into the computation of optimal charging profiles. This has been extensively studied for lithium ion batteries and will allow the supercapacitors to be implemented optimally.

- The "bump" observed in the real and imaginary capacitance values for structured electrodes are much more noticeable for the model than the experimental data. One hypothesis for this observation is that the boundary conditions of the model are much sharper than those experienced by the actual supercapacitor with structured electrodes, as the spraying technique used to manufacture the structured electrodes results in some mixing at the interface between the two layers. The proposed structured electrode model should be modified to include this phenomenon via the inclusion of an additional layer to act as a "mixing layer". Another approach to structured electrode design would be allow the variation

of the porosity of electrode to vary continuously, with an optimal porosity distribution being obtained. As porosity varies, the interaction of the ions in the pores would fundamentally change and the new parameters would have to be homogenized using the methods of [16]. Even though a continuously varying porosity distribution cannot yet be manufactured, this result would show the theoretically optimal electrode structure. Another key extension would be to obtain a physical reason for the improved high frequency capacitance properties exhibited by supercapacitors with structured electrodes, as currently this result is only an observation.

- The results on absolute stability theory of chapters 7 and 8 have opened a number of potential avenues of research. These include obtaining a graphical representation for the proposed stability conditions in terms of the phase of the transfer function as in [42, 177]. This graphical representation will allow the proposed conditions to be evaluated against Zames-Falb multipliers using the phase equivalence concept of [20]. The analysis could be extended to discrete time systems through an extension of the Tsypkin criterion [87]. By using coordinate transformations and the symmetrical state-space realisations of the transfer function, it may be possible to verify the stability conditions via the satisfaction of a single inequality, not a LMI. This will allow a Lyapunov function to obtained for the system even if an infinite sector is used. The conditions for the existence of a Lyapunov function could be extended to a contraction analysis, such that the stability results would be independent of the existence of a fixed equilibrium point. Using the integral inequalities of [159], it may be possible to extend the results to distributed parameter systems defined by PDEs. A long term aim would be to extend the stability results for signals in Sobolov spaces, which should allow Lyapunov functions to be constructed for higher order Zames-Falb multipliers. However, issues regarding the convexity of such conditions need to be addressed.

- The results of chapters 7 and 8 considered systems analysis but could be extended to optimal robust controller design. The resulting controllers should give improved performance over classical results in the control literature, as the controllers will be derived using additional information about the nonlinearity as expressed by the slope condition.

Bibliography

[1] M.A. Aizerman and F.R. Gantmacher. *Absolute Stability of Regulator Systems*. Holden-Day. Oakland, CA, 1964.

[2] M. Al Sakka, H. Gualous, J.I. Van Mierlo, and H. Culcu. Thermal modeling and heat management of supercapacitor modules for vehicle applications. *Journal of Power Sources*, 194(2):581–587, 2009.

[3] S. Allu, B. Velamur Asokan, W.A. Shelton, B. Philip, and S. Pannala. A generalized multi-dimensional mathematical model for charging and discharging processes in a supercapacitor. *Journal of Power Sources*, 256(0):369 – 382, 2014.

[4] A.C. Antoulas, D.C. Sorensen, and S. Gugercin. A survey of model reduction methods for large-scale systems. *Contemporary Mathematics*, 280:193–220, 2001.

[5] K.J. Aström and R.M. Murray. *Feedback Systems: An Introduction for Scientists and Engineers*. Princeton university press, Princeton, NJ, 2010.

[6] A. Berrueta, I. San Martín, A. Hernández, A. Ursúa, and P. Sanchis. Electrothermal modelling of a supercapacitor and experimental validation. *Journal of Power Sources*, 259:154–165, 2014.

[7] J.O. Besenhard and M. Winter. Advances in battery technology: Rechargeable magnesium batteries and novel negative-electrode materials for lithium ion batteries. *ChemPhysChem*, 3(2):155–159, 2002.

[8] A. Bizeray, S.R. Duncan, and D.A. Howey. Advanced battery management systems using fast electrochemical modelling. In *Proc. of the IET Hybrid and Electric Vehicles Conference*, pages 1–6. London, UK. IET, 2013.

[9] A.M. Bizeray, S. Zhao, S.R. Duncan, and D.A. Howey. Lithium-ion battery thermal-electrochemical model-based state estimation using orthogonal colloca-

tion and a modified extended Kalman filter. *Journal of Power Sources*, 296:400–412, 2015.

[10] H. Bode. Lead-acid batteries, John Wiley and Sons, Inc., New York, NY. 1977.

[11] R. Bott and R.J. Duffin. Impedance synthesis without use of transformers. *Journal of Applied Physics*, 20(8):816–816, 1949.

[12] J.P. Boyd. *Chebyshev and Fourier spectral methods*. Courier Corporation, North Chelmsford, MA, 2001.

[13] S. Boyd and L. Vandenberghe. *Convex Optimization*. Cambridge University Press. Cambridge, UK, 2004.

[14] S.P. Boyd, L. El Ghaoui, E. Feron, and V. Balakrishnan. *Linear Matrix Inequalities in System and Control Theory*, volume 15. SIAM, Philadelphia, PA, 1994.

[15] M. Bruna, M. Burger, H. Ranetbauer, and M-T. Wolfram. Cross-diffusion systems with excluded-volume effects and asymptotic gradient flow structures. *Journal of Nonlinear Science*, 27(2):687–719, 2016.

[16] M. Bruna and S.J. Chapman. Diffusion in spatially varying porous media. *arXiv preprint arXiv:1501.06549*, 2015.

[17] O. Brune. *Synthesis of a Finite Two-Terminal Network Whose Driving-Point Impedance is a Prescribed Function of Frequency*. PhD thesis, Massachusetts Institute of Technology, Cambridge, MA, 1931.

[18] S. Buller, M. Thele, R.W.A. A. De Doncker, and E. Karden. Impedance-based simulation models of supercapacitors and Li-ion batteries for power electronic applications. *IEEE Transactions on Industry Applications*, 41(3):742–747, 2005.

[19] A. Burke. Ultracapacitors: Why, how, and where is the technology. *Journal of Power Sources*, 91(1):37–50, 2000.

[20] J. Carrasco, W.P. Heath, and A. Lanzon. Equivalence between classes of multipliers for slope-restricted nonlinearities. *Automatica*, 49(6):1732–1740, 2013.

[21] J. Carrasco, M.C. Turner, and W.P. Heath. Zames-Falb multipliers for absolute stability: From O'Shea's contribution to convex searches. *European Journal of Control*, 28:1 – 19, 2016.

[22] P.D. Cha, J.J. Rosenberg, and C.L. Dym. *Fundamentals of Modeling and Analyzing Engineering Systems*. Cambridge University Press, Cambridge, UK, 2000.

[23] N.A. Chaturvedi, R. Klein, J. Christensen, J. Ahmed, and A. Kojic. Algorithms for advanced battery-management systems. *IEEE Control Systems Magazine*, 30(3):49–68, 2010.

[24] M.Z.Q. Chen and M.C. Smith. *Electrical and Mechanical Passive Network Synthesis*, pages 35–50. Springer London, London, UK, 2008.

[25] G. Chesi. Estimating the domain of attraction for non-polynomial systems via LMI optimizations. *Automatica*, 45(6):1536–1541, 2009.

[26] T. Christen and M.W. Carlen. Theory of Ragone plots. *Journal of Power Sources*, 91(2):210–216, 2000.

[27] T. Christen and C. Ohler. Optimizing energy storage devices using Ragone plots. *Journal of Power Sources*, 110(1):107–116, 2002.

[28] A. Chu and P. Braatz. Comparison of commercial supercapacitors and high-power lithium-ion batteries for power-assist applications in hybrid electric vehicles: I. Initial characterization. *Journal of Power Sources*, 112(1):236–246, 2002.

[29] L.O. Chua. Synthesis of new nonlinear network elements. *Proceedings of the IEEE*, 56(8):1325–1340, 1968.

[30] B.E. Conway. *Electrochemical Supercapacitors: Scientific Fundamentals and Technological Applications*. Springer Science & Business Media. Berlin, Germany, 2013.

[31] B.E. Conway, V. Birss, and J. Wojtowicz. The role and utilization of pseudocapacitance for energy storage by supercapacitors. *Journal of Power Sources*, 66(1):1–14, 1997.

[32] B.E. Conway and W.G. Pell. Double-layer and pseudocapacitance types of electrochemical capacitors and their applications to the development of hybrid devices. *Journal of Solid State Electrochemistry*, 7(9):637–644, 2003.

[33] R.F. Curtain and H. Zwart. *An Introduction to Infinite-Dimensional Linear Systems Theory*, volume 21. Springer Science & Business Media. Berlin, Germany, 1995.

[34] J.M. Gomes da Silva Jr and S. Tarbouriech. Local stabilization of discrete-time linear systems with saturating controls: An LMI-based approach. *IEEE Transactions on Automatic Control,*, 46(1):119–125, 2001.

[35] D. Dai, T. Hu, A.R. Teel, and L. Zaccarian. Piecewise-quadratic Lyapunov functions for systems with deadzones or saturations. *Systems & Control Letters*, 58(5):365–371, 2009.

[36] Y. Dai and V. Srinivasan. On graded electrode porosity as a design tool for improving the energy density of batteries. *Journal of the Electrochemical Society*, 163(3):A406–A416, 2016.

[37] S. De, P.W.C. Northrop, V. Ramadesigan, and V.R. Subramanian. Model-based simultaneous optimization of multiple design parameters for lithium-ion batteries for maximization of energy density. *Journal of Power Sources*, 227:161–170, 2013.

[38] R. De Levie. On porous electrodes in electrolyte solutions: I. Capacitance effects. *Electrochimica Acta*, 8(10):751–780, 1963.

[39] A. d'Entremont and L. Pilon. First-order thermal model of commercial EDLCs. *Applied Thermal Engineering*, 67(1):439–446, 2014.

[40] N. Devillers, S. Jemei, M. Péra, D. Bienaimé, and F. Gustin. Review of characterization methods for supercapacitor modelling. *Journal of Power Sources*, 246:596–608, 2014.

[41] A.G. Dewey. On the stability of feedback systems with one differentiable nonlinear element. *IEEE Transactions on Automatic Control*, 11(3):485–491, 1966.

[42] A.G. Dewey and E.I. Jury. A stability inequality for a class of nonlinear feedback systems. *IEEE Transactions on Automatic Control,*, 11(1):54–62, 1966.

[43] F. Díaz-González, A. Sumper, O. Gomis-Bellmunt, and R. Villafáfila-Robles. A review of energy storage technologies for wind power applications. *Renewable and sustainable energy reviews*, 16(4):2154–2171, 2012.

[44] M. Doyle, T.F. Fuller, and J. Newman. Modeling of galvanostatic charge and discharge of the lithium/polymer/insertion cell. *Journal of the Electrochemical Society*, 140(6):1526–1533, 1993.

[45] R. Drummond and S.R. Duncan. A Lyapunov function for a PDE model of a supercapacitor. *In Proc. of the Control and Decision Conference*, Osaka, Japan, 2015.

[46] R. Drummond, D.A. Howey, and S.R. Duncan. Low-order mathematical modelling of electric double layer supercapacitors using spectral methods. *Journal of Power Sources*, 277:317–328, 2015.

[47] R. Drummond, D.A. Howey, and S.R. Duncan. Parameter estimation of an electrochemical supercapacitor model. In *Proc. of the European Control Conference*, pages 1–6. Aarlberg, Denmark, 2016.

[48] G. Dullerud and F. Paganini. *Course in Robust Control Theory*. Springer-Verlag New York, New York, NY, 2000.

[49] A. Dzielinski and D. Sierociuk. Ultracapacitor modelling and control using discrete fractional order state-space model. *Acta Montanistica Slovaca*, 13(1):136–145, 2008.

[50] M. W Ellis, M.R. Von Spakovsky, and D.J. Nelson. Fuel cell systems: Efficient, flexible energy conversion for the 21st century. *Proceedings of the IEEE*, 89(12):1808–1818, 2001.

[51] V. Etacheri, R. Marom, R. Elazari, G. Salitra, and D. Aurbach. Challenges in the development of advanced Li-ion batteries: A review. *Energy & Environmental Science*, 4(9):3243–3262, 2011.

[52] H. Farsi and F. Gobal. Artificial neural network simulator for supercapacitor performance prediction. *Computational Materials Science*, 39(3):678–683, 2007.

[53] G. Feng, R. Qiao, J. Huang, B.G. Sumpter, and V. Meunier. Atomistic insight on the charging energetics in subnanometer pore supercapacitors. *Journal of Physical Chemistry C*, 114(41):18012–18016, 2010.

[54] M. Fetzer and C.W. Scherer. Full-block multipliers for repeated, slope restricted scalar nonlinearities. *International Journal on Robust and Nonlinear Control (submitted)*, 2016.

[55] S.D.A. Fletcher, P. Norman, S. Galloway, P. Rakhra, G. Burt, and V. Lowe. Modeling and simulation enabled UAV electrical power system design. *SAE International Journal of Aerospace*, 4(2011-01-2645):1074–1083, 2011.

[56] T. F Fuller, M. Doyle, and J. Newman. Simulation and optimization of the dual lithium ion insertion cell. *Journal of the Electrochemical Society*, 141(1):1–10, 1994.

[57] A. Garulli, A. Masi, G. Valmorbida, and L. Zaccarian. Global stability and finite $\mathcal{L}_{2m}$-gain of saturated uncertain systems via piecewise polynomial Lyapunov functions. *IEEE Transactions on Automatic Control*, 58(1):242–246, 2013.

[58] S.I. Gkavanoudis and C.S. Demoulias. A combined fault ride-through and power smoothing control method for full-converter wind turbines employing supercapacitor energy storage system. *Electric Power Systems Research*, 106:62–72, 2014.

[59] S. Golmon, K. Maute, and M.L. Dunn. A design optimization methodology for Li+ batteries. *Journal of Power Sources*, 253:239–250, 2014.

[60] E.A. Guillemin. *Synthesis of Passive Networks: Theory and Methods Appropriate to the Realization and Approximation Problems*. Wiley New York, New York, NY, 1957.

[61] S.V. Gusev and A.L. Likhtarnikov. Kalman-Popov-Yakubovich lemma and the S-procedure: A historical essay. *Automation and Remote Control*, 67(11):1768–1810, 2006.

[62] A. Halanay and V. Rasvan. Absolute stability of feedback systems with several differentiable non-linearities. *International Journal of Systems Science*, 22(10):1911–1927, 1991.

[63] E.J. Hancock and A. Papachristodoulou. Generalised absolute stability and sum of squares. *Automatica*, 49(4):960–967, 2013.

[64] J. Hauser and B. Bamieh. Dynamics of a driven Stirling engine. In *Proc. of the 54th IEEE Conference on Decision and Control*, pages 3730–3735. Osaka, Japan. IEEE, 2015.

[65] C.S. Hearn, M.C. Lewis, R.C. Thompson, and R.G. Longoria. Modeling and evaluation of a plug-in hybrid fuel cell shuttle bus. In *Proc. of the IEEE Vehicle Power and Propulsion Conference*, pages 221–228. Dearborn, MI. IEEE, 2009.

[66] W.P. Heath and G. Li. Lyapunov functions for the multivariable Popov criterion with indefinite multipliers. *Automatica*, 45(12):2977–2981, 2009.

[67] J.W. Helton. Systems with infinite-dimensional state space: The Hilbert space approach. *Proceedings of the IEEE*, 64(1):145–160, 1976.

[68] D. Henrion and A. Garulli. *Positive Polynomials in Control*. Springer-Verlag Berlin Heidelberg. Berlin, Germany, 2005.

[69] H. Hindi and S. Boyd. Analysis of linear systems with saturation using convex optimization. In *Proc. of the Control and Decision Conference*, pages 903–908. Tampa, FL, 1998.

[70] T. Hu, B. Huang, and Z. Lin. Absolute stability with a generalized sector condition. *IEEE Transactions on Automatic Control*, 49(4):535–548, April 2004.

[71] T. Hu, A.R. Teel, and L. Zaccarian. Stability and performance for saturated systems via quadratic and nonquadratic Lyapunov functions. *IEEE Transactions on Automatic Control*, 51(11):1770–1786, 2006.

[72] C. Huang and P.S. Grant. One-step spray processing of high power all-solid-state supercapacitors. *Scientific Reports*, 3, 2013.

[73] C. Huang, N. Grobert, A.A.R. Watt, C. Johnston, A. Crossley, N.P. Young, and P.S. Grant. Layer-by-layer spray deposition and unzipping of single-wall carbon nanotube-based thin film electrodes for electrochemical capacitors. *Carbon*, 61:525–536, 2013.

[74] C. Huang, N.P. Young, J. Zhang, H.J. Snaith, and P.S. Grant. A two layer electrode structure for improved Li ion diffusion and volumetric capacity in Li ion batteries. *Nano Energy*, 2016.

[75] C. Huang, J. Zhang, H.J. Snaith, and P.S. Grant. Engineering the membrane/electrode interface to improve the performance of solid-state supercapacitors. *ACS Applied Materials & Interfaces*, 8(32):20756–20765, 2016.

[76] J. Huang, R. Qiao, B.G. Sumpter, and V. Meunier. Effect of diffuse layer and pore shapes in mesoporous carbon supercapacitors. *Journal of Materials Research*, 25(08):1469–1475, 2010.

[77] H. Ibrahim, A. Ilinca, and J. Perron. Energy storage systems: Characteristics and comparisons. *Renewable and Sustainable Energy Reviews*, 12(5):1221–1250, 2008.

[78] D. Jiang, Z. Jin, and J. Wu. Oscillation of capacitance inside nanopores. *Nano letters*, 11(12):5373–5377, 2011.

[79] D. Jiang, D. Meng, and J. Wu. Density functional theory for differential capacitance of planar electric double layers in ionic liquids. *Chemical Physics Letters*, 504(4):153–158, 2011.

[80] A.M. Johnson and J. Newman. Desalting by means of porous carbon electrodes. *Journal of the Electrochemical Society*, 118(3):510–517, 1971.

[81] B. Johnston, M.C. Mayo, and A. Khare. Hydrogen: The energy source for the 21^{st} century. *Technovation*, 25(6):569–585, 2005.

[82] U. Jönsson. Lecture notes on integral quadratic constraints. *Department of Mathematics, KTH, Stockholm*, ISBN 1401-2294, 2000.

[83] U. Jönsson and A. Megretski. The Zames-Falb IQC for systems with integrators. *IEEE Transactions on Automatic Control*, 45(3):560–565, 2000.

[84] R. Josselson and G.V.S. Raju. Absolute stability of control systems with many sector and slope-restricted non-linearities. *International Journal of Control*, 19(3):609–614, 1974.

[85] M. Jun, K. Smith, and P. Graf. State-space representation of Li-ion battery porous electrode impedance model with balanced model reduction. *Journal of Power Sources*, 273:1226–1236, 2015.

[86] R.E. Kalman. Physical and mathematical mechanisms of instability in nonlinear automatic control systems. *Transactions of the ASME*, 79(3):553–566, 1957.

[87] V. Kapila and W.M. Haddad. A multivariable extension of the Tsypkin criterion using a Lyapunov-function approach. *IEEE Transactions on Automatic Control*, 41(1):149–152, 1996.

[88] A. Khaligh and Z. Li. Battery, ultracapacitor, fuel cell, and hybrid energy storage systems for electric, hybrid electric, fuel cell, and plug-in hybrid electric vehicles: State of the art. *IEEE Transactions on Vehicular Technology*, 59(6):2806–2814, 2010.

[89] H. Khalil and J.W. Grizzle. *Nonlinear Systems*. 3^{rd} edition. Prentice Hall. Upper Saddle River, NJ, 2002.

[90] M. Sabri Kilic, M.Z. Bazant, and A. Ajdari. Steric effects in the dynamics of electrolytes at large applied voltages. I. Double-layer charging. *Physical Review E*, 75(2):021502, 2007.

[91] J.W. Kimball, B.T. Kuhn, and P.T. Krein. Increased performance of battery packs by active equalization. In *Proc. of the IEEE Vehicle Power and Propulsion Conference*, pages 323–327. Arlington, TX. IEEE, 2007.

[92] S.A. Kislenko, R.H. Amirov, and I.S. Samoylov. Molecular dynamics simulation of the electrical double layer in ionic liquids. *Journal of Physics: Conference Series*, 418(1):12:21, 2013.

[93] Z. Li, Z. Xu, H. Wang, J. Ding, B. Zahiri, C.M.B. Holt, X. Tan, and D. Mitlin. Colossal pseudocapacitance in a high functionality–high surface area carbon anode doubles the energy of an asymmetric supercapacitor. *Energy & Environmental Science*, 7(5):1708–1718, 2014.

[94] L. Ljung. System Identification. In *Signal Analysis and Prediction*, pages 163–173. Springer. Berlin, Germany, 1998.

[95] M. Lu, F. Beguin, and E. Frackowiak. *Supercapacitors: Materials, Systems and Applications*. John Wiley & Sons, Oxford, UK. 2013.

[96] A.I. Lur'e and V.N. Postnikov. On the theory of stability of control system. *Applied Mathematics and Mechanics*, 8(3), 1944.

[97] G. Madabattula and S.K. Gupta. Modeling of supercapacitor. In *Proc. of the 2012 COMSOL Conference*, Bangalore, India, 2012.

[98] M.I. Masouleh and D.J.N. Limebeer. Non-linear vehicle domain of attraction analysis using Sum-of-Squares programming. In *IEEE Conference on Control Applications*, pages 1209–1214. IEEE, 2016.

[99] S. Mastellone, P.F. Hokayem, C.T. Abdallah, and P. Dorato. Nonlinear stability analysis for non-polynomial systems. In *Proc. of the American Control Conference*, pages 1725–1730. Bostan, MA. IEEE, 2004.

[100] A. Megretski and A. Rantzer. System analysis via integral quadratic constraints. *IEEE Transactions on Automatic Control*, 42(6):819–830, 1997.

[101] R.N. Methekar, V. Boovaragavan, M. Arabandi, V. Ramadesigan, V.R. Subramanian, F. Latinwo, and R.D. Braatz. Optimal spatial distribution of microstructure in porous electrodes for Li-ion batteries. In *Proceedings of the American Control Conference*, pages 6600–6605. Baltimore, MD. IEEE, 2010.

[102] C.W. Monroe, M. Urbakh, and A.A. Kornyshev. Double-layer effects in electrowetting with two conductive liquids. *Journal of the Electrochemical Society*, 156(1):P21–P28, 2009.

[103] A.P.S. MOSEK. *The MOSEK optimization toolbox for MATLAB manual. Version 7.1 (Revision 28).*, 2015.

[104] S.J. Moura, N.A. Chaturvedi, and M. Krstić. Adaptive partial differential equation observer for battery state-of-charge/state-of-health estimation via an electrochemical model. *Journal of Dynamic Systems, Measurement, and Control*, 136(1):011015, 2014.

[105] COMSOL Multiphysics. 4.3 User Guide, COMSOL. 2012.

[106] A. Nadeau, G. Sharma, and T. Soyata. State-of-charge estimation for supercapacitors: A Kalman filtering formulation. In *Proc. of the IEEE International Conference on Acoustics, Speech and Signal Processing*, pages 2194–2198. IEEE, 2014.

[107] J. Newman. Optimization of porosity and thickness of a battery electrode by means of a reaction-zone model. *Journal of the Electrochemical Society*, 142(1):97–101, 1995.

[108] J. Newman, K.E. Thomas, H. Hafezi, and D.R. Wheeler. Modeling of lithium-ion batteries. *Journal of Power Sources*, 119:838–843, 2003.

[109] P. Novák, R. Imhof, and O. Haas. Magnesium insertion electrodes for rechargeable nonaqueous batteries: A competitive alternative to lithium? *Electrochimica Acta*, 45(1):351–367, 1999.

[110] S. Ober-Blöbaum and H. Lindhorst. Variational integrators for nonlinear electric circuits. *PAMM*, 14(1):921–922, 2014.

[111] T. Ohzuku and R.J. Brodd. An overview of positive-electrode materials for advanced lithium-ion batteries. *Journal of Power Sources*, 174(2):449–456, 2007.

[112] N. Oreskes. The scientific consensus on climate change. *Science*, 306(5702):1686–1686, 2004.

[113] R.E. O'Shea. An improved frequency-time domain stability criterion for autonomous continuous systems. *IEEE Transactions on Automatic Control*, 12(6):725–731, 1967.

[114] H. Pacejka. *Tire and Vehicle Dynamics*. 2^{nd} edition. Butterworth-Heinemann. Oxford, UK., 2005.

[115] P. Park. A revisited Popov criterion for nonlinear Lur'e systems with sector-restrictions. *International Journal of Control*, 68(3):461–470, 1997.

[116] P. Park. Stability criteria of sector- and slope-restricted Lur'e systems. *IEEE Transactions on Automatic Control*, 47(2):308–313, Feb 2002.

[117] P.A. Parrilo. *Structured semidefinite programs and semialgebraic geometry methods in robustness and optimization*. PhD thesis, California Institute of Technology, Pasadena, CA, 2000.

[118] Y. Parvini, J.B. Siegel, A.G. Stefanopoulou, and A. Vahidi. Preliminary results on identification of an electro-thermal model for low temperature and high power operation of cylindrical double layer ultracapacitors. In *Proc. of the American Control Conference*, pages 242–247, Portland, OR, 2014. IEEE.

[119] C Pean, B Rotenberg, P Simon, and M Salanne. Multi-scale modelling of supercapacitors: From molecular simulations to a transmission line model. *Journal of Power Sources*, 326:680–685, 2016.

[120] D. Qu. Studies of the activated carbons used in double-layer supercapacitors. *Journal of Power Sources*, 109(2):403–411, 2002.

[121] J.J. Quintana, A. Ramos, and I. Nuez. Identification of the fractional impedance of ultracapacitors. *IFAC Proceedings Volumes*, 39(11):432–436, 2010.

[122] S. Raël and M. Hinaje. Using electrical analogy to describe mass and charge transport in lithium-ion batteries. *Journal of Power Sources*, 222:112–122, 2013.

[123] F. Rafik, H. Gualous, R. Gallay, A. Crausaz, and A. Berthon. Frequency, thermal and voltage supercapacitor characterization and modeling. *Journal of Power Sources*, 165(2):928–934, 2007.

[124] V. Ramadesigan, R.N. Methekar, F. Latinwo, R.D. Braatz, and V.R. Subramanian. Optimal porosity distribution for minimized ohmic drop across a porous electrode. *Journal of the Electrochemical Society*, 157(12):A1328–A1334, 2010.

[125] V. Ramadesigan, P.W.C. Northrop, S. De, S. Santhanagopalan, R.D Braatz, and V.R. Subramanian. Modeling and simulation of lithium-ion batteries from a systems engineering perspective. *Journal of the Electrochemical Society*, 159(3):R31–R45, 2012.

[126] A. Rantzer. On the Kalman-Yakubovich-Popov lemma. *Systems & Control Letters*, 28(1):7–10, 1996.

[127] B.W. Ricketts and C. Ton-That. Self-discharge of carbon-based supercapacitors with organic electrolytes. *Journal of Power Sources*, 89(1):64–69, 2000.

[128] D.B. Robinson. Optimization of power and energy densities in supercapacitors. *Journal of Power Sources*, 195(11):3748–3756, 2010.

[129] D.R. Rolison and L.F. Nazar. Electrochemical energy storage to power the 21^{st} century. *MRS Bulletin*, 36(07):486–493, 2011.

[130] A. Romero-Becerril and L. Alvarez-Icaza. Reduced order dynamical model for supercapacitors. In *Proc. of the 7th IEEE International Conference on Electrical Engineering Computing Science and Automatic Control (CCE)*, pages 71–76, Tuxtla Gutierrez, Mexico, 2010.

[131] M. Safonov. Computer-aided stability analysis renders Popov criterion obsolete. *IEEE Transactions on Automatic Control*, 32(12):1128–1131, 1987.

[132] V.R. Sastry. Finite regions of attraction for the problem of Lur'e. *International Journal of Control*, 14(4):789–790, 1971.

[133] A.P. Schmidt, M. Bitzer, A.W. Imre, and L. Guzzella. Experiment-driven electrochemical modeling and systematic parameterization for a lithium-ion battery cell. *Journal of Power Sources*, 195(15):5071 – 5080, 2010.

[134] B. Scrosati and J. Garche. Lithium batteries: Status, prospects and future. *Journal of Power Sources*, 195(9):2419–2430, 2010.

[135] L.F. Shampine and M.W. Reichelt. The Matlab ODE Suite. *SIAM Journal on Scientific Computing*, 18(1):1–22, 1997.

[136] L.F. Shampine, M.W. Reichelt, and J.A. Kierzenka. Solving index-1 DAEs in MATLAB and Simulink. *SIAM Review*, 41(3):538–552, 1999.

[137] P. Sharma and T.S. Bhatti. A review on electrochemical double-layer capacitors. *Energy Conversion and Management*, 51(12):2901–2912, 2010.

[138] D. Sheberla, J.C. Bachman, J.S. Elias, C-J. Sun, Yang S-H., and M. Dincă. Conductive MOF electrodes for stable supercapacitors with high areal capacitance. *to appear in Nature Materials*, 2016.

[139] L. Shi and M.L. Crow. Comparison of ultracapacitor electric circuit models. In . *Berlin, GermanyProc. of th Power and Energy Society General Meeting-Conversion and Delivery of Electrical Energy in the 21st Century.*, pages 1–6. Pittsburgh, PA. IEEE, 2008.

[140] R.E. Smalley. Future global energy prosperity: The terawatt challenge. *MRS Bulletin*, 30(06):412–417, 2005.

[141] K.A Smith, C. D. Rahn, and C.Y. Wang. Control oriented 1D electrochemical model of lithium ion battery. *Energy Conversion and Management*, 48(9):2565–2578, 2007.

[142] M.C. Smith. Synthesis of mechanical networks: The inerter. *IEEE Transactions on Automatic Control*, 47(10):1648–1662, 2002.

[143] R. L. Spyker and R. M. Nelms. Classical equivalent circuit parameters for a double-layer capacitor. *IEEE Transactions on Aerospace and Electronic Systems,*, 36(3):829–836, 2000.

[144] V. Srinivasan and J.W. Weidner. Mathematical modeling of electrochemical capacitors. *Journal of the Electrochemical Society*, 146(5):1650–1658, 1999.

[145] B.C.H. Steele and A. Heinzel. Materials for fuel-cell technologies. *Nature*, 414(6861):345–352, 2001.

[146] B. Suthar, P.W.C. Northrop, R.D. Braatz, and V.R. Subramanian. Optimal charging profiles with minimal intercalation-induced stresses for lithium-ion batteries using reformulated pseudo 2-dimensional models. *Journal of the Electrochemical Society*, 161(11):F3144–F3155, 2014.

[147] B. Suthar, P.W.C. Northrop, D. Rife, and V.R. Subramanian. Effect of porosity, thickness and tortuosity on capacity fade of anode. *Journal of the Electrochemical Society*, 162(9):A1708–A1717, 2015.

[148] B. Suthar, V. Ramadesigan, S. De, R.D. Braatz, and V.R. Subramanian. Optimal charging profiles for mechanically constrained lithium-ion batteries. *Physical Chemistry Chemical Physics*, 16(1):277–287, 2014.

[149] B. Suthar, V. Ramadesigan, P.W.C. Northrop, B. Gopaluni, S. Santhanagopalan, R.D. Braatz, and V.R. Subramanian. Optimal control and state estimation of lithium-ion batteries using reformulated models. In *Proc. of the American Control Conference*, pages 5350–5355. IEEE, Washington D.C., 2013.

[150] J.A.K. Suykens, J. Vandewalle, and B. De Moor. An absolute stability criterion for the Lur'e problem with sector and slope restricted nonlinearities. *IEEE Transactions on Circuits and Systems. Part I: Fundamental Theory and Applications*, 45:1007–1009, 1998.

[151] P.L. Taberna, P. Simon, and J-F. Fauvarque. Electrochemical characteristics and impedance spectroscopy studies of carbon-carbon supercapacitors. *Journal of The Electrochemical Society*, 150(3):A292–A300, 2003.

[152] M.M. Thackeray, C. Wolverton, and E.D. Isaacs. Electrical energy storage for transportation: Approaching the limits of, and going beyond, lithium-ion batteries. *Energy & Environmental Science*, 5(7):7854–7863, 2012.

[153] P. Thounthong, S. Raël, and B. Davat. Control strategy of fuel cell/supercapacitors hybrid power sources for electric vehicle. *Journal of Power Sources*, 158(1):806–814, 2006.

[154] P. Thounthong, S. Rael, and B. Davat. Energy management of fuel cell/battery/supercapacitor hybrid power source for vehicle applications. *Journal of Power Sources*, 193(1):376–385, 2009.

[155] D. Torregrossa, M. Bahramipanah, E. Namor, R. Cherkaoui, and M. Paolone. Improvement of dynamic modeling of supercapacitor by residual charge effect estimation. *IEEE Transactions on Industrial Electronics*, 61(3):1345–1354, 2014.

[156] L.N. Trefethen. *Spectral Methods in MATLAB*. SIAM, Philadelphia, PA, 2000.

[157] U. Tröltzsch, O. Kanoun, and H.R. Tränkler. Characterizing aging effects of lithium ion batteries by impedance spectroscopy. *Electrochimica Acta*, 51(8):1664–1672, 2006.

[158] M. C. Turner and M. Kerr. Lyapunov functions and $\mathcal{L}_2$ gain bounds for systems with slope restricted nonlinearities. *Systems & Control Letters*, 69:1–6, 2014.

[159] G. Valmorbida, M. Ahmadi, and A. Papachristodoulou. Semi-definite programming and functional inequalities for distributed parameter systems. In *Poc. of the Conference on Decision and Control*, pages 4304–4309. Los Angeles, CA. IEEE, 2014.

[160] G. Valmorbida, R. Drummond, and S.R. Duncan. Positivity conditions of Lyapunov functions for systems with slope restricted nonlinearities. In *Proc. of the American Control Conference*, pages 258–263. Boston, MA, 2016.

[161] J. Varghese, H. Wang, and L. Pilon. Simulating electric double layer capacitance of mesoporous electrodes with cylindrical pores. *Journal of The Electrochemical Society*, 158(10):A1106–A1114, 2011.

[162] M. Verbrugge and H. Gu. Finite difference routines for one and two dimensional problems utilizing a functional programming style. In *Proc. of the Douglas N. Bennion Memorial Symposium: Topics in Electrochemical Engineering*, volume 94, pages 153–188, Los Angeles, CA. 1994.

[163] M.W. Verbrugge and P. Liu. Microstructural analysis and mathematical modeling of electric double-layer supercapacitors. *Journal of The Electrochemical Society*, 152(5):D79–D87, 2005.

[164] J. Vetter, P. Novák, M.R. Wagner, C. Veit, K.C. Möller, J.O. Besenhard, M. Winter, M. Wohlfahrt-Mehrens, C. Vogler, and A. Hammouche. Ageing mechanisms in lithium-ion batteries. *Journal of Power Sources*, 147(1):269–281, 2005.

[165] M. Vidyasagar. *Nonlinear Systems Analysis*, volume 42. SIAM. Philadelphia, PA, 2002.

[166] C. L. Wadhwa. *Network Analysis & Synthesis (Including Linear System Analysis)*. New Age International, New Delhi, India, 2007.

[167] J. A. Walker and N.H. McClamroch. Finite regions of attraction for the problem of Lur'e. *International Journal of Control*, 6(4):331–336, 1967.

[168] Q. Wang, P. Ping, X. Zhao, G. Chu, J. Sun, and C. Chen. Thermal runaway caused fire and explosion of lithium ion battery. *Journal of Power Sources*, 208:210–224, 2012.

[169] J.A. Weideman and S.C. Reddy. A matlab differentiation matrix suite. *ACM Transactions on Mathematical Software*, 26(4):465–519, 2000.

[170] S. Weissenberger. Application of results from the absolute stability problem to the computation of finite stability domains. *IEEE Transactions on Automatic Control*, 13(1):124–125, 1968.

[171] J. C. Willems. Dissipative dynamical systems part I: General theory. *Archive for rational mechanics and analysis*, 45(5):321–351, 1972.

[172] N. Williard, W. He, C. Hendricks, and M. Pecht. Lessons learned from the 787 Dreamliner issue on lithium-ion battery reliability. *Energies*, 6(9):4682–4695, 2013.

[173] M. Winter and R.J Brodd. What are batteries, fuel cells, and supercapacitors? *Chemical Reviews*, 104(10):4245–4270, 2004.

[174] B. C Wood, T. Ogitsu, M. Otani, and J. Biener. First-principles-inspired design strategies for graphene-based supercapacitor electrodes. *Journal of Physical Chemistry C*, 118(1):4–15, 2013.

[175] M.R. Wright. *An Introduction to Aqueous Electrolyte Solutions*. John Wiley & Sons. Oxford, UK, 2007.

[176] B. Wu, M.A. Parkes, V. Yufit, L. De Benedetti, S. Veismann, C. Wirsching, F. Vesper, R.F. Martinez-Botas, A.J. Marquis, G.J. Offer, and N.P. Brandon. Design and testing of a 9.5 kwe proton exchange membrane fuel cell/supercapacitor passive hybrid system. *International Journal of Hydrogen Energy*, 39(15):7885 – 7896, 2014.

[177] V.A. Yakubovich. The method of matrix inequalities in the stability theory of nonlinear control systems: II. Absolute stability in a class of nonlinearities with a condition on the derivative. *Avtom. i Telemech.*, 26:577–592, 1965.

[178] J. Yan, Q. Wang, T. Wei, and Z. Fan. Recent advances in design and fabrication of electrochemical supercapacitors with high energy densities. *Advanced Energy Materials*, 4(4), 2014.

[179] Chen G.Z. Yu, L. Redox electrode materials for supercapatteries. *Journal of Power Sources*, 326:604–612, 2016.

[180] L. Zaccarian and A.R. Teel. A common framework for anti-windup, bumpless transfer and reliable designs. *Automatica*, 38(10):1735–1744, 2002.

[181] L. Zaccarian and A.R. Teel. *Modern Anti-windup Synthesis: Control Augmentation for Actuator Saturation*. Princeton University Press. Princeton, NJ, 2011.

[182] G. Zames and P.L. Falb. Stability conditions for systems with monotone and slope-restricted nonlinearities. *SIAM Journal on Control*, 6(1):89–108, 1968.

[183] F. Zhang, H. Trentelman, and J. Scherpen. Dynamic feedback synchronization of Lur'e networks via incremental sector boundedness. *IEEE Transactions on Automatic Control*, 61(9):2579–2584, 2016.

[184] L. Zhang, X. Hu, Z. Wang, F. Sun, and D.G. Dorrell. Experimental impedance investigation of an ultracapacitor at different conditions for electric vehicle applications. *Journal of Power Sources*, 287:129 – 138, 2015.

[185] L. Zhang, Z. Wang, X. Hu, F. Sun, and D.G. Dorrell. A comparative study of equivalent circuit models of ultracapacitors for electric vehicles. *Journal of Power Sources*, 274:899–906, 2015.

[186] L. Zhang, Z. Wang, F. Sun, and D. Dorrell. Ultracapacitor modelling and parameter identification using the extended Kalman filter. In *Proc. of the Transportation Electrification Asia-Pacific Conference and Expo*, pages 1–6. IEEE, Beijing, China, 2014.

[187] L. Zhang, Z. Wang, F Sun, and D.G. Dorrell. Online parameter identification of ultracapacitor models using the extended Kalman filter. *Energies*, 7(5):3204–3217, 2014.

[188] L.L. Zhang and X.S. Zhao. Carbon-based materials as supercapacitor electrodes. *Chemical Society Reviews*, 38(9):2520–2531, 2009.

[189] Y. Zhu, S. Murali, M.D. Stoller, K.J. Ganesh, W. Cai, P.J. Ferreira, A. Pirkle, R.M. Wallace, K.A. Cychosz, and M. Thommes. Carbon-based supercapacitors produced by activation of graphene. *Science*, 332(6037):1537–1541, 2011.